Investigation of Additive Manufacturing for Producing Electrical Steel Components and Texture Development via Laser Metal Deposition

Rasoul Karami

The University of Strathclyde

Department of Design, Manufacturing & Engineering Management

A thesis submitted for the degree of Doctor of Philosophy

April 2025

Supervisors: Prof. David Butler, Dr. Yashar Javadi and Dr. Saeed Tamimi

Declaration of Authorship

This thesis is the result of the author's original research. It has been composed by the author and has not been previously submitted for examination which has led to the award of a degree.

Signed:

Date: 09/10/2024

Previously published works

Parts of this thesis have appeared in the following peer reviewed publications:

- **Additive Manufacturing Innovations: Microstructure Optimisation for Ultra-High Silicon Electrical Steel Components**
  Rasoul Karami*, David Butler, Yashar Javadi, Saeed Tamimi
  Materials Characterization Journal, Vol. 224 Pages 115002,2025

- **Manufacturing of non-grain-oriented electrical steels: Critical Review**
  Rasoul Karami*, David Butler, Saeed Tamimi
  The International Journal of Advanced Manufacturing Technology 2024
  Published: 04 June 2024, Volume 133, pages 1083–1109, (2024)

- **Process window for manufacturing soft magnetic FeSi 6.5% by laser metal deposition**
  Rasoul Karami*, David Butler, Yashar Javadi, Saeed Tamimi
  21st International Conference on Manufacturing Research (ICMR2024), Glasgow, August 2024

- **3D Printing**
  Karami*, Rasoul and Berjozkina, Galina; Buhalis, Dimitrios, ed. (2022) *3D printing.* In: Encyclopedia of Tourism Management and Marketing. Edward Elgar Publishing, [S.I.]. ISBN 9781800377479

- **3D printing in tourism: an answer to sustainability challenges?**
  Karami*, R. and Berjozkina, G. (2021), "3D printing in tourism: an answer to sustainability challenges?", Worldwide Hospitality and Tourism Themes, Vol. 13 No. 6, pp. 773-788. https://doi.org/10.1108/WHATT-07-2021-0100

Abstract

This thesis presents the first successful application of additive manufacturing (AM), specifically Laser Metal Deposition (LMD), to fabricate high-silicon electrical steel (Fe-6.5 wt% Si) components for electrical machine applications. The alloy is extremely difficult to process due to its brittleness and high cracking tendency, making conventional manufacturing routes unsuitable. To address these challenges, this research focuses on optimising the alloy's metallurgical properties, microstructure, and crystallographic texture to enhance its magnetic performance through the innovative use of LMD.

A systematic process window was developed by varying laser power (400–500 W), scanning speed (360–440 mm/min), and powder feed rate (2.0 g/min) under controlled argon shielding. Porosity analysis revealed values ranging from 0.1% to 1.3%, with sub-optimal parameters leading to lack-of-fusion pores at low laser power and high scan speed, and to keyhole porosity and cracking at excessive laser power. Optimised conditions consistently yielded dense builds with porosity below 0.2%, with some samples entirely free of cracks.

Comprehensive microstructural analysis was performed using optical microscopy, scanning electron microscopy (SEM), electron backscatter diffraction (EBSD), and energy-dispersive X-ray spectroscopy (EDS). The study identified processing conditions that promote a strong <001> crystallographic texture while minimising the presence of undesirable <111> orientations—critical for optimising magnetic properties. The influence of laser power, scan speed, scan strategies, energy density, grain size, grain boundary characteristics, and kernel average misorientation (KAM) was examined, revealing how optimised LMD settings reduce defects and enhance microstructural quality. Mechanical properties were evaluated using Vickers hardness testing, which showed maximum values of 376–386 HV at higher energy densities, attributed to improved fusion, reduced porosity, and the formation of ordered phases (DO_3, B_2) that restrict dislocation movement.

The results confirm that LMD can produce FeSi 6.5 wt% components with minimal defects, good hardness, and improved texture alignment. The developed process window enables consistent, repeatable fabrication of core materials and other soft magnetic components for electric motors. Additionally, the use of 316L austenitic steel as a foundation layer during LMD successfully resolved the persistent cracking and bonding issues typically associated with direct FeSi deposition. By optimising process parameters, the bonding quality was greatly improved, leading to enhanced magnetic properties through the promotion of a strong <001> crystallographic orientation. This alignment is crucial for maximising magnetic performance and overall efficiency in advanced applications. Further geometric modifications strengthened the <001> texture, minimising residual stresses and completely eliminating cracking, even without the need for a foundation layer. This breakthrough demonstrates the potential of multi-material deposition and geometric design optimisation in advancing the fabrication of magnetic components, paving the way for superior performance in high-tech applications. Overall, this research provides pioneering insights into optimising the crystallographic texture of electrical steel via LMD, enabling the fabrication of high-performance components for electrical machines. Future work should explore novel stator designs, such as Hilbert structures, and hybrid manufacturing approaches to fully harness the potential of AM technologies in this field.

"As you start to walk on the way, the way appears"

Rumi

Acknowledgements

It has been a challenging experience, especially after resigning from my job at British Steel to start a PhD journey. The pandemic added layers of complexity, with lockdowns, personal struggles, and project delays, but the support from my family, friends and colleagues has kept me grounded. I would like to express my heartfelt gratitude to my supervisors: David Butler, Saeed Tamimi, and Yashar Javadi, who has been instrumental in my PhD journey. My sincere thanks also go to Dorothy Evans, Ioannis Violatos, and Paul Campbell, as well as the Saad Ahmed, the LMD machine technicians, Michael Canavan and Lewes Glen for their invaluable technical support, and to Kornelia Kondziolka for her assistance in the preparation lab. I am deeply grateful to Ryan O'Neill for his unwavering support in obtaining beautiful EBSD data. My gratitude extends to HMT for printing and depositing my materials, and to Peter Jon Solomon and Charlie Mann for their assistance.

I wish to acknowledge the friendship and encouragement I received from my fellow doctoral researchers, who are not just excellent co-workers but also good friends. I look forward to collaborating with all of you in the future and wish you every success in your endeavours. I must recognise my little brother, my mentor, Luis Reig Buades, whose relentless support, guidance, and encouragement have been invaluable throughout my PhD journey. I am grateful for the new friendships formed during this time, such as with Masanori Kamiya and his wife, who brought joy and laughter, and Paul Colombel, who dedicated his time to helping analyse the data.

I also want to thank Mauro Arcidiacono for being a wonderful presence next to my desk throughout this journey. Special thanks to Angus Coyne-Grell for helping me analyse some of the data, while also being a great friend and advisor throughout this process and also special thanks to Elen Williams for her help in analysing data and conducting tests together; I truly enjoyed our conversations. Although you joined AFRC later, your contributions exceeded my project, and your kindness has made a lasting impression. Also, I would like to extend my thanks to everyone, including colleagues who may not have directly contributed to my PhD. Your presence and challenges have pushed me to grow, step out of my comfort zone, and ultimately complete this journey. I would also like to thank Frances Roman, who inspired and supported me in bringing this chapter of my life to a close.

Most importantly, I am deeply thankful to the love of my life, Sogand, who encouraged me to keep pushing forward, never give up, and supported me through the darkest times of my PhD. She believed in me without hesitation or doubt. Even her presence in my life toward the end of my PhD made this challenging and difficult journey joyful and purposeful. I am truly grateful for the love and support I have received from everyone, especially from her.

I also wish to acknowledge my brothers, Saeed, Masoud, Farshid, and Ali, who have continuously encouraged me to pursue my dreams. Thank you all for your unwavering support.

Words cannot fully convey the love, gratitude, and admiration I have for my family. To my mother, who sacrificed so much to ensure my education and instilled in me the importance of dignity and perseverance, without your unwavering support, I would not be where I am today. To my father, who has provided both financial and emotional support, I am eternally grateful for your hard work and dedication to our family. I have always wanted to make you proud.

I dedicate this PhD to you Mom and Dad.

Thank you all for your time and support.

Table of Contents

List of Figures

List of Tables

Table of Abbreviations

NGOES	Non grain oriented electrical steel
GOES	Grain oriented electrical steel
BCC	Body centred cubic
ND	Normal direction
RD	Rolling direction
TD	Transverse direction
ASR	Asymmetric rolling
R-BUT	Repetitive bending under tension
SR	Skew rolling
PVD	Physical vapor deposition
CVD	Chemical vapor deposition
AM	Additive manufacturing
LMD	Laser metal deposition
CAD	Computer aided design
BD	Building direction
STL	Standard triangulation language
LPBF	Laser powder bed fusion
SLM	Selective laser melting
BJ	Binder jetting
EBSD	Electron backscatter diffraction
IPF	Inverse pole figure
PF	Pole figure
ODFs	Orientation distribution functions
HAZ	Heat affected zone
MIPAR	Materials image processing and automated reconstruction
SEM	Scanning electron microscope
PSD	Particle size distribution
EDS	Energy dispersive X-ray spectroscopy
EDM	Electrical discharge machining
XCT	X-ray computed tomography
Wt	Total power loss

Wh……Hysteresis loss
We……Eddy current losses
Hc……Coercivity
Br……Remanence flux
G……Thermal gradient
R……Solidification front velocity
KAM……Kernel average misorientation
GNDs……Geometrically necessary dislocations
LAGBs……Low angle grain boundaries
HAGBs……High angle grain boundaries
α…… α-fibre
α*…… α star-fibre
γ ……γ-fibre
θ ……θ -fibre
λ ……λ-fibre
η ……η-fiber

Chapter 1

1 Manufacturing of non-grain oriented electrical steels: Literature Review

1.1 Introduction

A section of this chapter has been adapted from a paper previously published in the International Journal of Advanced Manufacturing Technology, titled "Manufacturing of Non-Grain-Oriented Electrical Steels: Critical Review". This paper provides an in-depth review of the challenges and advancements in the manufacturing of electrical steels, with a particular focus on non-grain-oriented electrical steels. By incorporating this work, this thesis consolidates relevant background information, offering a comprehensive understanding of the current state of research in this area and providing a foundation for the subsequent discussions.

Many major countries have announced their ambitions to achieve NetZero greenhouse gas emissions by 2050 as the world attempts to limit the rise in global temperature to below 1.5°C. Immediate actions need to be taken to meet this goal, reduce overall emissions, and minimise energy consumption. Electrification has been identified as one of the means to help reduce emissions, with a particular focus on the transportation sector, including automotive, aerospace, and, more recently, the maritime industry. The manufacturing industry is a significant global energy consumer, and a substantial portion of its energy consumption can be attributed to the usage of industrial electrical motors. The electrical motor is crucial to the electrification drive, and its wider adoption is seen as one of the key thrusts of the decarbonisation movement [1].

Electrical motors consist of windings, cores (stator, rotor), permanent magnet materials and shafts, frames (casing), and caps. Most of the electrical motors windings are constructed of Cu and Al, whereas cores are formed of laminated electrical steel mainly due to their magnetic properties [2]. Electrical steel is a soft magnetic material which can be found in electrical motors, transformers, and generators [3]; it can be produced by several manufacturing routes [4, 5]. Significant research has been undertaken on the improvement of metallurgical characteristics of electrical steel through thermomechanical manufacturing processes like hot rolling [6], cold rolling [4], and multistage annealing [7, 8]. These manufacturing operations have a substantial impact on improving the mechanical and magnetic properties of electrical steel, while the focus on increasing the efficiency of electrical motor parts, such as laminated electrical steel sheets for magnetic purposes. It has also been reported that electrical steel with a high content of Si can be fabricated through additive manufacturing (AM) techniques [5, 9], which significantly improves the magnetic properties of laminated electrical steel and enhances the performance of electrical machines. Magnetic properties such as magnetic permeability, saturation magnetisation, hysteresis, and eddy current losses can influence the performance of electrical machines, including energy losses, power density, and efficiency [10-12]. In electrical machines such as motors and generators

energy losses occur due to various physical phenomena such as copper losses, iron losses, mechanical losses [13], and stray load losses [14]. In soft magnetic materials, one of the major energy losses is iron loss, which has been a recent focus for researchers [15-17]. More importantly, reducing energy losses is key for enhancing the efficiency of electrical motors, especially where energy consumption is a concern. Higher efficiency means lower operating costs as well as reducing the heat generated by electrical machines, which prolongs the lifespan of equipment [18]. Typical energy losses of a 50HP machine [19] can be seen in Figure 1. Further discussion on reducing losses in electrical machines and improving magnetic properties will be provided in other sections with more detailed analysis.

Manufacturing electrical steels remains an evolving field with certain challenges and gaps in its current progress. Despite recent advancements, some key areas such as processing technology and material compositions require further development. For example, maintaining consistent metallurgical properties across large-scale production [20] and eliminating defect formation during the manufacture of high silicon steel [21] present significant challenges. Another challenge is ensuring uniform grain orientation [22] and controlling grain boundary properties [23], which are essential for optimising the performance of electrical steel sheets and reducing energy losses, including eddy current and hysteresis losses [24]. Addressing these challenges necessitates further advancements in manufacturing techniques, materials design, optimising processing parameters, new characterisation techniques, recycling technology. These aspects will be covered in detail in subsequent chapters.

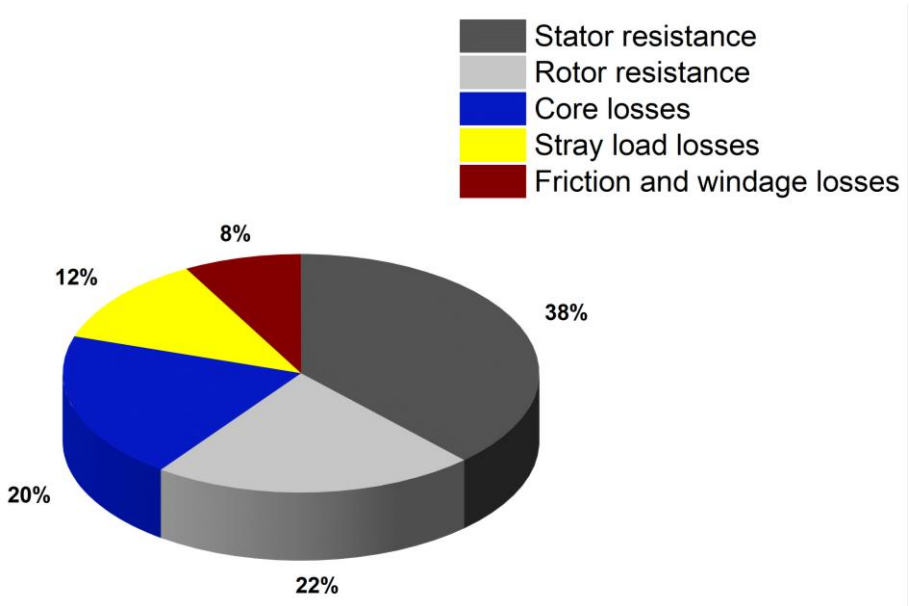

Figure 1. Typical energy losses in 50HP motor [19].

1.2 Scope of this review chapter

In this review chapter, the main focus is on the manufacturing of electrical steel, encompassing both conventional production methods and novel alternative thermomechanical processes. The impact of different manufacturing routes on

microstructure, texture development, and magnetic performance is also examined. Furthermore, an overview of various manufacturing process routes for electrical steel is presented, highlighting existing research gaps and challenges faced in this field.

1.3 Electrical Steel

In the 20th century, the demand for electrical steel increased dramatically due to the requirements for transportation and the generation of electrical energy [25]. Electrical steels are also referred to as silicon steel and were developed by Robert A Hadfield at Sheffield in 1886. Hadfield designed soft magnetic materials by adding different alloying elements to iron such as carbon, nickel, aluminium, and silicon. The results illustrated that most of the elements were not suitable for magnetic applications except silicon. Silicon significantly enhanced the magnetic permeability and electrical resistivity but it also could decrease the coercivity [25]. Hadfield's breakthroughs were investigated by other scientists, which confirmed that, among all the different soft magnetic materials, silicon steels (Fe-Si systems) could be the best candidate for magnetic applications. From a metallurgical perspective, there are relationships between magnetic properties and the percentage of silicon, microalloying, microstructure, and particular crystallographic textures. Based on the microstructure of electrical steel and their applications, they are classified into two types; grain-oriented electrical steel (GOES), and non-grain-oriented electrical steel (NGOES) as shown in Figure 2 [26]. The difference in grain structures arises from their processing: GOES undergoes a carefully controlled thermo-mechanical process, including primary recrystallisation and secondary recrystallisation, which produces large, elongated grains with a sharp Goss texture {110}<001>. In contrast, NGOES is processed without such strong texture control, leading to equiaxed grains with random crystallographic orientations, and therefore isotropic magnetic behaviour in the sheet plane [27, 28].

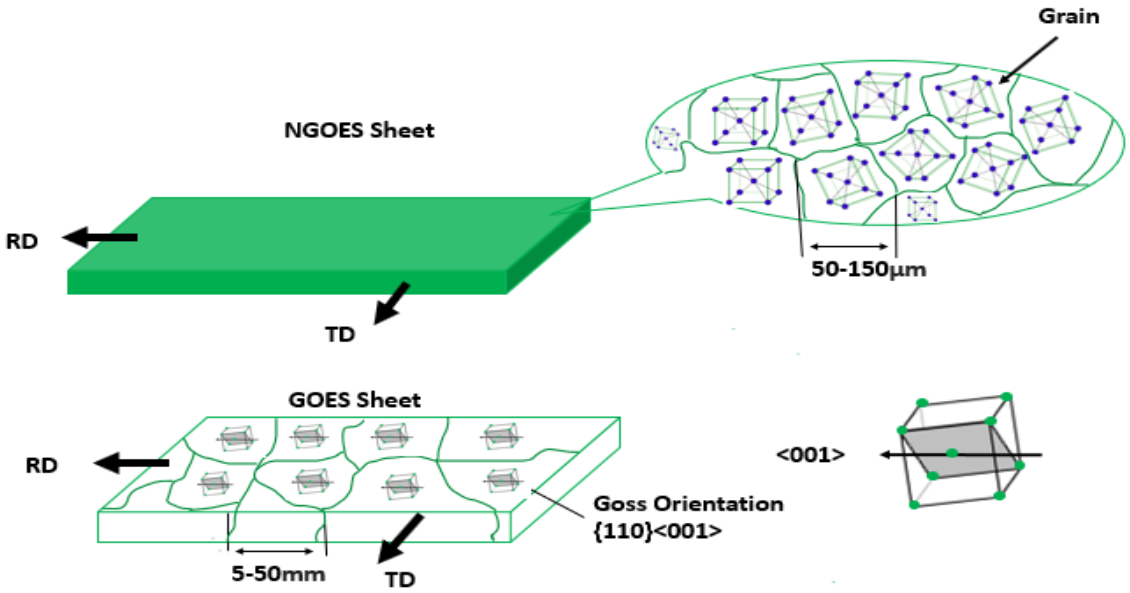

Figure 2. A schematic diagram showing non-oriented electrical steel (NGOES) and grain-oriented electrical steel (GOES) [29].

The GOES texture typically exhibits a distinct Goss texture {110} <001>, where the two easy magnetisation directions, <001>, align parallel to the magnetic field direction. Appropriate magnetic properties in GOES can be obtained in the rolling direction with high permeability and low core loss which can be used in core materials, especially in transformers, in order to increase the energy efficiency and improve performance [30].

In terms of quality, the iron core material must have good soft magnetic properties as well as be fully recrystallised. The desirable texture for the core would be achievable by secondary recrystallisation if the annealing temperature is high enough. Therefore, the elongated grains in GOES are the result of abnormal grain growth during secondary recrystallisation, whereas the equiaxed grains in NGOES arise from random orientations due to the absence of such selective texture development [27, 28].

In contrast, NGOES contain random textures with the same magnetic properties in the sheet plane. This type of electrical steel can be used in a variety of applications, such as rotating electrical machine parts in the electric motor, stator cores, turbogenerator stator, generators [6, 26, 31] and high-speed permanent magnet synchronous machine for an aircraft application [32]. It is significant to note that core loss and magnetic induction play a crucial role in NGOES. Core loss refers to the energy dissipated as heat in the magnetic core material when it is subjected to alternating magnetisation. It consists mainly of hysteresis loss, caused by repeated domain wall motion, and eddy current loss, induced by circulating currents within the material [33, 34]. Core loss directly impacts motor efficiency, with higher efficiency associated with lower core loss and magnetic induction is directly proportional to torque. Developing products with lower core loss and high magnetic induction in practical applications can be challenging [34].

The magnetic properties of the materials that are used in the construction of electrical machines are critical in order to achieve the highest magnetic performance. The production volumes of ferromagnetic materials increased in 2016, with NGOES accounting for almost 80%, while GOES and other soft magnetic materials contributed 16% and 3.9%, respectively [35-38]. Considering the market demand to have electrical motors with higher performance may create opportunities to develop new approaches. This requires the electrical steel manufacturers to produce electrical steel with the higher silicon contents to improve magnetic properties and thus take advantage of it. One of the methods used to improve magnetic properties of NGOES is the secondary recrystallisation process. For example, NGOES with a coarse grain structure and a pronounced rotating texture {100} <011> achieved through this process. This process leads to an improvement in the magnetic properties of NGOES due to an increase in grain size, as well as the obtaining of an appropriate final texture such as a cube crystallographic orientation [39]. Another example to improve the texture of NGOES during secondary recrystallisation was reported by [40]. The study focused on optimisation the microstructure of NGOES produced by compact strip production in order to improve magnetic performance. Having said that, secondary recrystallisation alone is not sufficient to optimise all desirable magnetic properties of NGOES. Additional factors such as

texture and microstructure optimisation, necessity content reduction need to be considered which will be covered in other sections in more detail.

1.3.1 Industry- statistics

Electrical steel with silicon content (>3.5%) is generally used in a variety of industrial applications such as transportation. The transportation industry, which contributes significantly to global pollution and climate change, especially motor vehicle emissions which account for 22% of all CO_2 emissions worldwide [41]. Therefore, the automotive industry can contribute to tackling climate change by producing more efficient motors in electric vehicles [42]. Tata motor [43] , ThyssenKrupp [44], and Kawasaki Steel [45] all produce sustainable electrical steel for automotive electrical components. These include electric motors, energy storage systems, conversion systems, electrical power steering, and fuel pumps. A 2018 report on the global NGOES and GOES market [38] highlighted production and market trends for these materials, estimating the industry's value at more than 24 billion USD, with an expected annual growth rate of 7.2% by the end of 2025 [37]. Moreover, the global market reported for 2024 [46] illustrated that the market size of NGOES has grown strongly from 14.32 billion USD to 15.05 billion USD from 2023 to 2024, with an annual growth rate of 4.3%. It also predicted that NGOES demand will contribute to further grow, with the market projected to reach 17.81 billion USD by 2028. Additionally, major countries such as China, Russia and Brazil are the leaders in silicon production with annual respective production volumes of 5.4 million metric tons, 540,000 metric tons and 340,000 metric tons [47]. Just over 5 million electric cars were purchased globally in 2018, and this number is anticipated to reach 23 million by 2030 [37]. As a result, the need for producing electrical steel as core materials in electrical motors for the mentioned applications is growing. In 2023 [48] alone, electric car sales rose by 3.5 million from the previous year, a 35% increase, reaching over 250,000 new registrations per week. This demand surge highlights the growing need for electrical steel, a core material in electric motors.

Conversely, in the case of electric aircraft applications, where the total weight of batteries and the efficiency of electrical motors play a crucial role [49]. Improving battery and electrical motor technologies is essential for reducing the environmental footprint in aviation, as these factors have a significant impact on air pollution (approximately 2-3%) and climate change [50]. Moreover, the electrification of flight plays a crucial role in the sustainability strategy aimed at achieving NetZero carbon emissions in the UK by 2050 [51]. The major driving force for growing electrification market is the collaboration between manufacturers such as Boeing [52], Rolls-Royce [53], Airbus [54], and Safran [55]. However, to achieve these goals with the current existing technologies is difficult. Nonetheless, recently, high-speed permanent magnet synchronous motors for the high-lift system in electric aircraft have been manufactured, as depicted in Figure 3. Fe-Si emerges as a promising candidate for future electric motors in the aerospace sector [32]. Moreover, as suggested by [56], ultra-thin GOES sheets show great promise for application in the propulsion systems of electric vehicles, particularly in permanent magnet synchronous motors.

Generally, electric aircraft manufacturers use Co-Fe rather than Fe-Si due to better magnetic induction, low core loss, and high permeability. The adoption of Fe-Si alloy in certain applications has gained traction due to its advantageous properties and specific suitability for various purposes. Its use has been prompted by considerations beyond solely technical factors, including aspects related to supply chain stability and material availability compared to Co-Fe [57]. However, the global production chain of NGOES faces various challenges, including supply chain vulnerabilities restricting access to raw material storage [58], market volatility [59], geopolitical tensions [60]. Additionally, there is a necessary need to comply with strict environmental regulations in accordance with government policies, crucial for promoting eco-friendly manufacturing practices and meeting emission standards [61, 62]. However, these challenges also present opportunities for NGOES production. This includes embracing advanced industrial practices, promoting recycling of materials, and building strong partnerships with stakeholders, research institutions, and suppliers. By effectively navigating these challenges, the NGOES production chain can switch the industry towards sustainable growth and align with evolving global market demands.

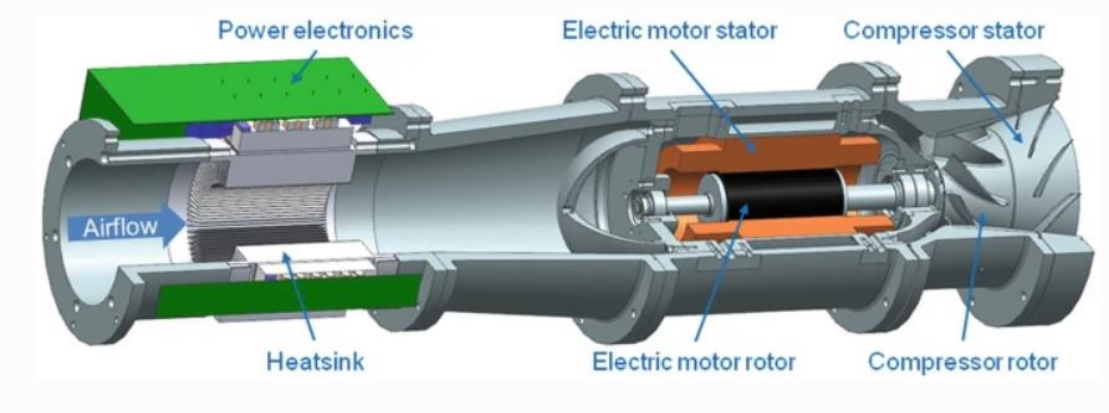

Figure 3. Illustrated high lift system powered electrically [63].

1.3.2 Research and academic publications- statistics

As can be seen from Figure 4, the number of publications on electrical steel in different areas has steadily risen from 200 in 2000 to around 600 in 2022, suggesting increased interest in this field [64]. There are several reasons that could support and explain why the publication of electrical steel has increased significantly. For example, energy efficiency regulations employed by governments across the globe aim to improve the efficiency of various industrial applications [62]. Electrical steel is a key player in meeting these regulations by reducing energy losses in generators, motors, and transformers [65]. Furthermore, advancements in the manufacturing process of electrical steel enable researchers to enhance its magnetic properties and reduce core losses. This leads to increased interest in electrical steel development as well as investment [66]. Also, the demand for renewable energy technologies, such as electric vehicles [34] and wind turbines [67], has increased dramatically, acting as a driving force for more efficient generators and electrical motors used in these devices. In the construction of generators and electric motors, electrical steel is a critical

component that can improve the efficiency of electrical motors and generators, thereby maximising energy conversion. This indicates how dynamic this area is at the universities and research, and these fields are rapidly expanding due to their environmental and industrial impact.

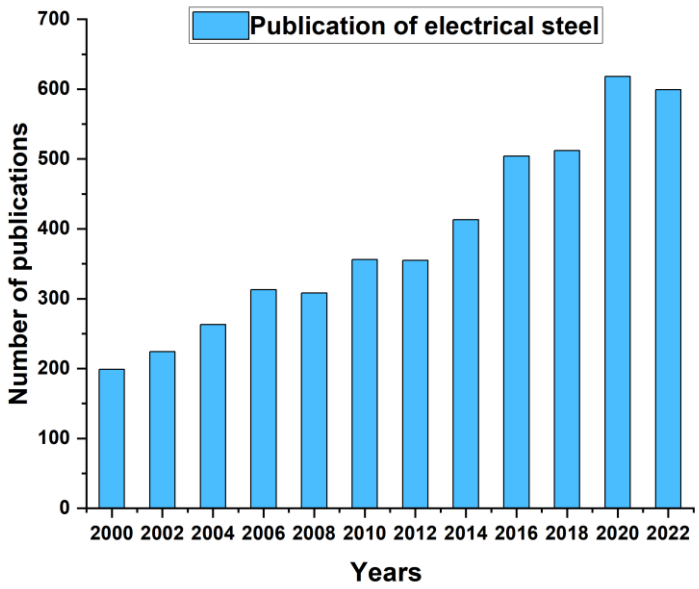

Figure 4.The number of electrical steel -related publications from 2000 to 2022 [64].

Figure 5 displays the number of publications in various areas related to electrical steel technologies from 2000 to 2022. It is evident that the scientific community has placed the highest focus on metallurgy, applied physics, and electrical engineering. These findings suggest that there is a greater level of activity and interest in the fields of metallurgy and physics compared to other areas. This occurs perhaps because these fields are at the forefront of technological innovations in materials science and engineering, with numerous applications of electrical steel in generators, transformers, electrical motors, transportation, and electronics [29]. Additionally, research institutions may prioritise projects and funding in metallurgy and physics due to their crucial role in advancing knowledge, as well as improving properties of materials [68]. Overall, it can be said that the increase in publications related to electrical steel in metallurgy and physics is driven by advancements in technology, industrial applications, and available funding.

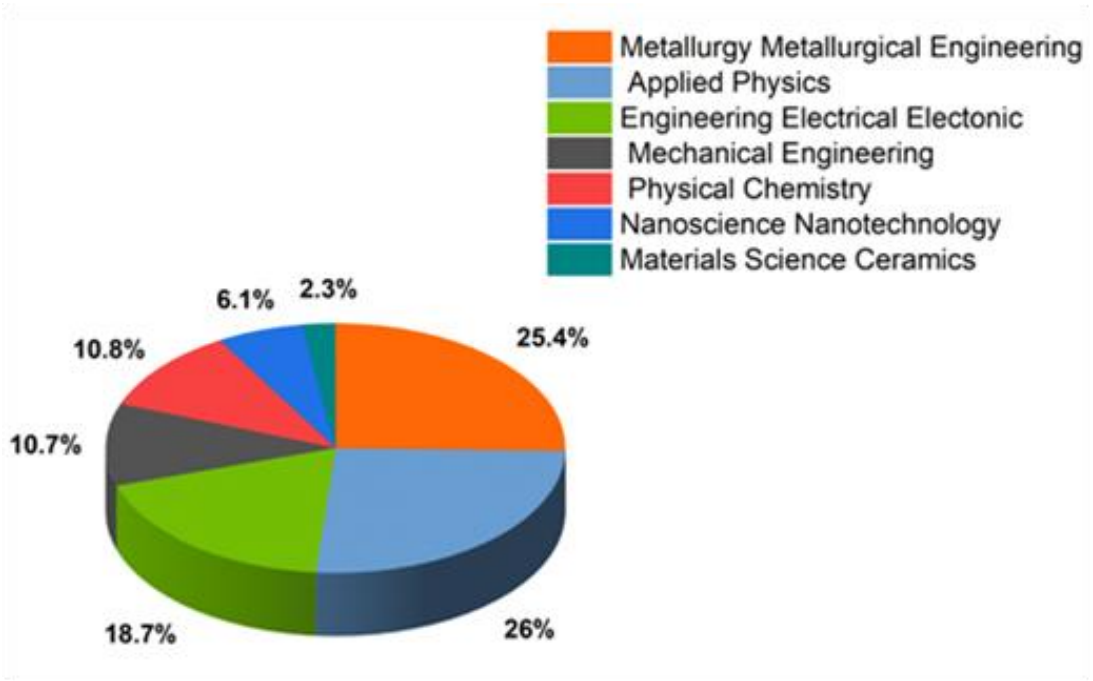

Figure 5. Analysis of the number of electrical steel-related papers published in different disciplines [64].

1.4 Metallurgy of electrical steel

Magnetic materials are generally classified into two types: soft magnetic and hard magnetic materials. Hard magnetic materials are those materials which are difficult to magnetise and demagnetise and have high hysteresis losses and coercivity, whereas soft magnetic materials are recognised as the materials with high permeability and low energy loss. The soft magnetic materials were developed early in the electrical application process and are considered as the main sources for progress in the second industrial revolution. These magnetic materials can be used in many different applications such as generators, transformer cores, automotive, electrical motor, and other appliances [69]. From a metallurgical point of view, soft magnetic materials can be categorised into several sub-classes for example: soft magnetic composite [70], soft ferritic, Fe-Si steel [35], Ni-Fe [71], Co-Fe [72], amorphous soft magnetic [73].

Soft magnetic composites are typically produced by bonding iron powder particles coated with electrically insulating layers, a process that minimises eddy current loss. In the conventional route, the coated powders are compacted in a die and subsequently cured or heat-treated to achieve the required mechanical and magnetic properties [74]. However, other fabrication approaches, such as additive manufacturing and advanced compaction techniques, are also being explored for soft magnetic materials hold great promise for manufacturing electrical machine parts like stators [70, 75-77].

Although soft magnetic composites offer certain advantages, studies have shown that they often display less favourable magnetic properties and reduced efficiency at higher operating frequencies, which can result in higher costs when compared with conventional laminated steels [78, 79]. On the other hand, these materials are easier to process, as they can be more

readily assembled, crushed, and separated for recycling [80]. In terms of market share, Fe–Si alloys remain the dominant soft magnetic material, accounting for more than 97% of today's applications across different industries [81], whereas Co–Fe alloys are used only in specialised, high-performance applications due to their limited availability and higher cost [36].

1.5 Adding Si to electrical steels as alloying element

Generally, silicon is a crucial element in the production routes and can exhibit a variety of beneficial characteristics. Silicon is the main alloying element for electrical steels (typically ranging from 0.5 to 6.5 wt.%, depending on the application) which improves their magnetic properties such as electrical resistivity, while as well as reducing saturation polarization which can be seen in Figure 6. For NGOES commonly used in motors, generators, and electric vehicle applications, the typical Si content is 0.5-3.5 wt.%, with saturation polarization ranging from 1.7-2.0 T and electrical resistivity from 20-50 μΩ·cm. In contrast, for high-performance applications such as advanced transformers or high-frequency devices where lower core losses are prioritized, higher Si contents up to 6.5 wt.% are used, resulting in saturation polarization around 1.5 T and electrical resistivity up to 80 μΩ·cm. These variations optimise the trade-off between magnetic performance and energy efficiency for specific uses. Figure 6 illustrated the trends in saturation polarization and electrical resistivity as silicon content varies, highlighting the trade-offs critical to tailoring steel properties for diverse applications [33, 82, 83].

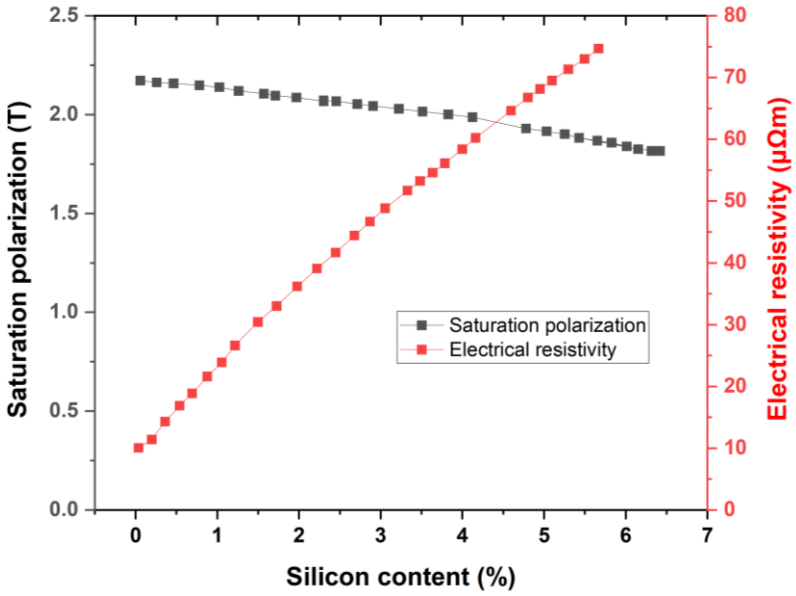

Figure 6. Influence of Si on magnetic properties of electrical steel [83].

Manufacturing high silicon electrical steel sheets (above 3.2%) presents challenges due to lower formability and increased brittleness [84], leading to the formation of cracks in electrical steel sheets during the process [85, 86]. The phase diagram of electrical steel, as depicted in Figure 7, shows that an increase in the silicon percentage of approximately 5.3 wt.% results in B_2 structure ordering (FeSi type), while the formation of DO_3 ordering ($FeSi_3$

type) begins when the Si concentration exceeds 6 wt.% and both phases are brittle. The formation of these ordered phases can make electrical steel brittle (i.e. up to 600°C for Si 6 wt.%) [25]. The main reasons for the formation of these phases include factors such as atomic arrangement, interatomic forces, thermodynamic stability, and phase transformation. For example, changing the percentage of silicon could impact the atomic arrangement as well as bonding, which promotes the formation of these phases. Also, the interaction between silicon atoms and other elements in the alloy could affect the stability of the crystal structure as well as interatomic forces, resulting in unfavourable brittle phases. Moreover, it can be said that the B_2 phase may be more dynamically stable when a specific percentage of silicon is added to the alloys, which could promote nucleation and growth of the B_2 phase. Although the B_2 phase is thermodynamically stable and favourable, other factors such as temperature, pressure, cooling rate [87], processing conditions, and thermal history could impact the dynamics of phase transformation [88]. These phases could have a negative impact on magnetic properties, which can be optimised, to some extent, by employing heat treatment [89].

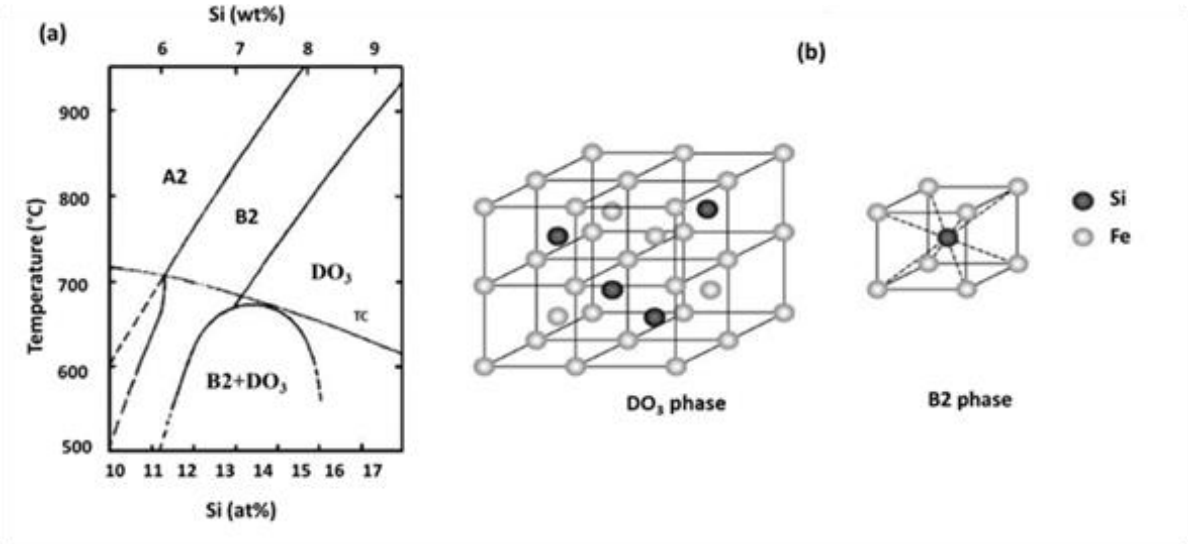

Figure 7. FeSi phase diagram (a) and the crystal lattice (b) of electrical steel [25].

As a result of these brittle phases, forming of the alloy requires to be conducted at higher temperatures however, this could be a challenge as cold rolling of electrical steel is a necessary process to achieve the final thickness with appropriate surface quality and to control the final microstructure. To overcome this limitation, approaches such as physical vapor deposition (PVD) [90], chemical vapor deposition (CVD) [91], fast quenching rate [92] and the direct powder rolling process [93] have been developed for obtaining high Si electrical steel. The Japanese company JFE steel [94] has introduced a continuous process to produce electrical steel as shown in Figure 8. The CVD technique is used to manufacture three different types of high silicon electrical steel sheets (super core). The first step in this process is to conduct cold rolling on a low silicon steel sheet (<4% Si) in order to obtain the desired thickness and, after that, the sheet is coated with a reagent supplied in the form of gas such

as $SiCl_4$ under a non-oxidising environment. A high-temperature atmosphere caused the reaction between Si and Fe on the surface of the silicon steel sheet and results in bonding silicon to the silicon sheet. Through the diffusion time, the chemical reaction below occurs [95].

$$SiCl4 + 5Fe \longrightarrow Fe3Si + 2FeCl2 \quad (1)$$

Following that, when the soaking time at high temperature is completed, this allows manufacturers to produce uniform high silicon content (6.5%) which provides superior magnetic properties [94]. These methods, however, are both costly and complex, and the laboratory-scale process is not environmentally friendly. Therefore, finding a suitable process in terms of economy, energy efficiency and a non-complex method has been prioritised by producers [96].

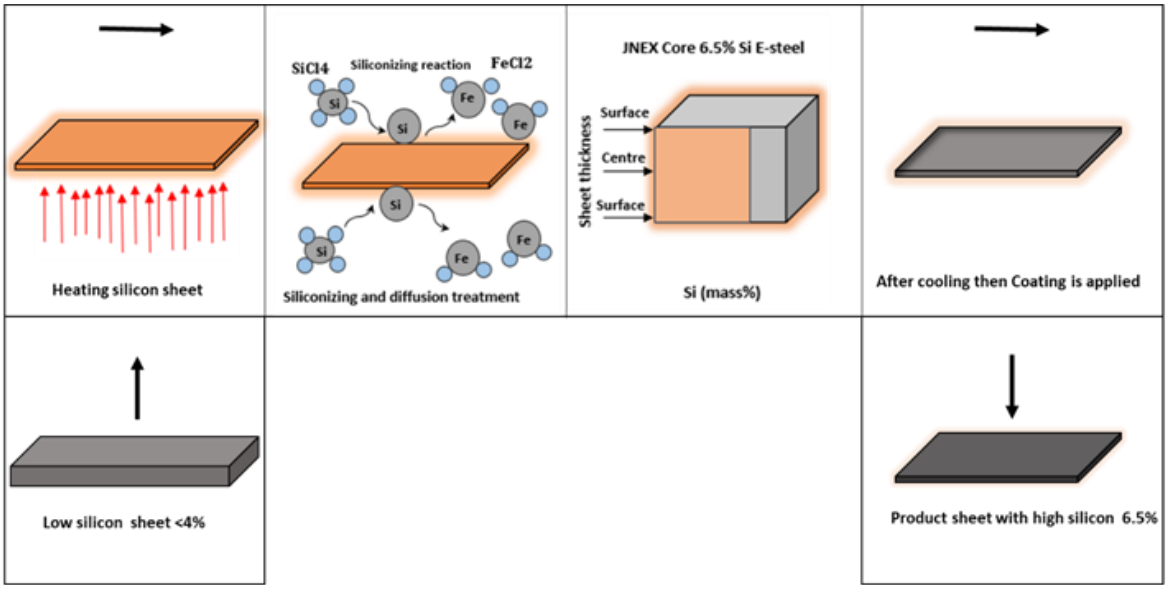

Figure 8. Manufacturing process of electrical steel by CVD technique [94].

On the other hand, the chemical composition could affect the magnetic properties of the electrical steel. For example, the existence of elements in the final product like titanium, boron, carbon, nitrogen, oxygen or sulphur can reduce the electrical resistivity of these materials, while silicon, aluminium, and manganese increase their electrical resistivity. For example, sulphur (exceeding 20ppm) is detrimental to the magnetic properties by generating a fine MnS precipitate and segregating the grain boundaries preventing the grain to grow. These precipitates behave as a barrier and prevent the magnetic domain wall moves, causing more iron loss. To compensate for magnetic losses, researchers recently applied manganese oxide coating on the surface of NGOES 2.4wt% FeSi. The results illustrate that optimal manganese diffusion occurs at 525°C, leading to a reduction in power losses such as eddy current and hysteresis loss by 9% due to increased resistivity [97]. The addition of phosphorus (0.14%) to NGOES sheet has been shown to decrease the undesirable {111} <112> component while increasing the favourable texture {100} [98]. This change in composition also leads to a finer grain size. Consequently, there is an increase in iron loss. However, the magnetic

induction was increased by adding phosphorus (0.14%) due to inhibiting recrystallisation of unfavourable texture such as {111} near the grain boundaries. Furthermore, the mechanical properties such as yield strength and tensile strength are improved due to the refinement of grain and solid solution strengthening mechanisms. Moreover, adding copper to NGOES can also considerably reduce core loss and increase magnetic induction by improving the recrystallisation texture due to the promotion of GOSS texture as well as hindering the hard magnetisation {111} texture [99]. The iron loss can also be related to different shapes of oxide inclusions. Oxides with an elongated shape prevent grains from growing, whereas spherical oxides would be less likely to affect grain growth. It is noted that if the amount of sulphur goes above a certain amount, this can cause a decrease in the grain size of the cold rolled electrical steel sheets [35].

The addition of silicon to electrical steels significantly influences their processing behavior in directed energy deposition (DED) techniques. Higher silicon content enhances the electrical resistivity and magnetic properties of the steel but also increases its brittleness, posing challenges during DED processing [100]. The increased brittleness can lead to issues such as cracking and porosity during deposition, which can adversely affect the mechanical and magnetic properties of the material. Additionally, the solidification rate during DED processing can be influenced by the silicon content, affecting the microstructure and overall quality of the deposited material [101].

1.6 The effect of grain size

The grain size is an important metallurgical factor which determines the magnetic properties in NGOES. Generally, in metallic materials, the finer grain structure means a higher strength and less ductility however, this is not ideal for Fe-Si due to the hindering motion of the domain walls (boundaries between two domains) and the negative impact on the magnetic performance Figure 9. The magnetic properties of NGOES are highly dependent on magnetic domains, while the mechanical properties rely on microstructure [102]. The results illustrate that some magnetic domains were compressed and fragmented, similar to grain deformation, while others were reconstructed like dynamic recrystallisation processes. This study [102] illustrates the complex relationship between magnetic domains, magnetic properties, and deformation process.

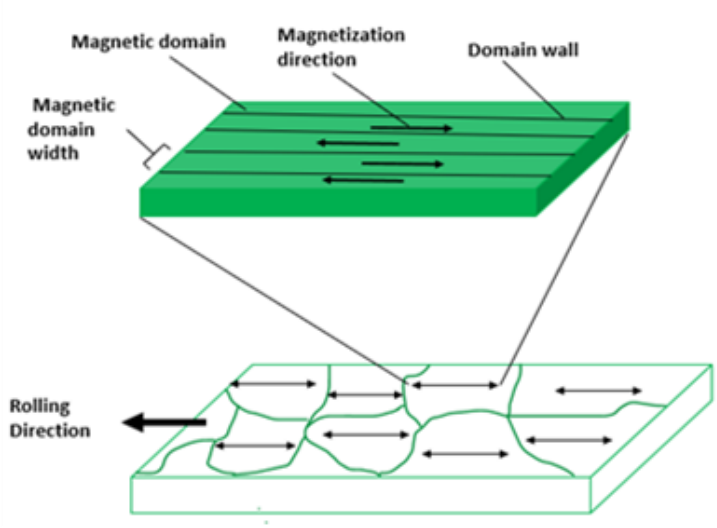

Figure 9. Demonstrated magnetic feature of GOES [102].

It is important to highlight that the effect of grain size on the magnetic properties of the blanking process (cutting electrical steel sheets into desired shapes using a punch and die) of NGOES (3.2wt.%Si) was also investigated by [103]. The results illustrated that blanking-related iron losses for the FeSi sheet with a thickness of 0.5mm decreased with increasing grain size (210 µm), whereas for the FeSi sheet with a thickness of 0.25mm, the iron losses increased with decreasing grain size (28 µm). This suggests that the grain size of NGOES significantly affects its magnetic properties and performance in electrical components. Therefore, to optimise magnetic efficiency, it is necessary to understand and control the grain size through appropriate processing technology. Recent evidence suggests the ideal grain size for magnetic purposes of NGOES would range between 50 to 150 µm [35]. Also, it was shown that the total power loss (Wt) equal hysteresis loss (Wh), and eddy current losses (We), in NGOES would decrease when the grain size reaches the optimum value of 150 µm [31], as illustrated in Figure 10**.** However, several studies have suggested that a larger grain size (e.g., 220 µm) can contribute to improving the magnetic properties of the NGOES [104]. This improvement is attributed to the increase in magnetic domain size with grain growth, which reduces both core and hysteresis losses. Also, smaller grain sizes lead to smaller magnetic domains, resulting in an increased number of domain walls and greater hindrance to their motion. Both mechanisms are key contributors to increased hysteresis losses in electrical steels [105].

The blanking process is not only a shaping operation but also a critical factor affecting magnetic performance. Poor control of blanking parameters, such as punch and die clearance, can introduce mechanical stresses, edge defects in the sheets, all of which increase local energy losses during magnetisation. Therefore, understanding and optimising the blanking process is essential to ensure high-quality electrical steel components with minimal losses. This contextualises why grain size effects during blanking are significant for practical electrical machine applications [106].

Computer simulation and modelling can be used to evaluate the relationship between grain size, microstructure, and texture to improve magnetic performance. These methods help assess the impact of different processing parameters on final products. The crystal plasticity finite-element method, for example, can predict the texture of cold-rolled NGOES sheets [103]. Additionally, texture and grain size during annealing can be analysed to understand the grain size development across the NGOES sheet [107]. In this study, based on simulation models and laboratory experiments, a relationship between processing parameters and magnetic properties was established for NGOES (3.16wt%Si). Simulation and modelling are effective for predicting the microstructure of NGOES, allowing scientists to forecast how the electrical steel microstructure and texture evolve during manufacturing processes such as cold rolling, annealing, and cooling. This predictive capability helps optimise processing parameters to obtain desirable microstructure properties such as grain size, crystal orientation and ultimately improve the magnetic properties of NGOES.

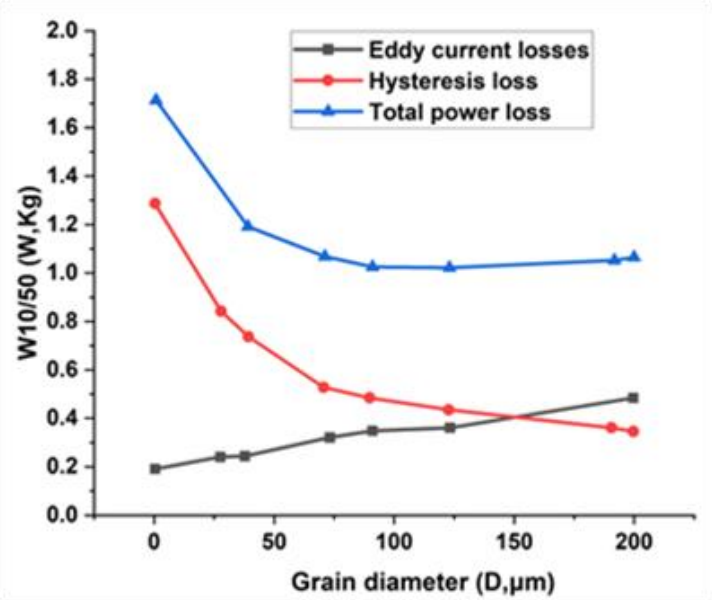

Figure 10. The effect of grain diameter on total power loss (Wt), hysteresis loss (Wh), and eddy current losses (We) [31].

As noted by Fiorillo (2016), magnetic power losses are strongly dependent on excitation frequency. At low frequencies (up to a few hundred Hz), hysteresis loss dominates, whereas at higher frequencies eddy current and excess losses become increasingly significant. In this context, the Steinmetz equation provides an empirical framework linking total core loss to frequency and magnetic flux density, highlighting the transition from hysteresis-dominated to dynamic loss-dominated regimes with increasing frequency. Consequently, for low-frequency applications (approximately 200–400 Hz), larger grain sizes are favourable, as reduced grain boundary density lowers hysteresis losses and minimises total energy dissipation. In contrast, for higher-frequency applications, smaller grain sizes are preferred, as they restrict eddy current path lengths and reduce dynamic losses (Figure 11) [73]. This behaviour is consistent with the Steinmetz-based loss separation approach, confirming the

frequency-dependent relationship between grain size and energy loss in soft magnetic materials [108]. However, this relationship is not linear, as magnetic losses are also influenced by domain wall motion, domain structure, microstructure, crystallographic texture, and intrinsic magnetic properties.

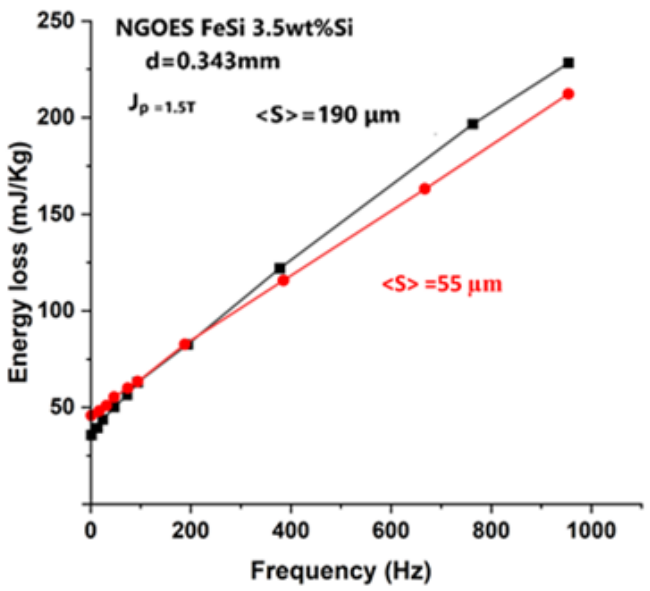

Figure 11. The overall energy losses of NGOES (0.343mm thick) were shown with two distinct grain sizes [73].

1.7 Crystallographic Texture

There is a significant number of research studies on how to improve the magnetic properties of electrical steel through crystallographic texture modifications e.g. [25, 109]. Typical texture components and crystallographic fibres in electrical steel with body centred cubic (BCC) structure are illustrated in Figure 12. When a small or strong magnetic field is applied to a specimen, the crystallite orientation may result in easy or hard magnetisation directions [26]. Recent studies reported that the hard and easy magnetisation axes in electrical steel are <111> and <001>, respectively [6, 35]. The easy magnetisation axis results in the increase in permeability and a decrease in energy losses in the transformer. Hence, the {110} <001> texture component (also known as the Goss component) is an ideal texture in electrical steel due to its <001> direction being parallel to the easy directions of the magnetic field [6, 110, 111].

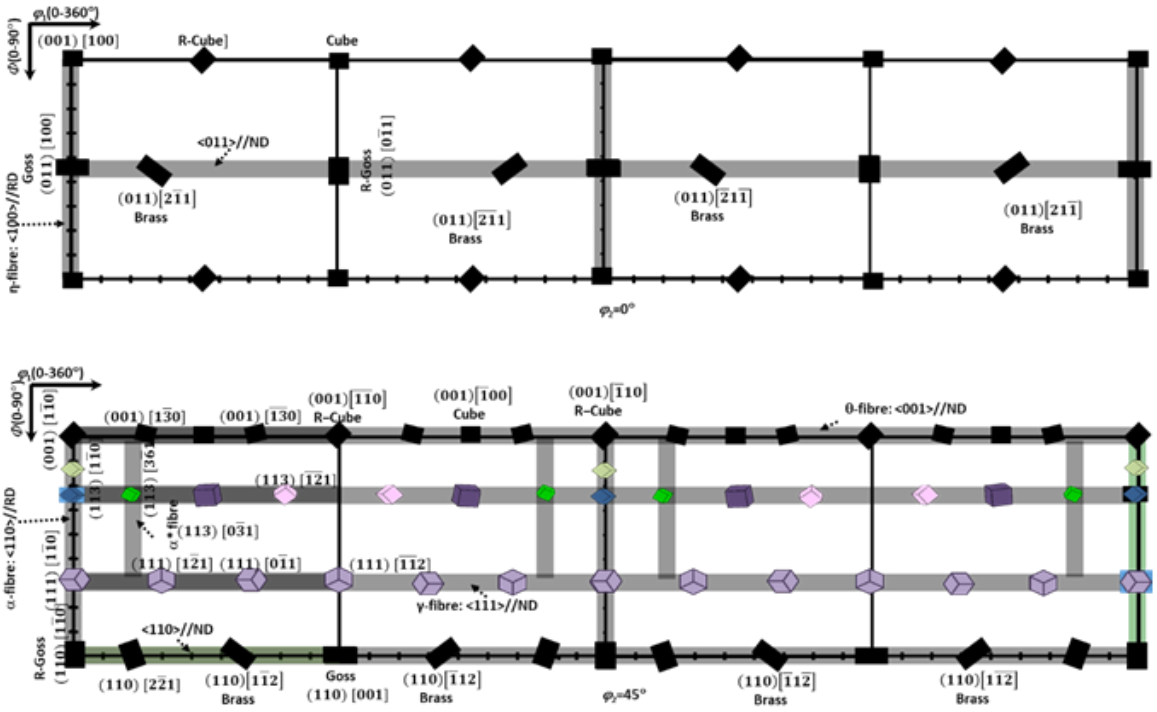

Figure 12. Common texture components and fibres in the BCC materials are demonstrated by using ODFs (orientation distribution functions) on the φ_2 = 0° and 45° sections (Bunge notation) [112].

In 1926, [113] recognised the magnetic anisotropy of iron, noting that the <100> direction serves as the easy axis of magnetisation, while the <111> direction acts as the hard axis due to differences in magnetocrystalline energy. This anisotropy is directly related to the atomic packing directions in the body-cantered cubic (BCC) structure of iron, where the <100> axes align with the cube edges for optimal magnetic stability, and the <111> axes, corresponding to the body diagonals, present greater resistance to magnetisation [114].

These insights extend to electrical steel, where key textures such as Goss texture {110}<001>, cube texture {100}<001>, and rotated cube texture, as depicted in Figure 13, are commonly found. Hence, it can be claimed that the crystallographic texture plays a critical role in defining the magnetic properties of electrical steel. On the other hand, in the core materials of rotating machines (i.e., core materials in stators and rotors), the angles between the rolling direction (RD) and the magnetisation field keep changing. Therefore, for rotating machines, the ideal crystallographic orientations would be the texture containing a less hard magnetisation axis, i.e., <111>. Hence, the (<100> // ND) fibre can be an ideal texture for NGOES as it has <001> easy magnetisation directions in the sheet plane and with random angles to the RD. This means that the sheet in its own plane will be isotropic to all possibilities in the rotation positions [26]. It is noted that by increasing the Si content (6.5 wt.% Si) the magnetostriction decreases along <100> but gradually increases <111> axes [91]. New methods have been proposed to test electrical steel for how easily it can be magnetised in different directions. In this study [115], the magnetic properties of GOES with 3 wt% Si were investigated using the Barkhausen effect, with its time-frequency representation used as a non-destructive testing tool. The Barkhausen effect refers to the series of voltage pulses produced when domain walls

move in sudden jumps as they encounter obstacles such as grain boundaries or precipitates. This phenomenon is important because it provides a direct link between microstructural features and magnetic behaviour, which makes it highly suitable for evaluating stress, texture and anisotropy in electrical steels. The results showed that this method is effective and has great potential for understanding the complex relationship between time and frequency characteristics in magnetic material behaviours. However, further improvements, such as the development of measurement systems and multi-thread analysis, are still needed [116].

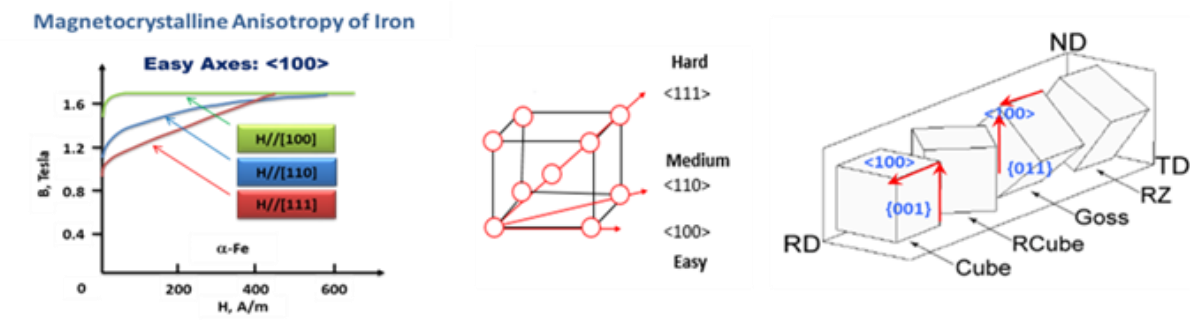

Figure 13. Magnetisation curve of pure Fe [35].

The texture development of electrical steels through recrystallisation has been studied by many researchers and this growing area contributes to improvements in understanding and performance [117-119]. The magnetic performance of electrical steel is highly dependent on the temperature of the final heat treatment annealing. For instance, when the electrical steel (3% Si) is annealed at 1070 °C for 50 hours, this can improve magnetic induction and decrease the minimum magnetic loss in the NGOES [120]. Additionally, a limited number of Goss grains can also selectively grow in the NGOES [60]. Kestens et al [121] conducted two stages of cold-rolling on the NGOES sheets. Random nucleation and subsequent selective growth can be used to explain the annealing texture of the traditionally rolled sheet (70% reduction). The latter is distinguished by the following physical characteristics: low angle grain boundaries with low mobility and (110) plane carrying the most slip during the deformation processes, and a small reduction in thickness of rolled sheet resulting in a low stored energy nucleation rate in the sample. Computer models further revealed that in the lightly rolled sheet, low stored energy nucleation is preferred [121].

1.8 The thermomechanical manufacturing process of electrical steel

The materials processing history such as casting, reheating, hot rolling, cold rolling, final annealing treatment and skin pass conditions can play a significant role in impacting on the mechanical and magnetic properties of electrical steel which can be seen in Figure 14 [6, 122, 123]. In conventional methods of manufacturing electrical steel, alloying elements are typically added during the casting stage to precipitate as normal grain growth inhibitors which determine the magnetic properties of the final product. During the reheating stage, the inhibitor materials (such as AlN and MnS) dissolve at high temperatures up to 1400°C [124].

During the high temperature slab pre-rolling can cause some surface areas of the slab to be remelted and create a problem during rolling and annealing processes. The hot rolling process in manufacturing electrical steel also promotes the production of finer precipitates of inhibitor elements, especially in GOES [125], but also influences texture and can lead to larger hot band grain sizes when finished at higher temperatures [126]. The main purpose of the cold rolling of electrical steel is to reduce the thickness of the sheet (~60 to 80%) which is one of the best ways to reduce core loss. After the cold rolling process, the decarbonisation process usually takes place to reduce carbon content (0.005% or lower) and reduce the magnetostriction effect [127]. By following that the annealing process conducted at ~700 up to 800°C, where certain crystals are preferentially formed from the primary recrystallised crystal with a desired magnetisation orientation. After passing through various stages in conventional manufacturing, the electrical steel sheet undergoes a final step wherein it is processed by a set of polishing rollers. This stage is crucial for smoothing the surface and controlling the thickness of the sheet. This gentle reduction and surface refinement process is known as the skin pass. During this stage, some deformation in the crystal structure can occur, potentially altering the crystallographic texture and magnetic properties to some extent. However, these changes are usually not as significant as those seen in other stages like cold rolling and annealing. Following this, the electrical steel sheet undergoes thermal compression and stamping for core fabrication [125]. However, internal or external mechanical stress can be induced at this stage by applying excessive compression force and tension during the shaping of laminations into a round shape and bending the electrical steel sheet during the edge-cutting process. This can be almost resolved by stress relief annealing treatment [128]. Following that the annealed thin sheet of electrical steel is usually subjected to skin pass to achieve a certain surface roughness as well as strength [129].

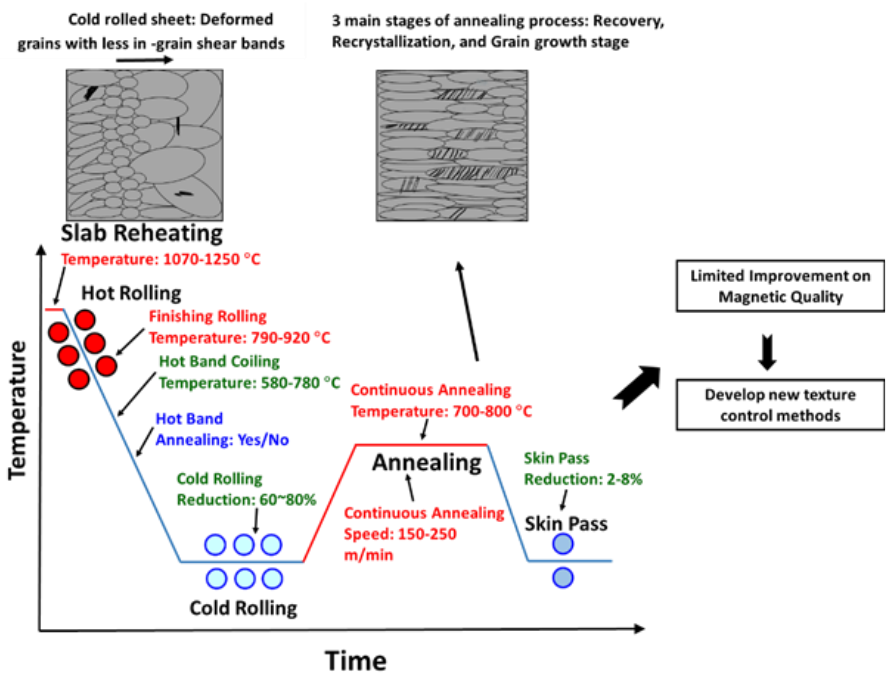

Figure 14. The traditional procedure to produce electrical steel (NGOES) [130].

It is important to note that electromagnetic devices are subjected to mechanical and thermal stresses during their operation. These stresses often arise from localised overheating, which can result from factors such as the manufacturing process, inherent material properties, and the conditions under which the device operates. Such stresses can significantly affect the magnetic characteristics of electrical steel [131]. For example, when the material is exposed to alternating magnetisation along different directions, such as the rolling direction and transverse direction at 50 Hz, uniaxial stress alters both hysteresis behavior and core loss. Specifically, tensile stress tends to reduce core loss along the RD, while increasing it along the TD. This demonstrates the crucial influence of tensile stress on both the mechanical and magnetic performance of electrical steel sheets [131].

One effective method to reduce internal stress impact is stress relief annealing treatment, which depends on factors like the material type, stress level, annealing time, and temperature and so on. For NGOES materials, annealing at 780°C for 2 hours has been found to effectively reduce the density of dislocations and low-angle boundaries while refining the grain size. This results in grain recrystallisation, enhancing the λ fibre {001} <uvw> while weakening the fibre. Consequently, this process leads to improvements in hysteresis losses and a reduction in residual stress [128]. Moreover, annealing (in Ar) of cold-rolled FeSi with a 4.5 wt% variation for 2 hours showed interesting results. As the annealing temperature increased from 600° to 800°C, the yield strength declined due to the recrystallisation process. Simultaneously, there was a decrease in hardness, yet an increase in workability was noted. However, between 400° and 500°C, the yield strength reached its maximum [132]. For a clearer understanding of the impact of annealing on the mechanical properties of electrical steel, Table 1 provides a concise overview of the effects of annealing treatments on yield strength, influenced by annealing time, temperature, and silicon percentage.

Table 1. Impact of annealing treatment on mechanical properties of electrical steel.

Electrical steel (Si%)	Annealing temperature (°C)	Annealing time (hr)	Yield strength (MPa)	Reference
0.57	700	2.5	165	[133]
0.57	850	2.5	135	
0.57	1000	2.5	122	
0.7	300	0.5	550	[134]
0.7	400	1	450	
0.7	500	1.5	390	
4.5	550	2	750	[132]
4.5	600	2	650	
6.5	700	5	400	[135]
6.5	800	2	370	[136]

In recent years, there has been a rising tendency to improve the magnetic properties of NGOES by using different types of thermomechanical processing. The magnetic characteristics of electrical steel can be significantly impacted by the materials previous processing history [137]. The microstructure characteristics obtained from thermomechanical processing can affect the magnetic properties by varying the grain size, the orientation of the crystallographic as well as defects [6, 122, 123]. These microstructure characteristics could act as a domain wall, which determines the magnetisation performance and hysteresis losses when the external magnetic fields are applied to materials. With respect to microstructure effects on magnetic properties, the texture impact is also vital especially in the materials with a BCC crystal structure because these materials exhibit various magnetisation performances with different crystallographic orientations. For example, the λ fibre texture (<001>//ND) is an ideal texture for developing superior magnetic performance while the γ fibre texture (<111>//ND) becomes the adverse texture for magnetisation [138-140]. Moreover, the most frequently observed fibre texture in electrical steel during the thermomechanical process (hot and cold rolling) is α^*, α and γ which are developed during these processes and are not desirable in terms of improving magnetic properties due to having hard magnetisation in this direction [141].

Numerous studies have focused on the development of the texture of electrical steel. In this context, experiments were conducted to improve the magnetic properties of electrical steel containing 2.4 wt.% Fe-Si and to investigate the relationship between grain morphology, texture, and process parameters [140]. Two sets of hot rolling parameters were applied for the primary and secondary groups in this research. The primary groups had a finishing temperature of 900°C and following that, all samples were cold rolled (0.50mm thickness), subsequently annealed at around 950 °C for 45 seconds and then cooled down to 200°C for 5 minutes. The results illustrated that the primary groups with different set-up process parameters in hot rolling led to the lowest γ fibre and the highest intensity of rotate cube component. These results are similar to those reported elsewhere [142] about the recrystallisation process of ultra-low carbon steel.

On the other hand, secondary groups had a finishing temperature of 800°C, and fast cooling from finishing temperature to 400 °C and cooled down to 200°C for 5 minutes could result in a completely recrystallised structure close to the surface. In contrast, in analysing the hot rolling microstructure of secondary groups, different texture intensities and microstructures obtained across the thickness of secondary groups such as the highest strength of fibre θ was observed after the hot rolling processing and the low concentration of the Goss texture {110} <001> and shear texture with the component of {112} <111> also seen at the surface [138, 140]. It was shown that the deformation region with high intensity of γ and α fibres, in the secondary groups was promoted to form a rotated cube orientation. Also, after the cold rolling process, the magnetic properties increased in the central region as well as the concentration of rotated cube components compared to the hot rolling process. Contrasting the texture of Fe-Si 2.4% after the annealing treatment and the hot rolling process has shown that if the temperature of the annealing process reached a maximum of 950°C, it resulted in the lowest intensity of θ fibre compared to that produced after the hot rolling process. Therefore, decreasing the intensity of θ fibre after annealing is not desirable for the magnetic properties [140].

Studies have shown that reducing deformation and lowering the hot rolling temperature during production can enhance the magnetic properties of NGOES [4, 141, 143, 144]. During the cold rolling process, shear bands can form, particularly when the steel has a coarse hot band grain structure without phase transformations. These shear bands serve as preferential sites for Goss-oriented grains to nucleate and grow during subsequent annealing, which is critical for minimising magnetic losses in electrical power transformers [4, 141]. Increasing the cold plastic strain (i.e., greater thickness reduction during rolling) significantly affects the development of final textures (γ, η) in 3% Si NGOES and, consequently, their magnetic properties. To achieve optimal magnetic characteristics, grains with favourable texture must be nucleated, making shear band formation during cold rolling essential. In one study, the optimal combination of B50, W15/60, and relative permeability (μr) was achieved when large-grain samples were hot rolled at 1000°C to 1.4 mm thickness and subjected to 64.3% cold strain [145].

It is a widely held view that one of the key elements influencing a certain orientation's behaviour during recrystallisation is the variation in the accumulated deformation energy in different crystallographic orientations [39, 141, 146]. In the cold rolling process, it has been proven that the nucleation of crystals starts at the grain boundaries and the deformation areas obtained from this process contain highly stored energy near the grain boundaries rather than the interior regions. This phenomenon occurred due to piling up the dislocation at grain boundaries and acting like a barrier. Furthermore, the deformation stored energy could be different for each grain with different orientations. For example, the deformation stored energy of grain with {111} orientations are higher than those in the cube and rotated cube {100} because these grains have the lowest crystal nucleation rate at grain boundaries which illustrates a direct relationship between high deformation stored energy and crystal nucleation. Consequently, the accumulation of stored energy can be a driving force for the recrystallisation process, and the strength of this energy relies on individual grains performance in crystallographic orientation and deformation history. It should be pointed out that, in this mechanism, during the recrystallisation process the grains with the highest density of dislocation would be recovered quickly and provide a suitable place for the nucleation of new grains in the next stage of recrystallisation process [141, 147]. A high heating rate during the recovery and recrystallisation process of NGOES has been shown to be beneficial for developing a desirable microstructure for magnetic applications. This benefit comes from rapid heating fostering a finer texture, enhancing magnetic permeability and reducing core losses by limiting orientations [122]. However, the high heating rate led to a decrease in the average grain size in both fine and coarse-grained samples which have a negative impact on core losses. Overall, the results [141] imply a correlation between the hot band texture and the crystallographic orientations observed following cold rolling. Furthermore, the orientations and texture of the hot band after the recrystallisation annealing treatment could result in improving the magnetic properties. It should be noted that the higher stored energy grains are not magnetically favourable for electrical steel because the recrystallisation process in electrical steel occurs in an area which has high stored energy. This could produce the hardest magnetisation direction as well as high anisotropy energy [141].

Xie et al. demonstrated that the improvement of textures in high Si electrical steel (6.5%) can be achieved through secondary rolling and annealing at temperatures ranging from 1000° to 1300 °C [148]. Based on the experimental results, the best magnetic properties with low core losses were achieved when the sheet was reduced in thickness to 30% by the secondary rolling process and annealing temperature set at 1300 °C which would increase the texture <001> from 34% to 44%, if the holding time at the annealing process increased from 1 hour to 5 hours. Similarly, the volume fraction of Goss and cube texture increased by 23% and 21%, respectively. Also, increasing the holding time during the annealing process could result in an increase in the grain size more than is required (600 μm) which has a negative impact on the magnetic properties. Furthermore, these results suggested that the surface energy and grain boundaries promote the growth of Goss and cube recrystallised grains [148].

A two-stage cold rolling process with intermediate annealing has been widely studied for NGOES [6]. To encourage the development of <001> crystallographic orientations, small reductions are applied during each rolling pass, which allows microstructure evolution and the formation of shear bands across the sheet thickness. Introducing an intermediate annealing step between the rolling stages influences both the recrystallisation texture and the final grain size (Figure 15).

In cold-rolled sheets, recrystallisation typically results in fewer shear bands and more grain fragments; however, higher intermediate annealing temperatures promote significant grain growth before the final rolling, enhancing shear band formation in the finished sheets. This is magnetically favourable because shear bands facilitate the nucleation of recrystallised grains with a preferred texture, aligning with the easy magnetisation direction, and help redistribute defects, improving magnetic flux density. The refined texture, including strengthened Goss and cube components and increased η fibre volume fraction, further boosts induction, while the larger grain size reduces hysteresis losses, thus contributing to enhanced magnetic performance, with induction reaching ~1.754 T and core losses as low as 2.9 W/kg [6].

These improvements are linked to enlarged grain size together with the development of λ and η fibre textures [6,148]. More recently, a three-stage cold rolling method has been proposed for grain-oriented electrical steels (GOES, ~3.25 wt% Si). By applying two intermediate annealing steps (870 °C for 3 minutes and 940 °C for 5 minutes), this technique not only produced grains up to 15 mm in size but also enabled higher silicon content and thinner sheet thickness, leading to reduced core losses [149]. Collectively, these findings highlight the importance of carefully controlling cold rolling and annealing parameters to optimise the texture, microstructure, and magnetic properties of electrical steels.

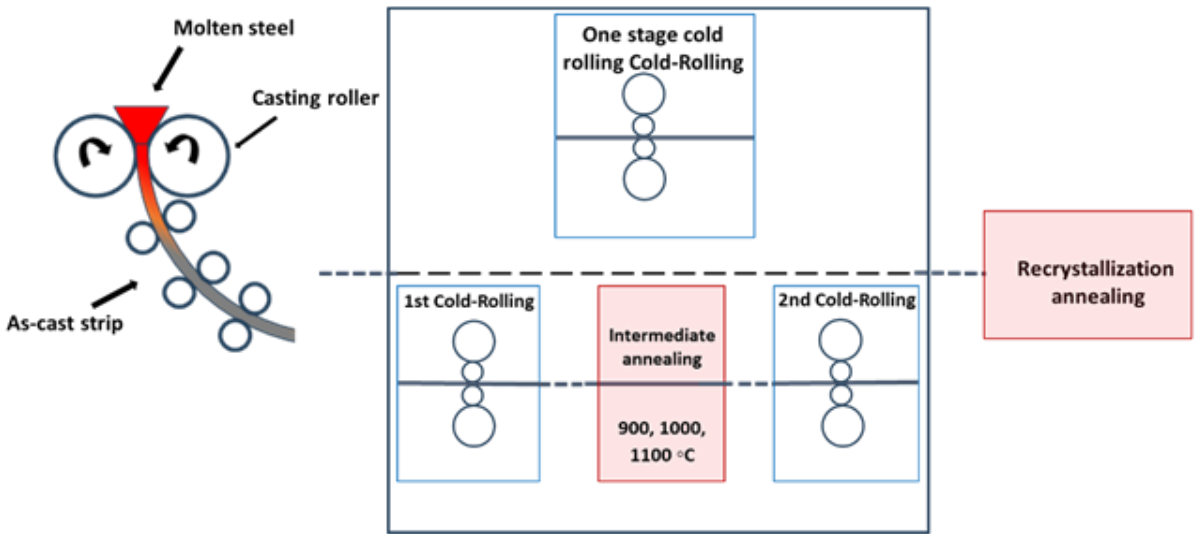

Figure 15. Schematic diagram of cold rolling steps of electrical steel [6].

1.9 Alternative thermomechanical manufacturing of electrical steel

Several alternative thermomechanical operations have been developed to improve the magnetic performance of NGOES. These processes aim to optimise microstructure and

crystallographic texture by introducing controlled plastic deformation and recrystallisation pathways. Key approaches include asymmetric rolling, repetitive bending under tension, cross rolling, and skew rolling [96, 150-154].

1.9.1 Asymmetric rolling

Shear plastic deformation during cold rolling generates shear bands and high dislocation-density zones in hot-rolled electrical steel, which provide favourable nucleation sites for <001> grains during recrystallisation [155]. In asymmetric rolling (ASR), the circumferential speeds of the upper and lower rolls differ, achieved by varying roll diameters, speeds, or rotations (Figure 16). It has been shown in [156] that applying ASR on NGOES with 2.1% Si promotes the development of <001> grains during final recrystallisation, while strengthening the η fibre and slightly reducing the γ fibre. This simultaneous improvement enhanced magnetic induction (by ~0.011 T) and reduced iron loss (by ~0.50 W/kg). However, ASR can introduce edge cracks and degrade surface quality due to increased friction, while also accelerating roller wear, which raises maintenance costs.

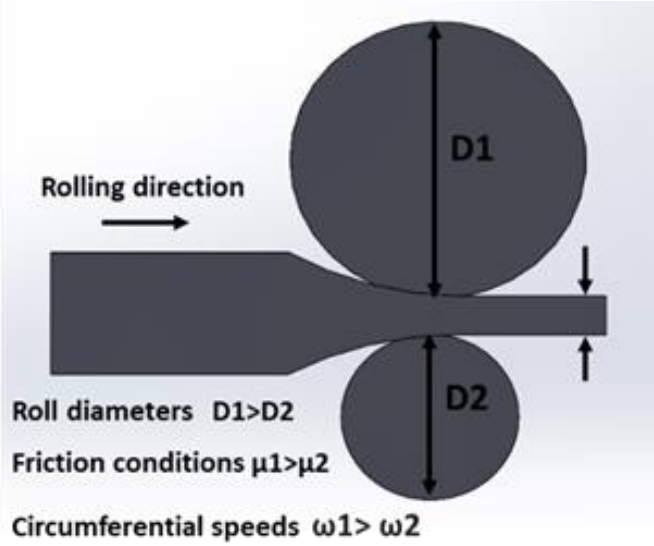

Figure 16. Schematic of asymmetric rolling [156].

1.9.2 Repetitive bending under tension

Repetitive bending under tension (R-BUT) induces cyclic bending and unbending of sheets under tension (Figure 17), creating shear bands that enhance {001} textures while suppressing unfavourable {111} orientations [112]. This technique has been applied to hot-band-annealed 1.8 wt.% Si NGOES, promoting desirable recrystallisation textures and extending the formability limits of high-Si steels. Although effective in refining texture and improving magnetic quality, R-BUT requires modifications to conventional production lines, limiting its industrial adoption.

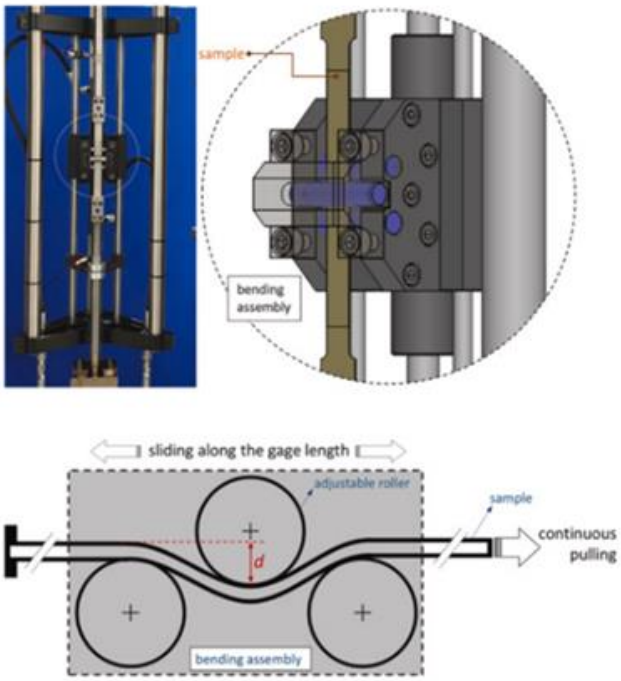

Figure 17. The experimental configuration includes a visual representation of the R-BUT testing setup, an illustration outlining the bending assembly [112].

1.9.3 Cross rolling

Cross rolling (CR) modifies texture by rotating the sheet 90° between rolling passes, thereby changing strain conditions and reducing γ-fibre formation during recrystallisation [157]. The α-fibre <110>//RD remains stable, while a τ-fibre <110>//TD develops. This produces a strong cube-rotated texture {001}<110>, which improves isotropy and reduces mechanical anisotropy [4,156]. Additional annealing stages after CR can further refine grain growth and reduce hysteresis losses, although some studies reported increased core losses (by ~21.4%) alongside higher induction (by ~2.84% at 50 A/cm) [4]. Despite these benefits, CR presents cost and productivity drawbacks, since sheets must be cut and reoriented during processing.

1.9.4 Skew rolling

Skew rolling (SR) is similar to cross rolling but involves rotating the sheet by smaller angles (e.g., 45°) between rolling stages [153]. This introduces different deformation modes due to frictional forces acting along both rolling and transverse directions, resulting in modified textures with higher intensity. SR suppresses unfavourable <111>//ND fibres while promoting <113>//ND (θ*) after annealing [158]. It also facilitates nucleation from shear bands, twin boundaries, and triple junctions—sites linked to rapid grain growth [159]. The final recrystallisation texture depends on orientation-selective growth, with <001>//ND grains expanding faster due to higher boundary mobility and stored energy. While promising, SR requires significant modification of rolling infrastructure, posing integration challenges [4].

1.9.5 Emerging approaches and limitations

While conventional rolling and annealing techniques remain central to the production of non-oriented and grain-oriented electrical steels, several emerging approaches have been

investigated to overcome the limitations of traditional processing and to further enhance magnetic performance. Among these, asymmetric rolling, repetitive bending under tension, cross rolling , and skew rolling have shown promising potential. In parallel, novel methods such as additive manufacturing (AM) are beginning to receive increasing attention.

ASR and R-BUT both utilise shear strain as a means to disrupt unfavourable texture components and promote <001>//ND orientations, which are highly desirable for improved magnetic induction. ASR, achieved by imposing different circumferential speeds between the upper and lower rolls, has demonstrated effectiveness in refining the microstructure and suppressing γ-fibre texture. However, the process can introduce surface quality issues, such as edge cracking and roller wear, which pose practical challenges in industrial-scale production [156]. Similarly, R-BUT facilitates the introduction of shear bands by cyclically bending and unbending sheets under tensile load, significantly improving the recrystallisation texture in high-Si steels. Nonetheless, its integration into conventional production lines would require notable infrastructure modifications, limiting its near-term industrial application [112].

Cross rolling and skew rolling provide alternative strategies by altering strain paths during deformation. CR, which involves rotating the sheet by 90° between rolling passes, reduces the stability of unfavourable γ-fibres while promoting cube textures, thereby lowering anisotropic mechanical behaviour. Despite improvements in texture and core loss, CR is disadvantaged by productivity and cost drawbacks, as it requires cutting and reorientation of sheets during processing [4]. SR, a variation of CR that rotates the sheet typically 45°, has shown particular promise in modifying deformation modes and favourably transforming texture components. However, the method also necessitates substantial modifications to conventional rolling infrastructure, raising questions about cost-effectiveness and scalability [153].

Beyond rolling-based modifications, AM has emerged as a disruptive approach for fabricating electrical steels with tailored compositions and microstructures. AM processes such as laser powder bed fusion and laser metal deposition enable the direct production of sheets or components with higher Si content (>6 wt.%), which is difficult to achieve by conventional casting and rolling due to poor ductility. Despite this promise, AM still faces significant limitations: defects such as porosity, cracking, residual stresses, and high anisotropy in microstructure remain major challenges. Moreover, the slower production rates and higher costs compared to established rolling methods hinder the widespread adoption of AM for large-scale electrical steel manufacturing [160].

Although residual stress is often cited as a critical issue in additively manufactured metals, its quantitative assessment remains challenging. In laser-based AM, residual stresses are highly localised, anisotropic, and transient, arising from steep and continuously evolving thermal gradients during layer-by-layer deposition. As a result, establishing robust correlations between residual stress, alloy composition, or individual process parameters is difficult without dedicated in-situ or full-field measurement techniques [161]. Furthermore, the use

of substrate preheating, as discussed in Chapter 3 of this thesis and widely reported in the literature, significantly reduces thermal gradients and cooling rates, leading to a substantial reduction in residual stress levels [162]. Under these conditions, residual stress becomes a less sensitive indicator of cracking behaviour. Instead, cracking susceptibility in brittle high-FeSi steels is assessed using microstructural indicators such as crack morphology and grain-scale damage, which more directly reflect the combined thermo-mechanical response of the material. This contrasts with deformation-based routes such as asymmetric rolling and cross rolling, where residual stresses are mechanically induced under relatively stable thermal conditions and can be directly correlated with strain path, rolling direction, and reduction ratio [163].

In summary, these emerging approaches illustrate the strong potential of thermomechanical and novel manufacturing techniques to address the inherent challenges in electrical steel production. However, their limitations—whether in terms of cost, productivity, or defect control—highlight the need for continued optimisation and further research before large-scale industrial implementation can be realised.

1.10 Additive manufacturing of soft magnetic materials

Additive manufacturing refers to a family of advanced fabrication processes in which three-dimensional parts are produced directly from digital models by adding material layer by layer, typically using a high-energy source such as a laser or electron beam. While AM has been widely applied in aerospace, medical, and automotive industries, its application for producing soft magnetic materials has only recently gained attention [164-166]. Conventional processing routes for Fe-Si steels with more than 3 wt.% silicon are restricted by poor ductility and embrittlement, which limit their formability during rolling [167]. AM offers an attractive alternative pathway, as it can bypass some of these challenges and provide opportunities for near-net-shape fabrication of silicon steels with controlled microstructures and textures that are highly relevant for magnetic performance. Despite these advantages, AM of magnetic materials remains challenging. Defects such as porosity, cracks, and lack of fusion between layers are often observed and can severely affect both mechanical integrity and magnetic properties [168].

Porosity, which can be detected using computer tomography (CT) scans, can be mitigated through optimised process parameters, such as increased energy input, tailored scanning strategies, or slower build rates that enhance layer bonding [169]. Furthermore, post-processing techniques—such as hot isostatic pressing (HIP) [170] or heat treatments—not only reduce porosity by consolidating the material and eliminating internal voids, but also relieve residual stresses, promote recrystallisation, and improve soft magnetic behaviour, leading to enhanced density and magnetic performance [171]. Furthermore, the properties of AM-produced steels are strongly dependent on process parameters, particularly energy input and scanning strategies, which directly affect solidification dynamics and grain orientation [172].

1.10.1 Laser powder bed fusion of Fe-Si Steels

The Laser powder bed fusion (L-PBF) process has been widely investigated for Fe-Si alloys. It has been demonstrated that Fe-3.5 wt.% Si fabricated by this method develops strong λ-fibre (<100>//ND), cube {001}<001> and rotated cube {001}<110> textures, which are beneficial for soft magnetic applications [173]. The influence of linear energy density (LED) [174], expressed as in Equation 1:

$$LED = \quad \mathrm{P}/(\mathrm{v}.\mathrm{h}) \qquad (2)$$

where *P* is laser power (W), *v* is scanning speed (mm/s), and *h* is hatch spacing (mm), has been shown to be critical. At low energy density, un-melted powder and pores are observed, whereas excessively high input promotes keyholing and crack formation. This highlights the importance of optimising LED to achieve dense microstructures and desirable crystal orientations [173].

Comparisons between L-PBF and 3D micro-extrusion showed that while L-PBF produced textured structures, micro-extruded samples exhibited significantly lower core losses [175]. Further studies on Fe-3 wt.% and Fe-6.5 wt.% Si alloys confirmed the extremely narrow process window, where high specific energy inputs (E= 350 J/m, V=0.5 m/s, P=175 W) resulted in porosity and cracks, while optimised parameters (E= 250 J/m, V=1 m/s, P=250 W) yielded 99.99% relative density with fully columnar microstructures [172]. The Fe-Si 3wt.% alloy has a strong <211> texture in the as-built condition, however following a heat treatment at 1150 °C, this texture transforms to a <001> cubic texture. As-built FeSi 6.5% metal has a cube texture that changes to a <110> Goss texture when heat treated. In both alloys, the absence of the hard magnetisation <111> direction in the samples' vertical and horizontal planes resulted a desirable microstructure for magnetic applications. The magnetic behaviours of both fabricated alloys are encouraging. Particularly, the FeSi 6.5 % steel which seems to have a significant amount of potential because it showed less eddy current effects than FeSi 3% and hence has a greater magnetisation capacity and more than 50% lower power losses [172].

Other investigations have shown that reducing energy density and laser power refines melt pool morphology and transforms grain structures [174]. The results show that reducing linear energy density (0.375 to 0.125 J/mm) and laser power (150 to 50 W) changes the morphology of the melt pool from large to small, resulting in a strong θ-fibre texture with a random distribution of grain orientations. Decreasing scanning speed (160 mm/s) and laser power (60 W) also transforms the melt pool shape to elliptical, yielding larger grains with fewer defects such as pores and a higher area fraction of <001> in the building direction, along with strong columnar grains that improve magnetic properties such as magnetic flux density and permeability. However, exposure to external magnetisation results in higher power loss and coercivity, possibly due to residual stress, defects, and high-density dislocation. Nevertheless, this research yielded a relatively high porosity level, which is undesirable, and the magnetic properties of the final products were not comparable to commercial products. Therefore, further annealing is necessary to remove residual stress and promote recrystallisation,

allowing for a better understanding of how the texture develops after these treatments. Conversely, a different observation was reported by [176] where high FeSi content (6.5 wt%) manufactured by LPBF at power 170 W and scan speed 400 mm/sec, using bidirectional scanning, resulted in large columnar grains with an elongated shape exceeding 2mm in the build direction. Additionally, these grains exhibited a preference for the <111> texture, which is not desirable for magnetic properties. These studies highlight the delicate balance between energy input, microstructure, and magnetic properties in L-PBF of Fe-Si steels. A further parameter often discussed is the normalised energy density, defined as in Equation 1:

$$E = \quad \mathrm{P}/(\mathrm{v.h.t}) \qquad (3)$$

where t is layer thickness (mm). This parameter enables consistent comparisons across machines and studies, as it incorporates build layer thickness, and is particularly useful for correlating porosity, microstructural evolution, and magnetic behaviour [177].

Manufacturing high silicon electrical steel (6.5wt%) and optimising the geometry of electrical machine parts through the LPBF process is gaining attention from scientists [135, 178]. This process offers a high cooling rate, which helps avoid the formation of brittle phases and improves magnetic properties, such as permeability up to 30,000 [178]. The Hilbert pattern is a specific geometric arrangement that can be used in constructing stators (FeSi 6.5wt%) for electrical machines Figure 18. This pattern aims to reduce eddy current losses and decrease the stator's weight by 34% compared to FeSi 3wt% (0.127mm laminations), while also improving the torque density of the AM Hilbert stator by 13%. However, core losses for the AM Hilbert stator at 1000 Hz are higher than for FeSi 3wt% (428 W, 0.35mm laminations). Further work is needed to address these losses and optimise processing parameters in AM Hilbert LPBF, as well as avoiding delamination and debonding during machining [179].

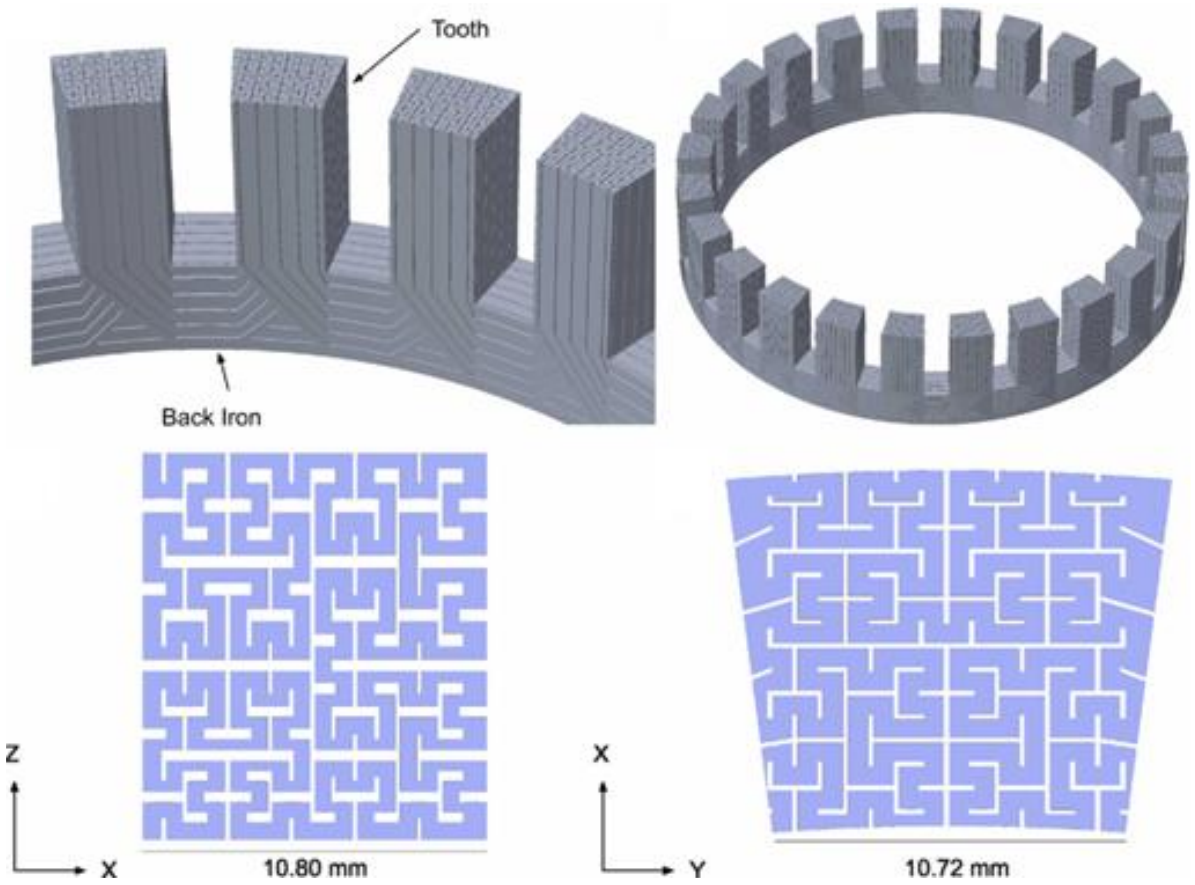

Figure 18. Design of AM Hilbert stator for manufacturing by the LPBF process [179].

High silicon electrical steel 6.5 wt.% also can be manufactured by the laser beam melting (LBM) process [180]. In this research, microstructure and magnetic characteristics are investigated in relation to the impacts of the LBM machine settings. The results demonstrated that the sample exhibits a columnar grain structure which is strongly correlated with the normalised energy. In other words, as the energy increased the grains tend to grow and become more coarser which improved magnetic properties especially coercivity value. Thus, minimising the formation of small grain sizes in the LBM process could help to improve the magnetic performance. However, the EBSD (electron backscatter diffraction) results showed that there is a weak relationship between texture and the magneto-crystalline energy and magnetic properties such as flux density. Based on the results, the authors suggest that for fabricating high silicon electrical steel, future research should focus on post-treatment processes such as the annealing process. This focus is necessary to produce a uniform coarse grain and recrystallised microstructure, as these types of post-treatments could lead to favourable crystallographic orientation and improved magnetic performance [180].

Selective laser melting (SLM) technology has been used to fabricate high silicon steels with a 6.9 wt.% Si content, revealing that SLM technology could be a potential manufacturing route to produce grain-oriented electrical steel for magnetic function [5]. Also, it was shown that the SLM has a potential to produce a near fully dense electrical steel at the higher energy of the scanning laser. During the SLM process, the cooling rates were high and in the range of

10^3 to 10^6 K/s. This can be beneficial due to the suppression of two phases such B_2 and DO_3 to form in Fe-Si 6.5w.t % system. These two phases make electrical steel more brittle and less electrically conductive [8, 181, 182]. Additionally, the final microstructure produced by raising the scanning speed from 140 to 280 J/m shifts from cube texture to long columnar <001> grains. However, increasing the energy of the laser caused increased crack formation and spherical porosities [5]. The main reason for the formation of spherical pores was the protuberant melting pool shape due to the higher laser energy input used during manufacturing process [183]. In addition to that, higher energy can be promoted to form keyhole defects in samples due to the vaporisation of materials from the surface and then, during solidification, these gas bubbles are trapped in the melting pool zone. Increasing the laser beam energy can also result in the introduction of thermal stresses to the SLM samples, which can lead to crack formation during the SLM process. Therefore, applying higher laser energy for a short time could play a significant role in forming defects as well as determining the effect of the thermal gradient and stress in the SLM samples [5].

Two distinct components with cubic and ring geometries were created to investigate the microstructure and magnetic characteristics. Due to heat input and residual stress effects in the ring shape sample, it was suggested that the laser energy density could not be higher than 420 J/m [184]. The analysis of performance loss in the ring sample revealed that with a further increase in laser energy, both the remanence flux (Br) and the maximum magnetising force, coercivity (Hc), gradually decreased. This effect was particularly observed when the laser energy increased from 140 to 280 J/m. However, no significant impact was observed when the laser energy increased from 280 to 420 J/m. Furthermore, the P50–1 analysis of total power losses revealed a distinct non-monotonic pattern, with the minimum value observed at E=280 J/m. Moreover, after stress relief treatment (5 hours at 700 °C), the magnetic permeability increased considerably. The increase in magnetic properties tends to affirm the efficacy of the heat-treatment implemented to diminish the internal stresses caused during processing. However, high laser energy might be detrimental to magnetic characteristics due to the formation of a cube texture. It has been suggested that post heat treatment is necessary to increase grain size which can have a significant influence on the magnetic properties [184].

The effects of the annealing treatment on microstructure features and magnetic properties of Fe-Si steel parts (6.9 wt.%) made by the SLM process were also studied [185]. The findings suggested that the rapid cooling rate during the SLM process could suppress the diffusion and reaction to avoid the coarsening process. Annealing the SLM part at 1150 °C for one hour could develop a recrystallised microstructure which is defined by mainly equiaxed grains (≤ 300μm). The most significant aspect of this treatment was that annealing preserves the SLM <001> texture along the building direction of the specimen, however, the texture strength of annealed samples at 700° and 1150°C in the build direction (BD) at different temperatures varied. The magnetic properties of the annealed ring were validated, revealing a maximum permeability of 24000 H/m, coercivity of 16 A/m, and a notable 36.8% increase

in flux density B10 (from 0.95 T to 1.3 T) subsequent to annealing at 700 °C. This is an interesting finding because an elevated temperature in annealing can be conducted to the built sample, and this can induce stress relief and grain development without degrading the crystallographic texture obtained by the SLM process. This occurred because of grain growth and stress relief which can decrease the lattice defects. This can also be compared to the commercial high silicon laminate steel fabricated through the CVD process in terms of quality [185].

1.10.2 Directed Energy Deposition

Directed energy deposition (DED) encompasses a family of AM processes in which focused thermal energy is used to melt feedstock material as it is being deposited. Depending on the energy source, DED can be classified into laser-based deposition (LMD), electron beam additive manufacturing (EBAM), and arc-based processes such as wire arc additive manufacturing (WAAM). In laser metal deposition (LMD), metal powders are delivered coaxially or off-axis into a laser-induced melt pool and consolidated layer by layer to build near-net-shape components [186-188].

Although no studies to date have specifically reported on the additive manufacturing of Fe–Si steels by DED, the technique has been successfully applied to a wide range of metallic systems, including nickel-based superalloys [189] , titanium alloys [190], and stainless steels [191]. DED processes provide several potential advantages compared with L-PBF. These include the capability to fabricate larger components, the ability to repair or remanufacture existing parts, and operation within a wider processing window with reduced crack sensitivity. In addition, the relatively lower cooling rates in DED compared with L-PBF may decrease thermal stresses and reduce crack formation in brittle alloys such as Fe–6.5 wt.% Si, while still enabling sufficient solidification control to influence grain morphology and crystallographic texture. A further advantage of LMD is that components such as circular tubes can be built without the need for internal support structures, which are often unavoidable in powder bed fusion processes such as selective laser melting. These characteristics suggest that DED, and in particular LMD, could represent a promising but as yet unexplored approach for the processing of high-silicon electrical steels [192].

1.10.3 Other AM Routes for Fe-Si Steels

In addition to L-PBF and DED, other AM technologies have been explored for Fe-Si alloys. Among the different processes of AM, the binder jetting (BJ) has recently been used to manufacture high density Fe-Si (6.5wt.%) stators. The researchers have examined the effects of magnetic and mechanical properties of the BJ silicon part [193]. The most noticeable result emerged from the experiment was that a crack free, near net shape (99% dense Si part) can be achieved when solid-state sintering is applied. Furthermore, different types of tests were performed on the fabricated Fe-Si parts which resulted in a low coercivity, an ultimate tensile strength of 434 MPa (similar to structure steel), a saturation magnetisation of 1.8T, and electrical resistivity of 98 μΩ cm as well as high relative magnetic permeability of 10.500 for a sample with thickness of 1.02mm. These results would seem to suggest that this process

can potentially replace the current CVD operation to fabricate 0.1 mm thickness 6.5 wt.% Si electrical steels due to its cost effectiveness, reasonable mechanical and magnetic properties [193]. In conclusion, AM provides a promising alternative to conventional methods for processing Fe-Si steels, particularly at higher silicon contents where hot rolling becomes unfeasible. L-PBF has demonstrated that dense components with tailored textures can be achieved, although process optimisation is critical due to the narrow processing window. DED represents an as yet unexplored but potentially valuable route for Fe-Si steels, offering advantages in scalability and reduced crack sensitivity. Binder jetting and selective laser melting have also demonstrated feasibility, although challenges such as porosity, residual stresses, and crack formation remain. Overall, AM presents an important opportunity to overcome the long-standing challenges associated with the processing of soft magnetic steels, provided that process optimisation and post-treatment strategies are carefully employed.

Chapter 2 Laser metal deposition process

2 Introduction

The previous chapter presented a detailed review of the manufacturing processes for non-grain-oriented electrical steels, including various traditional methods. Additionally, an introduction to several additive manufacturing techniques, such as laser powder bed fusion (LPBF), selective laser melting (SLM), and binder jetting (BJ), was provided. This chapter focuses specifically on laser metal deposition (LMD), the primary additive manufacturing method used in this research, and its application in the production of electrical steels. To better understand the LMD process and how it can be influenced by adjusting processing parameters, other materials manufactured using LMD are also reviewed. Furthermore, other directed energy deposition (DED) processes, including powder- and wire-fed systems, that have been used to manufacture Fe-Si alloys are discussed. No previous studies have applied LMD to manufacture Fe-Si electrical steels, making this the first attempt to do so.

Laser metal deposition is a technique for additive manufacturing that has been widely applied in industries such as automotive [194], medical [195], and aerospace [196]. In addition to new part fabrication, it is also reported for repair and remanufacturing applications due to its precise heat control and relatively small heat-affected zone (HAZ). The original idea of this technology was presented by Kratky (1937) [197] and Harter (1942) [198] and has since been refined by numerous researchers. LMD belongs to the broader family of directed energy deposition (DED) processes, which include powder- and wire-fed systems.

In recent years, directed energy deposition has emerged as a promising AM technique for producing soft magnetic materials, notably Fe-Si alloys. DED offers several advantages over traditional manufacturing methods, including the ability to fabricate complex geometries and tailor microstructures to meet specific performance requirements. Studies have demonstrated that laser-based DED enables near-net-shape production of Fe-6Si alloys, where scan path strategy and subsequent heat treatment strongly influence the microstructure, cracking behavior, and magnetic properties. Cross-hatch deposition strategies have been shown to produce crack-free microstructures and quasi-single-crystal grains after high-temperature annealing, highlighting the potential of DED to tailor microstructures for improved magnetic efficiency [101].

Other work has shown that DED can extend the silicon solubility limits far beyond conventional boundaries, successfully fabricating dense Fe-Si alloys with compositions up to 20 wt.% Si. The fabricated alloys exhibited significantly increased hardness, resistivity, yield strength, and ultimate tensile strength, while maintaining competitive soft magnetic performance. The high thermal gradients and rapid cooling rates in DED suppressed the formation of brittle ordered phases (B_2, $D0_3$), which typically hinder manufacturability at high silicon levels. This demonstrates the capability of DED not only to reproduce existing alloy chemistries but also to enable novel compositions unattainable by traditional methods [199]. Further research has focused on process optimisation for Fe-6.5 wt%Si using systematic

design of experiments, correlating laser power, scan speed, and powder feed rate with bead characteristics such as dilution, wetting angle, and powder efficiency. The resulting process parameter map provides a reproducible processing window for high-quality DED fabrication of electrical steels, which is essential for scaling the technique towards industrial applications in high-performance soft magnetic components [200]. Together, these studies underline the growing relevance of DED for advancing Fe-Si alloys: enabling near-net-shape fabrication, tailoring of microstructure through scan strategies, suppression of brittle phases via rapid solidification, and systematic parameter optimisation for industrial scalability. Rather than being confined to repair applications, DED is increasingly positioned as a transformative manufacturing route for developing high-performance bulk magnetic materials like FeSi, directly aligning with the objectives of this research.

LMD is a direct energy deposition process where a laser beam creates a melt pool on the surface of the metal substrate during the process in order to build a 3D component. In this method, the wire feeders or powder feeding hoppers can be continuously used as a material feedstock which is supplied to the laser focal region and, as soon as the laser beam hits the surface of substance, creates a melt pool which then solidifies (Figure 19). The process of LMD consists of five fundamental phases. The first stage is to develop a CAD file of the part. Second stage is to convert CAD file to AM file or to standard triangulation language (STL) file. At the stage three, the AM file sliced in 2D sections in order to define geometry of CAD file. In this stage, the slicing also preferred to be in the building direction because it gives better stability and reduce support structure of part during manufacturing process. The fourth stage is the building process, where the laser melts the substrate material to create a melt pool, forming a solid mass of a 2D profile. The laser then continues moving along the predefined path until the construction process is complete and the 3D component is fully formed. The last step is to remove the 3D part, support structure and clean it and perform any heat treatment process if required [201].

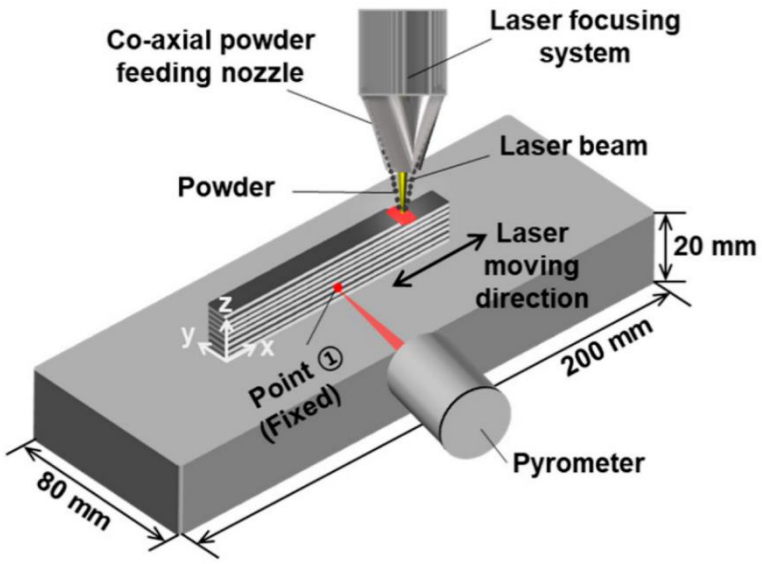

Figure 19. Schematic of laser melting deposition process[201].

2.1 Advantages of LMD and Solidification Mechanisms

There are also some advantages to the LMD process compared to conventional manufacturing processes which can be highlighted here. The LMD process can be used to repair, remanufacture, or manufacture a new component with better mechanical properties. Another advantage of LMD is that in this process the materials join each other layer by layer with better mechanical properties as compared to materials which are joining together by welding or bolts and nuts. For example, in the welding joining points are faced to high stress concentration, and it would be a place where the failure initiates, and this is can be eliminated by using the LMD process [202]. The final product obtained from LMD has less weight, greater materials utilisation, lower energy usage, and is generally more cost effective [201]. Furthermore, the flexibility of LMD, with its low heat input, allows manufacturers to create complex parts that would be difficult or impossible to achieve using traditional manufacturing methods. Despite all of these benefits, the LMD technique is fairly new, and this process in terms of physics is not yet well understood. The characteristics and performance of the final part is also not predictable and controllable due to many process variables. Furthermore, the final product has a relatively poor surface finish and may require further post treatment. In the LMD process the microstructure evolution is dependent on the solidification mechanism. The solidification rate can be affected by the initial temperature of the substrate or previous layer as well as the melt-pool. For example, if the initial temperature of substrate is low (cold) then the solidification rate would be high due to the absorption of heat by the substrate (which behaves like a heat sink) and its removal from the melt-pool towards the colder substrate. In the LMD process if the scanning speed is high then the melt-pool size is smaller resulting in less interaction time of the laser with the material and rapid solidification. Conversely, a low scanning speed with high power laser energy can increase interaction time between laser and powder which create a larger melt-pool and result in a slower solidification rate which is ideal for this study. This slower rate promotes the formation of columnar grains, enhancing the magnetic performance of electrical steel [201]. The solidification process is started by the transformation of liquid to a solid which usually starts in the interface region of liquid and solid. This interface region could be between the melt-pool and the substrate or previous layers with the melt-pool. In the solidification process, the crystal will be nucleated and grow with a crystalline structure at these interfaces. Also, this crystal growth with a specific crystallographic orientation which is known as epitaxial grains. As the solidification process progresses these grains grow towards the substrate in the opposite direction of the heat flow. This type of behaviour of grains growth and characteristic structure could be seen in the LMD process which is known as a columnar grain. In the heat affected zone, globular grains can also be observed due to transforming heat from melt pool zone to the cross-substrate. These grains near the melt pool grow larger due to the sufficient heat generated by the laser. As the heat increases, the grains expand, and conversely, they shrink when the heat decreases [201]

. The scanning velocity is correlated with the solidification rate. In other words, a high scanning velocity results in a higher solidification rate, which could influence the

microstructure [203]. For instance, columnar and globular grains with a small width and size can be developed when a high scanning speed is applied. In most metals and alloys, due to the high solidification rate, a martensitic microstructure can be formed, which is very hard and also promotes an equiaxed microstructure [201]. Furthermore, at a low solidification rate Widmastätten alpha pattern structure would appear. The cooling rate also can play a key role in developing microstructure for example, coarser microstructure can be developed when the cooling rate is low while, when the cooling rate is high then a finer microstructure can be produced [203]. In the LMD as layers are added, the microstructure created will continue to change, and this can lead to the formation of complex, heterogeneous, and anisotropic microstructures that are completely unattainable in conventionally produced parts. This demonstrates the crucial role that processing parameters play in producing the ideal solidification rate, as well as the appropriate microstructure and, ultimately, the desired characteristics [201]. Processing parameters in the LMD influence the microstructure development, and the mechanical and physical properties of the parts produced. In LMD the key processing parameters such as scanning speed, laser power, beam size, gas and powder flow rate have a significant effect on materials properties. In addition to that, this process is non-linear, and with a small adjustment in the process the properties of material can be changed significantly [201, 204]. This indicates that there is a strong relationship between the processing parameters, and some of them have a major impact on the properties of the materials, which will be addressed in the next subsections.

2.2 Laser power in the LMD process

The amount of heat energy supplied by a laser to process materials is referred to as laser power. Research [205, 206] shows that laser power significantly affects the properties of the processed material, including surface finish and other physical characteristics. The microstructural characteristics are greatly influenced by laser power during the LMD process; thus, the laser power needs to be controlled. Excessive laser power can cause high dilution between deposited materials and the substrate and might result in vaporisation or plasma formation. Conversely, insufficient laser power can lead to incomplete melting and porosity. Because of this, it is crucial to determine the ideal laser power in relation to other processing factors for the material being processed. As the laser power increases, the surface roughness of the final surface of alloys reduces in the LMD process [206]. This could be due to the high laser power fully melting the deposited materials and the low solidification rate, allowing the material to flow across the surface.

Similar research has also been conducted to investigate the effect of laser power on the melt pool size and surface finish using the LMD process [207]. The results of the investigation showed that a poor surface finish was caused by the adhesion of the unmelted or incompletely melted powder particles on the surfaces of the deposited layer. It was also found that increasing the melt-pool volumes, through higher laser power, assists in melting the unmelted powder particles leading to improved surface quality. In the study [207], a numerical model was created to forecast the surface quality, and the model was successfully

tested in experiments with good agreement. In addition to this study, similar findings have been reported, indicating that the surface finish can be improved in the LMD process [208]. Their results indicate that a smoother surface finish is achieved with higher laser power density, which leads to complete melting of the deposited powder, a larger melt pool size, and a lower solidification rate. This improvement can eliminate the need for secondary surface finishing operations for certain components.

In Fe-Si alloys, laser power has been shown to directly influence cracking susceptibility, grain morphology, and surface quality. During DED of Fe-6Si, higher laser power in concentric scan strategies promoted elongated grains and increased cracking during subsequent annealing, while optimised power ranges in cross-hatch strategies yielded dense, crack-free structures with improved surface finish [101]. Similarly, in DED of Fe-6.5Si, process mapping identified an optimised power (~796 W) that balanced wetting angle, dilution, and powder efficiency, producing stable clads suitable for magnetic applications. These results highlight that while high power can reduce unmelted particles and improve consolidation, excessive energy input may increase residual stresses and promote defect formation [200].

2.3 Laser power influences on microstructure in the LMD process

Laser power has a direct correlation with the melt pool created, as well as the solidification and cooling rate. In addition, it also exhibits a significant influence on the microstructure of laser-deposited metal parts. A high laser output often leads to the formation of larger melt pools and prolongs the solidification time resulting in a higher likelihood that an equilibrium microstructure will emerge. Thus, microstructure development in the LMD process is a crucial research area since it influences the properties of the manufactured part. In addition to that, it is crucial to regulate the laser power throughout the LMD process since it has a significant impact on the microstructure and subsequently the evolved properties [209]. It has been demonstrated that grain structures are significantly affected by both laser mode and power. Samples produced in pulsed wave mode tend to form finer equiaxed grains, while those manufactured in continuous wave mode develop larger columnar grains [210]. However, their findings [210] concluded that laser power has a more substantial impact on microstructure development than the laser mode, which has a relatively minor influence. Laser power plays a critical role in determining the material's properties and resulting microstructure.

Therefore, microstructure properties can be regulated through careful control of the laser power. It has been reported that at higher laser powers, a larger melt pool is formed, and the longer solidification time allows for the development of thicker dendritic arms and growth [211]. It was also observed that, as the laser power was decreased, the dentritic arms' thickness decreased. This type of microstructural creation can be explained by the fast solidification that occurs at lower laser power because of the small melt pool created, which favours thinner and more dentritic arms. Others authors (Yu et al. [212] ; Mahamood et al. [213]) have confirmed that in the LMD technique, it is feasible to make parts that are either softer and ductile or hard and brittle by simply adjusting the laser power. Moreover, a lower number of large grains were available for the melt pool to nucleate and develop epitaxially

due to the larger melt pool and slower solidification rate that allows more grains to grow in the heated affected zone area which is desirable for optimising magnetic properties of electrical steel [214].

In Fe-Si systems, microstructural development is particularly sensitive to laser power due to the brittle nature of high-silicon steels. For example, DED of Fe-6Si showed that concentric paths at high laser powers retained elongated columnar grains along the build direction, whereas cross-hatch deposition promoted more equiaxed morphologies [101]. These morphologies were further modified by annealing, where optimised powers supported abnormal grain growth and even quasi-single-crystal regions. Likewise, higher powers in Fe-6.5wt% Si clads were found to increase dilution and affect bead geometry, which directly could influences the final magnetic performance [200]. Beyond microstructure size, laser power also influences texture, which is a key factor in magnetic performance. Studies on electrical steel have shown that increasing laser energy density promotes strong <001> cube textures, improving permeability and reducing core loss, while sub-optimal powers lead to random orientations and degraded properties. This demonstrates that laser power not only governs grain growth but also controls crystallographic texture critical for electrical steel applications [215]. Furthermore, in high-Si steels processed by DED, excessive energy input encourages coarse grains that reduce ductility and magnetic softness, whereas optimized power enables finer grain structures that lower coercivity and improve core losses Thus, controlling laser power is essential not only for structural integrity but also for tuning the electromagnetic functionality of Fe-Si alloys [199].

2.4 Laser power influences on mechanical and tribological properties

The relationship between the laser power and the mechanical and tribological characteristics of materials manufactured using the LMD technique has been studied in great detail. In this section, several key scientific papers are examined. The effect of laser power density on microhardness after applying the LMD technique has also been investigated, showing that variations in power density can significantly influence the hardness of the deposited material [208]. They observed that as the laser power density increased from 18 to 80 J/mm^2 the microhardness increased. However, as the power density exceeded 80 J/mm^2 the microhardness subsequently decreased. This can be explained by microstructure changes at this laser power density and insufficient melting due to lower power density which resulted in unmelted powders and low microhardness. Another comparable investigation was carried out by Ju et al [212] who discussed how the mechanical characteristics of titanium alloy formed via the LMD process were affected by laser power (380 to 570 W). The findings demonstrated that a higher laser power increase microhardness, yield strength, and ultimate tensile strength (UTS) compared to conventional cast and annealed wrought materials.

The decrease in porosity in deposited samples with increasing laser power has been directly associated with improvements in material properties. However, excessive laser power can also cause grain coarsening, which reduces overall performance. For example, studies have

shown that when laser power increases from 1.8 to 2.4 kW, microhardness decreases due to coarser grain formation [216].

2.5 Scanning velocity in the LMD process

Another crucial processing variable in the LMD process is the scanning velocity which reveals how long the laser beam is in contact with the substrate and the materials being deposited. In the LMD the laser velocity can be achieved either moving the laser head or the substrate against each other. Several studies have investigated the impact that the scanning velocity has on the properties of the alloy manufactured by the LMD process. For instance, a low scanning speed suggests a prolonged interaction time between the laser and the materials. In addition to that, very low scanning speeds, resulting in a lower surface roughness being observed. Conversely because the laser material interaction period is shorter at higher scanning speeds, the deposited materials may not melt properly, resulting in a larger surface roughness. Furthermore, along with the poor melting of the deposited material which may also lead to rising surface roughness, the shorter laser material contact time creates a smaller melt pools that tend to solidify quickly and generate scales on the surface of the produced track [217].

In 2013 [218], a study carried out similar research on the alloy by using a 0.015 to 0.105 m/s range for the scanning speed. The results also demonstrated that, despite a nonlinear connection, the lowest surface roughness was seen at the lowest scanning speed of 0.015 m/s. Also, as the scanning velocity increased, it was observed that the average surface roughness initially increased and then began to decline. Furthermore, due to the longer laser-material interaction period, the alloy powder was properly melted, producing a smoother surface that was visible at low scanning speeds. However, the value of surface roughness increased when the scanning speed was enhanced because the laser-material interaction period started to shorten, causing additional unmelted alloy powder. Due to the limited time available at high scanning speed, the amount of powder delivered at higher laser power is smaller. In contrast to what was observed at low scanning speeds, the decreasing surface roughness observed above 0.65 m/s was caused by a decrease in the amount of powder being deposited, which led to a decrease in the density of unmelted alloy particles [218].

Beyond surface morphology, scanning velocity in Fe–Si alloys has been shown to strongly influence the melt pool dimensions, microstructural texture, and ultimately the magnetic and mechanical performance of the deposited components. Lower scan speeds (higher energy input) promote larger and deeper melt pools, often resulting in coarse columnar grains aligned with the build direction. In contrast, higher scan velocities (lower energy input) produce smaller, shorter melt pools, faster cooling rates, and more refined or layered microstructures [219]. These differences directly affect the electrical and magnetic behavior: layered microstructures obtained at higher velocities exhibited higher resistivity and reduced core losses but at the expense of saturation flux density, while slower velocities leading to fully dense structures enhanced saturation but increased losses due to eddy currents [219].

In addition, scan velocity interacts with scan strategy to determine residual stress and cracking susceptibility. Continuous, long-path scans at lower velocities have been reported to generate significant tensile residual stresses, which, in brittle high-silicon Fe alloys, can lead to transgranular cracking during or after post-build annealing. Conversely, higher scan velocities combined with shorter, segmented paths (such as cross-hatch strategies) reduce the residual tensile stress and significantly lower crack formation [101]. This highlights the dual role of scanning velocity in both controlling surface quality and influencing deeper aspects of the alloy's microstructure, cracking resistance, and functional magnetic properties.

2.6 Scanning velocity influence on microstructure

It has also been noted that the scanning speed affects the microstructure of the part manufactured by the LMD method. As soon as the liquid starts to solidify, microstructural formation commences. The size of the melt pool formed during the deposition process affects the final microstructure that is produced. Due to the prolonged interaction period between the laser and the material, low scanning speeds encourage the creation of large melt pools. On the other hand, a larger melt pool causes the solidification rate to be slow thus encouraging the creation of microstructures which affects the final properties of the deposited material. It is necessary to carefully understand how the scanning speed affects the microstructure during the LMD process in order to manage it and generate the appropriate metallurgical, mechanical, and tribological features. Scanning speeds between 0.005 and 0.095 m/s in the LMD process could alter the microstructure [220].

Also, in previous research [211] the impact of scanning speed on the alloy microstructure manufactured during the LMD was investigated. The results illustrated that dendrites and acicular structures were observed in the microstructure and, as the scanning speed was raised, it was observed that the dendrites' thickness grew. In addition to that, at higher scanning rates, snowflakes of dendrites formed next to the acicular microstructures. This kind of microstructural development may be responsible for the fast cooling produced at high scanning speed. Moreover, the rapid cooling may have contributed to the cracks seen at the higher scanning speed. In general, the thermal cycles that come from depositing materials in successive layers can also generate several metallurgical phenomena that change microstructures and may eventually lead to complicated forms of microstructures due to the thermal history experienced at various locations throughout the deposited sample in the LMD process. Microstructures such as fine Widmanstätten alpha, basket weave, colony structures, or even lamellae typically emerge as a consequence of fast cooling rates or solidification rates at high scanning speeds [218].

In the case of soft magnetic alloys such as electrical steels (NGOES and GOES), scanning velocity in DED plays a crucial role in controlling microstructure and crystallographic texture. Low scanning speeds, which correspond to higher energy input, generate larger and deeper melt pools that solidify slowly and promote coarse columnar grains aligned with the build direction. In contrast, higher scanning speeds shorten the melt pool and increase cooling rates, leading to finer or more equiaxed grains and layered microstructures [219]. These

microstructural differences directly affect magnetic behavior: dense, columnar-grained structures obtained at lower scan speeds exhibit higher saturation flux density but suffer from larger eddy-current losses, while finer-grained or layered structures formed at higher scan speeds exhibit higher resistivity and reduced losses but lower saturation [219]. Furthermore, scan velocity also interacts with scan strategy to influence residual stresses and cracking. Continuous, slow scans can introduce high tensile stresses and lead to transgranular cracking in brittle high-silicon Fe alloys, whereas faster scans with segmented paths help relieve residual stresses and reduce cracking [101]. This highlights the significance of scanning velocity in tailoring microstructure, texture, and magnetic performance for advanced soft magnetic materials manufactured by DED.

2.7 Scanning velocity influence on mechanical and tribological properties

The processing parameters in the LMD process, particularly the scanning speed, significantly influence the melting and solidification rates of the deposited material. These factors directly impact the microstructure and, consequently, the mechanical and tribological properties of LMD parts. The impact of scanning speed (5 and 20 mm/s) on the mechanical properties of alloy composites fabricated by LMD was investigated [221]. Their findings showed that higher scanning speeds led to an increase in average microhardness. However, as scanning speed increased, the wear resistance of LMD parts decreased. This reduction in durability is due to the mixing of the deposited material with the substrate and, in some cases, even the evaporation of the materials. Nevertheless, if the scanning speed is excessive then there is not enough time for the laser and the material to interact, thus, deposited substances may only partially melt or possibly not at all. It is evident that, in the LMD process, the scanning speed has an impact that is inversely proportionate to the impact of the laser power [201]. The relationship between laser power and scanning speed can be expressed using the laser power density formula, as shown in Equation 1 [222].

$$\text{Equation 1} \qquad E = p/dv$$

In this formula E represents laser energy density (J/mm^2), v is scanning velocity (mm/s), d is the diameter of laser beam (mm), and p is the power of laser (W). This means that the laser energy density can be changed just by varying the laser power or the scanning speed. Altering the laser beam's diameter is another way to adjust the laser's energy density .

2.8 Influence of scanning velocity on surface finish

Researchers [217] attempted to evaluate the effect of scanning speed on the surface finish of alloys obtained by the LMD technique. In this investigation, the laser power and powder flow rates were kept constant at 3.0 kW and 2.88 g/min respectively, while the scanning speed was adjusted in a range from 0.01 to 0.05 m/s. The findings of this investigation demonstrated that, as the scanning speed was raised, the surface roughness increased. This was explained by a similar phenomenon to the inverse relationship between the effect of scanning speed and laser power on surface roughness. Because the laser and material interaction time are longer at higher scanning speeds, more material is effectively melted, a larger melt pool is

created, and faster solidification occurs. The higher scanning speed was thought to be the cause of these observations due to the microstructural evolution. Additionally, when the scanning speed increased, the microstructure shifted from wide to fine. The combination of ductility behaviour and intermetallic phases led to greater yield strength and wear resistance being seen at higher scanning speeds. Other investigations [218] also found that microhardness increased with higher scanning speeds, likely due to incomplete melting of powder particles. While microhardness increased consistently with higher scanning speeds, wear resistance did not follow the same pattern. Initially, wear resistance improved with increased scanning speed, but it started to decline once the speed exceeded 0.065 m/s. This decline might be due to larger unmelted particles forming at higher speeds, which did not contribute to wear resistance.

In the context of soft magnetic alloys produced by AM, scanning velocity significantly influences surface quality and functional performance. At lower scan speeds, the prolonged interaction time between the laser and material results in smoother surfaces due to more complete melting and larger, stable melt pools. Conversely, higher scan speeds can lead to insufficient melting, increased roughness, and partially fused particles on the surface [223]. For instance, in soft magnetic materials manufactured by AM processes, Fe–4.5 wt% Si alloys have shown that low laser power combined with fast scanning speeds can lead to lack of fusion defects, while high laser power and slow scanning speeds may result in keyhole defects. Optimising these parameters is crucial to minimize defects and improve both surface quality and magnetic performance [224].

Similarly, research on Fe-Co-V alloys processed by laser engineered net shaping demonstrated that scanning velocity impacts grain structure and magnetic properties. Optimal magnetic performance was achieved at moderate scan speeds, where grain refinement and alignment were favourable for soft magnetic behavior [225]. These findings collectively emphasize that scanning velocity is a critical parameter in DED processes, influencing not only the surface finish but also the microstructure and magnetic properties of soft magnetic materials. Careful optimization of scanning speed is essential to achieve desired material characteristics for specific applications.

2.9 Influence of powder, wire flow rate and gas flow rate in the LMD process

A crucial factor in the LMD process is the flow rate of the powder or wire, which indicates how much material, in grams, is ejected from the delivery nozzle in a given time. Numerous studies [226-228] have demonstrated that the material flow rate significantly affects the physical, metallurgical, chemical, tribological, and mechanical properties of the deposited sample. The efficiency of the LMD process as a whole is also influenced by the material flow rate [229, 230]. Thus, the material flow rate should be carefully controlled to balance energy input with deposition, as an excessive flow rate can result in improper melting of the deposited powder or even no melting at all. The rate of delivery of the substance depends on the available energy density input. However, an excessively low powder flow rate is only helpful if the vaporisation of the material occurs due to high energy density. Conversely, if the

material flow rate is excessively high, the available energy density could be enough to adequately melt the deposited material, leading to poor material utilisation and unsatisfactory qualities of the deposited sample. Moreover, the material flow rate also significantly influences the distribution and density of the deposited component.

Similarly, a crucial factor in the LMD process is the gas flow rate, which is also referred to as the flow rate of the powder carrier gas. The powder is transported via a carrier gas—typically an inert gas—intended to shield the powder from environmental damage, particularly for reactive elements. Although the gas flow rate has only a little impact on the final qualities of the deposited samples, it must be properly adjusted for each application since a gas flow rate that is too low might result in incorrect protection of the materials being deposited, especially for highly reactive substances. In addition, a gas flow rate that is too high may cause the powder to be blown away from the melting point, which would be detrimental to the LMD process [217].

In additive manufacturing of soft magnetic materials, such as Fe–49Co–2V alloys, Fe–6.5 wt% Si electrical steel, and other Fe-based alloys, the control of process parameters like powder or wire feed rate and gas flow rate is critical for achieving optimal magnetic performance. Studies on wire-arc additive manufacturing (WAAM) of Fe–49Co–2V alloys have shown that the wire feed rate directly affects the deposition rate and thermal input, with optimal feed rates ensuring uniform microstructure and magnetic properties, while deviations can lead to defects such as porosity or lack of fusion, degrading magnetic performance [231]. Similarly, in DED processes, such as laser metal deposition of Fe–6.5 wt% Si electrical steel, the powder feed rate strongly influences the energy density, melt pool size, and cooling rate, with higher feed rates potentially producing coarser microstructures and lower magnetic performance, while lower feed rates may cause incomplete fusion and porosity[100]. Gas flow rate in both WAAM and DED is also critical, as it shields the melt pool from atmospheric contamination; insufficient gas flow can result in oxidation and reduced magnetic permeability, whereas excessive flow may disturb the melt pool and create surface irregularities [232]. Therefore, careful optimisation of powder or wire feed rate and gas flow rate is essential to control the microstructure, purity, and magnetic properties of AM-processed soft magnetic materials, directly impacting their suitability for applications in electric motors, transformers, and other electromagnetic devices.

Although oxidation can influence the manufacturability of reactive alloys like Fe–Si in additive manufacturing processes, it was not considered a primary factor in this study. The DED process was performed under continuous inert gas shielding (argon), which minimises oxygen exposure and effectively prevents significant oxide formation during deposition. Under these controlled conditions, oxidation did not appreciably affect microstructural development, melt pool stability—the key aspects of manufacturability examined here. Previous studies confirm that argon shielding in DED substantially reduces oxide scale formation compared to open environments, with oxidation effects more pronounced in pre-oxidised powders than in-process deposition under inert conditions [233, 234]. For Fe–Si electrical steels specifically,

oxidation primarily degrades electromagnetic performance during post-processing or high-temperature exposure, rather than inert deposition [235]. In Fe–Si soft magnetic composites, for instance, oxidation temperature modulates microstructure and properties, but this relevance emerges mainly under intentional elevated-temperature or prolonged exposure [235]. Thus, while oxidation is acknowledged in the literature, it was appropriately treated as a secondary factor in the present work, allowing the main emphasis on process parameters, microstructure, and magnetic performance.

2.10 Influence of size of the laser beam and the percentage of overlap in the LMD process

The quality that may be obtained from the LMD process is determined by a number of crucial processing parameters, including the laser beam diameter. The laser beam's diameter, which is determined at a specific focal distance and is referred to as the laser spot size is measured in millimetres. The energy density during the LMD process is significantly influenced by the size of the laser spot, and an inverse relationship exists between the laser energy density and the laser spot size. In the LMD process a larger laser energy density will be produced by a smaller spot size. In the process of LMD, shrinking the laser spot size results in a significant rise in the pressure inside the laser, known as the energy density. During the LMD process, the laser spot size also affects the thickness of layers that are formed. The laser point size needs to be highly precise if very fine detail is required to be printed. The laser spot size also has a significant impact on the component quality and the efficiency of deposition in the LMD process [236-238]. Overlap percentage is another important process parameter in the LMD process. The overlap percentage is the percentage of the preceding track that is covered by the succeeding track. To achieve high densification by using the LMD technique, a higher overlap percentage is crucial. In order to prevent inter-track as well as interlayer porosity, an appropriate overlap percent must be selected during the LMD process. Also a particular degree of track overlap is required to prevent porosity between tracks, which has a significant impact on the final density of the manufactured item [239].

2.11 Surface modification by LMD process

The LMD method is a prime choice for applications requiring surface modification. One study investigated the effect of laser power on the deposited material [240]. The material was processed at different laser powers between 0.4 and 3.2 kW. The results showed that microhardness and wear resistance changed with variations in laser power. When laser power was reduced, microhardness initially increased and then decreased, while increasing laser power improved wear resistance up to a point, after which further increases caused a decline. Based on the processing parameters in this study [240], a laser power of 2 kW was found to be ideal for surface modification. Furthermore, the effect of laser scanning speed on the deposited material was also investigated [218]. The results were consistent: wear resistance initially increased with scanning speed, and microhardness continued to improve as scanning speed increased further.

Chapter 3

3 Materials and methods

3.1 Introduction

This chapter provides a comprehensive overview of the materials, methods, and systematic approaches utilised in the current study, specifically focusing on the LMD process applied to electrical steel components. A section of this chapter has been adapted from the paper titled *"Process Window for Manufacturing Soft Magnetic FeSi 6.5% by Laser Metal Deposition"* presented at the 21st International Conference on Manufacturing Research. The chapter begins with a detailed characterisation of the materials, including an analysis of feedstock powder properties and substrate materials essential for LMD processes. A thorough examination of the powder morphology and particle size distribution is conducted to ensure consistent feedstock quality, which plays a crucial role in the deposition's microstructural and mechanical performance. Additionally, characterisation techniques such as scanning electron microscope (SEM) and materials image processing and automated reconstruction (MIPAR) analysis are employed to gain deeper insights into the microstructural features and overall quality of the deposited material. SEM analysis enables a close inspection of the powder's surface features, particle shape, and size distribution, providing essential data to predict behaviour during deposition. MIPAR characterisation further complements this analysis by automating the detection and quantification of specific microstructural attributes, thereby enhancing the precision and reliability of the characterisation process. In subsequent sections, the preparation of substrates for the deposition of FeSi powder is described, emphasising the necessary steps for optimising substrate surface conditions. The effectiveness of the LMD process relies heavily on substrate quality and preparation; thus, this section covers essential steps such as cleaning, surface texturing, and pre-heating, all tailored to improve the adhesion and uniformity of the deposited material.

The chapter also covers the customisation of the LMD platform itself. This section addresses specific modifications made to the platform's parameters and hardware settings to accommodate FeSi powders and optimise deposition outcomes. Tailored adjustments, including laser power settings, nozzle configuration, and feedstock flow rate, are highlighted as critical steps in achieving a consistent deposition and desired microstructure. The final sections focus on the optimisation of process parameters in LMD-based additive manufacturing, particularly for the deposition of electrical steel. This includes an in-depth discussion on optimising laser parameters such as power, scanning velocity, and layer thickness to minimise defects and achieve desired mechanical properties. By controlling these parameters, the study aims to enhance the LMD process's repeatability and reliability for industrial applications. This chapter focuses solely on the materials and methodologies employed, with results and discussions presented in a separate chapter (Chapter 4). This chapter concludes with a summary and conclusions, capturing the key methodologies, outcomes, and best practices established for material deposition and characterisation in LMD of E-Steel components.

3.2 Materials used for this research

This section outlines the materials and methods used in this study, with a specific focus on the application of high-silicon electrical steels (FeSi) for additive manufacturing using the LMD process. Electrical steels with a high silicon content (6-6.9 wt% Si) are especially valuable for their excellent magnetic properties, making them suitable for components in electrical motors and other applications requiring soft magnetic materials. The goal of this research is to optimise the processing of these FeSi powders through LMD, ultimately enhancing their flow characteristics, deposition quality, and resulting optimised microstructure, texture and mechanical properties. To achieve these aims, the study emphasises the role of FeSi powder composition and particle size, given that these factors significantly impact both the deposition process and final material properties. Establishing a consistent and thorough characterisation of FeSi powder is essential, as it allows for an understanding of how these attributes influence material behaviour during LMD. This section thus begins with a comprehensive characterisation of the feedstock powder, to assess its chemical composition, particle morphology, and flow properties.

The evaluation, characterisation and qualities of powder are crucial in the field of powder metallurgy and additive manufacturing, with different component manufacturing procedures requiring different powder properties. Better comprehension and control of these elements result in final material qualities that are more reliable and enhanced across a variety of applications. In this study, high silicon electrical steel gas-atomised powder batches were produced by MSE Supplies LLC company. The chemical composition of the powder includes Si (6-6.9 wt%), Mn (~0.05 wt%), C (~0.01 wt%), P (~0.01 wt%), O (~0.03 wt%), and Al (~0.2-0.6 wt%). The particle size ranged from 45-110 µm, with a mean particle size of 77.5 µm, a Hall flowmeter measurement of 19.0 s/50g (Measured following ASTM B213 [241]), and an apparent density of 4.06 g/cm^3. Simultaneously, an assessment of the powder was conducted for cross-checking, and additional details can be found in Table 2 below. Also, the substrate used was mild steel blocks, selected for their compatibility with FeSi deposition and ease of machining.

Table 2. FeSi powder chemical composition.

Chemical composition (wt%)				Size distribution (stv:± 3.0 µm)		
Fe (stv:±0.5wt%)	**Si** (stv:±0.03wt%)	**Al** (stv:±0.01wt%)	**Trace elements** (<0.01 wt%)	**D10**	**D50**	**D90**
92.90%	6.60%	0.46%	C,S,N	34.5	78.5	116

3.3 Powder and SEM characterisation

In addition, the Hall flow test was conducted in accordance with a standard facility following ASTM B213, using a 50g sample of FeSi powder. The expected flow time, as per the manufacturer's recommendations, was 19 seconds. To calibrate the powder flow rate for the LMD process, the Hall flow test was repeated multiple times, and the powder mass exiting the nozzle was measured continuously over a defined period using a digital balance with ±0.01 g repeatability. This procedure ensured that the powder flow rate was consistently adjusted to the target of 2.5 g/min for all deposits, with argon employed as the carrier gas to transport

the feedstock and minimise oxidation during delivery. However, the Hall flow test was conducted twice, and both tests yielded consistent results, with a flow time of approximately 23 seconds for the 50-gram sample Figure 20. The fine powder, usually with dimensions smaller than 10µm, is characterised by its poor flow characteristics.

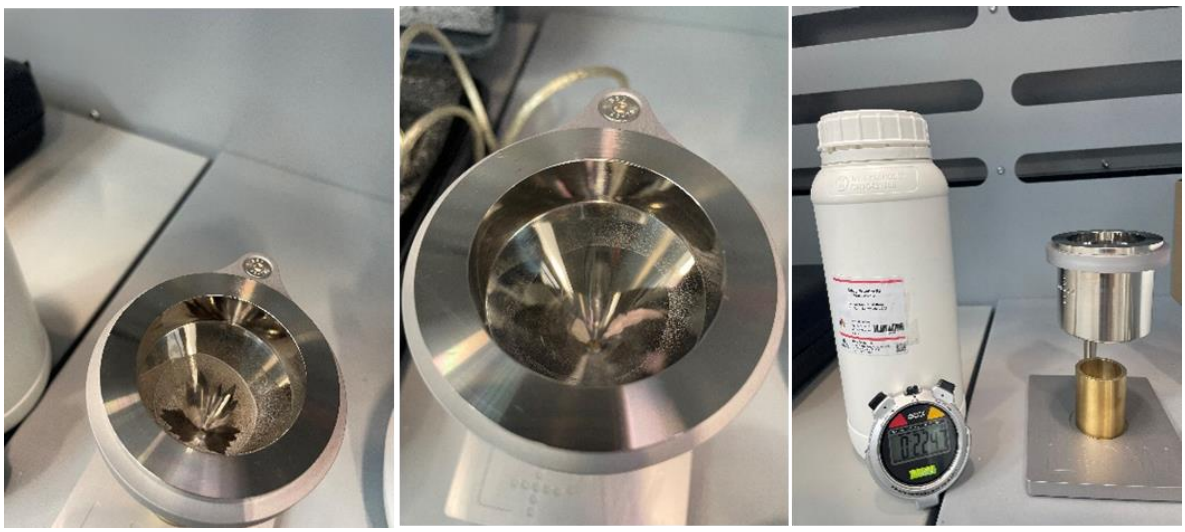

Figure 20. The Hall flow test of FeSi powder.

During the Hall flow test, a minor loss of 0.1 grams of powder occurred due to some sticking in the hopper. While this loss was negligible and did not significantly impact our research, it was important to consider that this batch of powder underwent handling during our initial trials. These handling procedures could have affected the powder's characteristics, such as its moisture absorption. To confirm the manual Hall flow tests, the Analystte 28 Image Sizer instrument was used to validate the results. The Hall flow test was conducted three times, yielding consistent results of 18.13, 18.69, and 18.92 seconds, which are close to the manufacturer's recommendation of 19 seconds for 50 grams. Comparing the manual and instrument results, it can be concluded that the manual Hall flow test may have some errors, as it does not closely match the manufacturer's recommendation, while the Analystte 28 Image Sizer instrument results align well with it. Considering the concern regarding moisture, precautions were taken. The powder was preheated in the hopper prior to manufacturing in order to minimise moisture absorption. In practice, complete removal of moisture would require higher temperatures or vacuum drying; however, the LMD system used in this study was limited to a maximum hopper preheating temperature of 50 °C. Based on recommendations from industry partners and the equipment supplier, the powder was therefore dried at approximately 50 °C for 2.5 h. Although this temperature is relatively low compared to conventional drying standards (where 100–200 °C or vacuum drying is often employed for metallic powders [242], preheating at 50°C was the most suitable option under the available process constraints. This procedure improved powder flowability and reduced the risk of moisture-related defects during deposition. In addition to that, this study focuses on the examination of metallic powders of FeSi utilised in the LMD for additive manufacturing,

specifically assessing, chemical composition, particle size and shape through SEM and MIPAR analysis.

To set up the analysis of FeSi powder by SEM, the procedure involved obtaining a stub that attached to the bottom of mounted samples, followed by the application of carbon tape onto the stub. Great care was taken to ensure that an appropriate amount of powder was applied – only a single layer was considered suitable for analysis. The stub was then gently tapped to remove any excess powder and subsequently placed within a desiccator for a duration of 5 minutes before its utilisation within the SEM. For the analysis of particle size distribution (PSD), SEM images were captured at a magnification level that allowed for the observation of approximately 80 to 100 particles within the field of view, with minimal overlap between particles. A minimum of four micrographs were obtained from distinct sample areas, with subsequent data analysis conducted. Regarding satellite particles, acquiring a few higher magnification images proved to be advantageous. As illustrated in Figure 21, the FeSi powder batch consists predominantly of spherical particles, with the presence of a few small satellite particles, which are a common feature of gas-atomised powders due to particle–particle collisions during solidification [243]. While such satellites are commonly observed, their occurrence can be reduced by optimising atomisation conditions, and they may be further removed by post-processing techniques such as sieving, or air classification [244].

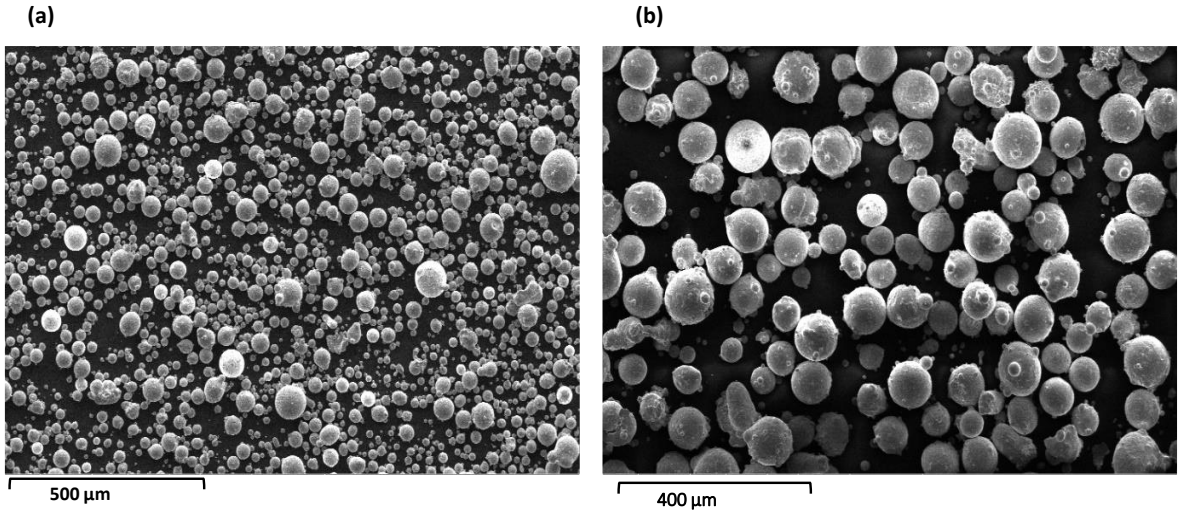

Figure 21. SEM images taken from FeSi powder with different magnification (a)100x and (b)125x.

SEM was performed using FEI Quanta 250 and 650 systems with accelerating voltages up to 25 kV. Limitations of SEM include the requirement for vacuum conditions, the need for conductive samples (addressed here by carbon taping), and resolution restricted to a few nanometres. When coupled with energy dispersive X-ray spectroscopy (EDS/EDX), the system provides semi-quantitative elemental analysis, with detection limits typically ranging from 0.1–0.5 wt% and potential spectral peak overlaps for elements with close atomic numbers [245]. In this study, SEM-EDS was employed to examine both particle morphology and elemental composition of FeSi powders. The analysis targeted a representative selection of the spherical and irregularly shaped particles visible in Figure 22, with a total of 5 EDS

measurements conducted across different particles. The detected elements—iron (Fe), silicon (Si), and aluminium (Al)—were in good agreement with the supplier's nominal composition, while sulphur (S) and oxygen (O) were excluded as their concentrations fell below the detection limit of 0.1 wt%. The accompanying table presents the average elemental composition in weight%, and standard deviations based on these measurements, reflecting variability and the semi-quantitative nature of EDS.

(a)

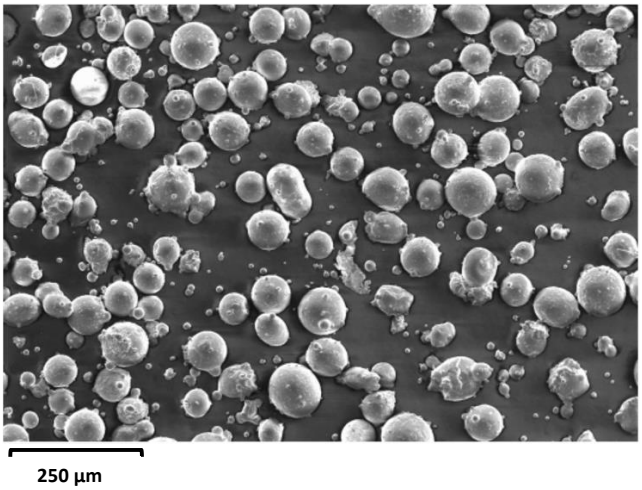

(b)

Map sum spectrum		
Element	Average Weight %	Standard deviations
Fe	91.13	±0.4
Si	5.17	±0.3
Al	2.95	±0.2

Figure 22. Particle morphology (a), elemental composition (b) of FeSi powder.

3.4 MIPAR characterisation

The area, diameter, and eccentricity of FeSi powder are extracted using the MIPAR (image analysis software) after a unique recipe for transforming SEM pictures with different magnifications (e.g., 100x and 125x) into binary data has been developed for quantification which can be seen in Figure 26 and Figure 27. MIPAR software automates the detection and quantification of microstructural features, offering a faster and more standardised alternative to manual analysis. Complex or overlapping features may be misclassified, and as it is limited to 2D analysis, true 3D connectivity cannot be assessed [246]. Furthermore, the Analystte 28 image sizer was used to validate the results of characterisation. The Analystte 28 image sizer provides accurate, reproducible measurements of particle shape and size for powders, bulk solids, suspensions, and emulsions. Using Dynamic Image Analysis, it offers detailed shape and size data within minutes [247].

Preparation substrates for deposition of FeSi powder

For this project, mild steel blocks were initially selected and cut into various sizes. Electrical discharge machining (EDM) was then used to prepare two cylindrical forms suitable for the rotating table, onto which FeSi 6.5% powder was deposited using the LMD process, as shown in Figure 23. In the first trial, the substrates were not preheated; however, in subsequent trials they were cleaned with acetone to remove contaminants, surface-machined to prepare the surface for printing, and preheated to 200 °C to minimise thermal gradients and reduce cracking. Preheating effectively reduced cooling rates and residual stresses, with uniform

heating assumed and oxidation considered negligible [248]. After manufacturing the single tracks, the samples were sectioned by EDM, mounted, and prepared for characterisation through sequential grinding (SiC papers 240–P2500 grit, water-cooled, 240 rpm, 27 N, 3 min), polishing with 3 µm Mg oil-based Metadi, and final polishing with a Microcloth (150 rpm, 27 N, 6 min, Buehler). Vibropolishing was also applied to achieve high-quality surfaces for assessing both microstructure and crystallographic texture [249].

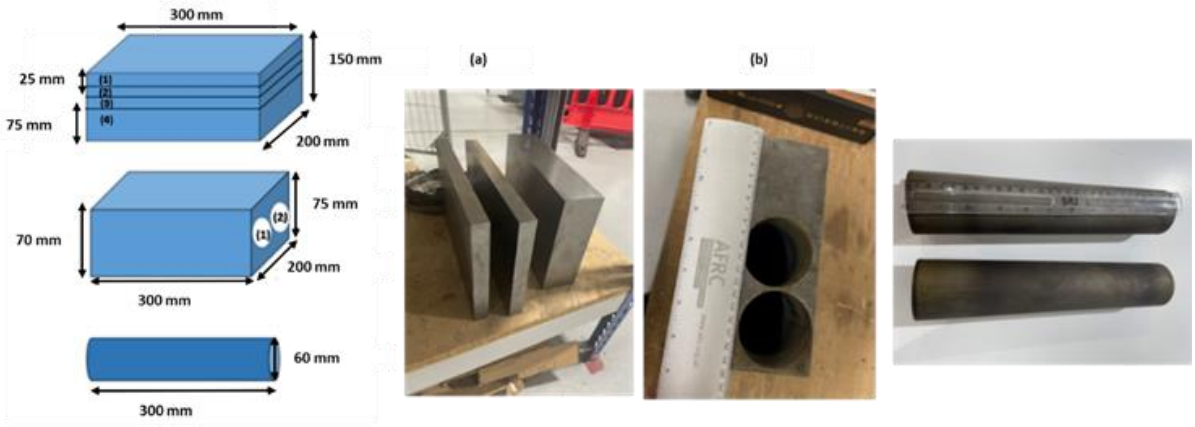

Figure 23. (a) substrates cut by Bandsaw and (b) EDM machine.

3.5 Laser additive customisation of LMD platform

For this project, hybrid LMD technologies were employed, featuring a 3+2 axis CNC Milling machine, a 1.5kW Ytterbium Fibre laser, and an Ar localised shielded from nozzle. In this study, only localised argon shielding was utilised for the deposition of 12 single tracks, 12 small cubes measuring 10 x 10 x 10 mm^3, including extreme conditions, and 5 thin walls measuring 15 x 10 x 2 mm^3 for the investigation of window process parameters. A 1mm spot size, and powder feed rates flow was 2.5 g/min was maintained for all deposits. The spacing between scan track centrelines within each layer was set at 0.6 mm in horizontal plane known as tracking space or hatch space, and the vertical distance or thickness between each layer known as z-step was fixed at 0.4 mm along the build direction. Argon was used as carrier and shielding gas to prevent oxidation. Continuous, localized coverage directly over the melt pool ensured that oxygen exposure was minimised during deposition. The powder delivery system was calibrated as described earlier, ensuring a consistent flow rate and stable material feed. Laser power stability was checked using a power meter before each run to ensure <5% variation, while alignment of the laser and nozzle was verified using a camera system to maintain a coaxial beam. These combined measures—argon shielding, controlled powder delivery, and stable, aligned laser operation—ensured that oxidation during deposition was negligible. Consequently, oxidation was not treated as a primary variable in this study, allowing the focus to remain on microstructural evolution, cracking behaviour, and texture development. The effect of oxidation on long-term magnetic performance remains an important topic for future work, which could be investigated through controlled exposure experiments and subsequent magnetic characterisation.

3.6 Optimising process parameters for AM of LMD-printed E-Steel

This series of research aims to produce almost solid soft magnetic components using the LMD by reducing the range of processing parameters windows. The study was divided into different phases to evaluate the effects of silicon concentration in the powders and other construction factors, such as laser power, scan speed, and energy density on the development of defects such porosity and cracks. Sample collection involved depositing single tracks, cubes, and thin walls in a step-by-step manner: first single tracks for initial parameter screening, then multi-layer builds. Assumptions include negligible environmental variations and consistent powder feed; approximations in energy density calculations ignore heat losses.

3.7.1 Laser power

The assessment initially focused on examining the impact of laser power and scan tracks on the final manufacturing of FeSi parts. To assess and enhance the process parameters of single tracks, laser power settings between 350 W and 550 W were chosen, all the while ensuring a consistent scan speed of 400 mm/min were maintained. Moreover, to better understand of processing parameters effect on single tracks, the 3D digital microscope RH-2000 Hirox [250] was used.

3.7.2 Scan speed

Another experiment was carried out to establish the ideal scan speed while maintaining a fixed laser power of 450 W. In addition to that, the scanning speed was varied between 400 and 650 mm/min, to determine the optimum scan speed. The scanning pattern employed was unidirectional (A-B A-B), with linear tracks aligned in the same direction.

3.7 Mechanical properties of Fe Si parts fabricated by LMD

This case study presents the material properties of electrical silicon steel alloys processed using the LMD process. While mechanical properties were not the primary criteria for this research, they remain crucial for ensuring the material can sustain mechanical loads and torque, particularly in high-frequency applications. Therefore, hardness tests and other mechanical property evaluations were conducted. This chapter examines how variations in processing parameters, such as energy density and processing conditions, influence hardness and its correlation with grain size in this soft magnetic alloy. Various samples, including thin walls, cubes, and discs, were sectioned and tested for hardness, as shown in Figure 24.

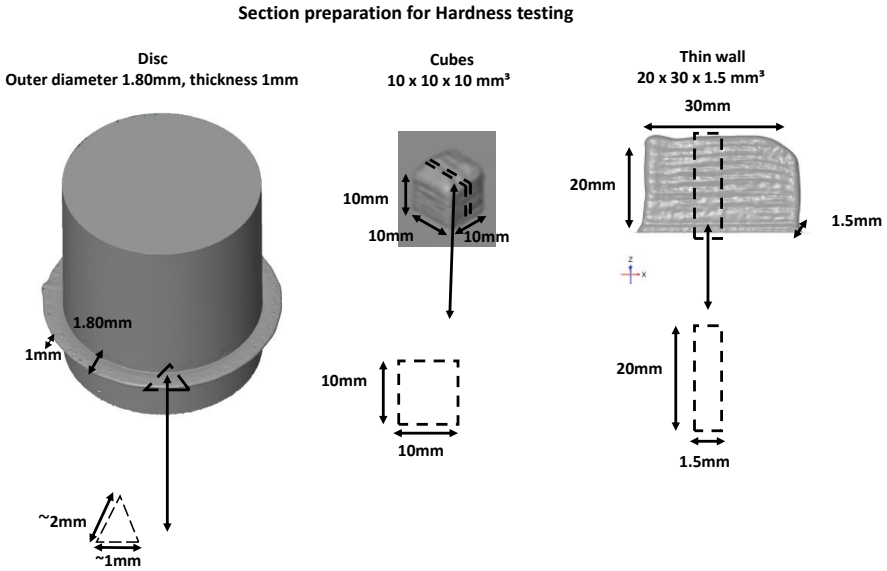

Figure 24. Cut sections of thin walls, cubes, and discs prepared for hardness testing.

In this section, thin walls, cubes, and discs sample of silicon steel with a silicon content of 6.5 wt% were processed using LMD with an optimal parameter set. To assess the effect of the processing parameters on the mechanical properties, micro-hardness was measured using a Vickers indenter. The indentation results are expressed as the mean ± standard error and are presented in the Figure 25 below.

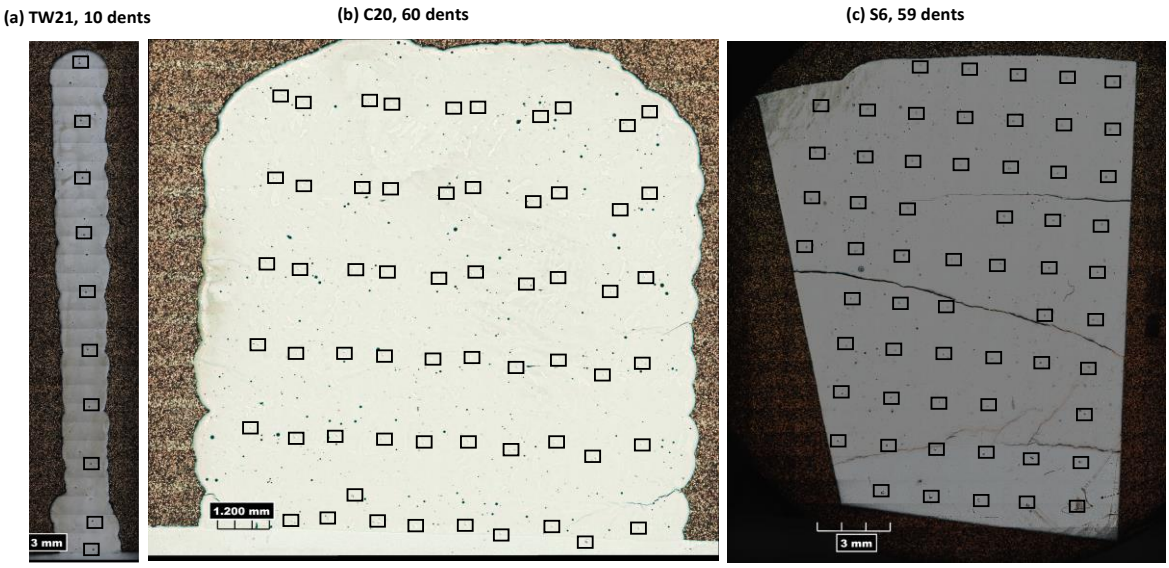

Figure 25. Vickers hardness test was conducted on different samples thin wall TW21, cubes C20 and disc S6.

3.8 Characterisation techniques

A combination of characterisation techniques was employed to evaluate the microstructure, texture, composition, and properties of the fabricated samples. Some of these methods have already been described in earlier sections; here, a concise overview is provided together with their main applications and limitations.

Optical microscopy was employed for initial surface morphology observations using a Leica and an RH-200 Hirox digital microscope. These instruments provided a rapid overview of surface features; however, the resolution was limited to approximately 0.2 µm, and the observations were restricted to two and three-dimensional imaging [251]. Scanning electron microscopy (SEM) combined with energy-dispersive X-ray spectroscopy (EDX) was carried out on an FEI Quanta 250 and 650 at 25 kV. SEM enabled high-magnification imaging, while EDX facilitated compositional analysis. However, the method requires vacuum conditions and conductive coatings for non-conductors, with EDX further constrained by a detection limit of ~0.1 wt%, peak overlaps, and reduced accuracy for light elements with atomic number [252].

Electron backscatter diffraction (EBSD) was performed using an Oxford Instruments detector on the FEI Quanta system at 25 kV with a 70° specimen tilt. This technique provided crystallographic orientation mapping with a spatial resolution of about 50 nm, although accuracy was strongly dependent on careful surface preparation and very small deformations could not be captured [253]. . EBSD data were further processed using AZtec and Crystal software to evaluate crystallographic texture. These analyses allowed the calculation of orientation distribution functions (ODFs) and pole figures, but they remained sensitive to noise and misindexing errors, with reliability depending on the quality of the EBSD dataset [254].

Mechanical properties were assessed through Vickers microhardness testing, using loads 0.1 Kgf. with dwell times of 10–15 s. This method provided local hardness values, but it required accurate surface preparation and appropriate spacing between indents (>2.5× diagonal). Furthermore, it was unsuitable for very thin layers, as a minimum thickness of approximately 1.5× the indent diagonal was necessary [255]. Quantitative microstructural measurements were also performed using MIPAR image analysis software, which enabled automated defect and microstructural quantification from SEM micrographs. Despite its usefulness, the method was limited by recipe dependency, difficulties with low-contrast images, and the absence of 3D analysis capability [246].

Finally, X-ray computed tomography (XCT) was used for non-destructive three-dimensional defect characterization with a Zeiss XCT system. This technique provided volumetric data with voxel resolutions in the range of 1–3 µm for small samples. However, increasing sample size led to reduced resolution, while the analysis of dense metallic materials was prone to artifacts and long scan times [256]. This chapter has described the materials, sample preparation, LMD setup, parameter optimization, and the characterization techniques used. These approaches were chosen to ensure consistent and reliable deposition of FeSi for electrical steel applications.

Chapter 4

4 Results and Discussion

4.1 Powder characterisation results

Figure 26 (a), (b), (c), and (d) illustrated the MIPAR image obtained for SEM FeSi 6.5% at 100x magnification, where 1 pixel corresponds to 1.92 µm. Only a few powders, as observable in the SEM image, were not selected in the MIPAR software due to ambiguous boundaries, such as satellite powders or physically attached clusters, which could distort measurements. The bar chart (b) shows the majority of the powder area ranges between 500 to 1500 μm^2 with a few outliners from 1500 to 4000 μm^2 with a mean size of 1088 μm^2. Chart (c) illustrates the equivalent diameter (µm) of FeSi 6.5% powder, representing the typical or mean size of the sample ~35.34 µm. The majority of powder diameters range between 20 to 40 µm, with a few outliers ranging from 40 to 70 µm. In addition, the bar chart (d) illustrates the eccentricity of FeSi 6.5%, which shows the shape and morphology of the powder, as well as circularity and elongation. A low eccentricity value, close to 0, indicates that the powder is more circular, while a value closer to 1 suggests that the powder is more elongated. In this case, the majority of the FeSi 6.5% metallic powder particles are closer to being perfectly circular ranging from 0.1 to 0.7, while a minority of the powder particles are highly elongated or non-circular ranging from 0.7 to 1 with a mean size of 0.59.

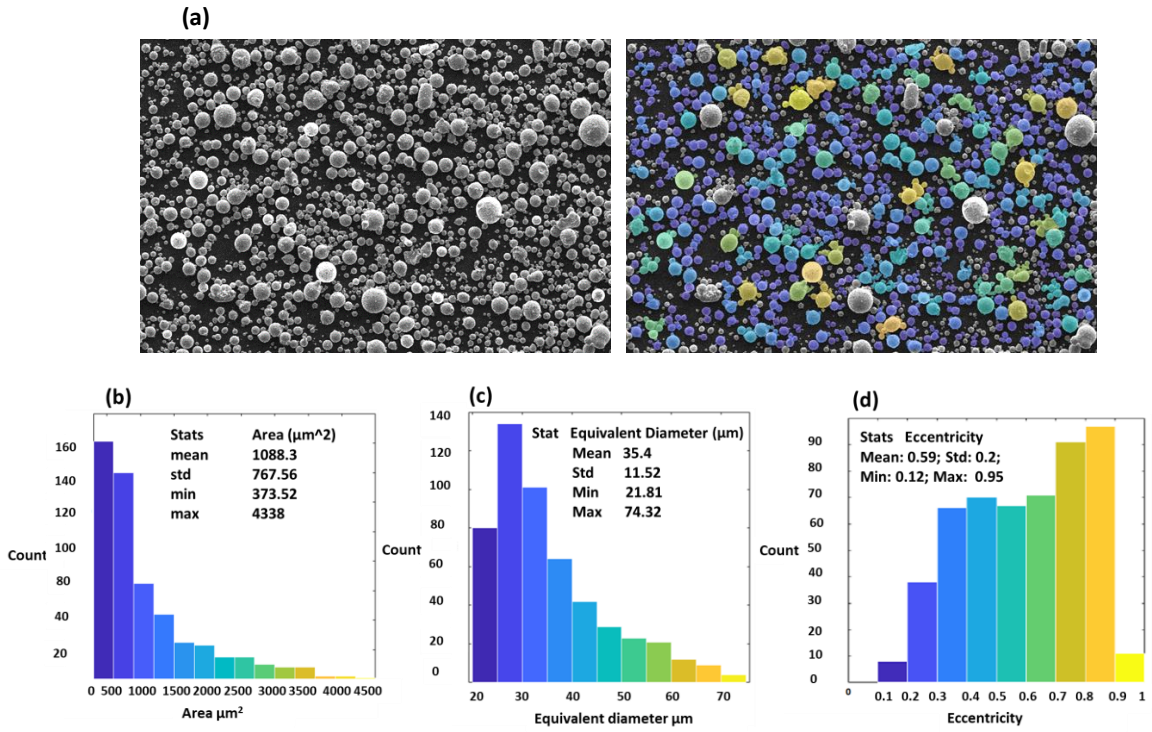

Figure 26. (a) MIPAR data obtained from SEM FeSi 6.5% powder with magnification 100x , (b) area µm2 (c) equivalent diameter µm and (d) eccentricity powder.

Figure 27. (a) MIPAR data obtained from SEM FeSi 6.5% powder with magnification 125x , (b) area µm2 (c) equivalent diameter µm (d) eccentricity of powder. Figure 27 (a), (b), (c), and (d) presents the MIPAR image acquired for SEM analysis of FeSi 6.5% at 125x magnification, where each pixel represents 1.54 µm. The bar chart (b) illustrated most of the powder area ranges between 1000 to 8000 μm^2 with a few outliners from 8000 to 10000 μm^2, with a mean size of 3788 μm^2 . Chart (c) illustrates the equivalent diameter (µm) of FeSi 6.5% powder, representing the typical or mean size of the sample ~67 µm. The majority of powder diameters range between 30 to 100 µm, with a few outliers ranging from 20 to 30 µm and 100 to 110 µm. Furthermore, the bar chart (d) demonstrates the eccentricity of FeSi 6.5%. It reveals that most metallic powder particles in FeSi 6.5% exhibit a perfectly circular shape, falling within the range of 0.1 to 0.6. However, a minority of these particles appear highly elongated or non-circular, with eccentricity values ranging from 0.6 to 0.7.

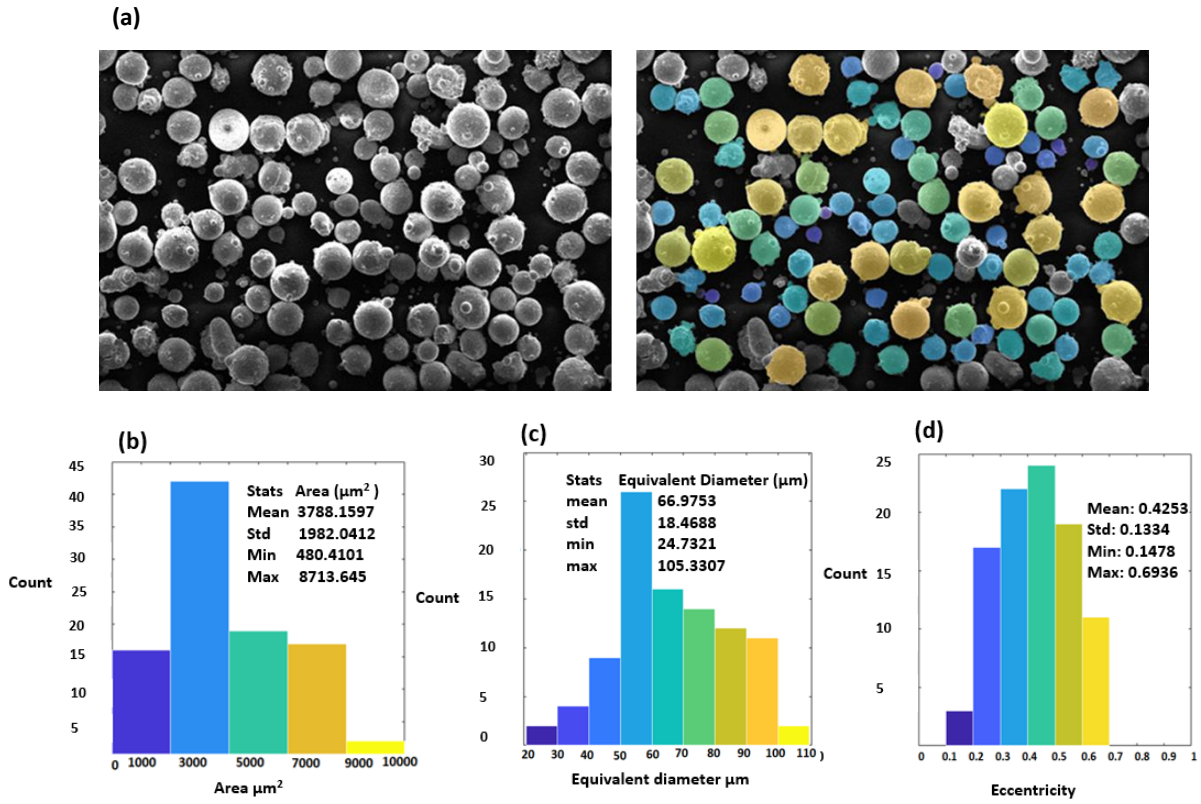

Figure 27. (a) MIPAR data obtained from SEM FeSi 6.5% powder with magnification 125x , (b) area µm2 (c) equivalent diameter µm (d) eccentricity of powder.

As it can be seen the scatter plot Figure 28 illustrates the relationship between the aspect ratio and the equivalent circular diameter of particles within an FeSi 6.5wt%. The x-axis represents the equivalent circular diameter in µm, while the y-axis shows the aspect ratio, ranging from approximately 0.15 to 0.95. The aspect ratio is a measure of particle shape, with values near 1 indicating nearly spherical particles and lower values suggesting more elongated or irregular shapes. The plot reveals distinct clusters of particles, each coloured differently to

indicate varying size and shape distributions within the sample. The dense red/orange cluster is concentrated on the lower end of the equivalent circular diameter, indicating smaller particles with a broad range of aspect ratios between 0.3 and 0.95. This suggests that smaller particles in the sample exhibit a significant variety of shapes, likely due to differences in their formation processes. In contrast, the blue cluster, which extends towards larger equivalent circular diameter, shows a more spread distribution. These larger particles display a wide range of aspect ratios, from highly elongated to nearly spherical. This spread implies that as particle size increases, the diversity in particle shape also becomes more pronounced, reflecting the complex morphology of the FeSi 6.5 wt% alloy. Overall, this scatter plot highlights the diversity in particle size and shape within the alloy sample, indicating a mixture of morphologies that could significantly influence the material's properties, such as flowability, packing density, and reactivity. Understanding this distribution is crucial for optimising the material's performance in various industrial applications, such as additive manufacturing processing as well as powder metallurgy or sintering, where particle shape and size play critical roles [257].

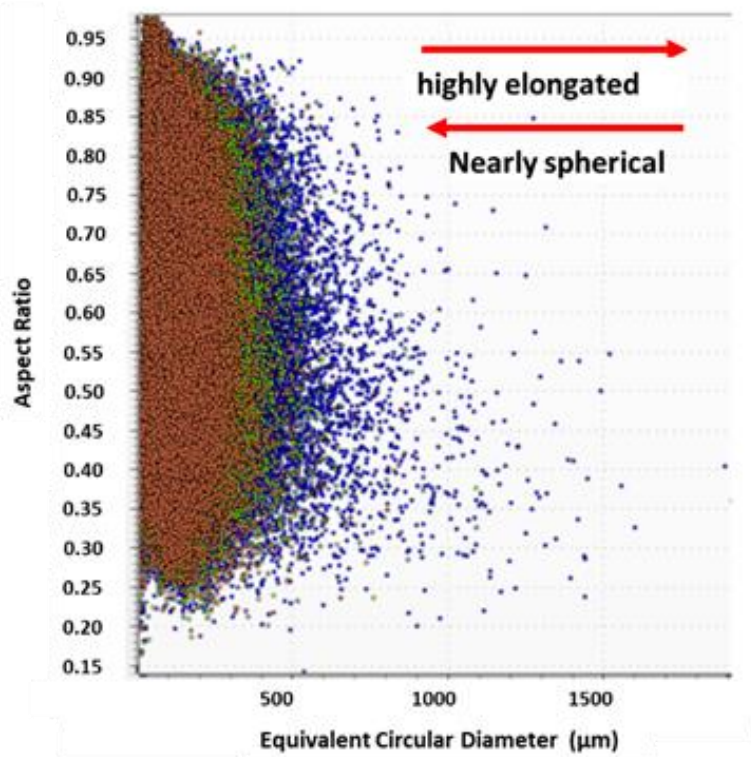

Figure 28. Relationship between equivalent circular diameter and aspect ratio of FeSi 6.5 wt%.

4.2 Laser metal deposition results

Figure 29 showed the surface morphology of the first layer single tracks under various laser powers (300 up to 550 W) and scanning speeds (350 up to 650 mm/min). Under the given processing parameters, twelve continuous single tracks were formed on the substrates, with some defects present, which will be covered in more detail later.

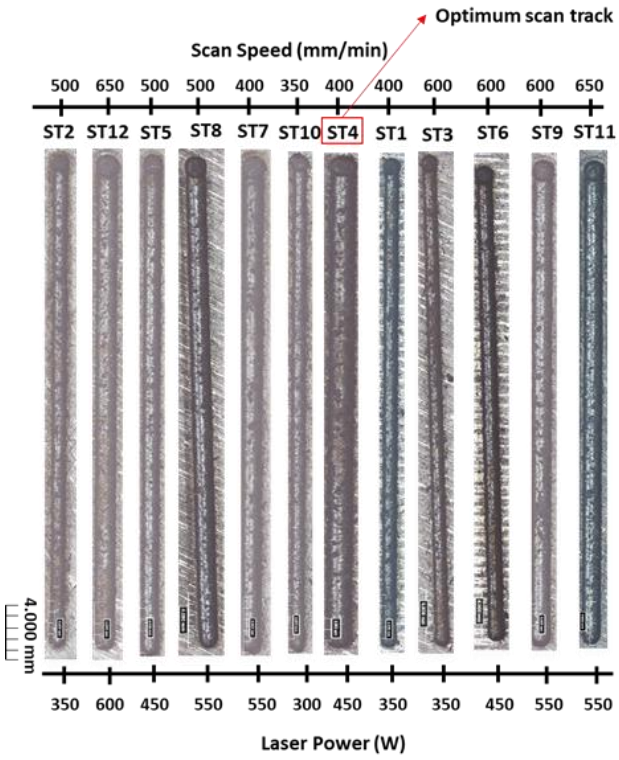

Figure 29. 3D single track morphology with different laser power and scanning speed.

Additionally, the study examined the 3D vertical and horizontal profiles, along with heat maps of each individual track height, using the RH-2000 Hirox microscope. The heat map was generated by the Hirox microscope's imaging system, which maps height variations across the sample surface using colour gradients based on the 3D profile data collected during scanning. The 3D profile was measured using the Hirox microscope's optical scanning system, which captures height variations by analysing reflected light across the sample surface to construct a detailed topographic model. The 3D profile measurement revealed the height and width of the displayed sections using waveforms. In this context, the heights ranged from 0.5 mm (ST6) to 0.84 mm (ST2). Furthermore, the heat map illustrated that among all the samples, ST4 exhibited uniform height and width across the length of the samples compared to others, as shown in Figure 30 and Figure 31. The presence of continuous single tracks at each set of input parameters for laser power and scanning speed indicates that the morphology of single tracks is largely dependent on the processing parameters. Additionally, the crack size of ST4 was measured using ImageJ [258], revealing the smallest crack size (1.02%) compared to the other samples. Based on the data extracted from the Hirox surface roughness measurement microscope, and Image J, the single track 4 (ST4: power 450 W) was determined to be the optimising laser power for FeSi 6.5%.

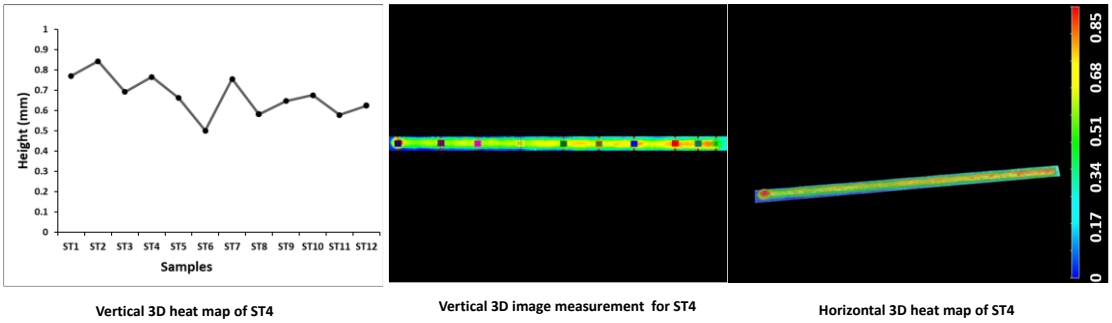

Figure 30. Illustrated a single tracks height measurement for each sample, heat map, 3D profiles vertical and horizontal measurement for ST4 using the RH-2000 Hirox microscope.

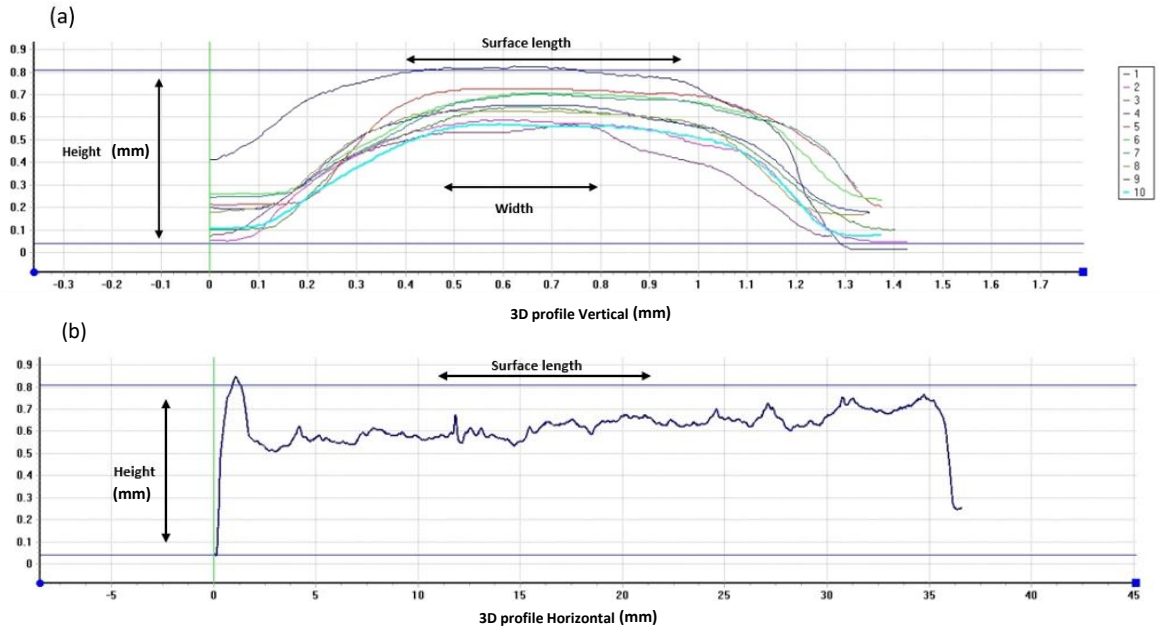

Figure 31. Illustrated 3D profile vertical (a), and horizontal (b) of sample ST4.

The result demonstrated that low scan speed of 400 mm/min has stable scan tracks, the lowest porosity size (0.3%), and the maximum relative density compared to other single tracks. The samples were sectioned by EDM, mounted, and prepared through sequential grinding, polishing, and final vibropolishing, as described in the previous section, to ensure a deformation-free surface suitable for high-quality Kikuchi pattern acquisition. For detailed microstructure analysis, electron back-scatter diffraction (EBSD) data obtained from a FEI Quanta 250 and 650 Oxford Instrument EBSD camera with a 25kV accelerating voltage and 70-degree sample tilted to the laser beam. EBSD mapping was conducted with a step size of 3 µm, and the data were acquired and indexed using AztecCrystal software (Oxford Instruments). Furthermore, based on the EBSD analysis of the three single tracks—ST14, ST4, and ST32 (shown in the IPF maps, Figure 32), ST4 was selected as the optimal processing parameter for manufacturing high-silicon steel 6.5 wt% due to its columnar grain structure and favourable magnetic properties as well as less defects. As observed in the IPF maps (Figure 32b), sample ST4 demonstrates a uniform growth of large columnar grains, extending perpendicularly from the interface to the surface, with a crystallographic preference in the

<001> direction. This orientation is particularly advantageous for magnetic applications, as it aligns well with the applied magnetic field, thereby enhancing the material's magnetic properties which is desirable for this study.

Compared to ST14 (a) and ST32 (c), ST4 shows an elongated and columnar grain structure. Specifically, as the laser power increases from 430 W in ST14 to 450 W in ST4, with a corresponding increase in energy density from 64.5 J/mm² to 67.5 J/mm², the grain becomes thinner and size decreases by approximately 10.9%, from 64.52 µm (sdv:± 6.8 µm) to 57.50 µm(sdv: ± 5.2 µm). Grain size was determined using the equivalent circle diameter method implemented in the Aztec Crystal software, consistent with the recommendations of ASTM E2627 [259] for EBSD-based grain size measurement. However, the key advantage of ST4 lies in its large, elongated and columnar grain structure in the building direction. Larger and uniformly crystal oriented <001> grains in the building direction contribute significantly to improved magnetic properties by reducing magnetic domain wall pinning, leading to lower hysteresis losses and enhancing the magnetic performance of FeSi 6.5wt% [260]. While ST32 Figure 32 (c) at a higher energy density of 68.3 J/mm² also shows a further reduction in grain size to 51.9 µm (sdv: ± 6.7 µm), the overall uniformity and alignment of the grains in the BD in the sample ST4 make it the preferable choice. As highlighted in previous studies, the uniform orientation of red grains in the <001> direction in ST4 is critical for optimising the magnetic properties of high-silicon steel. This specific grain orientation, noted for its impact on reducing energy losses and enhancing magnetic efficiency, makes ST4 the most suitable sample for the intended application. In conclusion, the processing parameters of ST4—specifically the combination of 450 W laser power and 67.5 J/mm² energy density—produce a microstructure characterised by large columnar grains with a strong <001> crystallographic orientation, which is particularly advantageous for magnetic performance. While the columnar grain shape provides uniformity and reduces grain boundaries, it is the <001> orientation that primarily enhances magnetic properties by aligning with the easy axis of magnetisation, thereby reducing hysteresis losses and improving flux conduction. This conclusion is drawn from representative EBSD measurements, with the observed grain structure and orientation clearly indicating the favourable microstructural characteristics for magnetic performance.

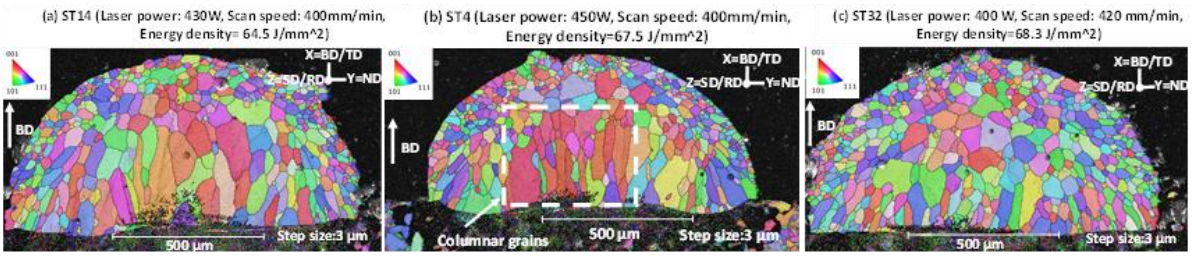

Figure 32. EBSD images of (a), (b), and (c) IPF maps of cross sections for single tracks with different processing parameters.

Therefore, the single track 4 (ST4: scan speed of 400 mm/min) was determined to be the optimum scan speed for FeSi 6.5%. Also, ST4 with laser power of 450 W, and scan speed of 400 mm/min was considered the best compromise between speed of production and quality of the final parts. Consequently, the optimum processing parameters of a single track were used as reference parameters for manufacturing cubes and thin walls which highlighted in green in Table 3. Additionally, to explore the effect of processing parameters on FeSi 6.5%, both low and high scanning speeds, as well as power variations, were applied. For the initial trials, the scanning speed ranged from 350 to 650 mm/min, while the laser power varied between 300 W and 600 W, with z-step 0.4mm and hatch space 0.6mm.

Table 3. The design of the experiment for the initial printing trial of FeSi 6.5%.

		Sample	Laser power (W)	Scan speed(mm/min)	Powder flow (g/min)
1st Run	DOE1 of Single tracks	ST3	350	600	2.5
		ST11	550	650	2.5
		ST9	550	600	2.5
		ST4	450	400	2.5
		ST7	550	400	2.5
		ST12	600	650	2.5
		ST8	550	500	2.5
		ST5	450	500	2.5
		ST1	350	400	2.5
		ST6	450	600	2.5
		ST10	300	350	2.5
		ST2	350	500	2.5
2nd Run	DOE1 of Cubes	C3	350	600	2.5
		C11	550	650	2.5
		C9	550	600	2.5
		C4	450	400	2.5
		C7	550	400	2.5
		C12	600	650	2.5
		C8	550	500	2.5
		C5	450	500	2.5
		C1	350	400	2.5
		C6	450	600	2.5
		C10	300	350	2.5
		C2	350	500	2.5
3rd Run	DOE1 of Thin wall	TW3	350	600	2.5
		TW1	350	400	2.5
		TW11	550	650	2.5
		TW4	450	400	2.5
		TW9	550	600	2.5

The scanning pattern employed was unidirectional (A-B A-B), with linear tracks aligned in the same direction, as illustrated in Figure 33. Figure 33 (a) and (b) showed single scan tracks, thin

walls, and cube specimens manufactured by LMD machine, and demonstrating an assessment of the impact of processing parameters on the final product's quality. It was observed that among all cube's samples, C4 (P: 450 W, V: 400 mm/min) met the geometry criteria in the first trial (10 x 10 x 10 mm^3), while the other cube samples did not meet the initial criteria. Additionally, during the manufacturing of sample C12 (P: 600 W, V: 650 mm/min), substantial damage to the substrate occurred due to the high power employed, as well as nozzle clogging caused by substrate spattering. This indicates that this power and scanning speed setting need to be optimised for manufacturing FeSi 6.5%. Furthermore, among all thin walls, none of them met the geometry expectations, but TW4 was higher than the others in terms of height which is a positive sign. This suggests that by applying appropriate processing parameters, the geometry criteria for cubes and thin walls could be improved.

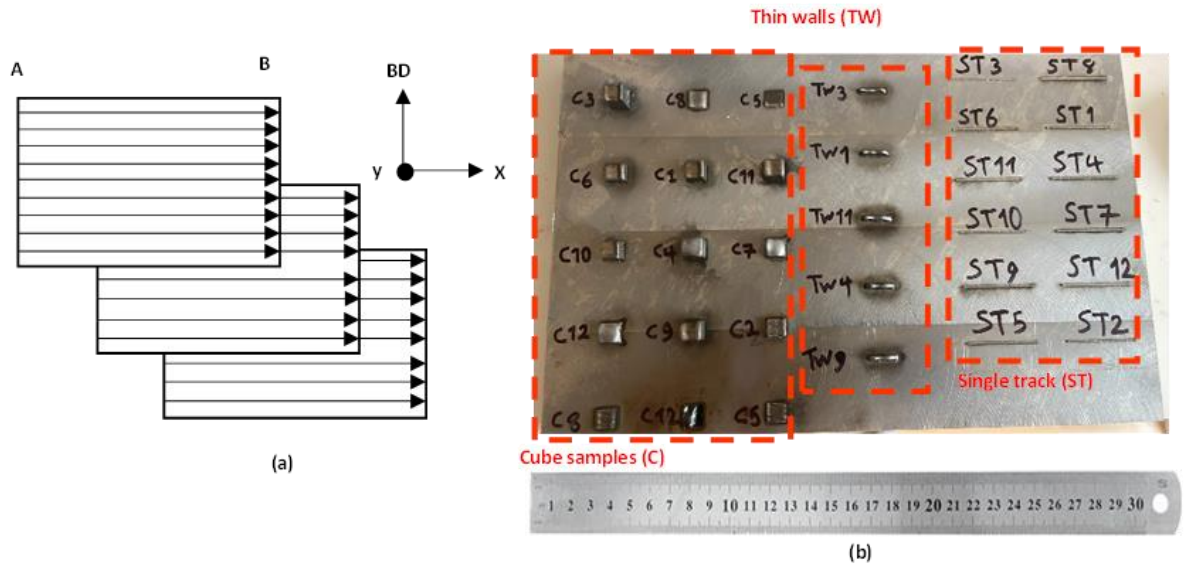

Figure 33. (a) Unidirectional scanning strategy, (b) 6.5% Silicon thin steel walls (TW), cube samples (C) and single track (ST) fabricated by LMD machine for parameter optimisation.

In the initial trial, after considering all available evidence, the boundaries for processing parameters were identified. It was observed that the first printed cube (C4: laser power:450 W, scan speed:400 mm/min, E=67.5 J/mm^2) was built very well compared to the rest of the cubes. Therefore, in the second trial, instead of concentrating solely on the powder and scanning strategy, the primary emphasis was placed on the energy density between ±10% of 67.5 J/mm^2 to improve the geometry, minimise cracks, and achieve the appropriate texture. As it can be seen in the Figure 34, the cubes with laser power 405 W and scanning speed 375 mm/min, E=64.8 J/mm^2 (C13), were well-built with minimal cracks, reaching up to 15mm, which is considered overbuilt (it should be 10mm).

Additionally, a thin wall (TW31) was produced using a laser power of 455 W, scanning at a speed of 425 mm/min, and employing an energy density of E = 64.2 J/mm², achieving a nominal height of 15 mm. However, upon comparing the machine's reported height of 10.2 mm to the actual sample, it was determined that the machine's measurement was inaccurate. This overbuilding (actual height exceeding the intended 10 mm) likely occurred in LMD due to several factors, including excess material deposition from powder flow variations, melt pool dynamics causing material accumulation, thermal distortions, and limitations in machine height sensing [261]. Consequently, the process was stopped to prevent potential nozzle damage. In the second trial, excessive deposition led to actual nozzle interference and damage. To mitigate these challenges, the z-step of cubes was reduced to 0.3 mm, providing finer control over layer height and reducing the risk of overbuilding. These outcomes suggest that, despite the challenges in layer control, the selected processing parameters are promising for producing thin wall structures. For reference, the parameters used in the first and second trials are outlined in Table 4.

Figure 34. Thin wall and cube were manufactured by LMD machine.

Table 4. Processing parameters used for second trials (a), the parameters used in the 1st and 2nd trials (b).

(a)

Sample	Laser Power (W)	Scan Speed (mm/min)	Energy Density (J/mm²)	Powder Flow (g/min)
C13	405	375	64.8	2.5
TW31	455	425	64.2	2.5

(b)

Processing Parameters	First Trial	Second Trial
Laser Diameter	1mm	1mm
Track Spacing	0.6mm	0.6mm
Z Step	0.4mm	0.3mm
Tracks per Layer	3 passes per layer	3 passes per layer

In the third set of trials for thin-wall deposited materials the same processing parameters were maintained. These parameters included a 1 mm spot size, a powder feed rate of 2.5 g/min, a spacing of 0.6 mm between scan track centrelines within each layer (for foundation layers), and a fixed layer spacing (z-step) of 0.45 mm along the build direction. To calculate and prevent any issues during printing, five layers were deposited on the substrate to calculate the z-step. The measured height should have been 3 mm, but it was 2.3 mm. Therefore, the z-step for thin walls sample TW20 (z=~2.3/5=0.46mm) with the power of 430 W, scanning speed of 380 mm/min, energy of 67.9 J/mm^2, (for test dimensions: L40, H:30, T:2 mm). Only localised argon shielding was used for the deposition process, which comprised of 20 single tracks, 20 thin walls measuring 20 x 30 x 1.5 mm^3, and 7 small cubes measuring 10 x 10 x 10 mm^3. To ensure the z-step is accurately set for the cubes and prevent over or under building, an initial deposition of 4 layers with a height of 3.8 mm was printed out on the substrate. Calculating the z-step (z= ~3.8/4 = 0.95mm) revealed it was almost twice that of the thin walls' z-step (z=0.45). Moreover, to better understand the effect of the z-step and scanning strategy on the geometry, cracks, and porosity of cubes, and thin wall couple of samples were printed with different z-step values. This will be covered in more detail in other sections. To prevent under building of the cubes, the z=0.95 mm was reduced to z= 0.85mm. In addition to that, all necessary adjustments were made to explore an optimal processing window for parameters, aiming to achieve appropriate geometry, crack-free results, as well as a suitable microstructure and texture. As shown in the Table 5 (new DoE), the scanning speed ranged from 360 to 440 mm/min, while the laser power varied between 400 and 500 W. The scanning pattern for the thin wall consisted of unidirectional (A-B A-B) linear tracks aligned in the same direction as well some bidirectional samples (AB BA). For the seven cubes, four had a unidirectional scanning pattern and the other three had a bidirectional pattern with 90^0 rotations. This variation was implemented to investigate the effect of scanning strategy on the processing parameters of FeSi.

Table 5. Design of the third experiment trials involving varied power, scan speed, and energy density, highlighting low, medium, and high energy levels in yellow, green, and red respectively.

Energy Density Range 61 >E <74 (J/mm^2)													
61.00	62.0	63.0	64.0	65.0	66.0	67.0	68.0	69.0	70.0	71.0	72.0	73.0	74.0

Scanning speed Range (360-440) mm/min	Power Range (405-490W)																			
	400	405	410	415	420	425	430	435	440	445	450	455	460	465	470	475	480	485	490	500
360	66.7	67.5	68.3	69.17	70.00	70.83	71.67	72.50	73.33	74.17	75.00	75.83	76.67	77.50	78.33	79.17	80.00	80.83	81.67	83.33
365	65.8	66.6	67.4	68.2	69.04	69.86	70.68	71.51	72.33	73.15	**73.97**	74.79	75.62	76.44	77.26	78.08	78.90	79.73	**80.55**	78.95
370	64.9	65.7	66.5	67.3	68.1	68.9	69.73	70.54	71.35	72.16	72.97	73.78	74.59	75.41	76.22	77.03	77.84	78.65	79.46	81.08
375	64.0	64.8	65.6	66.4	67.2	68.0	68.8	69.60	70.40	71.20	72.00	72.80	73.60	74.40	75.20	76.00	76.80	77.60	78.40	80.00
380	63.2	63.9	64.7	65.5	66.3	67.1	**67.9**	**68.7**	69.47	70.26	**71.05**	71.84	72.63	73.42	74.21	75.00	75.79	76.58	77.37	78.95
385	62.3	63.1	63.9	64.7	65.5	66.2	67.0	67.8	68.6	69.35	70.13	70.91	71.69	72.47	73.25	74.03	74.81	75.58	76.36	77.92
390	61.5	62.3	63.1	63.8	64.6	65.4	66.2	**66.9**	**67.7**	68.5	69.23	70.00	70.77	71.54	72.31	73.08	73.85	74.62	75.38	76.92
395	60.8	61.5	62.3	63.0	63.8	64.6	65.3	66.1	66.8	67.6	**68.4**	69.11	69.87	70.63	71.39	72.15	72.91	73.67	74.43	75.95
400	**60.0**	60.8	61.5	62.3	63.0	**63.8**	**64.5**	65.3	66.0	**66.8**	**67.5**	68.3	69.0	**69.75**	70.50	**71.25**	72.00	72.75	73.50	**75.00**
405	59.3	60.0	60.7	61.5	62.2	63.0	63.7	64.4	65.2	65.9	66.7	67.4	68.1	68.9	69.63	70.37	71.11	71.85	72.59	74.07
410	58.5	59.3	60.0	60.7	61.5	62.2	62.9	63.7	64.4	65.1	**65.9**	66.6	67.3	68.0	68.8	69.51	70.24	70.98	71.71	73.17
415	57.8	58.6	59.3	60.0	60.7	61.4	62.2	62.9	63.6	64.3	65.1	65.8	66.5	67.2	68.0	68.7	69.40	70.12	70.84	72.29
420	57.1	57.9	58.6	59.3	60.0	60.7	61.4	62.1	62.9	63.6	64.3	65.0	65.7	66.4	67.1	67.9	68.6	69.29	70.00	71.43
425	56.5	57.2	57.9	58.6	59.3	60.0	60.7	61.4	62.1	62.8	**63.5**	64.2	64.9	65.6	66.4	67.1	67.8	68.5	69.18	70.59
430	55.2	56.5	57.2	57.9	58.6	59.3	60.0	60.7	61.4	62.1	62.8	63.5	64.2	64.9	65.6	66.3	67.0	67.7	68.4	69.77
435	55.2	55.9	56.6	57.2	57.9	58.6	59.3	60.0	60.7	61.4	62.1	62.8	63.4	64.1	64.8	65.5	66.2	66.9	67.6	69.0
440	**54.5**	55.2	55.9	56.6	57.3	58.0	58.6	59.3	60.0	60.7	**61.4**	62.0	62.7	63.4	64.1	64.8	65.5	66.1	66.8	68.2

As it can be seen in the Table 5 based on the energy density level, 20 processing parameters conditions were selected to manufacture samples using the LMD machine which is highlighted in black and bold in the table. In the section below, the processing parameters for FeSi thin wall development will be covered in more detail. The initiation of the manufacturing process involved ensuring the proper setup of machines and printing based on the new DoE. Instead of following a sequential order, random and diverse processing parameters were chosen. Upon determining the appropriate z-step, the first print for the $TW20_{1st}$ single pass started. However, numerous issues including cracks, delamination, and debonding between the substrate and the FeSi part were observed. These issues occurred due to thermal expansion mismatches between the substrate and the deposited material, as well as the brittleness of the high-silicon alloy. Rapid cooling creates thermal gradients that cause cracking and weak bonding. Additionally, residual stresses from uneven heating and cooling contribute to these issues. Optimising process parameters, such as laser power, can help reduce these defects [214, 262]. The printing process was stopped after depositing 20 layers, reaching a height of 9mm ($TW20_1$) Figure 35 (a). To address these issues, the power was increased from 430 W to 600 W, while maintaining a constant scanning speed at 380 mm/min ($TW20_2$) for a foundation layers. The aim was to achieve better bonding between the substrate and the FeSi part. Despite achieving the desired geometry, debonding and cracks persisted Figure 35(b). A new strategy was implemented wherein different powers were used for the foundation and deposit layers—600 W and 430 W, respectively—while maintaining the scanning speed at 380 mm/min ($TW20_3$) and employing a single pass. This approach resulted in outcomes like previous attempts but with fewer cracks and improved substrate bonding (Figure 35 (c) green colours are scan artefacts, not sample discolouration).

To gain deeper insights, another test was conducted using 3 passes and 4 layers, with power set at 600 W and scanning speed at 380 mm/min ($TW20_4$). This test was stopped at a 5mm height to investigate the material behaviour after deposition on the substrate. The results revealed no cracking during the process and indicated enhanced bonding between the

substrate and the printed part. However, delamination was observed after the cooling process Figure 35 (d). A subsequent printing strategy aimed to enhance the foundation of deposited materials by increasing the power to 600 W, maintaining a scan speed of 380 mm/min for better bonding, and reducing the delamination effect. Additionally, the depositing top layers continued by applying a power of 430 W and a scan speed of 380 mm/min ($TW20_5$). The results demonstrated the potential to achieve appropriate geometry with reduced cracks and delamination Figure 35 (e). Considering all observations, a final step involved reducing the length of parts from 40 mm to 30 mm. Different processing parameters were applied for foundation layers (laser power: 600 W, scan speed: 380 mm/min) and top deposit layers (laser power: 430 W, scan speed: 380 mm/min) ($TW20_6$). This adjustment resulted in very good bonding between the substrate and the deposited part, with minimal delamination and small cracks Figure 35 (f). Further investigate the elimination of cracks and delamination defects, various materials were utilised for the foundation layer, including 316L austenitic steel powder (gas atomised, composition: Fe, 17% Cr, 12% Ni, 2.5% Mo, 2.3% Si) with a particle size range of 45 to 106 µm. The processing parameters for the foundation layer (316L austenitic steel) were set at power: 600 W and scan speed: 380 mm/min, while for the top layer of deposited materials, laser power: 430 W and scan speed: 380 mm/min were used ($TW20_7$). Three passes were applied for the foundation layer and one pass for deposited FeSi. It was observed that there was no delamination indicating improved bonding between the substrate and deposited materials Figure 35 (g). Based on these findings, the deposition process involved applying 316L austenitic steel as the foundation layers (3 passes) using a power of 600 W and a scan speed of 380 mm/min. Additionally, FeSi (one pass) was deposited on top with a power of 430 W and a scan speed of 380 mm/min ($TW20_8$). The outcome appeared promising as there were no indications of delamination at the interface between the substrate and the deposited materials. Nevertheless, one crack did propagate through the thin wall after the cooling process Figure 35 (h). This occurrence highlights the need for further investigation into the cooling conditions and thermal stress distribution, as these factors may contribute to crack propagation in the final structure [263].

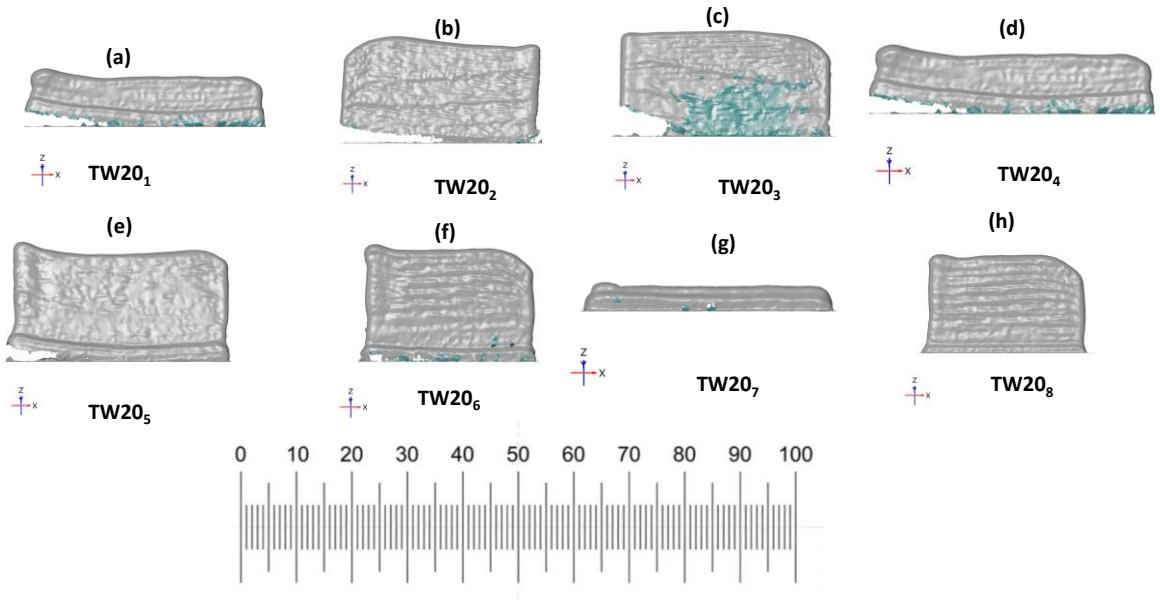

Figure 35. Illustrated FeSi thin wall production with varying processing parameters.

It has been proven that during the additive manufacturing process, the deposited materials are exposed to substantial residual stresses, similar to the welding process. This could result from the thermal gradient in temperature between the surface and the centre of the deposited materials during the solidification process [264]. This can be true for FeSi parts due to tension or cracking at the edges in the building direction (z direction), as well as compression at the centre of the deposited materials, which has been observed by [265, 266]. To rectify these issues, preheating the substrate is adopted to reduce the thermal gradient between sample and substrate, cooling rate, thermal distortion, and cracking [267, 268]. Furthermore, the preheating process increases the substrate temperature, which can lead to an improved, more uniform temperature distribution during the manufacturing process. Preheating the substrate can improve fracture resistance and reduce the brittleness of materials [267]. As the height of deposition increases, the cooling rate also decreases. This can be observed in this project, where there are no cracks at the top of the deposited materials.

It is significant to mention that the impact of preheating on enhancing the resistance to brittle failure of high-strength electrical steel at 100°C was previously reported by [269]. Therefore, based on these observations and considering the brittleness behaviour of FeSi materials during printing, the identified conclusive solution to address cracks, detachment, and delamination issues in this project was preheating the substrate. In addition to that, due to lack of knowledge in regards of pre-heating FeSi 6.5% in the LMD process, as well as there has been no reported systematic work to study the corresponding processing windows so far. Accordingly, to eliminate cracks and delamination issues in this work the relation between the preheating and cracking issues appearing during printing of FeSi was investigated.

To build thin walls by the LMD process, if the preheating temperature is increased from 300–400 °C to 500–600 °C, higher preheating can improve surface finish, increase hardness,

promote coarser morphologies (e.g., columnar grains), reduce residual stresses, and minimise thermal distortion [268]. However, it is important to note that this high temperature has also led to observed issues such as deflection and delamination of the parts at the edges. Therefore, preheating is advantageous in enhancing mechanical properties and minimising cracks; however, it should be appropriately implemented to ensure effectiveness based on the specific manufacturing requirements. For this project, 200 °C was selected as the reference point based on recommendations from the industry partner and other AM projects [268, 270-272]. This choice aims to investigate the impact of temperature on the LMD process, with a focus on avoiding issues such as cracking, detachment, reducing thermal gradients, and preventing delamination of deposited materials. Consequently, the substrate was heated up, by an induction machine, to ~200 °C and then printing TW20 (laser power= 430 W, scan speed= 380 mm/min) was started. As seen in Figure 36, there was no delamination, detachment, or cracks observed except for sample TW26. That means the manufacturing of thin walls can be achieved with a suitable processing parameters and preheating temperature, as depicted in Table 6.

Although TW33 and TW35 shared the same base processing parameters, TW35 was produced with a smaller hatch spacing (0.4 mm) and a bidirectional scanning strategy. These changes might influence deposition quality, as smaller hatch spacing improves track overlap and reduces porosity, while bidirectional scanning promotes uniform heat distribution and lowers residual stresses [273]. It is also noteworthy that for TW26 (P = 440 W, V = 390 mm/min) at a preheating temperature of 90 °C, a small delamination occurred at the edge of the sample. This emphasizes that preheating temperature must be optimised for successful manufacturing of FeSi thin walls.

It is well-established that elevating the preheating temperature enhances bonding between the substrate and deposited FeSi parts in LMD. Preheating reduces thermal gradients, promoting uniform melting and wetting, which strengthens metallurgical bonding and reduces porosity and cracking. It also mitigates residual stresses, improving build integrity, and increases powder melting efficiency. These effects are supported by LMD studies on Fe-based alloys, where preheating eliminates cracks and enhances microstructure uniformity [274].

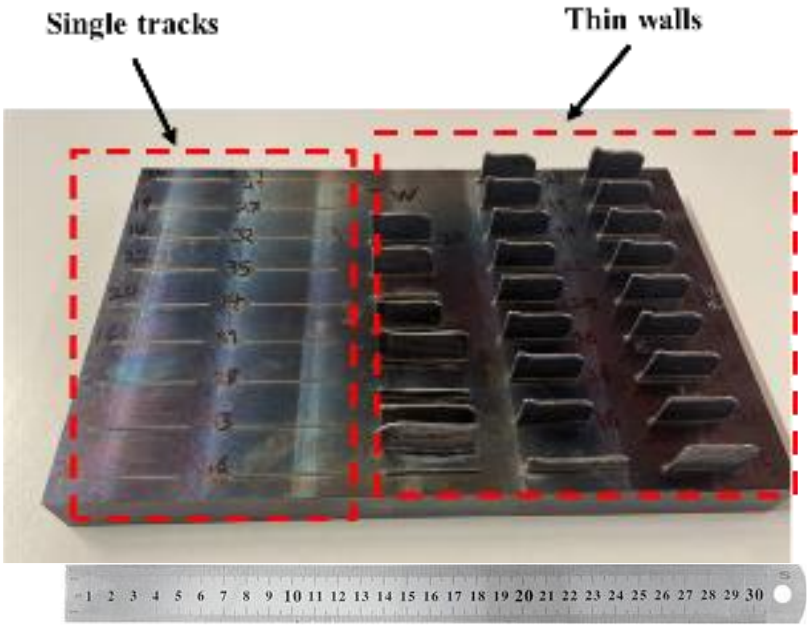

Figure 36. Single tracks and thin walls were fabricated using the LMD process.

Table 6. Average preheating temperature and DoE for thin walls.

	Sample	Laser Power (W)	Scan Speed(mm/min)	Powder flow (g/min)	Enegy Density (J/mm^2)	Average Temperature (°C)	Z steps (mm)	Hatch space (mm)	Scanning Strategy
DOE2 of Thin wall	TW20	430	380	2.5	67.9	200	0.45	0.6	Unidirectional
	TW18	465	400	2.5	69.8	110	0.45	0.6	Unidirectional
	TW26	440	390	2.5	67.7	90	0.45	0.6	Unidirectional
	TW16	450	380	2.5	71.1	200	0.45	0.6	Unidirectional
	TW24	435	390	2.5	66.9	125	0.45	0.6	Unidirectional
	TW22	445	400	2.5	66.8	200	0.45	0.6	Unidirectional
	TW14	430	400	2.5	64.5	135	0.45	0.6	Unidirectional
	TW19	450	365	2.5	74.0	200	0.45	0.6	Unidirectional
	TW29	435	380	2.5	68.7	125	0.45	0.6	Unidirectional
	TW15	400	400	2.5	60.0	200	0.45	0.6	Unidirectional
	TW21	425	400	2.5	63.8	140	0.45	0.6	Unidirectional
	TW28	450	395	2.5	68.4	200	0.45	0.6	Unidirectional
	TW17	475	400	2.5	71.3	140	0.45	0.6	Unidirectional
	TW25	450	410	2.5	65.9	200	0.45	0.6	Unidirectional
	TW30	500	400	2.5	75.0	140	0.45	0.6	Unidirectional
	TW23	450	425	2.5	63.5	200	0.45	0.6	Unidirectional
	TW27	450	440	2.5	61.4	170	0.45	0.6	Unidirectional
	TW13	490	365	2.5	80.5	150	0.45	0.6	Unidirectional
	TW32	400	440	2.5	54.5	125.0	0.45	0.6	Unidirectional
	TW33	450	400	2.5	67.5	200.0	0.45	0.6	Unidirectional
	TW35	450	400	2.5	67.5	200.0	0.45	0.4	Bidirectional

Additionally, in this project, 3D scans were captured and measured of the height and thickness of single tracks and thin walls using the Hexagon absolute arm laser. The laser scans the part into polyworks software to create a mesh model. The output was stl format and then transferred into Zeiss quality suite software and then all the analysis and results were generated, as depicted in Figure 37. It is evident that by applying the appropriate processing parameters, thin walls with the desired height and thickness can be manufactured compared to the first and second trials [275].

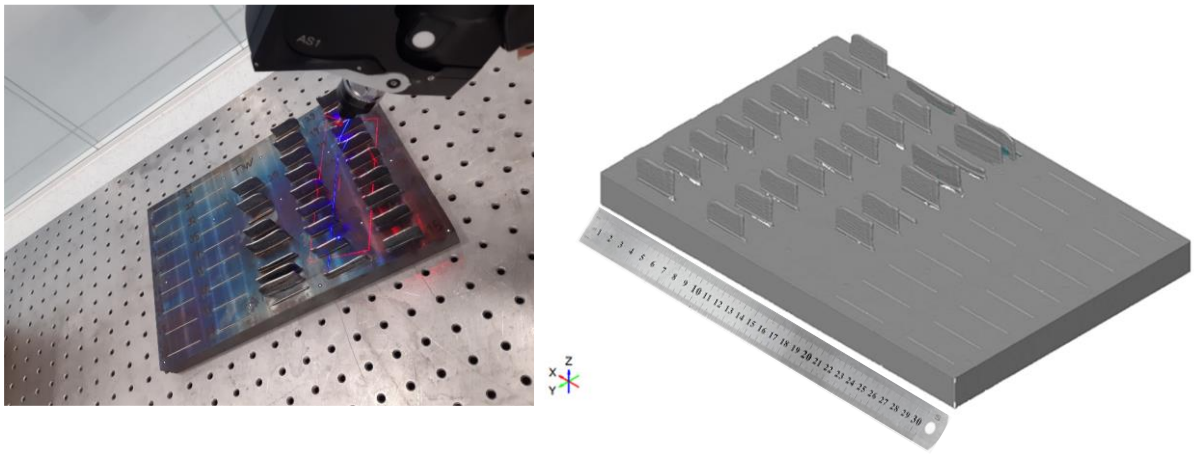

Figure 37. The Hexagon absolute arm utilises 3D laser scanning to inspect manufactured thin walls.

Based on the results obtained from printing FeSi thin walls and determining the optimised processing parameters for FeSi parts, the next phase of the project involves producing 7 cubes. Cubes were chosen because they allow for consistent evaluation of volumetric properties, thermal distribution, and scanning strategy effects. To ensure proper layer deposition for the larger cubes, the initial z-step was calculated as ~0.95 mm, which is nearly twice the z-step used for thin walls (0.45 mm) because of the larger geometry. For printing, it was slightly reduced to 0.85 mm to avoid under-building. Various scanning strategies will be tested, including unidirectional (A-B A-B) and bidirectional (AB BA) with a 90° rotation, to further analyse their impact on the material properties. For this stage of the project, four different power and energy densities; low, medium, and high-were selected based on observations, behaviour, and the manufacturing of FeSi thin walls. These selections, combined with a constant scan speed (400 mm/min) with different scanning strategies, and different laser power ranging from 400, 435, 475 and 600 W, aim to investigate the effects of processing parameters on geometry, cracks, microstructure, texture, and effects of preheating of substrate. All these adjustments, including the z-step optimisation, were made to ensure accurate layer bonding, avoid defects, and maintain consistent deposition quality in the cubes (Table 7).

Table 7. Processing parameters for manufacturing FeSi cubes.

	Sample	Laser power (w)	Scan speed (mm/min)	Powder flow (g/min)	Energy density (J/mm^2)	Average temperature (°C)	Z-steps (mm)	Tracking spacing (mm)	Scanning strategy
DoE of Cubes	C15	475	400	2.5	71.3	204	0.85	0.6	Unidirectional
	C16	400	400	2.5	60	182	0.85	0.6	Unidirectional
	C17	435	400	2.5	65.3	214	0.85	0.6	Bidirectional
	C18	400	400	2.5	60	225	0.85	0.6	Bidirectional
	C19	435	400	2.5	65.3	225	0.85	0.6	Unidirectional
	C20	475	400	2.5	71.3	232	0.85	0.6	Bidirectional
	C21	600	400	2.5	90	200	0.85	0.6	Unidirectional

As seen in the Figure 38 cubes were manufactured using an LMD machine (substrate dimension: 200*150*25mm). To prevent any cracks, thermal stress, and minimise thermal gradients, the substrate was preheated to temperatures above 180°C with an induction

machine. The Figure 39 line graphs represent temperature measurements during AM of high silicon steel (6.5 wt%) using LMD. These measurements, taken with Picolog thermocouples placed in (6 holes) pre-drilled 2mm-diameter holes about 5mm deep from the surface, provide valuable insights into the thermal behaviour of the material as layers are added. Throughout the process, the temperature trends exhibit peaks followed by declines, which correspond to the sequential deposition of layers as the time passes. Each peak in the graph indicates the initiation of a new layer, where the temperature temporarily rises due to the immediate heat input from the laser. However, as time progresses, the temperature of substrate begins to decrease. Sample C15 Figure 39 (a) shows more peaks because its preheating temperature (204 °C) was higher than that of C16 Figure 39 (b) (182 °C), which produced fewer peaks due to the lower initial thermal input. Other samples (C17: 214 °C, C20: 232 °C, C18: 225 °C, C19: 225 °C) also show multiple peaks consistent with higher preheating. Similar effects were observed where the temperature evolution of thin wall layers deposited by the DED process decreased over time, particularly as the substrate thickness decreased from 25 mm to 5 mm. Additionally, because the substrate was cold during the deposition of the first layers, high thermal gradients developed between the deposited material and the substrate. This led to the formation of residual stresses [276]. This decline may be influenced by several factors inherent to the additive manufacturing process. As more layers are deposited, the height of the printed material increases, causing the distance between the thermocouples and the active deposition layer to grow. Since the thermocouples are fixed within the substrate, they record lower temperatures as the time progresses with each additional layer because the heat from the laser has to travel further through the material, losing intensity along the way. Additionally, the thermal conductivity of high silicon steel allows heat to dissipate over time, with the increased material thickness further impeding heat transfer to the lower layers where the thermocouples are located.

The overall manufacturing time also contributes to the temperature profile. As time passes, heat excess becomes more pronounced, with each new layer drawing heat away from the already printed material. This ongoing heat loss, combined with the increasing distance between the heat source and the thermocouples, leads to the gradual decline in temperature observed in the graphs. In the LMD process, maintaining a sufficiently high temperature is crucial for ensuring consistent thermal behavior and achieving a robust bond between the substrate and high silicon steel (FeSi 6.5 wt%). This temperature promotes proper fusion between layers, reducing the risk of defects like cracking or distortion that could compromise the printed component's structural integrity. The temperature is determined for different alloys by considering their thermal properties, such as melting point and thermal conductivity, and is adjusted through changes to laser power, scanning speed, and powder feed rate, validated by experimental and modelling approaches. The optimal temperature ensures effective fusion and minimises defects by balancing these alloy-specific properties and process parameters [277]. In summary, the temperature measurements during the LMD process of high silicon steel reveal a clear pattern where the temperature peaks with each new layer being printed, followed by a decline as the heat dissipates and the distance

between the thermocouples and the deposition layer increases. This behaviour is consistent with the physical dynamics of the AM process, the thermal properties of the material, and the need to maintain sufficient temperature to ensure strong bonding and avoid cracking between the substrate and the deposited layers.

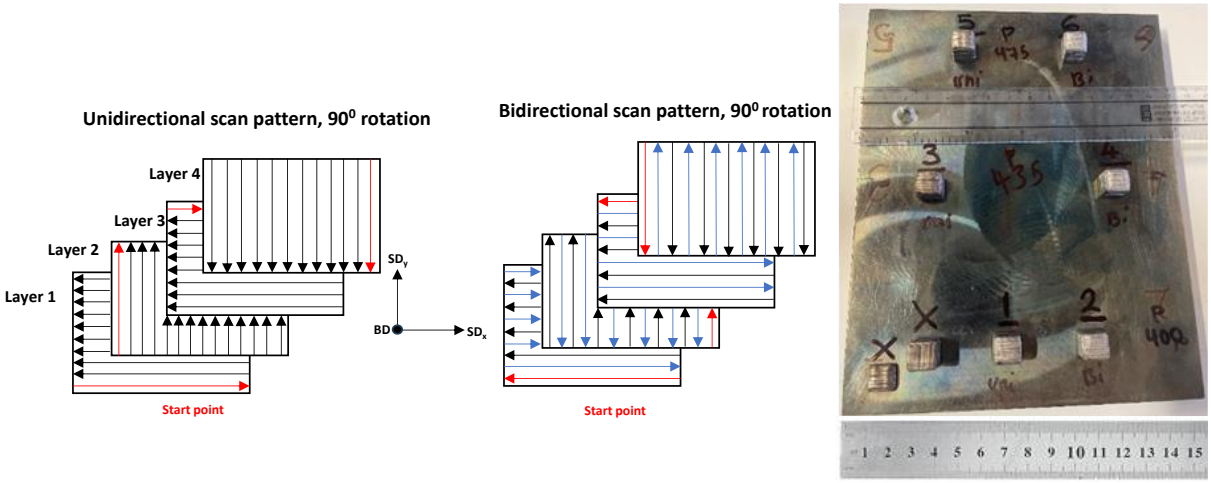

Figure 38. Cubes manufactured with different processing parameters and different scanning strategies with 90^0 rotations.

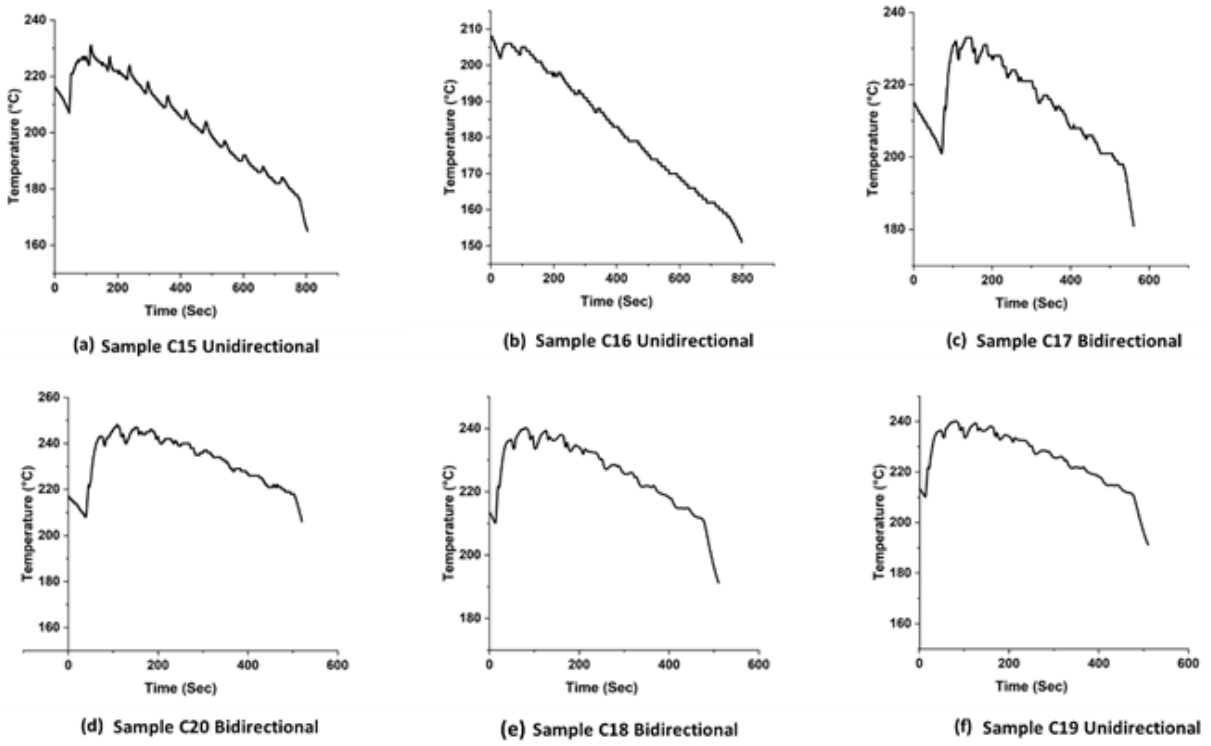

Figure 39. Temperature measurements for each cube during manufacturing by Picolog thermocouple.

Additionally, 3D scans of the cubes, along with measurements of their height and thickness, were performed using the Hexagon Absolute Arm laser scanner, as illustrated in Figure 40. It

is observed that utilising the correct processing parameters enables the production of cubes with the desired height and thickness, unlike the initial trial.

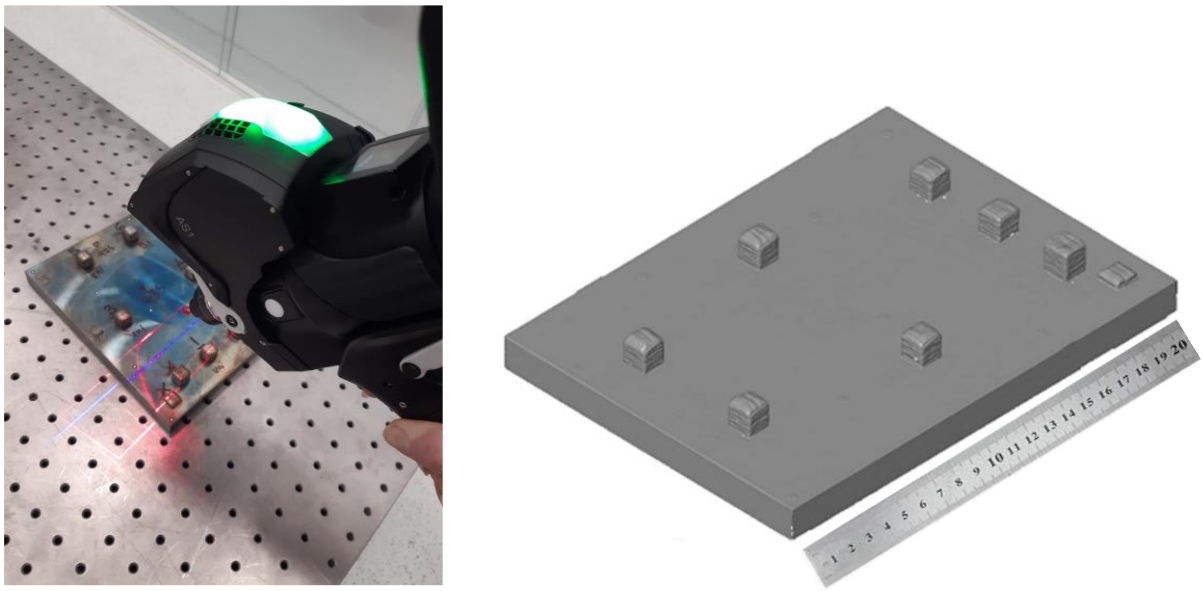

Figure 40. The Hexagon absolute arm utilizes 3D laser scanning to inspect manufactured cubes and provide a 3D perspective.

4.3 Mechanical properties results

The mechanical properties of the deposited FeSi parts were evaluated through Vickers microhardness testing to assess the effect of energy density and microstructural variations. The analysis of the provided graphs reveals a clear relationship between energy density and hardness for both thin wall and cube samples Figure 41 (sdv: ±0.10%). For thin walls, the regression line shows a moderate correlation ($R^2 \approx 0.55$), indicating that while the general trend is positive, some scatter is present due to the influence of geometry and thermal gradients. In contrast, the cube samples exhibit a strong correlation ($R^2 \approx 0.92$), where hardness increases consistently with energy density. The positive slopes in both cases confirm that higher energy density enhances densification and reduces porosity, thereby improving hardness. A linear fit was chosen as the relationship is monotonic and approximately linear within the investigated range.

For thin walls, the average hardness increases from around 364 HV_1 at an energy density of 54 J/mm² to approximately 377 HV_1 at 80.5 J/mm². This represents an increase of about 3.6% (13 HV_1). Similarly, the average hardness for thin walls rises from roughly 353 HV_1 at a grain size of 443 µm to about 378.6 HV_1 in 1828 µm, indicating an increase of about 7.2% (25.6 HV_1) Figure 42. For cube samples, the relationship between energy density and hardness follows a similar trend but with slightly different magnitudes. The average hardness of cubes increases from around 360 HV_1 at an energy density of 60 J/mm² to about 376 HV_1 at 90 J/mm², signifying an increase of approximately 4.4% (16 HV_1). Additionally, the average hardness for cubes goes up from around 362 HV_1 at a grain size of 160 µm to approximately 376 HV_1 at 249 µm, representing an increase of about 3.9% (14 HV_1). Comparing thin walls and cubes,

hardness consistently rise with increasing energy density, with thin walls showing a slightly greater percentage increase (3.6% to 7.2%) than cubes (3.9% to 4.4%). Moreover, the average Vickers hardness of the thin walls and cubes is higher than the experimental results from a recent study [271], which investigated the metallurgy of high-silicon steel parts produced using selective laser melting. The alloy in that study had a composition of 6.9% Si, and the reported hardness was approximately 328.55 HV_1. The observed increase in hardness with higher energy densities can be attributed to the refinement of the microstructure. Higher energy densities promote more complete melting, leading to more uniform grain structures. This grain refinement enhances hardness, increasing the material's strength. In SLM, rapid cooling rates associated with high energy densities can lead to the formation of a fine-grained microstructure. Fine grains can inhibit dislocation movement, a primary mechanism of plastic deformation, thereby increasing hardness in specific areas. Additionally, appropriate melting and solidification processes can minimise residual stresses, which might otherwise lead to micro-cracking and decreased hardness. The effect of larger grain sizes on hardness can also be explained by solidification dynamics during the AM process, such as LMD. Larger grains typically form at slower cooling rates. The presence of larger grains in high-silicon electrical steel alloys, along with the formation of ordered phases intermetallic compounds such as Do_3 and B_2, can influence mechanical properties. While these phases may enhance certain characteristics, they can also contribute to brittleness, which may affect hardness [105]. Electrical steels with high silicon content, such as Fe-6.5 wt% Si, predominantly consist of disordered A2 and minimally ordered B2 (FeSi) phases. These phases can impede dislocation movement, thereby increasing the material's hardness. However, excessive ordering can lead to brittleness [95, 271, 278].

Higher energy densities contribute to increased hardness in thin walls and cube samples processed by LMD. For thin walls, average hardness increased by approximately 3.6% and 7.2% with higher energy density, while for cubes, the increase was around 4.4% and 3.9%. The highest hardness values were 385.8 HV_1 for thin walls and 376 HV_1 for cubes, while the lowest values were 353.5 HV_1 for thin walls and 358 HV_1 for cubes. The high hardness can be attributed to the developed microstructure from different solidification rate, and the formation of ordered phases or intermetallic compounds due to the high silicon content in the electrical steel alloy. These findings explain the importance of optimising LMD process parameters to produce high-performance materials for electromagnetic devices, such as transformers and electric motors. This optimisation has the potential to save more than 10,000 gigawatt-hours of energy per annum [101].

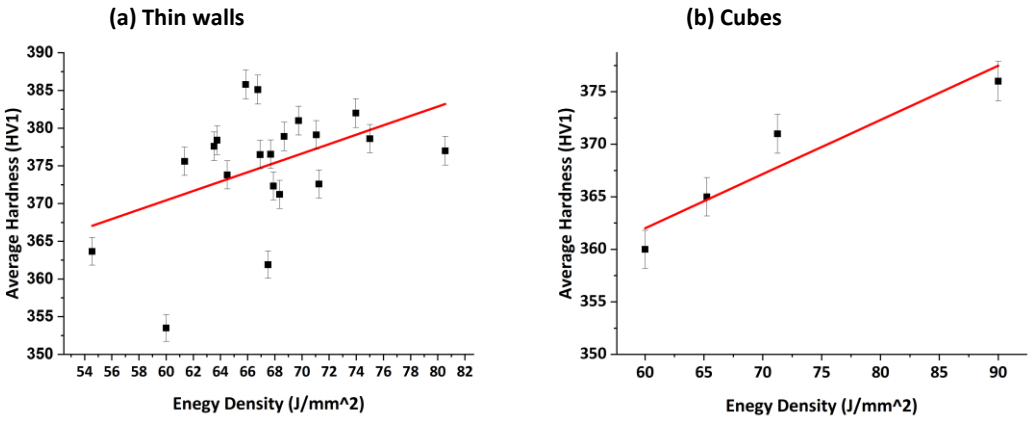

Figure 41. Impact of energy density on hardness of FeSi 6.5wt%.

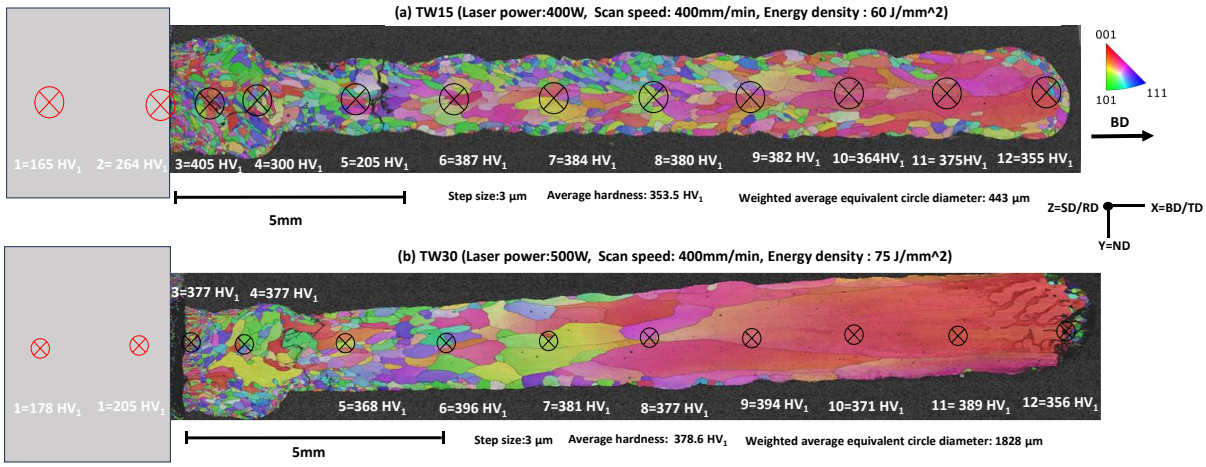

Figure 42. EBSD maps illustrating the location of hardness and grain development in TW15 (a) and TW30 (b).

Furthermore, the hardness data for thin walls, cubes, and discs reveal individual trends and significant changes from the first deposited layer, reflecting the impact of their respective processing parameters. For the thin walls, which were processed with a variety of laser powers and scan speeds, the hardness starts at around 150 HV_1 at the first deposited layer (0 mm height). There is a significant increase in hardness, reaching a maximum of approximately 400 HV_1 at around 1 to 2 mm in height. Beyond this point, the hardness gradually stabilises between 350 to 400 HV_1 from 5 mm up to 20 mm although a coarser microstructure is created. Regarding the substrate (mild steel) hardness, measurements for samples such as TW15 and TW30 were taken, yielding values of 165 HV_1 and 264 HV_1 for TW15, and 178 HV_1 and 205 HV_1 for TW30. These values are notably lower compared to the hardness of the deposited electrical steel material, which is consistent with the typical hardness range for mild steel substrates. The minimum hardness observed is 353.5 HV_1 (TW15: laser power: 400 W, scan speed: 400 mm/min), while the maximum is 385.8 HV_1 (TW25: laser power: 450 W, scan speed: 410 mm/min) and sample TW22 (laser power: 445 W, scan speed:400 mm/min), with values of 385.11 HV_1, (Figure 43 (a)). The thin wall specimens exhibited an overall variation of ±30 HV_1 (±10%).

For the cubes processed with uniform laser power and scan speeds, the hardness of deposited FeSi remains stable with slight variations, while substrate hardness values were not measured. The hardness remains mostly within the range of 350 to 400 HV_1 from the first deposited layer at 2 mm to heights up to 10 mm. The minimum hardness observed is around 358 HV_1 (C18: laser power: 400 W, scan speed: 400 mm/min), and the maximum is about 376 HV_1 (C21: laser power: 600 W, scan speed:400 mm/min) (Figure 43 (b)). The consistent processing parameters result in uniform material properties, leading to stable hardness values with minor fluctuations due to slight variations in local processing conditions or material characteristics with an average variation of ±19 HV_1 (±5%).

The discs, processed with a laser power of 425 W and a scan speed of 400 mm/min, exhibit a distinctive hardness profile as shown in Figure 43 (c). At the initial deposited layer (0 mm height) the hardness is relatively low. As the height increases, there is a rapid rise in hardness, peaking around 400 HV_1 at 1 to 2 mm. This high hardness is maintained between 350 to 400 HV_1 up to 15 mm in height. The minimum hardness observed is about 307 HV_1 (S6 cross section), while the maximum is 400 HV_1 (S2 surface). The initial lower hardness values are due to the processing conditions. The significant increase and subsequent stabilisation at high hardness levels reflect the effective influence of the laser power and scan speed on the material's properties as more layers are deposited with an average variation of ±26 HV_1 (±7%). Moreover, small grains are evident in the first deposited layer and are generally more susceptible to cracking compared to large grains. This susceptibility arises from smaller grain sizes having a higher grain boundary area per unit volume, a result of the small melt pool size due to the high cooling rate during solidification. These grain boundaries can act as initiation sites for cracks under stress, leading to the nucleation and formation of microcracks, particularly when dislocations occur at the interface of the deposited material and any inclusions [279]. In contrast, larger grains (columnar) often have fewer grain boundaries and can provide more uninterrupted paths for dislocations, making them less prone to crack propagation. In the context of LMD, when the first layer of deposited material (FeSi) has a small grain size due to high cooling rates, it can lead to increased susceptibility to cracks. This susceptibility is particularly influenced by the properties of electrical steel, which can intensify cracking at the interface between the substrate and the deposited material. Consequently, the initial layer of deposited FeSi material may exhibit lower hardness due to these defects. As the height increases, the material properties improve due to optimal laser power and scan speed, resulting in higher hardness values .

As the height increases, slower cooling rates and subsequent thermal cycles promote the growth of larger grains and the formation of ordered phases such as Do_3 and B_2. These ordered phases and larger grain sizes contribute to the higher hardness values observed at greater heights. Additionally, it can be suggested that a high density of dislocations inside the grains contribute to increased hardness by networking dislocations together and hindering their movement, which not only increases the hardness of FeSi but also could enhances its yield strength [280]. Furthermore, the hardness of electrical steel depends on the percentage

of silicon content [181, 281]. For example, 1 to 2% Si results in a modest hardness range of 150 to 220 HV [282], while 6-6.5 wt% Si achieves a hardness above 350 HV_1 [281], which is consistent with the results obtained in this study. The hardness of FeSi alloys, particularly those with a 6.5 wt% silicon content, significantly influences their magnetic properties, including magnetostriction and magnetic saturation. Increasing the silicon content in iron enhances electrical resistivity and reduces magnetocrystalline anisotropy, leading to improved magnetic performance specifically, Fe-6.5 wt%Si alloys exhibit near-zero magnetostriction, minimising transformer noise and enhancing efficiency [214]. However, it's important to note that while saturation magnetisation decreases with higher silicon content, reaching approximately 1.8 T at 6.5 wt% Si, the overall magnetic performance is optimised due to the reduction in magnetostriction and eddy current losses.

The relationship between hardness and magnetic properties in FeSi alloys is influenced by the LMD process parameters, silicon content, and resulting microstructure [25]. In this study, hardness reflects the material's resistance to localised plastic deformation during deposition, which is critical for maintaining structural integrity and minimising cracks in the brittle FeSi 6.5 wt% alloys. Excessive hardness, however, can increase brittleness, potentially reducing mechanical robustness under operational stresses. Therefore, optimising hardness through appropriate selection of laser power, scan speed, and substrate preheating is essential to balance mechanical strength and magnetic efficiency. The results show that thin walls and discs exhibit a significant increase in hardness from the first deposited layer to the top layers, stabilising at higher values. This trend indicates the influence of cumulative thermal cycles and cooling rates on microstructural evolution. In contrast, cubes maintain relatively uniform hardness with minor fluctuations, reflecting consistent thermal conditions during deposition. These observations demonstrate that the processing parameters play a crucial role in determining the hardness distribution and, by extension, the performance of FeSi parts manufactured by LMD.

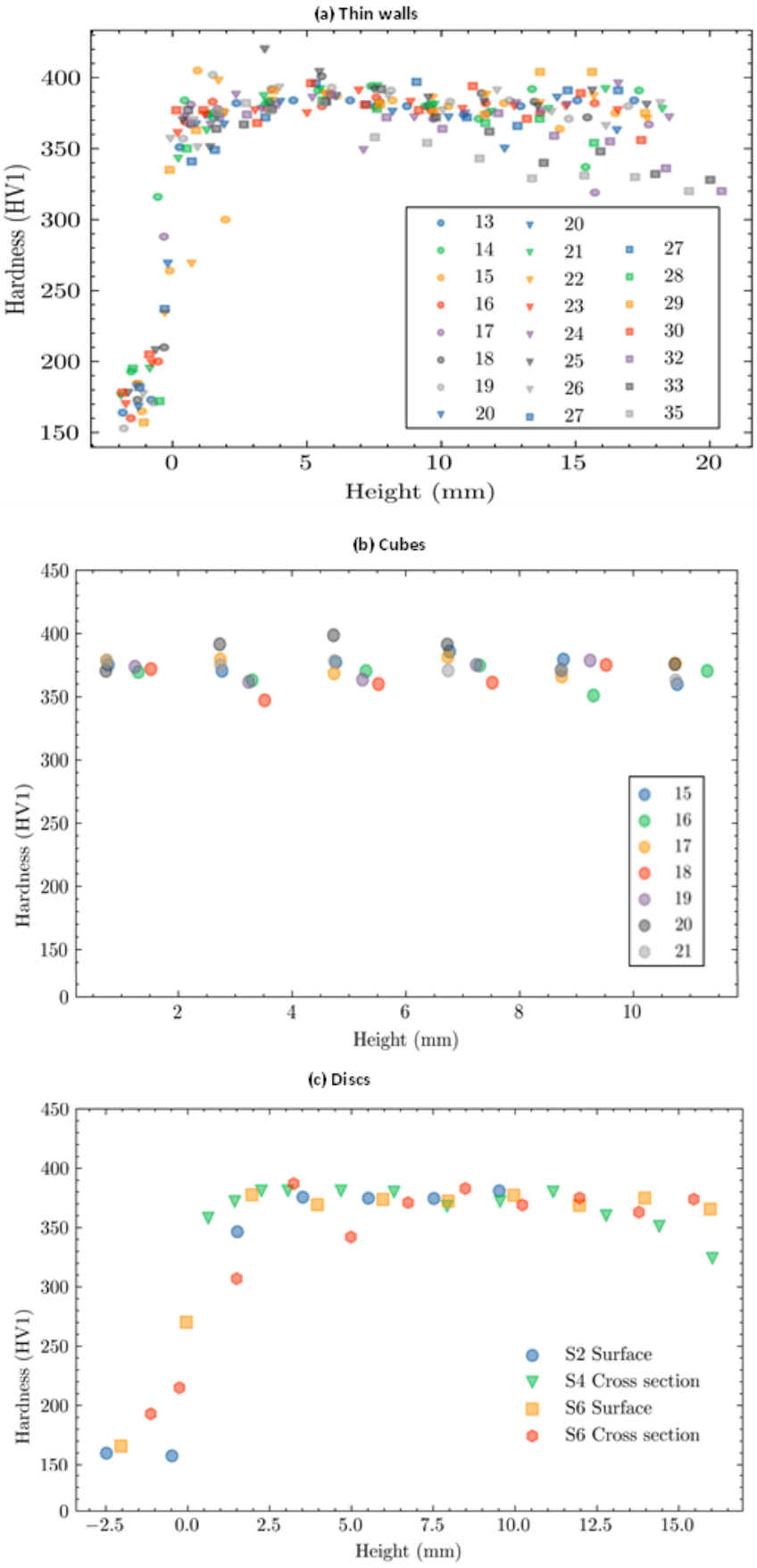

Figure 43. The average hardness at a given height for (a) thin walls, (b) cubes, and (c) disc.

Chapter 5

5 Sample preparation and evaluation of porosity and cracks

5.1 Introduction

This chapter focuses on the sample preparation procedures and the evaluation of porosity and crack formation in components produced by the LMD process. A section of this chapter has been adapted from the paper titled *"Process Window for Manufacturing Soft Magnetic FeSi 6.5% by Laser Metal Deposition"*, presented at the 21st International Conference on Manufacturing Research. The main objective was to examine the impact of laser parameters and scan strategy on both crack density and crack orientation by constructing various samples.

These samples underwent a series of processes which included sectioning by an EDM machine, followed by grinding and polishing using standard metallurgical methods. The grinding process involved the use of SiC water-cooled paper, using -cooled papers with grit sizes of 240, 400, 800, and P1200 (with a platen speed of 240 rpm and force of 27 N for 3 minutes) and P2500 grit papers. Water was used not only for cooling but also to remove debris during the process. Subsequently, polishing was carried out using 3 µm Mg oil based Metadi in sequence, culminating in a final polishing stage utilising a Microcloth, all of which were provided by Buehler [249] (with a platen speed of 150 rpm and force of 27 N for 6 minutes). As mentioned previously in the literature review, defects such as porosity, lack of fusion, unmelted powder, and keyholes in the additive LMD process can lead to early failure because pores have the potential to serve as points where the crack start and propagate. Therefore, optimising the process window parameters is a key factor in reducing or even eliminating these defects in FeSi 6.5%. These defects could result in poor mechanical, physical, and magnetic properties i.e., fatigue life [283], low ductility, high current losses. Consequently, the ability to control these factors is crucial during the AM process [25].

The characteristics such as shape, location, and spread of pores could influence the attributes of parts produced through additive manufacturing. Therefore, to evaluate porosity and cracks of specimens, optical micrographs were captured of the XY plane using a Hirox and Leica microscopes. As shown in Figure 44 (a), metallurgical pores were typically 100–300 µm in size, which is considered large compared to keyhole pores that were generally 10–50 µm [284]. Metallurgical pores included both gas-entrapped and shrinkage pores often exhibited irregular and interconnected morphologies due to inadequate material flow during solidification [2]. It is evident that all the samples exhibited different types of porosities such as metallurgical pores, keyhole pores, and lack of fusion. In this instance, as it can be seen in the Figure 44 (a), metallurgical pores are large in terms of size and have an irregular shape compared to keyhole pores. Keyhole pores may arise due to instability within the molten pool, while metallurgical pores can form from low scan speeds and increased energy in materials, causing gas entrapment within the molten pool [285]. While small spherical pores are less detrimental on their own, irregular shrinkage and lack-of-fusion pores with sharp edges are

more harmful as they act as weak points in the material compared to spherical keyhole pores [286] as shown in Figure 44 (b) and (c). This is because irregular shrinkage and lack-of-fusion pores have sharp edges that act as weak points, increasing the likelihood of crack initiation. Under cyclic loading, such as that experienced by FeSi electrical machine components exposed to magnetostriction stresses and thermal cycling, even small pores can accelerate crack initiation and propagation, thereby reducing fatigue life and reliability [176]. One possible explanation for this phenomenon could be attributed to the gas atomisation process used in producing FeSi powder, which can introduce trapped gases leading to pore formation [287]. During this process, gas bubbles might become trapped within the FeSi powder, or there could be gas present between the powder particles. As these particles dissolve in the melt pool during deposition, some unmelted powder may also get trapped. The materials are then deposited, and due to the high cooling rate surrounding them, they solidify, forming spherical voids or pores within the structure.

Lack of the fusion also termed incomplete fusion, commonly happens when there is an inadequate supply of energy input in the LMD process. These types of defects can occur when the particles are not fully melted on top of the previous layers or between adjacent deposited layers [288]. Additionally, inadequate interlayer bonding may result from low laser energy and insufficient penetration, contributing to incomplete fusion. This circumstance could lead to discontinuities, reducing the quantity of molten metal available for solidification and resulting in poor bonding, as depicted in Figure 44 (d) [289]. The cracks visible in Figure 44 (d) are likely due to incomplete fusion defects: when there is insufficient melting between adjacent tracks or layers, weak interfaces are created which serve as weak points in the material. These weak points maybe initiate cracks because the metallurgical bond has not been achieved during solidification [290]. As shown in Figure 44 (e) and (f), during the LMD process, the highlighted feature in Figure 44 (e) is better described as a crack rather than a pore. Its elongated shape and the occurrence of un-melted powder particles along its path suggests these unmelted particles act as weak points in the material, which maybe promote crack initiation and propagation rather than being simple trapped spherical pores. Similarly, in Figure 44 (f), the crack path seems altered by unmelted powder particles. These unmelted particles may likely trigger crack initiation and subsequent growth under residual or applied stresses, rather than being harmless pores [291].

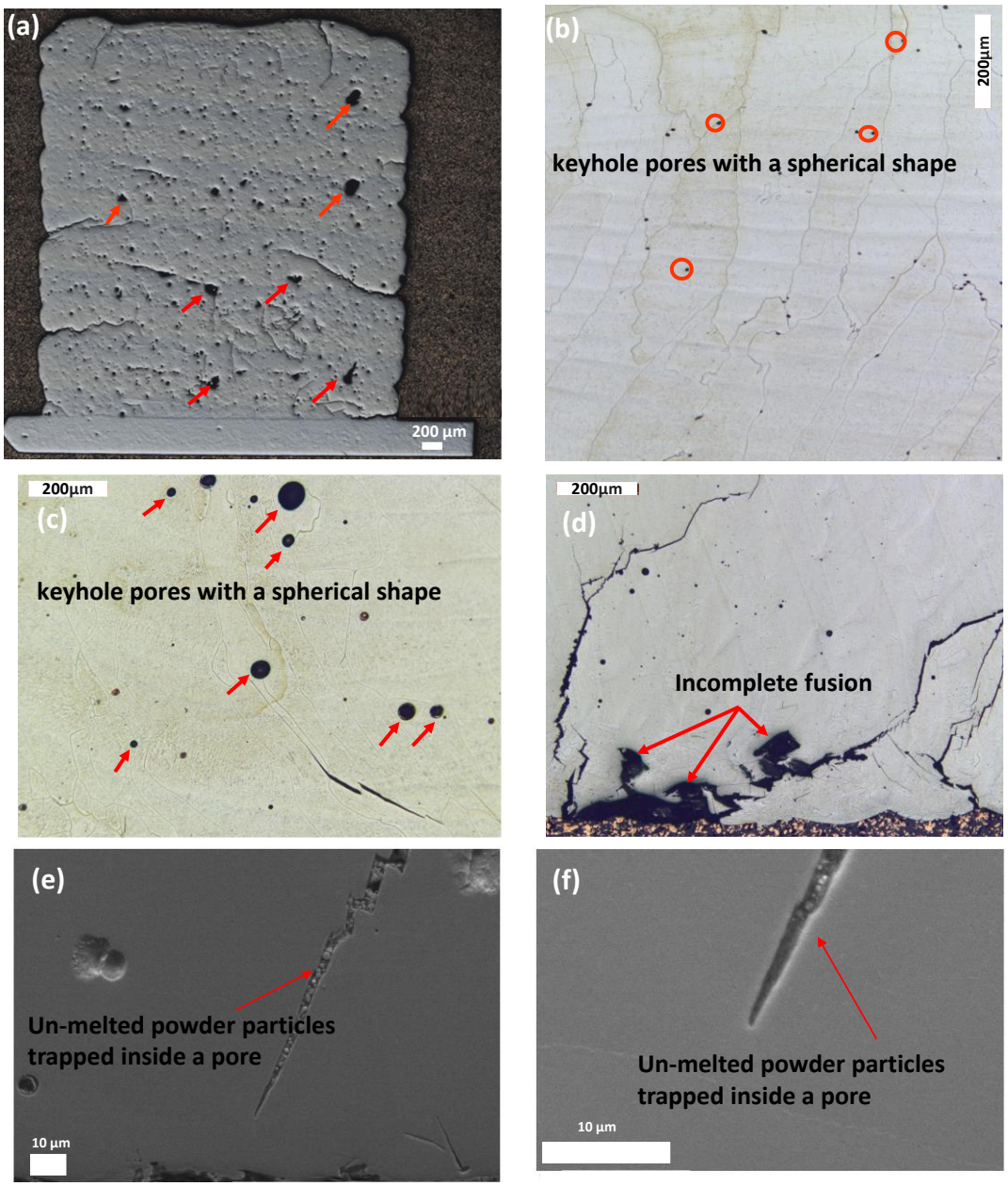

Figure 44. Different types of porosity (a) irregular keyhole pores, (b), (c) spherical pores, (d) incomplete fusion, (e) and (f) SEM micrograph un-melted powder particles trapped inside a pore.

5.2 Impact of laser power and scan speed on porosity formation in thin walls

Several factors can contribute to the occurrence of different porosity defects during the manufacturing of FeSi parts by LMD technology. For instance, FeSi materials may be prone to porosities because gases are unable to escape properly. This also could be caused by inappropriate processing parameters such as laser power, scan speed, feed rate, or inadequate vacuum during the manufacturing process, among other factors [292]. which will be addressed in more detail. Before analysing the effect of processing parameters, it is essential to define the borderline for porosity. This will allow the identification of process window pores from manufactured parts such as thin walls at specific laser power and scan speeds. In this context, a porosity percentage of 0.2% (sdv: ± 0.1%) serves as the defining

threshold for thin walls, with values above or below highlighted respectively in red and green, as depicted in Figure 45 (a). It can be seen from Figure 45 (a) that with the exception of few outliers (TW13:1.3%,TW16:0.49% porosity), porosity percentage is variable within a range of approximately 0.1 to 0.5%, across all samples that have been made using different process parameters. In this scenario, except for a few outliers, laser power below 460 W has the lowest percentage of pores, ranging from 0.1% to 0.2%. However, simultaneously, as the laser power increased from 400 to 500 W, the average size of the pores decreased from approximately 50 to 20 µm. It can be said that, with increasing laser power, there is an increase in laser density delivered to deposited materials which can lead to better penetration, better melting and, fusion resulting in reduced porosity [293]. Also, higher laser power can reduce the cooling rate of molten materials which allows more gas bubbles to escape from the melt pool and reduces the formation of porosity [294]. Despite this reduction in size, the pores were uniformly distributed, and numerous small spherical pores were observed across the samples. In Figure 45 (b), it can be seen that the number of pores (or porosity level) was decreased from 1.3 % to 0.1% with the increase of the scanning speed from 360 to 440 mm/min. Moreover, as the scan speed increased, the average size of pores decreased from 61 µm to 27 µm. It can be said that, with higher scanning speed, less time was available for deposited materials to cooldown and resulting in faster solidification which is likely to be attributed to reduce pore formation as there is less time for gas entrapment to occur [295]. Moreover, the interaction between deposited materials and laser power can be changed with increasing scan speed, in other words, there is less time for the laser to interact with deposited materials resulting in more uniform energy distribution and less heat input [296]. Importantly, while lower laser power and higher scanning speeds are effective for reducing porosity, they also promote faster solidification and grain refinement. In FeSi alloys, finer grains increase coercivity and reduce permeability, which may degrade soft magnetic performance, whereas coarser grains formed at higher laser power improve permeability but can raise eddy current losses [297].

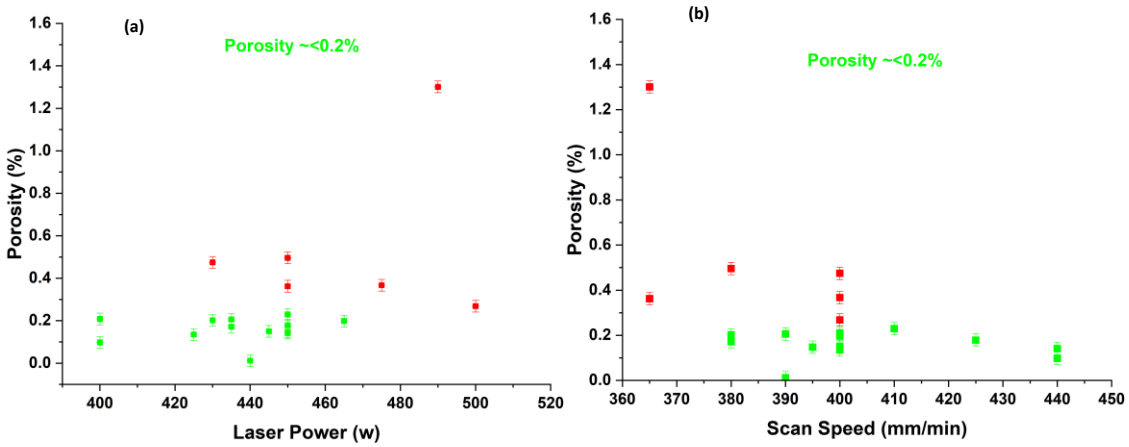

Figure 45. Experimentally measured porosity of thin walls as a function of laser power (a) and scan speed (b). The red and green markers respectively identify values above and below the bordering line.

5.3 Analysing and evaluating cracks in thin wall

Cracking in electrical steel, as highlighted in the literature review, is a frequent issue during the manufacturing process, notably when the silicon content surpasses 3wt%. This phenomenon is linked to the formation of brittle ordered phases like B_2 and DO_3. However, in the LMD process, these phases might be mitigated due to the rapid cooling rate. Similar positive effects on phase suppression were previously observed in FeCo [298] and FeSi [5]. Therefore, the ductility of FeSi materials can be improved if these phases are supressed during the manufacturing process. Additionally, electrical steel exhibits a high thermal expansion coefficient [271] and low thermal conductivity [299] similar to nickel super alloys [300] and 316L stainless steel [301] which causes the material to become more susceptible to crack formation. In other words, electrical steel exhibits a greater change in size due to thermal expansion when subjected to a temperature gradient; for example, the thermal expansion coefficient of FeSi decreased from 1.758×10^{-5} to 1.402×10^{-5} (1/K) as the temperature increased from 70 to 150 °C [302]. This susceptibility may arise due to the nature and properties of FeSi materials such as thermal gradient, thermal stress [172], and residual stress during the LMD process, leading to the crack initiation and propagation [266]. These cracks can significantly impact the mechanical and magnetic properties of electrical steel parts which must be controlled. For instance, cracks reduce the permeability by acting as pinning sites [172], which hinder the motion of domain walls. Additionally, crack propagation can lead to catastrophic failure [176].

Manufacturing parts without cracks is optimal and to address the cracking issue during the manufacturing of FeSi 6.5%, preheating is crucial with the aim of mitigating the impact of the thermal expansion coefficient. However, given the characteristics of the LMD process and FeSi materials, the occurrence of cracks in thin walls and cubes is probable. Consequently, before investigating the impact of processing parameters, it is crucial to establish a limit for crack occurrence. This explanation will aid in identifying the process parameters that lead to cracks in manufactured parts like thin walls at particular laser powers and scan speeds. As mentioned earlier, to prevent cracking and debonding at the interface, three foundation layers were deposited beforehand. Following this, a single pass of FeSi was applied on top. Additionally, cracks at the interface between the deposited FeSi parts and the substrate are not considered because focus for this project was on single pass of FeSi deposited.

The morphology of the cracks was determined by optical and SEM Figure 46. Cracks were observed in the majority of samples. Existing iron carbide (Fe_3C) content in ordered phases such as DO3 and B2 can act as stress concentration points, making high silicon steel (6.5%) more susceptible to cracking [302]. However, in this project, the effect of carbon can be neglected because the carbon content is very low at 0.01wt%. Moreover, the unmelted regions observed in the process might serve as points where cracks begin to develop when subjected to external loads, resembling the findings reported by G. Stornelli [172]. Additionally, the high silicon content may contribute to embrittlement, increasing the susceptibility of FeSi 6.5% to cracking [262]. In this case, to characterise the distribution of

silicon, the EDS technique was used (Figure 47) for analysing cracks area from Figure 44 (f). The EDX data illustrated that around 6% Si is present in the crack area, indicating that silicon segregation occurred during the solidification process. The high silicon content migrates and concentrates at specific locations, such as grain boundaries or areas of high stress. This is particularly evident in the layer-by-layer deposition in LMD, where thermal gradients and residual stresses play a significant role. To better understand the behaviour of cracks in enriched silicon areas the EBSD map of crack areas was analysed, as can be seen in Figure 47 (e). When the grain boundaries were weak the intergranular fracture occurred along the grain boundaries as well as transgranular fracture was also observed inside the grain due to thermal stress and less formability of FeSi 6.5 % which is similar to other reports [303-305]. In addition to that, the high cooling rate in LMD can cause cold cracking in deposited layers and, due to the thermal gradient between deposited materials and base metal, cause an increase in thermal residual stress in the interface layers forming cracks in deposited layers [306].

Only a few samples—TW13, TW23, TW25, TW28, and TW29—exhibited cracks at the interface between the substrate and the deposited FeSi. Conversely, samples such as TW20, TW21, TW24, TW27 and TW33 showed no signs of cracks, which is a promising outcome for manufacturing FeSi 6.5 wt%. Additionally, the observed cracking behaviour is complex, primarily occurring along the build direction and propagating perpendicular to it, aligning with findings reported by other researchers [172, 271, 307]. This occurrence might be from the rapid heating and subsequent cooling inherent in the LMD process of FeSi. These fluctuations can cause different thermal conductivity and expansion coefficients, leading to concentrated residual stresses in certain areas. Consequently, this stress concentration results in cracks forming along the building direction [308].

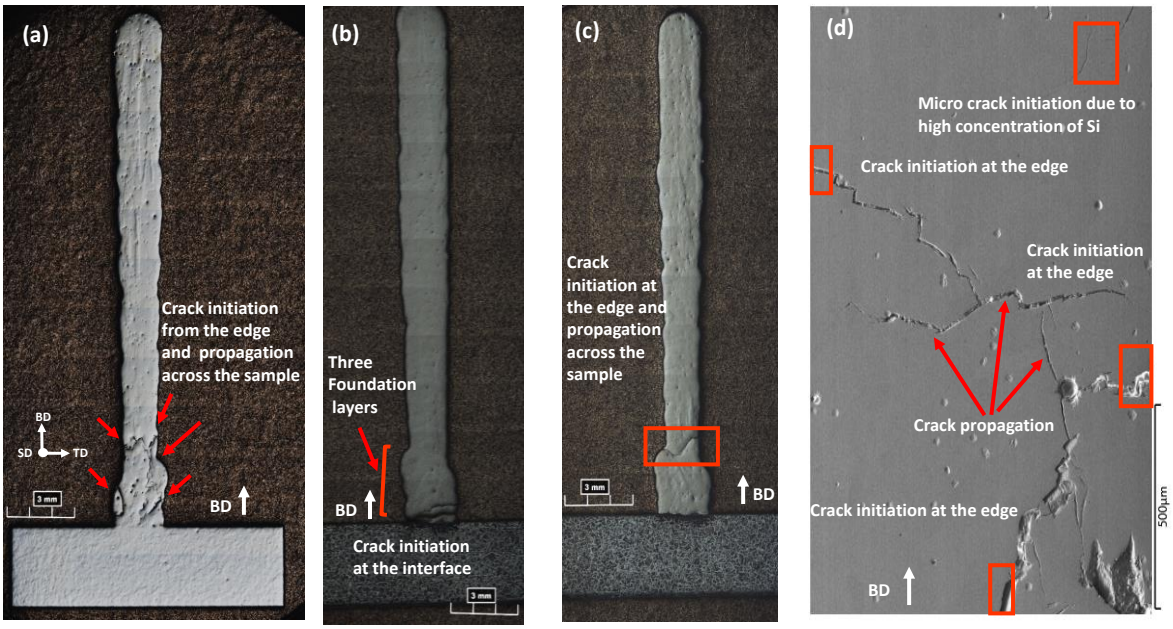

Figure 46. Optical micrographs (a-c) and (d) SEM micrograph, display the initiation of cracks and micro cracks from the edges, at the interfaces, and the propagation of cracks from these points and pores, as well as cracks propagation in the build direction.

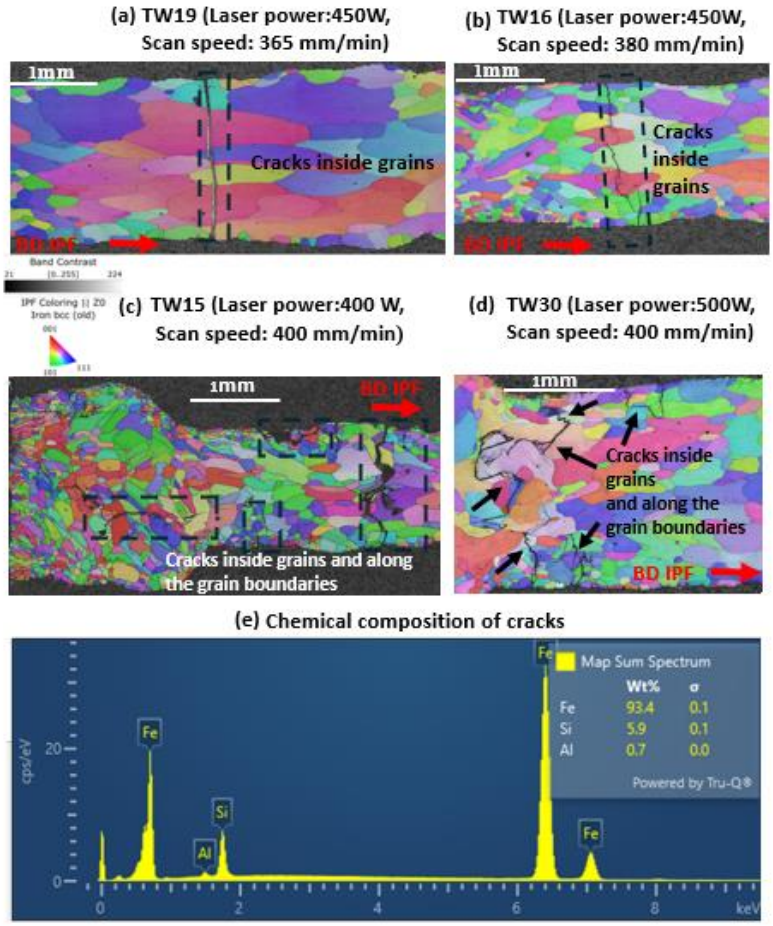

Figure 47. EBSD map (a)-(d) illustrated cracks inside grain and along boundaries, enrich with silicon, (e) presents chemical composition of cracks from Fig (23) (f) obtained from EDS.

5.4 Analysing porosity and cracks in thin walls using XCT

X-ray computed tomography (XCT) is a non-destructive image testing method extensively used in AM to detect internal defects, especially porosity. This study utilises X-ray XCT to examine the presence of cracks and porosity. Furthermore, the influence of different process parameters—including laser power, on the formation of these defects was briefly analysed. The XCT analysis of sample TW20 reveals varying degrees of porosity and internal defects, as well as cracks between the substrate and deposited materials, particularly evident in Figure 48 (c) [256]. The XCT images labelled (a) through (d) shows different areas of sample TW20 and TW29 (e) with varying porosity levels. Image (a) and (b) shows minimal porosity with some voids. Additionally, image (c) and (d) shows porosity similar to other areas. The findings indicate that most porosities appeared during the initial laser melting of each layer, as shown in the image (e). Subsequent laser movements resulted in fewer porosities. This trend may be attributed to initial inconsistencies in melting or insufficient laser energy absorption between layers, leading to greater porosity formation. As the laser continued along the samples, it likely stabilised, resulting in more uniform melting and fewer porosities [309, 310]. Overall, this analysis of XCT images provides essential insights for optimising manufacturing processes and enhancing material quality, ensuring the reliability and performance of the final product.

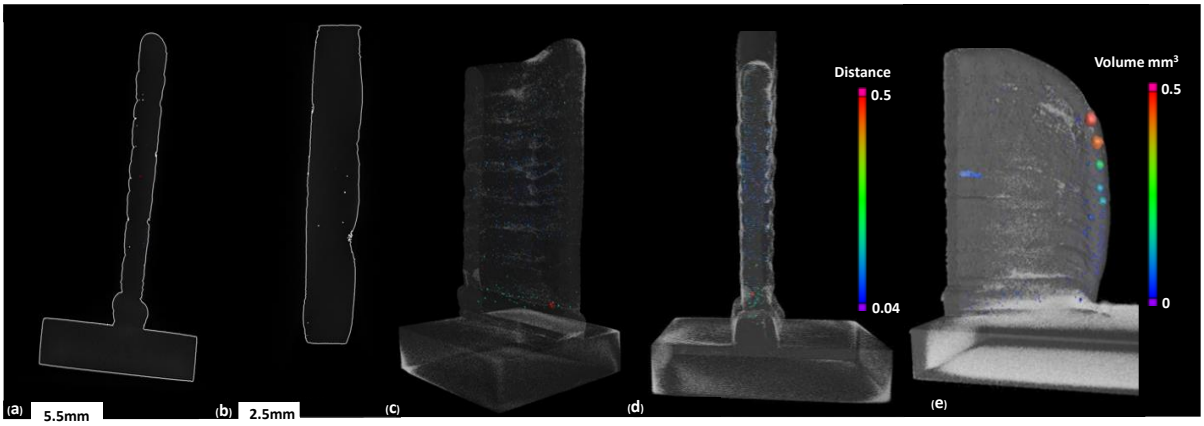

Figure 48. Porosity analysis workflow showing the cropped image from XCT data for sample TW20 (a) to (d) and TW29 (e).

5.5 Impact of laser power and scan speed on cracks formation in thin walls

As mentioned earlier, cracks significantly impact mechanical and magnetic properties. Therefore, it is crucial to manufacture thin walls without cracks. Previous studies [306, 311] have shown that process parameters, such as laser power and scan speed in LMD, can greatly influence crack formation. This study aims to explore the potential for reducing cracking by manipulating these process parameters, specifically laser power and scan speed. In this context, a crack size of zero (sdv: ± 0.4%), is established as the critical threshold for thin walls. Values exceeding this threshold are marked respectively in red. As depicted in Figure 49 (a) average crack size generally tends to increase, though the relationship is not strictly linear between crack formation and laser power. It can be said that crack formation occurs due to high thermal stresses and gradients during the cooldown process. As the laser power increases, more heat is introduced into the deposited layers, creating a larger melt pool and increasing the area that must solidify. This leads to a higher thermal gradient and greater residual stress. If the thermal stress exceeds the material's yield strength, cracks will form [312]. The highest measurements were 1.71mm (TW19:450 W) while the lowest were ~0.2mm (TW22, TW23,TW14,TW25,TW29). Having said that, TW20 (430 W), TW21 (425 W), TW24 (435 W), TW27 (450 W), TW28 (450 W), TW29 (435 W) and TW33 (450 W) showed no presence of cracks. In Figure 49 (b), the average crack size in thin walls is most prominent at scan speeds between 365 and 400 mm/min. Overall, with a few exceptions, the decrease in crack size from 1.71mm to 0mm is evident with the constant laser power of 450 W, as the scan speed increases from 365 mm/min to 440 mm/min. Moreover, samples with different scanning speed such as TW27 (440 mm/min), TW28 (395 mm/min), and TW33 (400 mm/min) showed no presence of cracks with a constant laser power of 450 W.

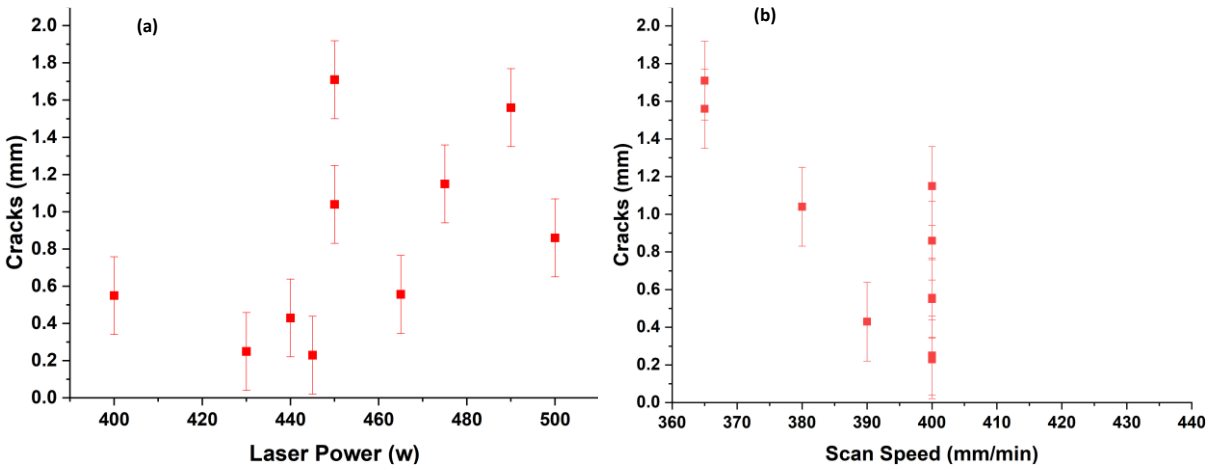

Figure 49. Experimentally measured cracks of thin walls as a function of laser power (a) and scan speed (b).

5.6 Impact of laser power and porosity and cracks formation in cubes

Prior to examining processing parameters' impact, it is crucial to establish a porosity threshold for identifying process window pores in manufactured parts, particularly cubes. A porosity percentage of 0.6% (sdv: ±0.25%) serves as the threshold, with values above or below highlighted in red and green. Figure 50 (a) illustrates the porosity percentage analysis across all samples created using various process parameters. In this instance, as the laser power increased from 480 to 600 W, the percentage of pores roughly decreased from 1.83% to 0.12%. Simultaneously, the average size of the pores decreased from approximately 120 to 12 µm. However, below 475 W of power, the pores were uniformly distributed, and numerous small spherical pores were observed across the samples. These findings suggest increasing the laser power in the deposition of FeSi 6.5 wt% via the LMD process improves overall quality due to increased melting and fusion of the powder materials and substrate. This leads to better fusion between layers and the FeSi deposit, resulting in fewer voids and less porosity. Additionally, the higher temperature in the melt pool increases fluidity, allowing the material to flow better and fill gaps, further reducing pore formation. The higher temperatures also promote better metallurgical bonding at the interfaces, helping to eliminate micro-voids and create a more homogeneous structure. These factors contribute to a significant reduction in porosity [294, 313, 314].

Figure 50 (b) illustrates the crack size analysis across all cubes samples created using various process parameters. In this context, a crack size of 0.7 mm is determined as the critical threshold for cubes. Values exceeding or falling below this threshold are respectively marked in red and green. In this instance, as the laser power increased from 400 to 600 W, the cracks size roughly decreased from 1.89 to 0.27mm. Several factors contribute to this improvement. The reduction in porosity eliminates potential sites for crack initiation and propagation. Additionally, the higher laser energy creates a larger and more stable melt pool, leading to better heat distribution and reduced thermal stress during the solidification process [315]. Furthermore, the increased laser power decreases the exposure time of the melt pool to the

atmosphere, resulting in less contamination. This reduction in contamination lowers stress concentrations in the melt pool, leading to fewer cracks [316].

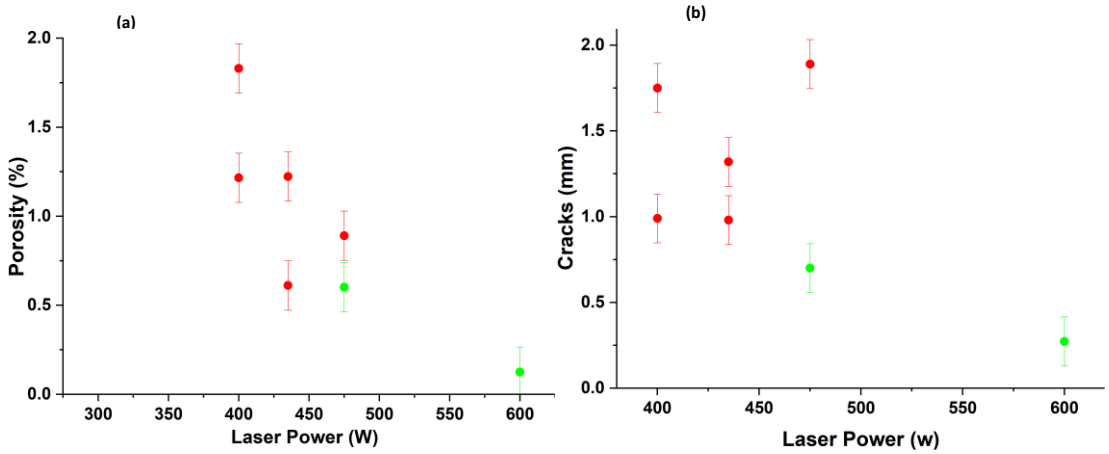

Figure 50. Experimentally measured porosity (a) and cracks of cubes (b) as a function of laser power.

5.7 Analysis of cracks, porosity and the effects of laser power in cubes

Different studies [317, 318] have shown that by increasing the energy density in the direct energy deposition process, such as SLM, better powder melting, a more stable melt pool, and a resulting part with high densification can be achieved. As shown in the Figure 51 (b) by increasing the laser power from 400 to 600 W, the average crack size was reduced from 1 mm to less than 0.27 mm, and the area fraction of porosities decreased from 1.83% to 0.12%. This reduction is significant for achieving fully dense parts and, in this case, as the laser power increased by 50%, better bonding between the substrate and deposited materials was achieved. It has been suggested that in processes such as LMD [183], the formation of cracks is influenced by residual stresses arising from the poor heat conductivity of the powder and the high thermal gradients generated during processing, but other factors also contribute. These include microstructural features, material defects, and variations in process parameters, such as energy density, scan speed, and layer thickness, all of which can affect crack initiation and propagation around the laser spot.

Additionally, the thermal expansion of deposited materials like FeSi contributes to crack initiation during solidification, as the contraction of the upper deposited layers during cooling is resisted by the underlying layers, creating internal stresses. This creates compressive and tensile stresses, and if defects such as pores exist in these stress areas, it can serve as sites for crack initiation and propagation. EBSD analysis provides valuable insights into these mechanisms by highlighting various types of cracks and their formation pathways. These cracks include edge-initiated, pore-initiated, grain boundary, and intragranular cracks. Understanding the initiation and propagation of these cracks is crucial, especially given the material's composition such as FeSi 6.5 wt% and the processing parameters used. It can be suggested that the edge-initiated cracks are prominently seen in sample Figure 51 (a), produced with a laser power of 400 W. These cracks initiate from the edges of the sample, likely due to the high thermal gradient and rapid cooling rates at the boundaries. The sudden

temperature changes induce tensile stresses at the edges leading to crack formation. This type of cracking is worsened by the relatively lower laser power, which may not provide sufficient energy for effective melting and consolidation of the material at the edges. Moreover, pore-initiated cracks are observed in both samples Figure 51 (a) and (b). These cracks originate from pores within the material, which act as stress concentrators. Pores are typically formed due to incomplete melting or gas entrapment during the AM process. The presence of these voids significantly weakens the material, making it more susceptible to crack initiation under thermal or mechanical stresses. In sample Figure 51 (a), processed at 400 W, the occurrence of pores is more pronounced, whereas sample Figure 51 (b), processed at 600 W, shows a reduction in porosity due to the higher energy input, although pore-related cracks are still present. On the other hand, grain boundary cracks are evident in EBSD maps, indicating crack propagation along the grain boundaries. This type of cracking suggests weak bonding between grains, which can result from improper solidification.

The rapid cooling rates inherent to additive manufacturing limit atomic diffusion across grain boundaries, resulting in weak intergranular bonding. This effect is particularly pronounced in high-silicon alloys such as Fe–Si 6.5 wt%, where silicon segregation at grain boundaries increases brittleness and promotes crack initiation and propagation [187, 319]. Furthermore, intragranular cracks were observed in both samples, indicating that crack propagation also occurs within grains and reflecting the presence of internal stress fields and microstructural heterogeneity. These internal stress fields encompass residual stresses arising from the AM process, which contribute to overall crack susceptibility alongside the microstructural factors described.

Although residual stress is inherently generated during AM due to steep thermal gradients and cyclic heating and cooling, it was not established as a primary quantitative metric in this project. Residual stress generation mechanisms, measurement approaches, and their relevance to AM are discussed elsewhere in the manuscript with appropriate references, and the present work builds on established literature rather than duplicating detailed residual stress characterisation. In AM components, residual stress is highly localised, anisotropic, and strongly dependent on transient thermal history, making it difficult to correlate unambiguously with either alloy composition or individual process parameters without in-situ diffraction techniques or layer-resolved stress mapping. Such measurements require dedicated experimental campaigns and were therefore beyond the scope of the present project. While residual stresses play a role in cracking, their practical impact on manufacturability was evaluated through crack morphology, grain-scale damage, microstructural features, and texture, which provide a more physically meaningful indication of performance in brittle high-silicon Fe–Si alloys [320]. In these materials, limited ductility arising from ordered phases (B_2, DO_3), solute segregation, and potential inclusions dominates crack susceptibility, such that microstructural fracture behaviour is a more reliable indicator than residual stress magnitude alone.

This methodological choice contrasts with conventional thermomechanical processing routes such as asymmetric rolling and cross-rolling, where deformation is imposed under comparatively stable thermal conditions and residual stress arises primarily from mechanically applied strain paths. In those processes, residual stress can be more readily measured and directly correlated with rolling direction, strain heterogeneity, and reduction ratio. In additive manufacturing, however, thermally driven solidification and cooling stresses dominate and evolve continuously during layer deposition, rendering residual stress a secondary and difficult to isolate variable within the scope of the present work [321, 322].

Comparing the two samples, Figure 51 (b) produced at 600 W exhibits a more refined and homogeneous grain structure compared to sample Figure 51 (a). The higher laser power improves the melting process, leading to a reduction in porosity and enhancing the grain structure's overall strength. However, the inherent brittleness of the Fe- Si 6.5wt% alloy means that even with optimised processing parameters, some degree of cracking is unavoidable. In conclusion, the EBSD maps of the Fe- Si 6.5wt% samples reveal multiple types of cracks, including edge-initiated, pore-initiated, grain boundary, and intragranular cracks. The initiation and propagation of these cracks are heavily influenced by the brittle nature of the high-silicon alloy and the thermal stresses induced during AM. Optimising laser power and other processing parameters can mitigate some defects, but the material's inherent properties necessitate careful control to minimise crack formation and enhance material integrity. This analysis explains the critical need for balancing alloy composition and processing conditions to achieve optimal results in the AM of brittle materials such as high silicon steel [314].

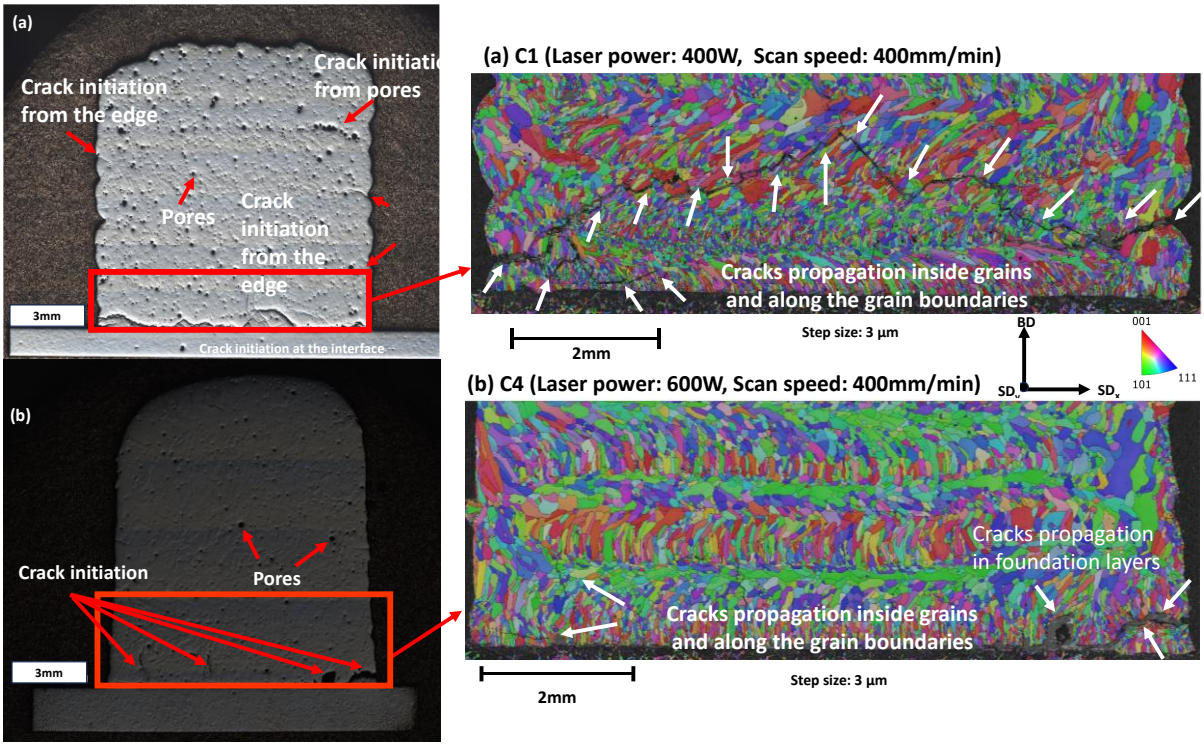

Figure 51. EBSD map (a) and (b) illustrated intergranular cracks within grain and along boundaries influenced by diffract laser powers.

5.8 Effect of processing laser energy input on porosity formation in cubes

Figure 52 illustrates the relationship between energy density and porosity in samples produced using the LMD process. A clear trend is observed in the figure, showing that increasing the energy density leads to a reduction in porosity. For instance, sample (C16 and C18), with an energy density of 60.0 J/mm^2, shows the highest porosity at 1.8% and 1.2% respectively. Increasing the energy density to 65.3 J/mm^2, as in sample C17, the porosity decreases to 0.6%, a significant reduction of 66.7%. Similarly, sample C19, also with 65.3 J/mm^2, shows a porosity of 1.2% (sdv: ±0.25%), indicating other influencing factors might be at play such as scanning strategy. However, further increasing the energy density to 71.3 J/mm^2 in samples C15 and C20 results in porosity values of 0.9% and 0.6%, respectively, demonstrating a continued reduction in porosity. Notably, sample C21, with the highest energy density of 90.0 J/mm^2, exhibits the lowest porosity of 0.1%, confirming the trend that higher energy density reduces porosity. The percentage change in porosity with increasing energy density explain this trend: from sample C16 to C17, porosity decreases by 66.7%; from sample C19 to C20, by 50%; and from sample C20 to C21, by 83.3%.

This decrease in porosity with increasing energy density and laser power can be attributed to the LMD process, where higher energy densities provide more energy to melt the powder completely, resulting in better fusion of the material and fewer voids or pores. Lower energy densities may lead to incomplete melting and higher porosity due to insufficient energy to fully fuse the material. Thus, increasing the energy density during the LMD process effectively reduces porosity in the samples, leading to improved material properties. This finding is crucial for optimising manufacturing parameters to achieve the desired quality and performance in LMD components [323].

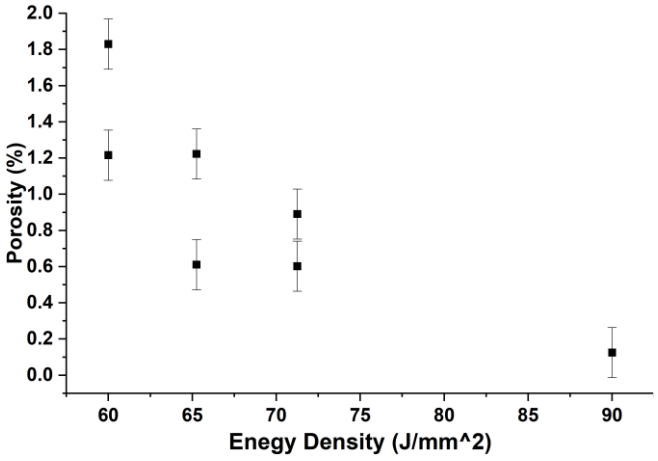

Figure 52. The Effect of energy density on porosity in cubes samples manufactured by LMD process.

5.9 Impact of scanning strategy on cracks

For the successful manufacturing of thin walls and cubes, it is essential to select the proper process parameters, including laser power, scan speed, powder feeding rate, z-step, and

hatch space. This section will briefly cover the impact of scanning strategy. To investigate the effects of processing parameters such as scanning strategy, samples produced under nearly identical parameters, were examined. Cube samples C17 and C19, manufactured using bidirectional and unidirectional scanning strategies, respectively, showed that bidirectional scanning reduced crack size from 1.22 to 0.61 mm and porosity from 1.32 to 0.98%. A similar trend was observed in C15 and C20, where bidirectional scanning decreased porosity from 0.89 to 0.6% and crack size from 1.89 to. 0.7mm. Moreover, by increasing the laser power to 600 W while maintaining a constant scan speed of 400 mm/min, the lowest porosity and crack size can be achieved, measuring 0.12% and 0.27mm, respectively. These findings indicate that bidirectional scanning has a significant impact on reducing defects during the manufacturing of FeSi 6.5wt%. Both unidirectional and bidirectional scanning deposition play a significant role in the development of microstructure and grain orientation, which will be covered in more detail in the metallurgy chapter [324].

5.10 Analysing porosity and cracks in cubes using XCT

The XCT images of sample C18 (Figure 53 (a) to (c)), produced under a laser power of 400 W and a scan speed of 400 mm/min, provide critical insights into the material's internal structure and defect distribution. The energy density applied during the process was 60 J/mm², with a hatch space of 0.60 mm and a z-step of 0.85 mm. These parameters are integral in determining the material's microstructure and overall integrity. The porosity level in sample C18 was found to be 1.2%, as illustrated in the porosity map, indicating a relatively high concentration of internal voids. This heterogeneous distribution of porosity suggests that the material contains numerous defects that could potentially compromise its mechanical properties. In comparison to sample C21, which exhibited the lowest porosity level of 0.12%, sample C18's porosity is significantly higher, pointing to inconsistencies in the fabrication process. Furthermore, the XCT analysis revealed the presence of substantial cracks within sample C18, with the largest crack measuring 1.75 mm. This is notably larger than the cracks observed in sample C21, which had a maximum size of 0.27 mm. The presence of such large cracks in sample C18 could lead to premature failure under mechanical stress, thereby diminishing the material's reliability and performance.

Sample C21, which displayed significantly lower porosity and smaller crack sizes, was produced with the same scanning speed of 400 mm/min but with a higher laser power of 600 W. This comparison indicates that the increased laser power may contribute to a more uniform melt pool and improved solidification process, thereby reducing the formation of defects. The combination of a laser power of 400 W and a scan speed of 400 mm/min for sample C18, resulting in an energy density of 60 J/mm², plays a crucial role in the formation of the melt pool and its subsequent solidification. The interplay of these parameters influences the porosity and crack formation significantly. The hatch space of 0.60 mm and z-step of 0.85 mm were intended to ensure enough overlap between successive laser scans and layers. However, despite these settings, sample C18 exhibited significant internal defects, indicating that these parameters were not sufficient to prevent the formation of porosity and

cracks. In conclusion, sample C18 demonstrates a high level of porosity and large cracks compared to other samples such as C21. The processing parameters used in its fabrication appear to have been inadequate in eliminating these defects. Therefore, optimisation of these parameters, such as increasing the laser power or changing the melting strategy, are essential to reduce porosity and crack formation, thereby enhancing the material's overall quality and performance. This analysis explains the importance of precise control over manufacturing conditions to achieve superior material properties in the LMD fabricated components [325].

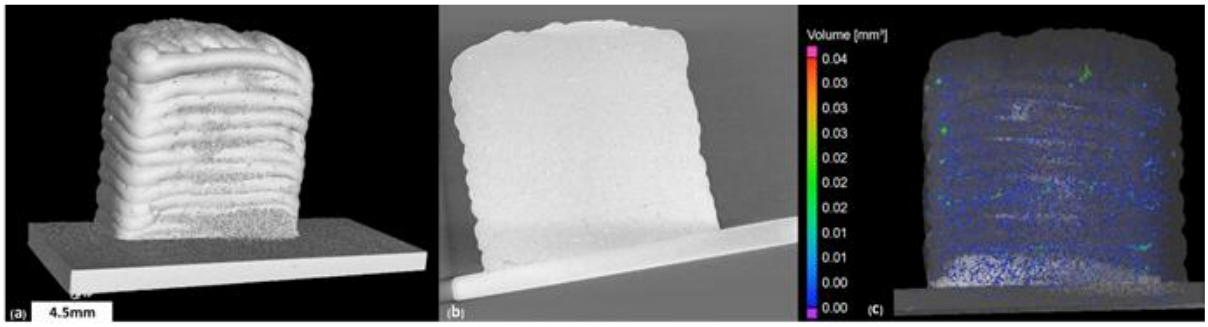

Figure 53.Porosity analysis workflow showing the cropped image from XCT data for sample C18.

5.11 Identifying the optimal processing parameters for thin walls and cubes

High-silicon electrical steel, specifically FeSi with 6.5 wt% silicon, is essential for its excellent magnetic properties. However, manufacturing components like stator and rotor cores presents challenges, particularly due to defects such as cracks and porosity during lamination. This research focuses on optimising manufacturing parameters to enhance part densification, eliminate cracks, and reduce porosity, ultimately improving the magnetic properties. A similar approach has been previously proposed for 316L stainless steel [326], highlighting the importance of determining the process window to achieve high-quality components. In this context, fine-tuning of the parameters is crucial for achieving better texture and microstructure while minimising defects. Given the variability in processing parameters, such as z-step and part geometries, it is necessary to establish optimum conditions for thin walls and cubes separately. Additionally, the presence of various defects including lack of fusion porosity, keyhole pores, metallurgical pores, and unmelted powder, underlines the need for strict processing window parameters as illustrated in Figure 54 (a). Each colour in the figure represents the quality of the samples: green indicates samples within the restricted process window (thin-wall samples with <0.2% porosity and no cracks; cube samples with <0.6% porosity and cracks smaller than 0.7 mm), while red indicates samples outside this process window. This comprehensive approach aims to enhance the quality and performance of FeSi components in electrical machines. It can be seen that, at the higher laser power of 450 W, when utilising a scan speed range from 410, to 440 mm/min, the result is an absence of cracks and porosity levels below 0.2% in thin-wall samples. Similarly, this holds true for samples printed at lower laser powers of 430 and 435 W, with a scan speed range between 380 and 390 mm/min, exhibiting no cracks and less than 0.2% porosity. Nevertheless, process

optimisation is still necessary to eliminate porosity completely and achieve parts without any cracks or porosity. Figure 54 (b) illustrates the potential processing window parameters for cubes. With a medium laser power and a constant scan speed of 400 mm/min, an increase in laser power from 400 to 600 W resulted in a decrease in porosity and cracks. This trend holds true at higher laser powers, for instance, when both laser power and scanning speed were increased from 475 to 600 W, there was an overall reduction in porosity from 0.6% to 0.12% and a decrease in crack size to 0.27mm. Nevertheless, optimising the processing parameters for cubes is necessary to manufacture FeSi parts without any cracks and porosity. Conducting trials by decreasing the z-step, reducing the hatch spacing, increasing laser power and scan speed, and adjusting the powder feed rate would help evaluate how the materials respond to these parameter changes.

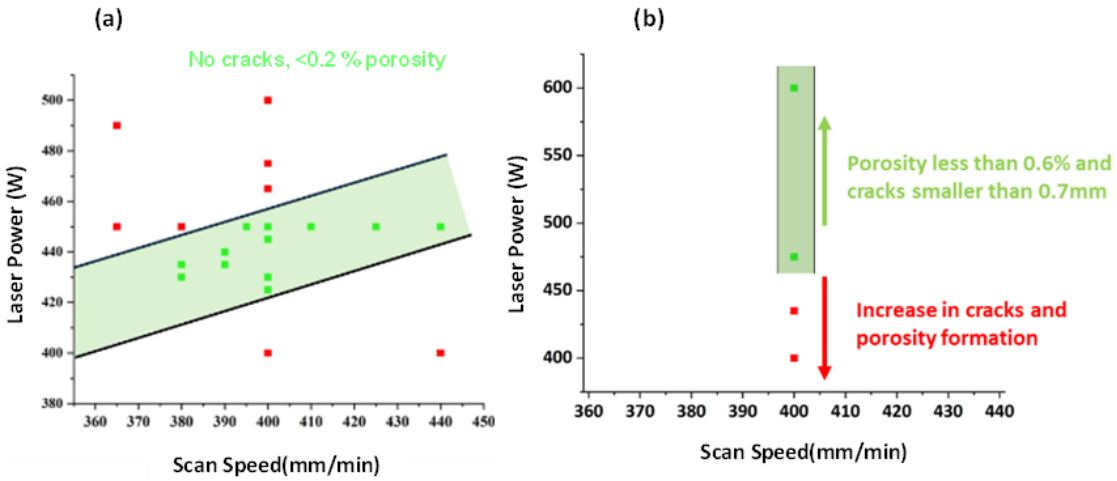

Figure 54. Processing window for thin walls (a) and cubes (b) considering of laser power and scan speed.

Chapter 6

6 Microstructure evolution during LMD of FeSi 6.5 wt%

The microstructure of FeSi 6.5 wt.% fabricated by LMD was found to consist predominantly of long columnar grains aligned with the build direction, as illustrated in Figure 55. This morphology is characteristic of high thermal gradients and directional solidification within the melt pool, a phenomenon also widely reported in AM of silicon steels [172, 176, 180]. However, fine equiaxed grains were observed at the first and last deposited layers, as well as along the free edges of the deposits. These regions are subjected to enhanced cooling due to substrate heat sinking and multi-surface exposure, conditions that promote rapid solidification and nucleation of new grains. Similar behaviour has been described in conventional processing of non-grain-oriented electrical steels, where localised shear deformation or rapid cooling promotes recrystallisation and fine grain formation [156, 327]. This observation of equiaxed grains at regions of rapid cooling can be critically compared with thermomechanical processing routes such as asymmetric rolling and repetitive bending under tension, discussed in Section 1.9. In those routes, shear bands and high dislocation densities act as nucleation sites for <001>-oriented grains during recrystallisation [112, 156]. Although the mechanism in LMD is thermal rather than mechanical, the outcome is similar: localised conditions promote nucleation and grain refinement, while bulk regions favour columnar growth. This highlights that both AM, and thermomechanical methods influence texture evolution by manipulating the balance between nucleation and competitive growth, although through different driving forces.

LMD involves interactions between the incident laser source, powder feed, and substrate material. The combined effects of these interactions, along with the deposition of numerous tracks and layers, generate a unique thermal history within the component. A section of this chapter has been adapted from our paper titled *"Additive Manufacturing Innovations: Microstructure Optimisation for Ultra-High Silicon Electrical Steel Components"*, published in *Materials Characterization*. This chapter examines the microstructure of as-deposited LMD FeSi 6.5 wt% and enhances our comprehension of the changes in microstructure that take place throughout the LMD process. In all specimen investigated in this work, the microstructure consisted of columnar grains up to several millimetres in length aligned in the build direction. However, as shown in fine equiaxed grains were observed in the first and last layers, as well as in some areas along the long edges of the FeSi 6.5% deposits during printing. This behaviour is also observed in the development of texture non-grain oriented electrical steel, is primarily due to a significant temperature gradient within the melt pool which promotes the rapid growth of columnar grains and reduces the likelihood of new nucleation sites forming during solidification. However, the formation of fine grains in these specific regions likely results from the substrate acting as a thermal sink during the initial deposition, with the edges exposed to the atmosphere and the top of the sample cooling from multiple faces. This increases the cooling rate, encouraging fine grain development. Additionally,

reducing laser exposure time in these areas minimises heat accumulation due to shorter laser travel time, further promoting the nucleation of new fine grains.

When compared with powder-bed-based AM processes, the present LMD results demonstrate clear advantages in terms of microstructure and magnetic properties. While L-PBF of Fe–Si alloys produce columnar or equiaxed microstructures depending on the processing parameters [172, 175], it is also associated with extremely high cooling rates, which frequently lead to residual stresses, cracking, and porosity [173, 328]. Moreover, as reported in the literature review, L-PBF can produce grains oriented along hard magnetisation directions such as <111>, which are detrimental for soft magnetic performance [176]. In contrast, in our LMD research, the majority of grains are columnar and aligned with the build direction, as observed in our optical micrographs, highlighting a key difference between these AM methods.

LMD FeSi 6.5wt% achieves a predominantly columnar grain structure with strong texture along the build direction, which is beneficial for magnetic performance. The columnar grains reduce the number of grain boundaries, facilitating domain wall motion and improving magnetic properties, as highlighted in sections 1.9 and 1.10 of the literature review. Moreover, the lower cooling rates and controlled thermal gradients in LMD contribute to fewer cracks in some samples compared with other AM processes [186, 192]. Although fine equiaxed grains are present at the first and last layers and along free edges, the bulk of the material maintains large, well-aligned columnar grains, which are highly desirable for soft magnetic applications. This microstructural stability and texture development can provide superior performance compared with other AM routes, as it allows for better control of magnetic domain alignment and minimises defects that hinder magnetic properties.

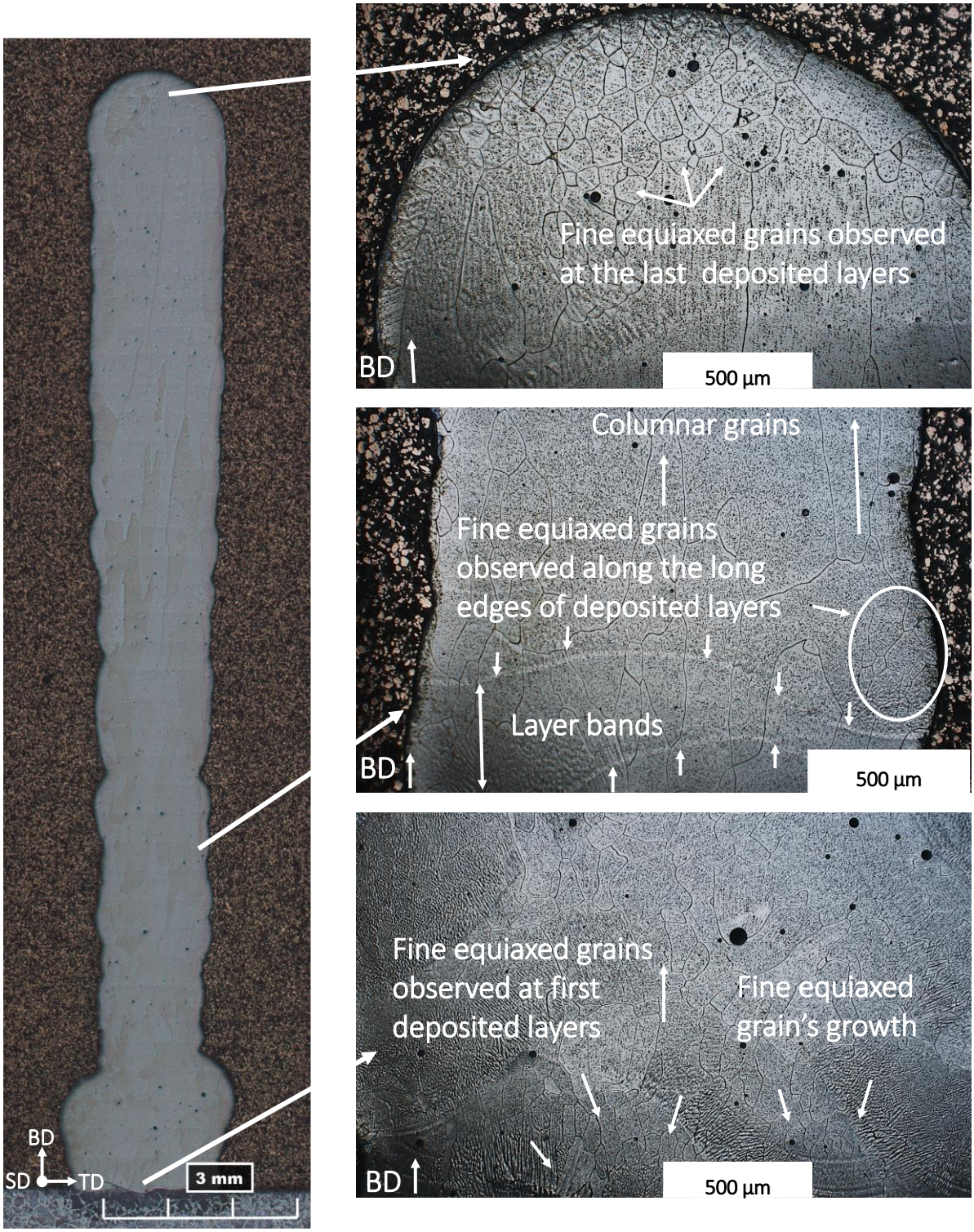

Figure 55. Optical micrograph of an etched FeSi 6.5% specimen, showing different sections of the sample, highlighting the grain structure and areas of interest such as fine equiaxed and columnar grains, and layer bands.

Optimising processing parameters such as laser power during the AM process is crucial to avoiding physical defects like keyholing and porosity at the bottom of the melt pool [329]. Ideally, the melt pool should remain in conduction mode without defects such as entrapped gas porosity or keyholing. However, at high laser power, these defects are more likely due to

turbulence within the melt pool, which can lead to gas entrapment and the formation of spherical pores [330]. Additionally, rapid cooling rates and thermal gradients during the LMD process can induce other defects, such as cracks, particularly in high-silicon steels like FeSi 6.5%. Cracks often form due to the high thermal stresses generated by uneven cooling, especially in regions with steep temperature gradients, as the material undergoes significant contraction during solidification [262]. This issue is compounded by the material's low ductility at elevated temperatures, which limits its ability to accommodate the residual tensile stresses that develop during solidification, making it prone to hot cracking. The solidification behavior, including dendritic microstructure and elemental segregation, creates localized weak zones that cannot deform plastically under these stresses, further promoting crack formation [331].

Furthermore, residual stresses play a critical role in defect formation and material integrity. At the surface, residual stresses can cause distortion and cracking due to rapid cooling and exposure to the atmosphere, while at the bottom areas near the substrate, residual stress arises from the thermal mismatch between the deposited layer and the substrate, potentially leading to delamination or interfacial cracking [214]. These defects highlight the need for careful control of thermal cycles during processing. Therefore, melt pool characteristics, including thermal phenomena and heat transfer mechanisms (conduction, convection, radiation), play a key role in maintaining melt pool stability during the AM process [316]. The schematic of thermal phenomena, melt boundary, and grain development in FeSi 6.5% during the LMD process is shown in Figure 56. This figure illustrates the interaction of the laser with the substrate, forming a melt pool where heat transfer occurs through conduction into the substrate, convection within the melt pool, and radiation from the surface. The schematic also highlights the formation of a keyhole at the centre of the melt pool, which can occur at high laser power and lead to defects like porosity. Additionally, the figure depicts the grain structure within the melt pool, showing how thermal gradients and cooling rates influence grain development. Specifically, the rapid cooling at the melt pool boundaries, driven by heat conduction into the substrate and radiation to the surroundings, promotes the nucleation of fine grains, while the central region of the melt pool may develop larger columnar grains due to slower cooling rates. These thermal gradients also contribute to the buildup of residual stresses, intensifying the risk of cracking and other defects. This interplay between thermal phenomena, residual stresses, and grain development highlights the importance of controlling laser power and scanning strategies to achieve a stable melt pool and desired microstructure in FeSi 6.5% deposits.

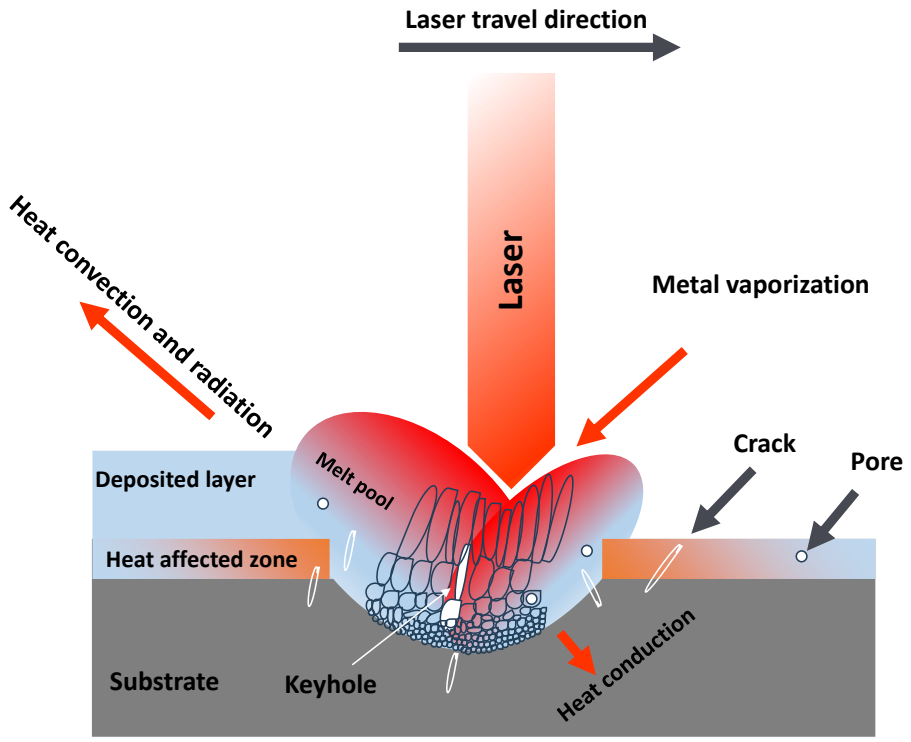

Figure 56. Schematic of melt pool boundary, thermal phenomena and columnar grain development occurring during the LMD process.

The nature of LMD-related defects also provides an important contrast with rolling-based processing. In ASR and cross-rolling, the main risks are surface cracking or productivity reduction [4, 156], whereas AM defects are often internal (e.g., pores, keyholes, microcracks), which can significantly degrade both mechanical and magnetic properties [168, 183]. Furthermore, as outlined before, the most desirable orientation for magnetic performance is <001>//ND, while <111> grains are detrimental [112]. The prevalence of columnar grains in this work suggests strong orientation along the build direction, but whether this is favourable or detrimental requires correlation with crystallographic texture analysis. This reinforces the importance of controlling columnar-to-equiaxed transitions in LMD to achieve both structural integrity and functional magnetic performance.

To investigate and understand the evolution behaviour of the microstructure during the layer-by-layer deposition process, optical images were obtained. In this case, the melt pool size depicted in Figure 57 is notably larger as also observed in [332], primarily resulting from the high laser power's influence on the LMD process. This effect outweighs other factors such as feed rate and powder mass flow. Additionally, the melt pool size is further increased, particularly in structures like thin walls due to the preheating of the substrate. Preheating increases the depth of the melt pool in the conduction area, leading to a deeper melt pool [333]. Furthermore, as depicted in Figure 55 and Figure 57 numerous layer bands are observed, similar to the findings reported in [334] and [335]. This observation may be attributed to the superheating effect which initiates melting in the previous layers forming a narrow band with a temperature exceeding the solidus temperature. However, due to the

thermal conditions, the material remains in the solid phase. In this case, as it can be seen in Figure 57, the formation of a shallow melt-pool with a curved surface occurs during the LMD process, where the melt-pool is in motion. The solidification substructure primarily grows parallel to the build direction (BD) due to the high thermal gradient, which is perpendicular to the melt pool. Notably, in this case, the melt pool tilts in the direction of the laser movement. This phenomenon has been reported by other researchers in more detail [336], and its impact on grain growth in the BD will be further explored in the EBSD case studies in this thesis. Regarding magnetic performance, grain boundaries generally have a stronger effect than layer band structures. grain boundaries act as sites of magnetic domain pinning and can increase magnetic losses, whereas layer bands primarily influence local anisotropy and minor variations in magnetic properties. Therefore, controlling grain boundaries density and orientation is more critical for optimising the magnetic performance of LMD-produced Fe-Si alloys [25].

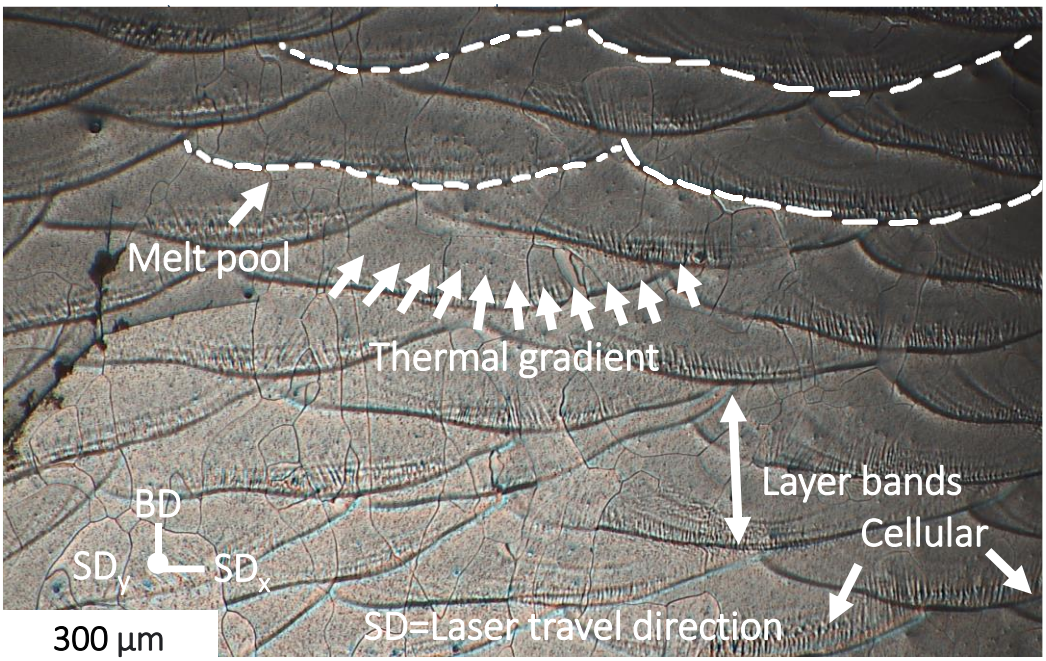

Figure 57. Optical microscope illustrated of the direction of maximum thermal gradient with respect to the melt pool geometry.

Defects such as porosity can adversely affect the mechanical and magnetic properties, as well as the microstructure development of the material [337]. As it can be seen in Figure 58 pores can act as thermal sinks and absorb all heat provided by laser and thus not allowing the heat to distribute through expected heat conduction across the sample and causing the melt pool temperature to rise. This abnormal melt pool temperature condition can result in the formation of two different areas of equiaxed and elongated grains. At the tip of the pore, the equiaxed grain is formed due to the existence of an airgap which block the heat conduction, distribution. This results in a lack of heat transfer, coupled with a higher cooling rate, leading to the formation of smaller grains. Also, in absent of defects, the above equiaxed grains due to higher heat input, rapid change in temperature across sample, and directional solidification

inherent in LMD, the grain starts to grow in specific direction and leading elongated grain structures [338].

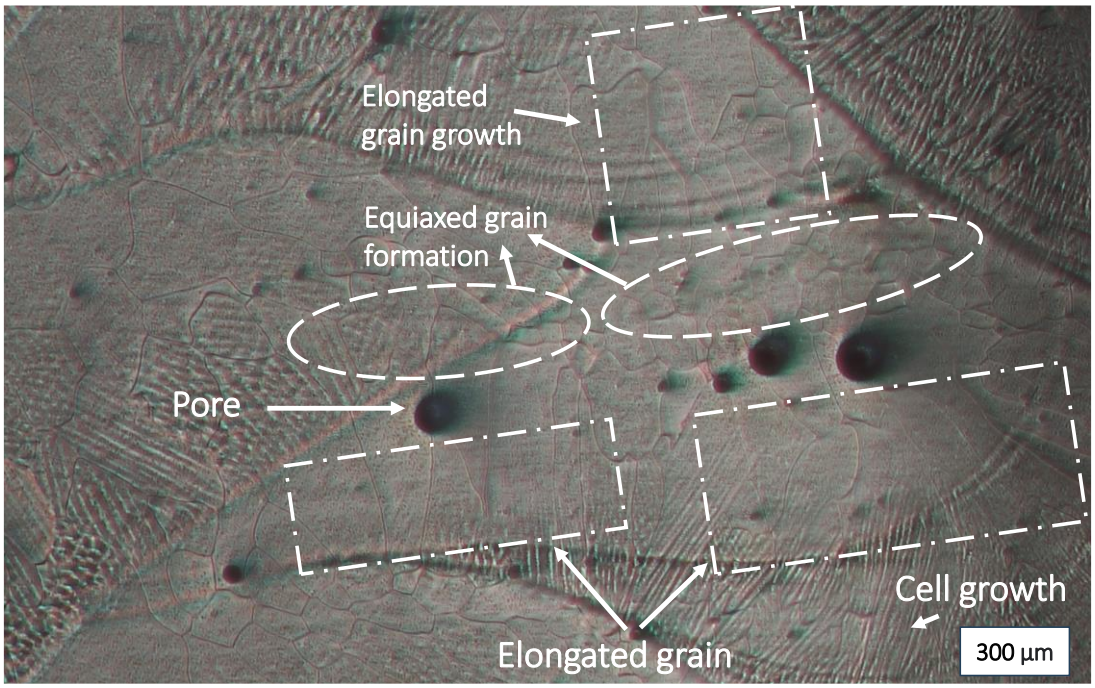

Figure 58. Effect of porosity on microstructural development.

During the solidification process in BCC materials such as FeSi, as materials transition from a liquid to a solid state, it is easy for atoms to stick to the less closely packed planes such as {001} due to their low energy configurations. These planes are favourable orientations for the growth of crystals <001> and become more prominent during the solidification process [339]. As can be seen in Figure 59 the schematic illustrates the development of crystal orientation <001> in the build direction for high silicon steel 6.5% deposited by the LMD process. This phenomenon has also been observed in other additive manufacturing studies, such as [5, 340]. In these studies, grains with a preferred crystal growth direction, such as <001>, tend to form along the building direction, aligning closely with the thermal gradient direction where rapid solidification occurs. Grains with less favourable orientations, however, are poorly aligned. In other words, the grains with <001> direction aligned more closely to the vertical thermal gradient direction which is the BD, and these preferred grains grow and dominate, creating a columnar grain growing perpendicular to a surface in BD. Since epitaxial growth requires minimal undercooling to occur, cellular and columnar grains grow in an epitaxial manner from the substrate grain and creating a columnar grain growing [341].

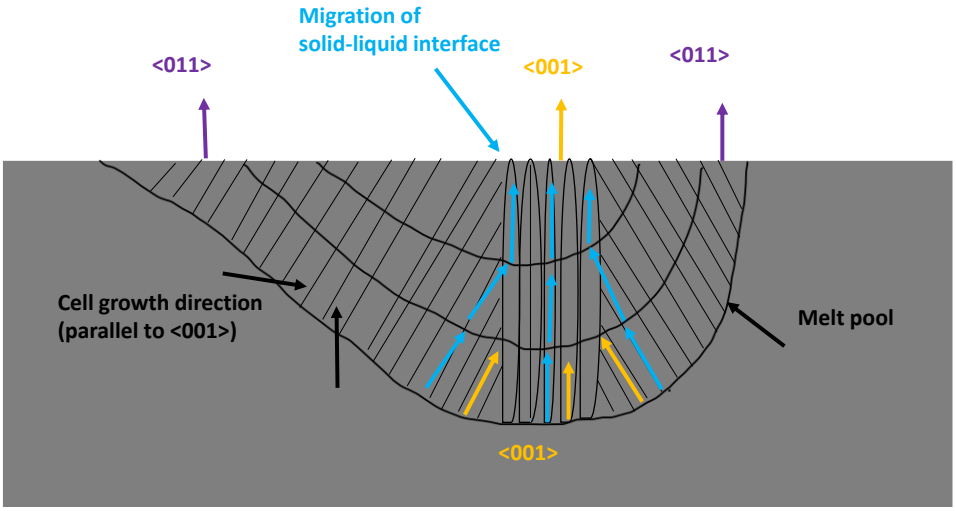

Figure 59. Development of crystal orientation <001> in build direction of FeSi 6.5% deposited by LMD process.

6.1 Study of crystallographic texture

6.2 EBSD case studies of thin walls FeSi 6.5 wt%

For detailed microstructure analysis, electron back-scatter diffraction (EBSD) data obtained from a FEI Quanta 250 and 650 Oxford Instrument EBSD camera with a 25kV accelerating voltage and 70-degree sample tilted to the laser beam [342]. AZtech Crystal software was used to collect EBSD maps from each sample covering the whole area of thin wall with a step size of 3µm. Figure 60 (a) shows inverse pole figure (IPF) orientation maps of the entire cross-section of thin walls of TW21. The IPF map corresponds to the orientation parallel to the BD. These maps reveal columnar grains elongated in the building direction with a crystallographic orientation close to <001>. This alignment could significantly improve magnetic properties by aligning columnar crystals with the direction of magnetic flux. This implies that applying LMD techniques to FeSi 6.5wt% NGOES can significantly improve the final texture by producing a strong crystallographic orientation, such as <001>. Additionally, it optimises the microstructure by promoting the formation of large grain sizes, which are desirable for enhancing magnetic properties such as permeability and magnetic flux density [343].

The IPF map shows that the movement of the laser during the LMD process induces varying thermal gradients (G) and solidification front velocities (R), which significantly influence the grain growth rate and morphology. Larger grain sizes are observed in higher layers due to a slower cooling rate compared to the initial layers, where rapid solidification dominates. The solidification rate, governed by the G/R ratio, plays a pivotal role in determining grain development. For example, in the upper layers, heat accumulation lowers the thermal gradient (G) and decreases the solidification front velocity (R), resulting in a reduced G/R ratio compared to initial expectations. Nonetheless, the conditions remain within the columnar grain growth regime. This promotes extended grain growth by allowing more time for grains to coarsen. Processing parameters such as laser power, scanning speed, energy density, layer thickness, thermal history, and chemical composition further modulate these solidification

conditions [344]. Across the melt pool, variations in grain morphology can be explained similarly. Near the centre of the melt pool, a higher temperature and slower cooling rate (due to reduced heat dissipation) decrease the G/R ratio to some extent but favouring larger, columnar grains aligned with the build direction. Conversely, at the edges, higher cooling rates—combined with a lower thermal gradient—can reduce the G/R ratio, promoting finer, more equiaxed grains due to greater undercooling, as explained in [345]. This aligns with the observations from the optical micrographs discussed earlier.

In terms of microstructure evolution, grain boundary migration and coalescence contribute to larger grains along the BD, with distinct grain size distributions arising from the varying thermal history. For example, the sample's centre exhibits significantly larger grains than the edges, reflecting differences in local cooling conditions. Figure 60 (b), showing IPF maps from the surface view, highlights elongated grains with uniform size following the laser movement (heat flow) [346]. This results from a consistent thermal gradient and rapid solidification at the surface, contrasting with the bottom layers. The crystallographic orientation in these surface IPF maps reveals a preference for <001> directions along the BD, which is critical for optimising magnetic properties like permeability and reducing core losses. Consistent orientation minimises magnetic anisotropy and enhances magnetic flux density. Since the magnetic flux flows perpendicularly through the sample's cross-section (thickness), the material properties in this direction directly affect flux transmission efficiency. Thus, appropriate grain orientation along the BD is essential for maximising magnetic permeability and minimising energy losses during operation [347].

To ensure statistical reliability, each EBSD map covered the entire thin-wall section with a step size of 3 µm, capturing several hundred grains per section (typically > 500). Multiple fields of view were analysed, and the ODFs obtained were consistent across repeated scans. Therefore, the texture findings shown here are considered reproducible, and the small differences between cross-section and surface section are minor and attributable to local thermal variations rather than insufficient sampling.

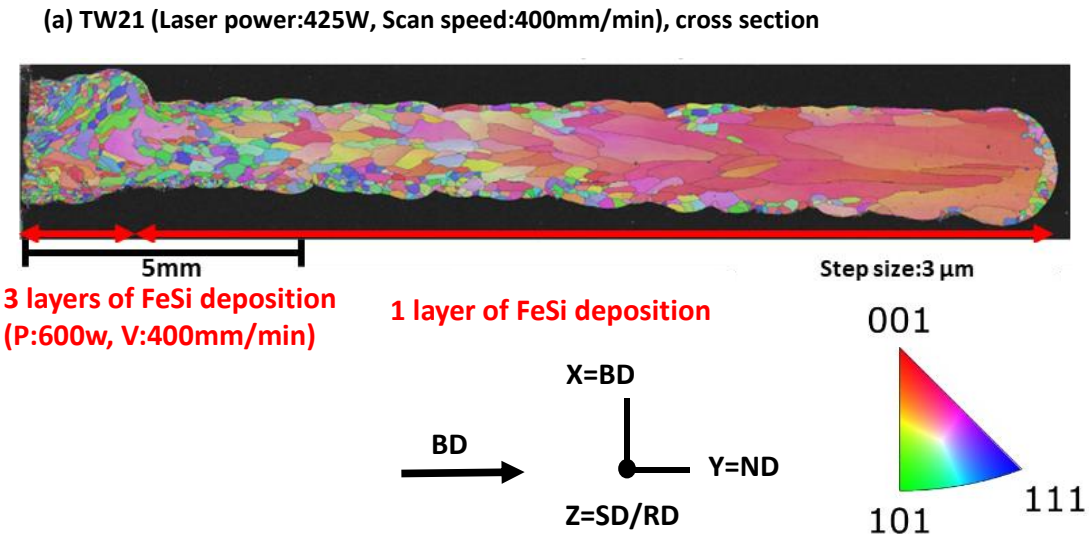

Figure 60. (a) IPF map of front view of cross section, and (b) surface sections of thin wall FeSi 6.5% manufactured by LMD machine (TW21).

The ODFs for the cross-section and surface section of the thin wall sample TW21 (Figure 61), processed under conditions of P = 425 W and V = 400 mm/min, are analysed to understand the crystallographic texture. Since both views represent the same sample, a uniform texture is expected, with only minor variations arising from heterogeneity across different locations. In the ODF at φ_2 = 0° for the cross-section (Figure 61 (a)), a strong near-cubic texture is observed, indicating a high degree of grain alignment along the cube orientation. Similarly, the surface section Figure 61 (b) shows a strong Goss and near cubic textures that, upon closer inspection, mostly aligns closely with the cross-section, with potential refined differences attributable to local variations in thermal conditions or sample heterogeneity rather than distinct solidification mechanisms. At φ_2 = 45°, the cross-section exhibits strong (113)[$3\bar{6}1$] and (113)[$0\bar{3}1$] orientations, reflecting a preferred crystallographic alignment influenced by

the thermal gradient and cooling rates during deposition. The surface section at the same Euler angle also shows comparable orientations, with a possible enhancement of the theta fibre (<001>//ND) due to surface-specific thermal gradients and cooling paths. These observations suggest that the thermal gradient, which is typically steeper at the surface, and the associated cooling rates play a role in fine-tuning the texture, alongside minor contributions from mechanical stresses or surface energy minimisation [348]. The image data indicates that the texture differences between the cross-section and surface section are minimal and likely result from localised variations rather than fundamentally different microstructural development processes. Analysing the ODFs and considering these influencing factors provides valuable insights into the microstructural evolution during the LMD process.

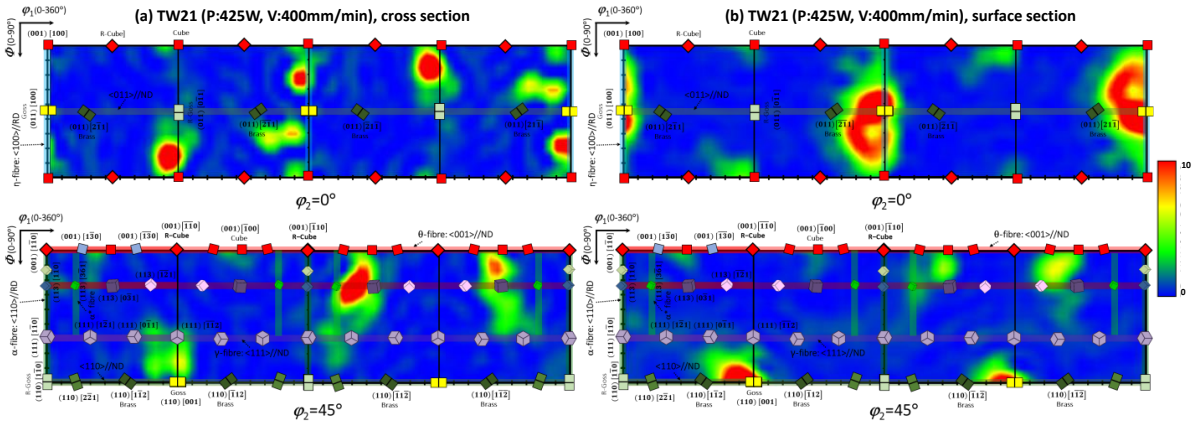

Figure 61. Illustrated φ_2 = 0° and 45° ODF sections for cross section (a) and (b) surface sections of TW21.

EBSD data analysis illustrate a crystallographic texture in the grains of LMD high silicon steel 6.5%. The pole figures in Figure 62 (a), (b), and (c) illustrate the crystallographic orientations for samples TW15 (laser power:400 W, scan speed:400 mm/min, energy density: 60 J/mm^2), TW18 (laser power:465 W, scan speed:400 mm/min, energy density: 69.75 J/mm^2), and TW30 (laser power:500 W, scan speed:400 mm/min, energy density:75 J/mm^2). Pole figure plots quantify the texture intensities for the three crystallographic direction families such as easy, medium, and hard magnetisation <001>, <101>, <111> respectively. These samples were processed with varying laser powers: TW15 at 400 W, TW18 at 465 W, and TW30 at 500 W, all at a constant scanning speed (400 mm/min). Sample TW15 (E=60 J/mm²) showed a strong <001> texture along the BD, indicating easy magnetisation. The <101> and <111> orientations have less pronounced textures. TW18 (E=69.75 J/mm²) also demonstrated a strong <001> texture but with a more balanced distribution among <001>, <101>, and <111> orientations compared to TW15. The increased energy input begins to shift the fibre-texture to a cube-texture. TW30 (E=75 J/mm²) exhibited a balanced crystallographic texture similar to TW18. The higher energy input further enhanced the cube-texture, aligning the <001> axes with the BD and promoting a more pronounced texture. All samples showed a preferred <001> orientation, crucial for easy magnetisation. Higher laser power (energy input) increases

texture intensity and balances the distribution among <001>, <101>, and <111> orientations. The shift from fibre-texture to cube-texture is evident as energy input increases from 60 J/mm² to 75 J/mm², highlighting the impact of laser energy on crystallographic texture. In summary, increasing the laser energy input in the LMD process enhances the <001> texture, aligning it with the BD and promotes a more intense and balanced crystallographic texture in high silicon steel.

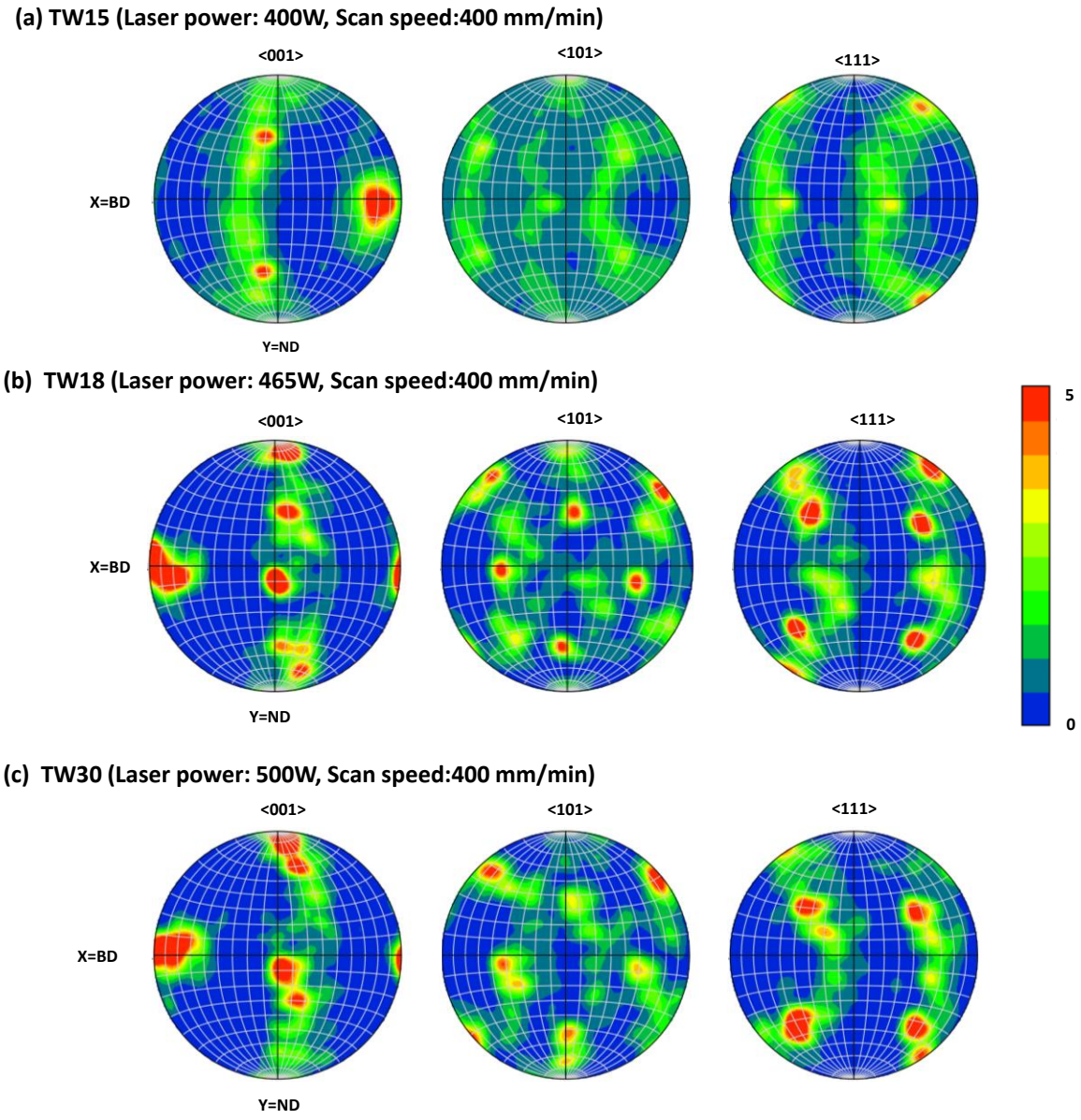

Figure 62. Pole figures showing the preferred orientation of the three crystallographic of <001>, <101>, and <111> for different samples TW15,TW18, and TW30.

Figure 63 presents EBSD maps and IPFs for samples TW15, TW18, and TW30 in different directions, conducted on the XY plane (X = build direction, BD; Y = normal direction, ND), to analyse crystallographic texture in the BD-TD plane, highlighting the correlation between grain morphology, energy density, and <001> texture along the BD.

The EBSD maps for samples TW18 and TW30 show that most long columnar grains preferentially orient their axes along the BD, supporting the hypothesis of epitaxial grain growth as the laser energy density increases from 60 to 69.75 and 75 J/mm². In contrast, TW15 exhibits fewer red grains, indicating a less pronounced <001> texture. The observed crystallographic texture aligns with the EBSD maps. Figure 63 (d), (e), (f), show a lower peak intensity for TW15 (2.52) compared to the higher peak intensities for TW18 (8.73) and TW30 (8.08). This increase in intensity with higher laser energy density suggests that varying energy inputs during FeSi deposition influence heat distribution and cooling rates, leading to different thermal gradients across the materials. These thermal variations significantly impact the microstructure and texture of FeSi parts [173, 349]. Research studies [5, 174, 184, 350] have shown that increasing laser energy density not only elongates grains but also increases the depth of the melt pool, causing the <001> fibre texture to shift towards a cube texture. Higher laser power, from 400 W to 500 W, results in a deeper melt pool and partially remelted grains with a <001> crystallographic direction along the BD, which then serve as a foundation for newly processed materials to solidify in an epitaxial manner, enlarging oriented grains and strengthening texture intensities. However, heat transport dynamics further refine this interpretation. As noted in [351] columnar grain growth in NGOES is driven by strong temperature gradients across the material thickness during recrystallisation. This phenomenon is particularly relevant in LMD due directional heat dissipation along the BD. Additionally, the higher cooling rate along directions—compared to other crystallographic axes—favours dendrite alignment and cube-texture development, particularly evident in TW30's stronger texture intensity [351]. Increasing laser energy density also expands the HAZ, altering temperature distribution and thermal gradients [352]. In TW18 and TW30, this leads to elongated columnar grains with axes preferentially along BD, as seen in front-view EBSD maps (Figure 63(b–c)), alongside a broader HAZ that intensifies remelting and texture evolution. These factors—epitaxial growth, rapid cooling, and HAZ effects—collectively explain the transition from a weaker fibre-texture in TW15 to a pronounced cube-texture in TW30, with larger grains and stronger alignment. This suggests that LMD parameters can be tuned to control texture and microstructure in FeSi 6.5 wt%, balancing orientation benefits against potential defects like cracks observed at higher energies [173, 349]. Thus, the EBSD analysis of TW15, TW18, and TW30 demonstrates that increasing laser energy density promotes epitaxial grain growth, enhances the <001> texture along the BD, and results in more pronounced and balanced crystallographic textures, ultimately impacting the microstructure and properties of the deposited FeSi materials.

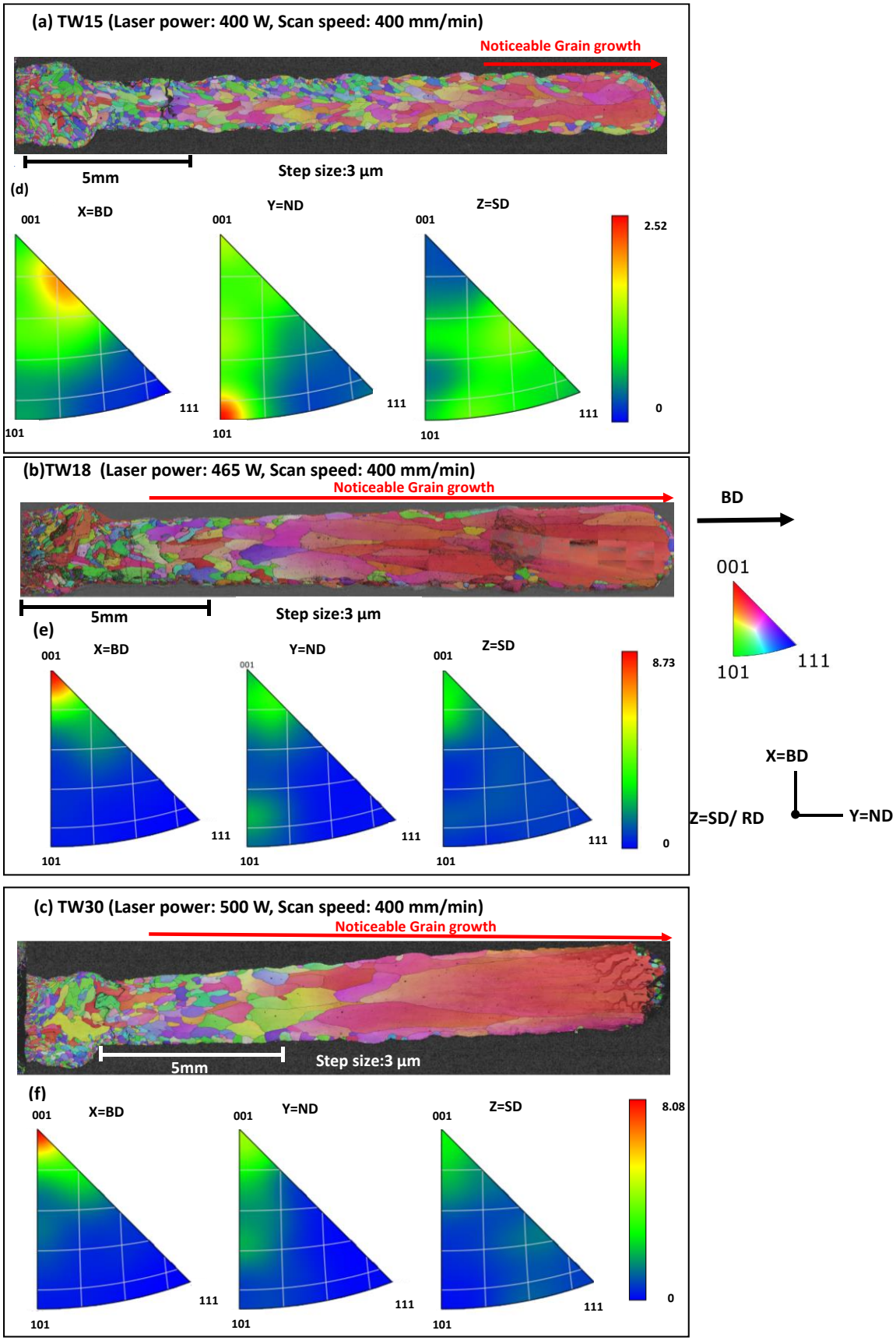

Figure 63. EBSD maps (a, b and c) and IPFs for TW15, TW18 and TW30 in different directions.

6.3 Orientation distribution functions of thin wall

Figure 64 presents the orientation distribution functions (ODFs) for FeSi 6.5 wt% samples TW15 (a), TW18 (b), and TW30 (c) on φ_2 = 0° and 45° sections, providing a detailed analysis of texture evolution during multiple layer deposition using the LMD technique. The ODFs were calculated in Euler space using Bunge's notation with Aztec Crystal software [353], covering an area of 2.3 mm with a step size of 3 µm. All samples show a texture intensity of 10 for comparison. Despite the uniform intensity, significant differences in texture types are observed. Sample TW15, processed at 400 W, exhibits a more diffuse texture with fewer pronounced components. Conversely, TW18, processed at 465 W, and TW30, processed at 500 W, show stronger and more defined cube textures.

In the φ_2 = 0° section, TW18 and TW30 display a transition to a strong cube texture with increasing laser energy from 400 W to 500 W, particularly near the 90° rotated Goss texture components (011)[011] and Goss texture (110) [100]. This transition is beneficial for the magnetic properties of electrical steel, as cube textures improve magnetic performance. The φ_2 = 45° section further illustrates those components close to (113)[121] and Goss (110)[001] in TW18 and TW30 also transition into a strong cube texture (001)[100]. Regarding the evolution of {110} orientations, such as the Goss texture (110)[001], their presence is prominent in TW15 (φ_2 = 45°) and to a lesser extent in TW18 (φ_2 = 45°,(110)[001]) due to smaller melt pools and rapid solidification rates, which restrict extensive recrystallisation or grain reorientation compared to TW30. As laser power increases from 400 W (TW15) to 465 W (TW18) and 500 W (TW30), the {110} orientations diminish gradually, giving way to a dominant cube texture (001)[100]. This shift is driven by enhanced epitaxial growth and steeper thermal gradients at higher energy densities [354], which favour alignment over {110} planes as well as formation of large columnar grains [355]. In TW18 (φ_2 = 0°), traces of {110} persist, including the Goss (011)[100], possibly 90° rotated Goss (011)[011] and indicating partial preservation due to localised solidification conditions and incomplete stress relaxation. The role of internal stresses is pivotal in this texture evolution during LMD, rapid cooling in TW15 generates significant thermal stresses from thermal contraction and phase transformation, locking in {110} orientations by limiting grain boundary mobility. In contrast, for TW18 and TW30, higher energy densities (69.75–75 J/mm^2) reduce cooling rates, expand the HAZ leads to better heat distribution, and facilitate stress relaxation through remelting and recrystallisation, promoting a shift to − dominated textures. Thus, internal stresses act as a competing factor—initially stabilising {110} in TW15 but yielding to as stress relaxation and grain growth dominate at higher powers. Notably, almost all samples lack //BD (γ-fibre) or < 110>// RD (α-fibre) orientations, which are detrimental to the magnetic properties of electrical steel. This absence indicates a favourable texture for magnetic applications. Comparing all samples together, TW18, and TW30 exhibit more pronounced and balanced cube textures, suggesting that higher laser power promotes stronger and more beneficial texture components for magnetic properties. Increasing laser energy density (60 to 75 J/mm^2) in the LMD technique enhances the cube texture of FeSi, improving its magnetic properties. As laser power rises from 400 W to 500 W, the cube texture becomes more defined,

significantly boosting the material's performance, particularly in FeSi 6.5 wt%. This cube texture, ideal for NGOES used in electric motor core laminations, is difficult to achieve with conventional rolling and annealing methods, especially in steels with more than 3.4 wt% Si [112, 356]. However, LMD provides a viable solution to optimise texture and material performance.

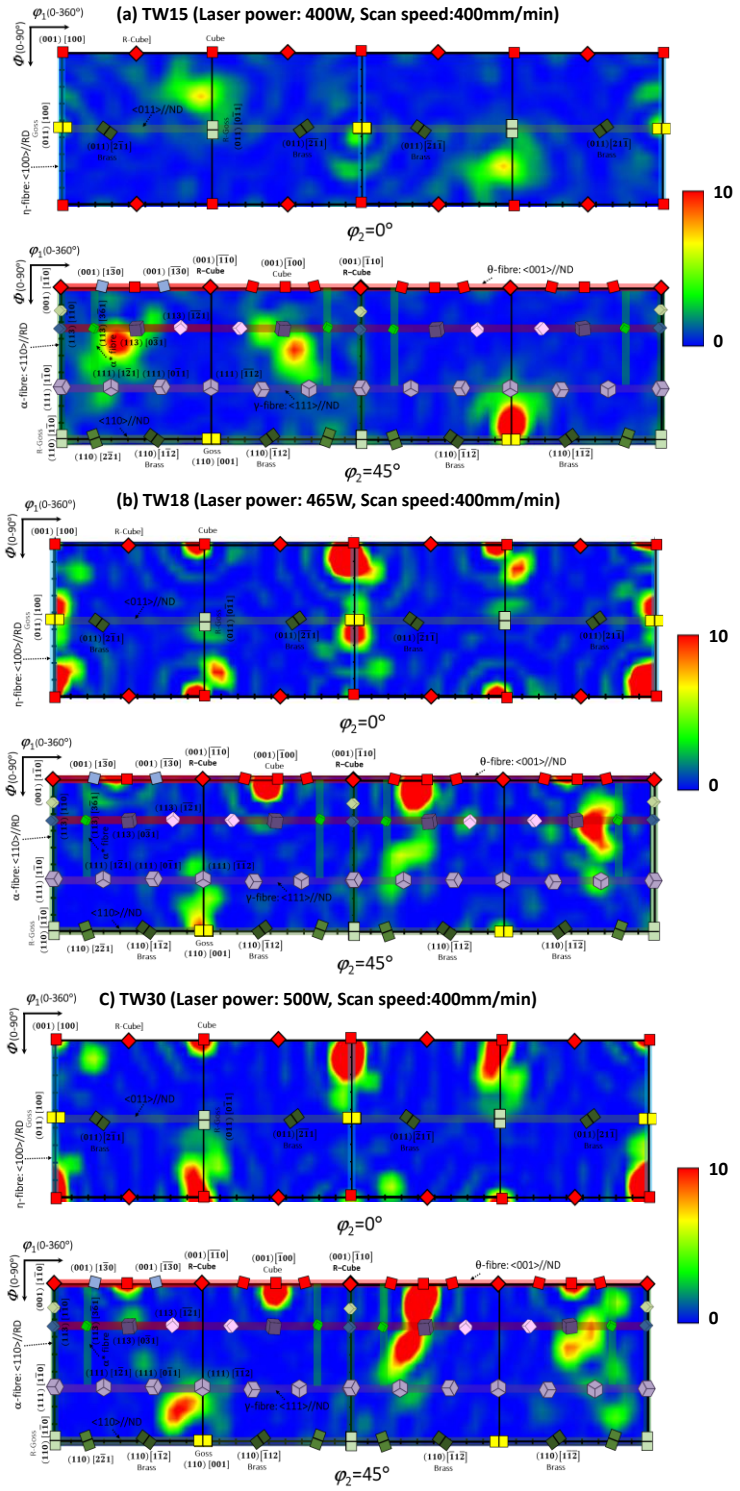

Figure 64. Texture of FeSi shown on φ_2 = 0° and 45° ODF sections for sample TW15 (a) and sample TW18 (b), and TW30 (c).

6.4 Grain structure and crystallographic orientation in top view of thin wall samples

To better understand the effects of laser power on grain development and the evolution of <001> crystallographic orientation, the top side of two samples, TW15 and TW30, was investigated, as can be seen in Figure 65. The EBSD images provide detailed insight into how these processing parameters influence the microstructure of the electrical steel, particularly the grain size and crystallographic texture. The samples, TW15 (processed with 400 W laser power and 400 mm/min scan speed) and TW30 (processed with 500 W laser power and 400 mm/min scan speed), reveal the crystallographic orientation and grain structure, specifically focusing on the <001> orientation.

The most noticeable difference between the two samples is the average equivalent circle diameter of the grains, referred to here as grain size. Sample TW15, processed at lower laser power, exhibits smaller and more uniform grains, with an average diameter of 221.3 µm. In contrast, sample TW30, processed at higher laser power, shows significantly larger grains with an average diameter of 801.7 µm, approximately 3.6 times larger than those in TW15. The increase in grain size with higher laser power is significant, about 262.5%, indicating that the heat input during deposition has a considerable effect on grain growth. Higher laser power results in increased energy input, leading to a longer cooling time and allowing grains more time to grow before solidification. This explains why the grains in TW30 are much larger. Another key observation is the difference in crystallographic orientation, particularly in the centre of the samples. In both samples, the centre tends to exhibit more <001> orientation grains, which is favourable for the magnetic properties of electrical steel. However, TW30 has a much greater proportion of <001> oriented grains compared to TW15. The larger grains in TW30 are more aligned in the <001> direction, especially in the centre of the sample, which can be attributed to the increased laser power. Higher energy promotes directional solidification, favouring the growth of grains along the <001> orientation. In TW15, the lower energy input results in a more random grain structure. Although <001> grains are present, they are smaller and less concentrated in the centre compared to TW30. This type of grain structure, characterised by fewer <001> grains and a higher intensity of <111> grains, is commonly observed in conventional manufacturing processes for electrical steel, such as rolling [357].

The laser's impact on grain size and orientation is also evident in the grain distribution. In TW15, the grain structure appears finer and more uniformly distributed across the sample, while TW30 exhibits larger grains, particularly concentrated in the centre. This can be explained by the heat distribution during laser processing. In the centre of the sample, where heat spread out more slowly, the grains have more time to grow in the preferred <001> direction, resulting in the larger and more oriented grains seen in TW30. The edges, which cool more quickly, do not experience the same grain growth, leading to a more uniform grain structure in TW15 but less pronounced <001> orientation. When comparing the top views of these samples to the cross-sectional views (as was showed in previous Figure 63), it appears that the top view shows a greater number of grains. This is likely because the top view

captures the surface grains in their full elongated form, whereas a cross-sectional view would cut through fewer grain boundaries. The top view, therefore, provides a more comprehensive picture of the grain structure and orientation, and for these samples, it is likely more representative of the overall grain development. In summary, at constant scan speed 400 mm/min, the increase in laser power from 400 W in TW15 to 500 W in TW30 has a significant impact on both grain size and crystallographic orientation. TW30 shows much larger grains, with a substantial concentration of <001> oriented grains in the centre, while TW15, processed at lower power, has smaller grains with less pronounced <001> texture. These differences suggest that higher laser power promotes both grain growth and the development of preferred <001> orientation, which is critical for enhancing the magnetic performance of electrical steel.

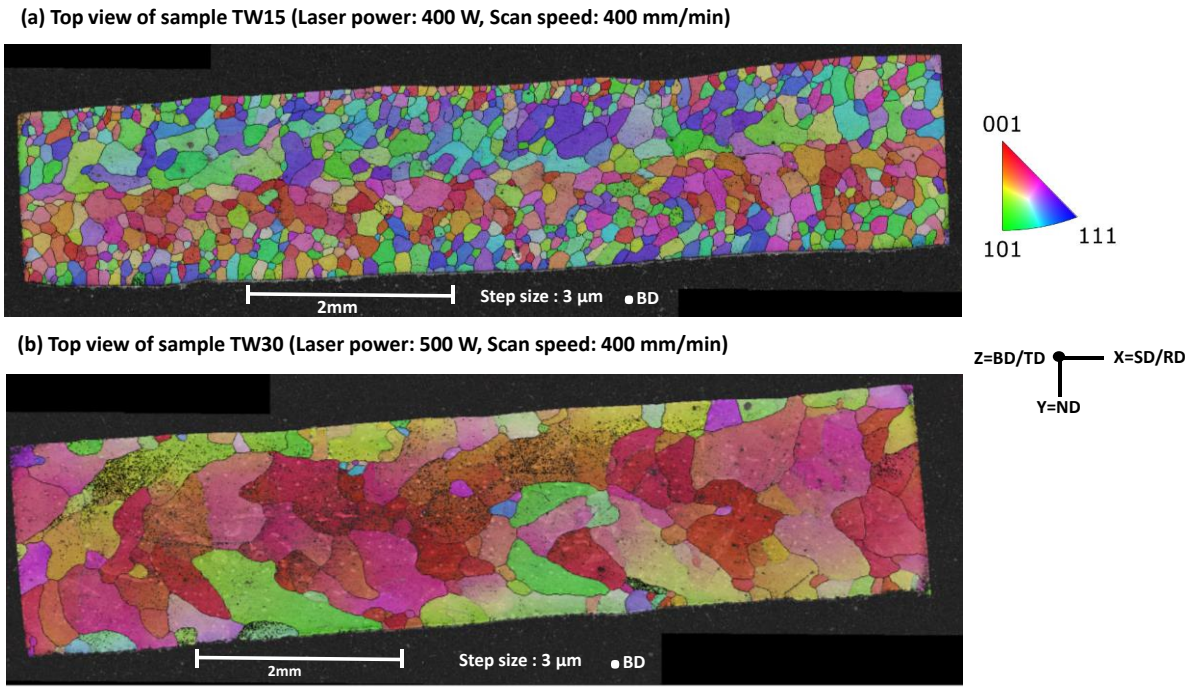

Figure 65. EBSD top view showing smaller grains in TW15 (a) and larger <001> oriented grains in TW30 (b).

6.5 Kernel average misorientation analysis of thin wall FeSi 6.5wt%

Kernel Average Misorientation (KAM) analysis serves as a valuable tool for evaluating the microstructural quality of electrical steels, such as FeSi alloys, by revealing local strain and defect distributions that influence magnetic properties, which are critical for applications like electrical motors and transformers [358, 359]. KAM provides insight into the local lattice distortions within the material, which are typically associated with dislocations and sub grain boundaries. This information is critical because the dislocation density within the material can directly influence its magnetic performance [360]. As was stated before, in electrical steels, magnetic properties such as permeability and coercivity are heavily dependent on the movement of magnetic domain walls .These walls must move freely across the material to

minimise energy losses, specifically hysteresis losses, which are a primary source of inefficiency in electrical applications [214]. However, dislocations act as obstacles to the movement of domain walls. When dislocations are present, they create local stress fields that hinder the domain wall motion, leading to an increase in coercivity and a reduction in the overall magnetic permeability of the material [361]. Overall, it degrades the performance of electrical steel by increasing energy losses during magnetisation and demagnetisation cycles.

The KAM analysis helps in detecting regions of higher dislocation density by measuring the local misorientation between neighbouring grains. It is particularly useful for identifying sub grain boundaries and areas where residual stresses may be concentrated. In electrical steels, it is crucial to maintain, low-dislocation grains to ensure optimal magnetic performance. Sub-grain boundaries, with misorientations typically between 2.5° and 10°, can disrupt magnetic domain movement, causing localised domain wall pinning, and also influence grain growth and abnormal growth of Goss grains. As such, understanding the distribution and magnitude of these sub grain boundaries is essential for improving the magnetic performance of the material [362, 363]. In addition to the effects on domain wall motion, KAM analysis can reveal areas of residual stress in the material [364]. Residual stresses and dislocations can collectively pin magnetic domain walls, hinder their motion and leading to increased energy dissipation. This results in higher core losses, which are particularly detrimental in applications such as transformers and electrical motors, where energy efficiency is critical. By identifying regions with high KAM values, it is possible to locate areas where dislocation density and residual stresses are elevated, thus offering opportunities for process optimisation.

For the KAM calculations in this research, Aztec Crystal software [353] was used, and a first-order neighbour KAM calculation was performed to focus on nearest-neighbour interactions within the microstructure. Grain boundaries with misorientations with minimum angle of 2° and greater than 10° were ignored to concentrate the analysis on sub-grain boundaries and local dislocations, while sub-grain boundaries greater than 2.5° were excluded to maintain the focus on the most relevant regions for magnetic performance. By examining the KAM across different sample geometries, including thin walls, valuable insights can be gained about how local lattice distortions affect the overall performance of electrical steel. The findings of the KAM analysis are critical for optimising the microstructure to reduce dislocation density, minimise residual stresses, and ultimately improve the magnetic properties of the material. This information is especially important for designing high-efficiency electrical steel components such as stator for applications where minimising energy losses is a priority.

As shown in Figure 66, the length of columnar grains in samples TW15 (energy density 60 J/mm²) and TW30 (energy density 75 J/mm²) reflects epitaxial growth influenced by energy density, where new cells nucleate on parent cells during solidification, aligning preferentially in the <001> direction along the BD due to the local thermal gradient in the melt pool [365]. The KAM maps highlight the effect of energy density, with TW15 showing an average KAM of 0.44° and TW30 a lower value of 0.34°, as seen in (b) and (d), indicating that increasing energy

density from 60 to 75 J/mm² reduces local misorientation by promoting uniform grain growth and minimising lattice distortions. This trend is further evidenced by the sub-grain distribution: TW15 contains 11% sub-grains (2°–10°) with 89% high-angle grain boundaries (HAGBs >10°), while TW30 has 25% sub-grains, reflecting how higher energy density fosters more sub-grain formation and reduces overall misorientation. Across other samples, KAM values vary with energy density: TW33 (0.06° at 67.50 J/mm²), TW26 (0.72° at 67.70 J/mm²), TW13 (0.51° at 80.5 J/mm²), TW20 (0.56° at 67.90 J/mm²), TW32 (0.17° at 54.5 J/mm²), TW19 (0.45° at 74 J/mm²), TW27 (0.46° at 61.4 J/mm²), and TW35 (0.20° at 67.5 J/mm²), suggesting that higher energy densities generally correlate with lower KAM, though exceptions like TW26 indicate processing variations. Scanning speed also influences KAM, as increasing from 365 to 440 mm/min (TW19 to TW27) at a constant laser power of 450 W resulted in stable KAM values (~0.45° to 0.46°), while a change in scanning strategy from unidirectional (TW33) to bidirectional (TW35) at 67.5 J/mm² increased KAM from 0.059° to 0.20°, reflecting altered thermal conditions. The presence of low-angle grain boundaries (LAGBs, 2.5°–10°), particularly in smaller grains of TW15 at the foundation layers, supports the lower KAM values, while TW30's coarser columnar grains exhibit fewer LAGBs [366]. These LAGBs enhance the magnetic properties of electrical steel by causing less disruption to magnetic domain walls compared to HAGBs, reducing eddy current losses and improving magnetic domain alignment for better performance [260]. Noise from poor preparation and solvent marks, noted in Figure 64 (a) and (c), was minimised through recalculation to ensure accurate KAM values. For a deeper understanding of energy density effects on dislocation density, further analysis using transmission electron microscopy is recommended.

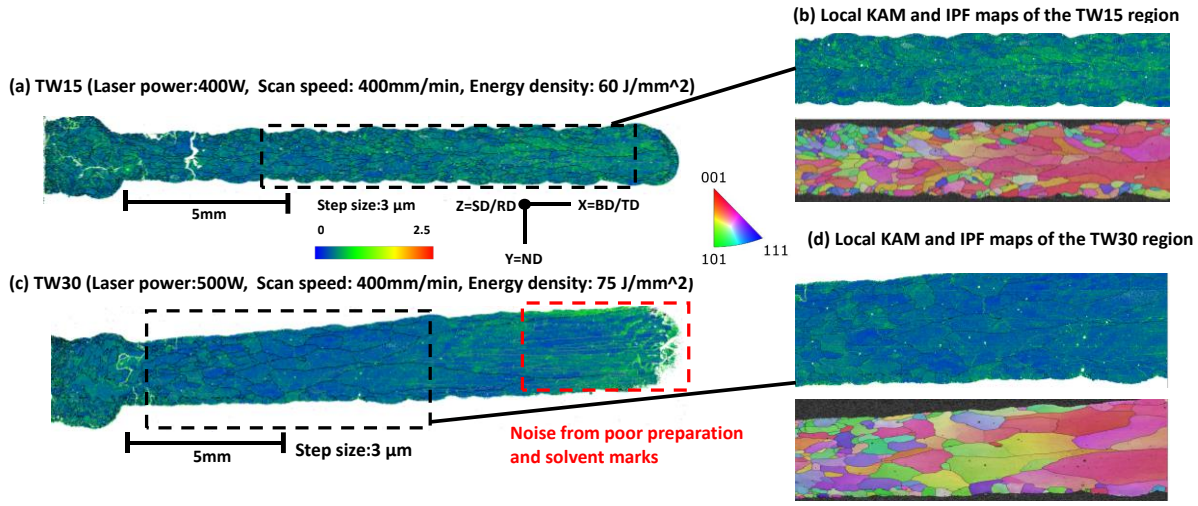

Figure 66. Overview of microstructures of as-built samples in the BD: KAM map (a), (c), and (b), (d) enlarged view of KAM maps and IPF maps of each sample TW15 and TW30.

6.6 Effect of laser energy density on texture evolution of thin wall

MTEX is a free MATLAB™ toolbox for analysing and modelling crystallographic texture using pole figure and EBSD data. It offers functions for data import, visualisation, texture computation, and simulation. The provided graphs Figure 67 (a) to (c) illustrate the

relationship between energy density and the area fraction of different fibre orientations in thin walls, determined through MTEX measurements along the BD direction (sdv: ±0.10%) [367]. The graphs depict the area fractions of fibres oriented along <100>, <101>, and <111> directions relative to the BD. For fibres oriented along <100> // BD, which provide better magnetic properties due to their easy magnetisation, the area fraction increases slightly with increasing energy density. The data show a positive correlation, suggesting that higher energy densities lead to a greater proportion of fibres in the <100> orientation. This could be due to the thermal conditions and solidification rates that favour the formation of <100> fibres at higher energy inputs. In contrast, the fibres oriented along <101> // BD, which have medium magnetisation properties, exhibit a relatively stable area fraction across the range of energy densities. The data show that energy density has a minimal effect on the formation of <101> fibres. This stability suggests that the <101> orientation is less sensitive to changes in energy density compared to <100> and <111> fibres. Lastly, for fibres oriented along <111> // BD, known for their hard magnetisation properties, the area fraction decreases as the energy density increases. The negative correlation indicates that higher energy densities result in fewer <111> fibres compared to <100>//BD. This reduction could be attributed to the specific crystallographic growth conditions that become less favourable for <111> fibres at higher energy inputs. In summary, increasing energy density in the LMD process tends to promote the formation of <100> fibres while reducing the formation of <111> fibres, with <101> fibres remaining largely unaffected. These observations highlight the critical influence of energy density on fibre orientation, which in turn affects the magnetic properties of the manufactured thin walls. This understanding can be helping to optimise the LMD process for desired magnetic characteristics by carefully controlling the energy density applied during manufacturing.

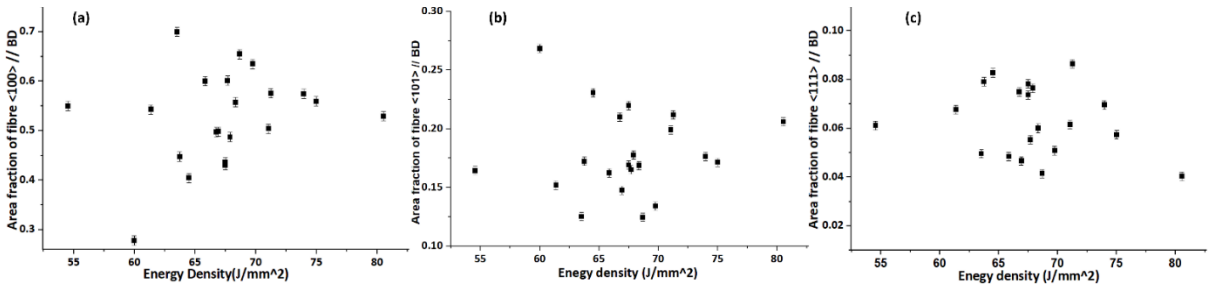

Figure 67. Effect of energy density on fibre orientation in LMD thin walls samples in <100>//BD, <101>//BD, <111>//BD direction.

The bar chart in Figure 68 presents the area fractions of different fibre orientations (common fibres in the rolling process) in electrical steel samples manufactured using LMD across various energy densities (sdv: ±0.10%). The fibres include cube orientation, and Goss orientation, each displaying unique behaviours influenced by energy density. Figure 68 (a) shows that the area fraction of Goss orientation remains relatively stable and randomly scattered as energy density increases, indicating no strong linear correlation. Interestingly, the Goss orientation appears more prominent in LMD samples compared to conventional methods [112], possibly due to specific thermal cycles during the process that do not favour its formation. Notably,

the highest Goss fractions are observed at lower energy densities, suggesting that lower energy inputs may be more favourable to developing this orientation. This implies that factors beyond energy density, such as cooling rates and thermal gradients, are likely to be more influential in determining the microstructure. In Figure 68 (b) the area fraction of cube orientation increases with energy density, showing significant peaks at higher densities. Cube orientation peaks around energy densities of 60, 64, 66, 70, and 74 J/mm², indicating that the thermal cycles and energy inputs in LMD facilitate the alignment of grains in this orientation. The high area fraction of cube orientation is beneficial for magnetic properties and highlights the advantage of LMD in promoting desirable textures that are difficult to achieve through conventional methods [214, 368, 369].

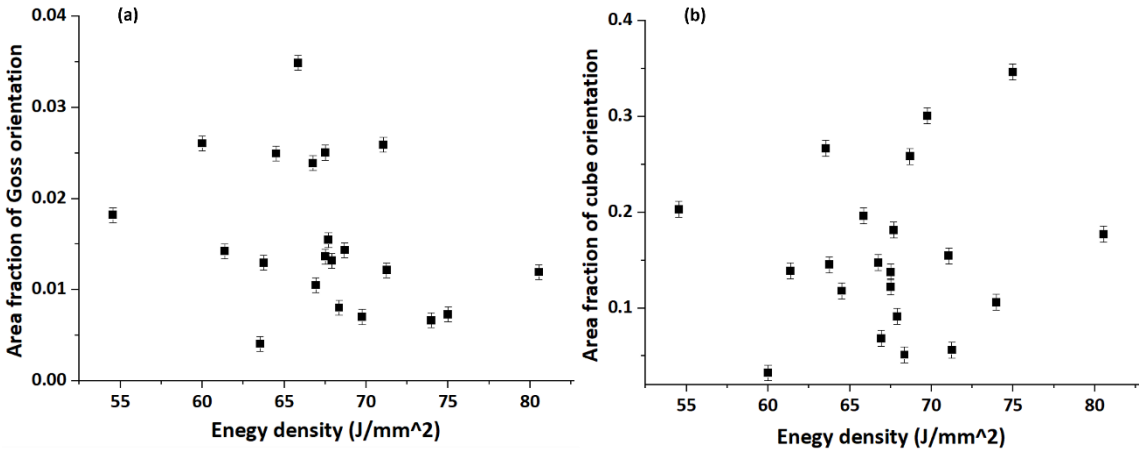

Figure 68. The impact of energy density on fibre formation in electrical steel based on the BD for cubes and Goss orientation.

6.7 Effect of laser energy density on grain size evolution of thin wall

The effect of the laser energy density on surface morphology, microstructural evolution of FeSi 6.5% was investigated. The LMD FeSi 6.5wt% parts were subjected to a series of advanced materials characterisation techniques such as EBSD. To obtain representative values for overall grain sizes, the weighted average equivalent circle diameter was used to measure the average grain size (sdv: ±0.25%). The results indicate that increasing the energy density from 54.5 to 80.5 J/mm² led to a significant increase in the weighted average equivalent circle diameter, rising by approximately 260% (from 500 µm to over 1800 µm), as shown in Figure 69 (linear fit: $R^2 = 0.3157$). This trend was observed across 20 samples printed with different processing parameters, where higher laser power, which directly increases laser energy density, consistently led to larger grain sizes. Similar findings [323] have been reported, highlighting the correlation between energy density and microstructural changes, a relationship driven by laser power's influence on energy input per unit area. Other studies reinforce this link, noting that elevated energy density promotes grain growth, while recent research [370] indicates that grain size evolution is critical for balancing the magnetic and

mechanical properties of electrical steel, emphasising grain structure's role in optimising material performance.

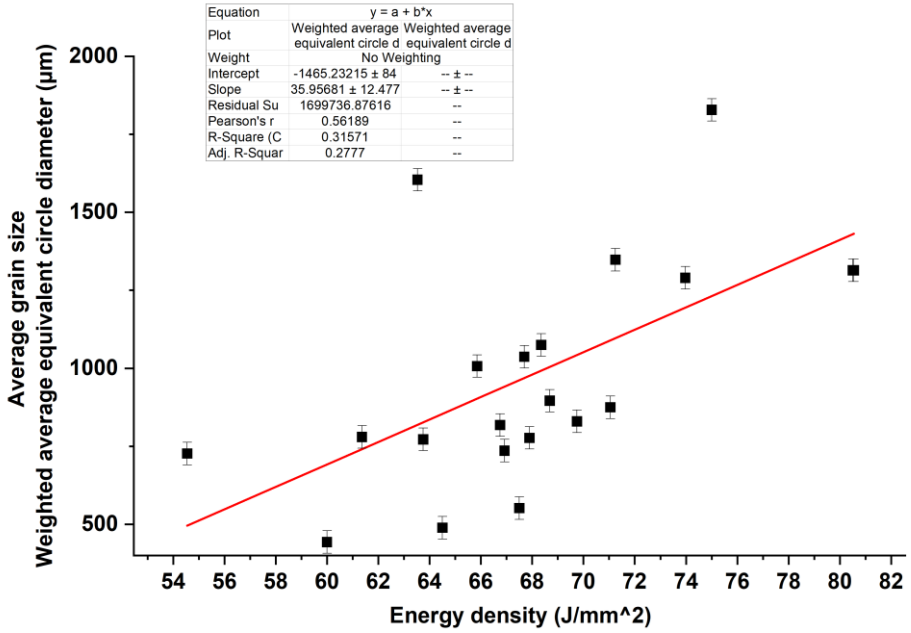

Figure 69. Effect of the laser energy density on grain growth in thin wall samples.

Several factors contribute to the increase in grain size, especially in the LMD process. One such factor is the high thermal gradient experienced by the metal during rapid heating and cooling, affecting grain nucleation and growth. This phenomenon results in larger grain sizes, particularly in areas where heat accumulates, as noted in the BD [346]. Adjusting the thermal gradient during the manufacturing process, as suggested in [371], can alter the texture, while increasing laser energy density can lead to intensify texture. Additionally, the solidification rate plays a crucial role in influencing grain size. For instance, altering the local solidification conditions by adjusting the building orientation can influence the morphology of grains, leading them to become either equiaxed (smaller) or columnar (larger). In simpler terms, changing the solidification process can modify the appearance of grains, a characteristic closely tied to the undercooling conditions. Undercooling, in turn, depends on the thermal gradient (G) and the rate of solidification interface movement between solid and liquid (R). Consequently, a low (G/R) ratio results in increased undercooling, which is advantageous for forming equiaxed solidification morphology [345]. Moreover, as the solidification rate decreases, there is more time for atoms to migrate and form larger grains, resulting in coarser and larger grain sizes [372]. In this scenario, a high thermal gradient and rapid solidification have led to the formation of columnar grains along the BD, aligned with the heat flow. Consequently, the combination of these factors not only promotes the elongation of grains but also contributes to an increase in grain size. Residual stress induced during the LMD process also impacts the microstructure [373]. In regions with higher residual stress, preferential grain growth may occur, leading to larger grain sizes.

However, contrasting results were reported by [374] where the small grains formed when there is low residual stress existing. Additionally, process parameters like laser energy density can influence the thermal profile and cooling rate, consequently affecting the formation of columnar grains on the side and top planes. This can also lead to an increased depth of the molten pool and a transition from a crystallographic fibre texture to a cube texture [5, 184]. Thus, laser energy density plays a crucial role in the microstructural evolution, particularly in grain growth during the LMD processes. For example, as can be seen Figure 70 (a), (b) and (c) provided bar charts compare three samples, TW15, TW18 and TW30, in terms of grain size distribution and the effects of different laser power settings used in their preparation. Sample TW15, prepared with a laser power of 400 W and a scan speed of 400 mm/min, illustrates a grain size distribution predominantly within the 0 to 2000 µm range. Specifically, approximately 71 % (area weighted fraction) of the grains fall within the 0 to 500 µm range, 22 % between 500 and 1000 µm, and 7 % between 1000 and 2000 µm. This indicates a narrow grain size distribution with negligible grains beyond 2000 µm. In contrast, sample TW18, prepared with a higher laser power of 465 W but the same scan speed of 400 mm/min, exhibits a broader and more varied grain size distribution. In TW18, about 26 % of the grains are within the 0 to 500 µm range, 14 % between 500 and 1000 µm, 17 % between 1000 and 2000 µm, and a significant 43 % at the 5000 µm mark. This indicates the presence of much larger grains in TW2 compared to TW15. Sample TW30, prepared with a laser power of 500 W and a scan speed of 400 mm/min, exhibits a grain size distribution that is more spread out compared to TW15. Notably, the majority of grains are concentrated in two distinct size ranges: 0 to 2000 µm and a significant peak around 4000 µm. Specifically, the data shows that approximately 33 % of the grains are around 4000 µm, indicating a substantial presence of larger grains, while the remainder is mostly within the 0 to 2000 µm range 67 %. This broader distribution, particularly the increase in larger grain sizes, can be attributed to the higher laser power used in TW30, which likely led to slower cooling rates and more extensive grain growth during solidification. This indicates the presence of much larger grains in TW18, TW30 compared to TW15. The comparison highlights that the increase in laser power from 400 W in TW15 to 500 W in TW30 results in a substantial shift in grain size distribution. For example, TW18 shows a reduction in the fraction of smaller grains (0 to 500 µm) from 71 % to 26 %, a decrease of approximately 63.4 %, and an increase in the proportion of larger grains (5000 µm) to 43 %, compared to none in TW15. In other words, by increasing the energy density, the grain size increased by 177.78 %. This notable grain growth is also apparent in Figure 63.

These findings demonstrate that higher laser power promotes larger grain growth, resulting in a broader and coarser grain size distribution in sample TW18. This is primarily attributed to the increased heat input from the 465 W laser power in TW18, which deepens the molten pool, slows the solidification rate, and extends the time available for grain coalescence and epitaxial growth. Consequently, TW18 exhibits a significant fraction of larger grains compared to TW15. In contrast, TW30, processed at 500 W, shows an even broader grain size distribution, yet the more pronounced thermal impact at 465 W in TW18 suggests an optimal heat distribution at this power level. This mechanism aligns with studies on laser power

effects in additive manufacturing, which indicate that higher energy inputs enhance grain growth by reducing cooling rates and stabilising thermal gradients [375]. These microstructural changes are likely to influence the material's mechanical strength and magnetic properties, warranting further detailed investigation.

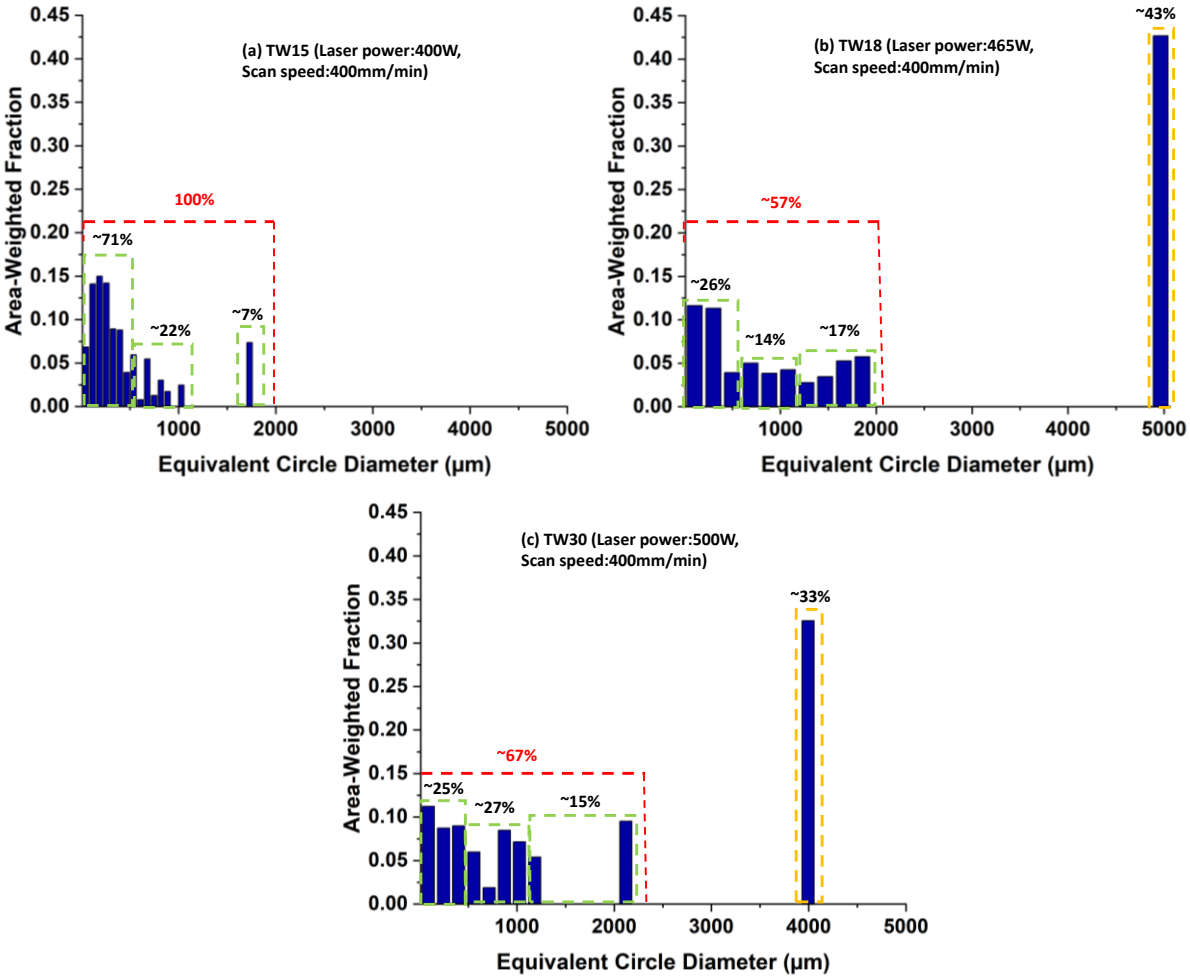

Figure 70. Grain development based on area weighted fraction of different samples (a) TW15, (b) TW18 and (c) TW30.

6.8 Effect of scanning speed on grain development

The effect of the scanning speed on microstructural evolution of FeSi 6.5% was investigated. The scatter graph Figure 71, illustrates the relationship between scan speed (measured in mm/min) and grain size (represented by the weighted average equivalent circle diameter (μm) (sdv: ±0.15%). As the scan speed increases from 360 mm/min to 400 mm/min, there is a noticeable decrease in grain size. Specifically, at a scan speed of 360 mm/min, the grain size is approximately 1290 μm. When the scan speed increases to 380 mm/min, the grain size drops to around 875 μm, representing a reduction of about 32.2%. Further increasing the scan speed to 400 mm/min results in the grain size decreasing to approximately 552 μm, which is

a significant reduction of 57.2% from the initial size at 360 mm/min. However, beyond 400 mm/min, the relationship between scan speed and grain size becomes more complex. For instance, at 425 mm/min, the grain size increases to approximately 1025 µm, indicating an 85.5% increase from the 400 mm/min measurement. At 440 mm/min, the grain size further fluctuates, reaching around 780 µm, which is a 23.9% decrease from 425 mm/min but still higher than the grain size at 400 mm/min. These fluctuations suggest that at higher scan speeds, the relationship between scan speed and grain size is not straightforward. Rapid thermal cycles and other dynamic factors at these higher speeds may cause inconsistent grain sizes. Overall, while there is an initial inverse relationship between scan speed and grain size, with a clear reduction in size up to 400 mm/min, the relationship becomes less predictable at higher speeds. Additionally, a similar trend was observed [376] with increasing laser scanning speed, which can reduce grain size. This occurs because higher scanning speeds decrease the amount of powder melted and lower the energy density of the laser. As a result, there is less interaction time between the laser and the powder, leading to a smaller melt pool, which in turn results in a finer grain structure.

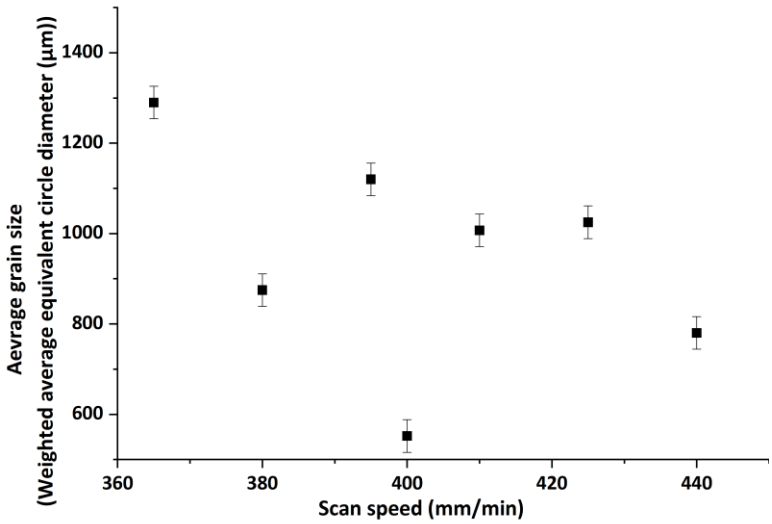

Figure 71. Effect of the scanning speed on grain growth in thin walls.

6.9 Impact of scanning speed on microstructure features

The EBSD images in Figure 72 reveal distinct differences in grain development and morphology between samples TW19 and TW27, manufactured by LMD with varying scanning speeds while maintaining constant laser power (450 W). Sample TW19 has a weighted average equivalent circle diameter of 1290 µm, while TW27's is 780 µm, representing a decrease in grain size by approximately 40%. The larger grains in TW19 indicate more time for growth, resulting in elongated grains typical of directional solidification in LMD processes. In contrast, sample TW27's smaller, thinner grains suggest a higher nucleation rate and less time for growth, leading to smaller, narrower pancake shape grains. At higher scanning speeds, as in TW27, the laser moves quickly, resulting in a faster cooling rate and less time for interaction with the FeSi 6.5% material, producing finer grains [344]. Moreover, the increased

scanning speed and cooling rate drive a transition from columnar to equiaxed grain structures, causing grain breakdown [296]. However, despite the higher scanning speed in TW27, some columnar grains remain due to the directional heat flow within the melt pool and the thermal gradient in the BD, induced by the high laser power. This directional heat flow promotes the growth of columnar grains alongside finer equiaxed grains shapes [377]. An important observation is that TW19 shows cracks along the cross-section, while TW27 does not. Perhaps, the presence of cracks in TW19 can be attributed to the larger grain size and the resulting internal stresses during solidification. Larger, elongated grains can induce higher residual stresses, leading to solidification cracking due to thermal contraction of the alloy during the final stage of solidification, when the material transitions from a semi-solid to a fully solid state and easy for cracks to propagate in area with less grain boundaries. In contrast, TW27's finer grains, resulting from rapid cooling and higher nucleation rates, distribute stresses more evenly, reducing the likelihood of crack formation [378]. The higher scanning speed in TW27 (440 mm/min) leads to rapid cooling and solidification, producing smaller, more numerous, and less defined grain boundaries. Conversely, the lower scanning speed in TW19 (365 mm/min) allows for larger and more elongated grains with pronounced boundaries due to higher energy density (73.97 J/mm^2) compared to TW27 (61.4 J/mm^2) which results in a larger melt pool aligned with the heat flow direction (BD). These observations suggest that the 40% reduction in grain size, caused by higher scanning speeds, leads to the formation of smaller, pancake-shaped grains in some areas. Although grain refinement generally improves both strength and ductility, in this case, the rapid cooling and high energy input induce local residual stresses and brittleness, which can reduce ductility despite the finer grain size [379]. The thermal history of the melt pool significantly influences microstructure development. Variations in the cooling rate can result in either coarser or finer grains, thereby impacting mechanical properties like, tensile strength [380]. Moreover, the absence of cracks in TW27 further highlights the benefits of smaller, and thinner grains in mitigating internal stresses. This information is critical for understanding and optimising the mechanical and magnetic properties of the materials based on their grain structure.

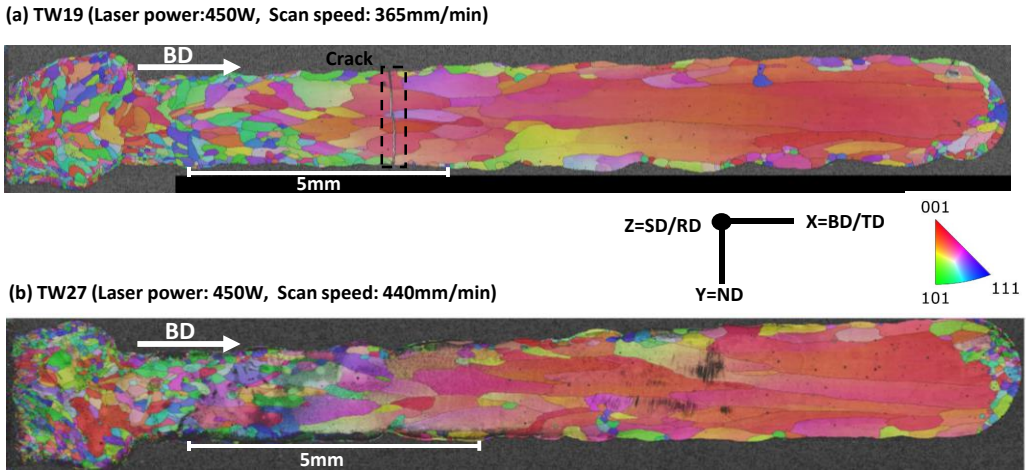

Figure 72. EBSD maps (a and b) for TW19 (a) and TW27 (b) illustrated the grain development.

The ODF maps in Figure 73 reveal that by increasing the scanning speed to 440 mm/min, the Goss orientation area fraction increases by 110% (from 0.0067 to 0.014), and the {011}<211> Brass texture decreases in φ_2 = 0° and 45° ODF. Both TW19 and TW27 show almost the same texture, by increasing the scanning speed from 365 to 440 mm/min at a constant laser power of 450 W. This contrasts with the effects of laser power at a constant scanning speed, which were covered in previous sections. Furthermore, both TW19 (E= 73.97 J/mm^2) and TW27 (E= 61.4 J/mm^2) exhibit strong preferred orientations in the <001> orientation, with PF map intensity values of 11.24 and 11.68, as well as with the 0.58 and 0.54 area fraction of fibre <100> //BD, respectively. This slight difference indicates that while scanning speed affects grain size and morphology, the overall strength of the <001> texture remains robust. These observations confirm that the LMD process consistently produces a strong <001> texture in both samples, highlighting the uniformity of grain orientation despite variations in processing parameters.

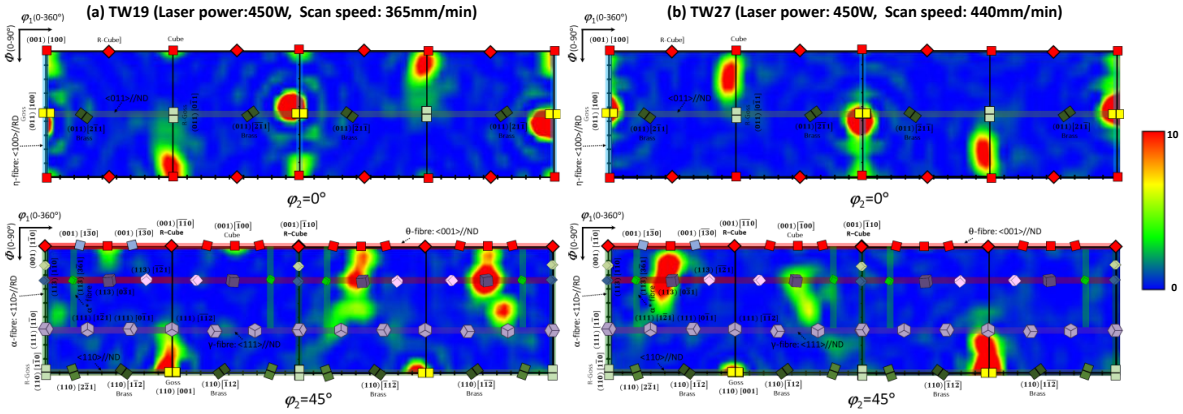

Figure 73. φ_2 = 0° and 45°ODF maps of the FeSi 6.5wt% for different samples TW19 (a) and TW27 (b).

6.10 Effect of scanning strategy on grain development

In this study, thin-wall components were produced using LMD. This process involved moving a laser beam source layer by layer to melt the powder feed material onto a substrate. As illustrated by [381] optimising the performance of manufactured samples heavily depends on the design of scanning paths, as they impact the thermal history of each layer. Samples such as TW33 and TW35 were printed with a same process parameters of scan speed of 400 mm/min and laser power of 450 W but, different scanning strategies such as unidirectional and bidirectional respectively, as shown in the cross section of these samples in Figure 74. This study shows how different scanning strategies such as unidirectional and bidirectional significantly influence the microstructure of manufactured samples, even when the laser power and scan speed remain constant. The unidirectional scanning strategy (TW33), characterised by the laser beam moving in a single direction for each layer, creates a uniform thermal gradient and steady cooling rates which can have an impact on the shape of the melt pool [380, 382]. This results in a decrease in the grain sizes, with a weighted average equivalent circle diameter of 550 µm. Also, the unidirectional heat flow during solidification promotes elongated grains with a uniform <001> crystallographic orientation, aligning with

the preferred crystal direction [383]. In contrast, the bidirectional scanning strategy (TW35) involves the laser alternating direction with each layer. As a result, the next scan vector begins in a region with a higher temperature, since the previous scan ends nearby. This introduces complex thermal histories and varying cooling rates compared to the unidirectional scan. This leads to larger grains compared to TW33, with a weighted average equivalent circle diameter of 624 µm, representing a 13 % increase in grain size over the unidirectional scanning. This value suggests a statistically significant change in grain size. The alternating heat input disrupts the solidification front, resulting in grains with varied orientations and a less uniform microstructure which can have an impact on residual stress [384]. These differences might happen because the consistent heat flow in unidirectional scanning promotes controlled grain growth and alignment, while the variable heat flow in bidirectional scanning causes fluctuations in the solidification process, leading to diverse grain sizes and orientations. Understanding these effects is crucial for optimising the mechanical and magnetic performance of deposited parts through careful selection of scanning strategies [383].

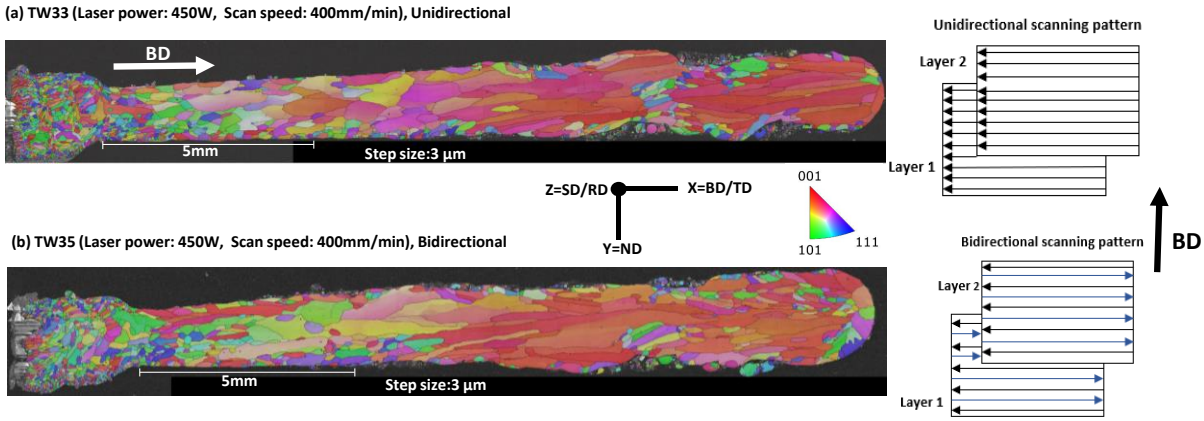

Figure 74. EBSD maps of (a) TW33 unidirectional, (b) TW35 bidirectional, which fabricated under the same process parameters.

The analysis of ODF images in Figure 75 for samples TW33 and TW35, manufactured using unidirectional and bidirectional scanning strategies respectively, demonstrates significant differences in texture. In φ_2 = 0°, TW33 exhibits a pronounced cube texture {001} <100> and near rotated Goss texture {011} <011>. In contrast, TW35 shows a higher intensity, featuring a more pronounced near cube texture and near Goss texture as well as low Brass component {110} <112>. In φ_2= 45°, TW33 maintains a more pronounced near rotated cube texture {001} <110> and visible rotated Goss texture and less γ fibre {111}, whereas TW35 continues to exhibit a more pronounced near the Brass component and less pronounced near rotated cube texture, with the rotated Goss texture becoming less visible as well as less γ fibre {111}.

As previously mentioned, these variations happen due to the different thermal histories induced by the scanning strategies. Unidirectional scanning (TW33) promotes a consistent thermal gradient, resulting in a steady solidification front that favours the growth of stable textures like the cube texture and near rotated cube texture [385]. This consistent thermal environment aligns with the formation of finer, thinner, smaller grain sizes. Conversely,

bidirectional scanning (TW35) introduces variable thermal gradients and fluctuating solidification fronts. These conditions enhance the development of different textures due to the changes in thermal conditions. The increased overall larger grain sizes (a 13 % increase compared to TW33), highlight the impact of the bidirectional strategy in promoting more pronounced textures due to higher energy input and complex thermal profiles. Recognising these effects is vital for refining the microstructure and mechanical properties of fabricated parts by precisely managing the scanning strategies. Based on the analysis, TW35 it might be better for magnetic properties. TW35, manufactured using the bidirectional scanning strategy, has a slightly higher cube orientation area fraction//BD (0.44), high Goss texture area fraction (0.025) //RD, and lower γ fibre// BD (0.074, decreased by 6% compared to TW33) and less Brass component fractions compared to TW33. The cube texture {001} <100> is beneficial for magnetic properties, promoting higher permeability and lower core losses. In contrast, TW33, made with the unidirectional scanning strategy, shows more pronounced γ fibre {111}//BD (0.078) and more Brass components, which are less favourable for magnetic properties. Therefore, TW35 would likely exhibit better magnetic properties than TW33.

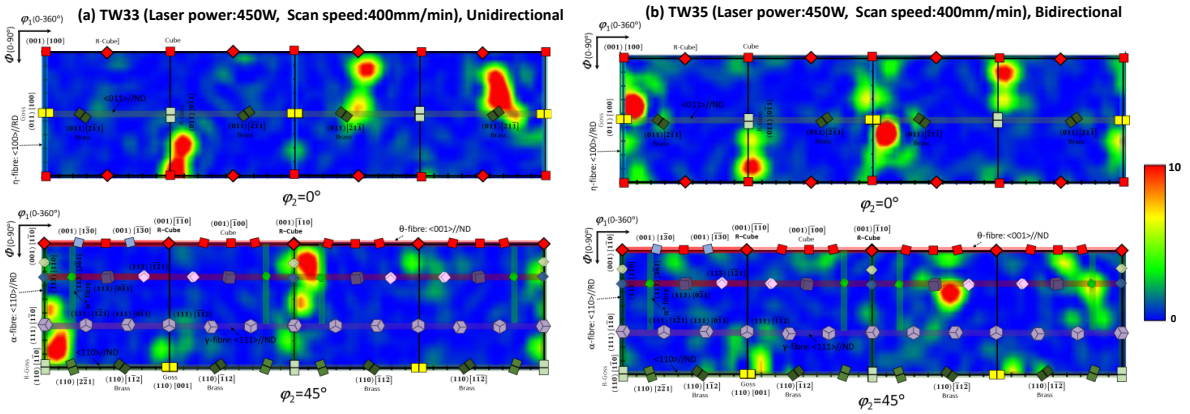

Figure 75. ODF analysis: texture and grain orientation in TW33 (unidirectional) vs TW35 (bidirectional).

To understand the impact of scanning strategy on grain structure and texture, EBSD, IPF, and PF maps of TW33S (surface area) and TW35S (surface area) samples, processed with identical parameters (450 W laser power, 400 mm/min scan speed), were analysed. The TW33S sample, fabricated using a unidirectional scanning strategy, exhibits smaller, thinner grains (weighted average equivalent circle diameter of 750 µm) that tilt toward the heat source, reflecting an irregular texture in the IPF map. This might arises from a unidirectional heat flow creating an uneven thermal gradient, which disrupts the solidification front and promotes misoriented grains. In contrast, the TW35S sample, processed with a bidirectional scanning strategy, displays larger, thicker grains (weighted average diameter of 1100 µm, a 47.25% increase) elongated along the BD. The pole figures (PFs) in Figure 76 clearly illustrate the texture differences: TW33S shows a weak <001> texture with more scattered intensity (maximum ~4), indicating greater misorientation, while TW35S exhibits a stronger <001> texture with concentrated peaks (maximum ~5) aligned along the BD. The angle between the

primary peaks in TW35S's PF is approximately 20^0 degrees, highlighting the improved alignment due to the bidirectional strategy's alternating heat flow, which balances thermal gradients and fosters a more uniform solidification front. These differences reduce from the bidirectional strategy's alternating heat flow, which balances thermal gradients and fosters a more uniform solidification front. Thus, despite identical processing parameters, the scanning strategy significantly influences thermal history, grain morphology, and crystallographic texture. A key factor contributing to the superior grain structure and orientation in TW35S is the heat flow associated with the bidirectional scanning strategy. In bidirectional scanning, the heat flow during deposition is more uniform and balanced, as the laser scans back and forth across the surface. This balanced heat flow allows for more consistent thermal gradients and cooling rates, which minimises the grain tilting that occurs in unidirectional scanning and grain growth in BD direction. As a result, the grains in TW35S grow more uniformly, and their alignment in the BD is significantly improved. This reduction in grain tilt means that fewer grains are misaligned, allowing more to adopt the favourable <001> orientation in the BD direction [383]. In contrast, the unidirectional scanning strategy used in TW33S creates an uneven heat distribution, with a more localised temperature gradient, leading to the thinner, tilted grains observed in the EBSD map. The uniform heat distribution in bidirectional scanning also has additional benefits beyond improving grain orientation. The more consistent cooling rates help in achieving larger grains, as evidenced by the larger grain size in TW35S compared to TW33S. In some application larger grains are beneficial in magnetic materials because they reduce the number of grain boundaries, which act as barriers to magnetic domain movement. Fewer grain boundaries lead to lower eddy current losses and enhanced magnetic performance, especially in high-frequency applications where grain boundary effects are more pronounced. In summary, the bidirectional scanning strategy employed for TW35 not only increases grain size and improves crystallographic alignment but also corrects the tilted grain structure seen in TW33 by ensuring more uniform heat flow during deposition. The bidirectional heat flow leads to fewer misaligned grains, promoting the desirable <001> orientation in the building direction, which is critical for improving the magnetic properties of FeSi alloys. This results in better magnetic permeability, reduced core losses, and overall enhanced performance of the material. Conversely, the unidirectional scanning strategy in TW33 produces thinner, tilted grains with a more scattered crystallographic texture, making it less ideal for optimising the material's magnetic properties.

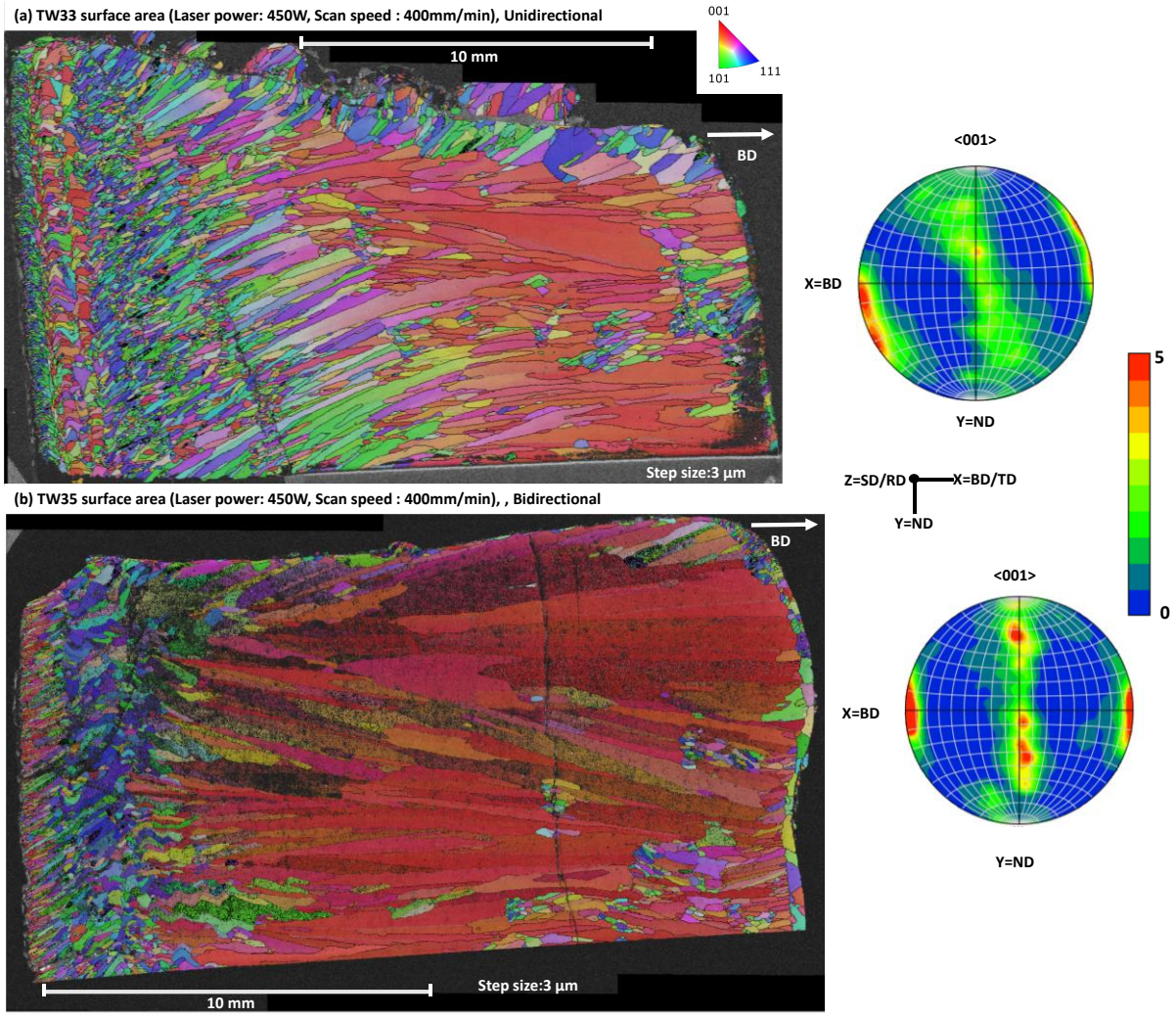

Figure 76. EBSD maps BD//IPF of TW33 and TW35 from surface area of TW33S unidirectional (a), TW35S bidirectional (b) as well as PF map.

6.11 Effect of scanning strategy on fibre formations of thin walls

The comparison of TW33S (unidirectional) and TW35S (bidirectional) surfaces shows clear differences in fibre formations and crystallographic orientations that directly affect the magnetic performance of FeSi 6.5 wt%. Both samples were processed under the same conditions, but the scanning strategies had a significant impact on the microstructure and resulting magnetic properties. The bar chart data Figure 77 reveal that the bidirectional scanning strategy used in TW35S leads to more desirable fibre formations and reduced detrimental ones compared to the unidirectional scanning strategy used in TW33S. Figure 77 (a), shows the area fraction of <100> fibres in the BD, which aligns with the easy magnetisation axis, enhancing magnetic properties. This fraction increased by 82% in TW35S compared to TW33S. Similarly, the fraction of theta fibres (<001>//ND), another orientation that improves magnetic performance by reducing energy losses, showed a 52% increase in TW35S. The cube orientation, important for lowering magnetic losses, increased by 65%, and the Goss orientation, which enhances magnetic properties, had a particularly large increase of 155% in TW35S compared to TW33S. These changes highlight the effectiveness of the

bidirectional scanning strategy in promoting favourable crystallographic orientations. On the other hand, in Figure 77 (b) undesirable fibres that negatively impact magnetic performance, such as <111> fibres, decreased by 48% in TW35S. Gamma fibres (<111>), which are also unfavourable, saw a 61% reduction, and alpha fibres (<110>) decreased by 54%. These reductions indicate that the bidirectional scanning strategy not only develop preferable fibres for magnetic applications but also suppresses the growth of those that degrade the material's magnetic properties. The fibre orientation with a high area fraction observed in this study is significantly greater than that reported in previous research on electrical steel manufactured using conventional processes like rolling [153, 156, 386]. In summary the bidirectional scanning strategy used in TW35 produces a microstructure with thicker, more elongated grains in the BD, more aligned with preferable texture of <001> orientations. This leads to improved magnetic performance by promoting favourable fibre formations while significantly reducing detrimental ones. The differences in fibre formation, supported by the bar chart data, clearly demonstrate that the bidirectional strategy is superior for optimising the microstructure of FeSi 6.5 wt% for magnetic applications.

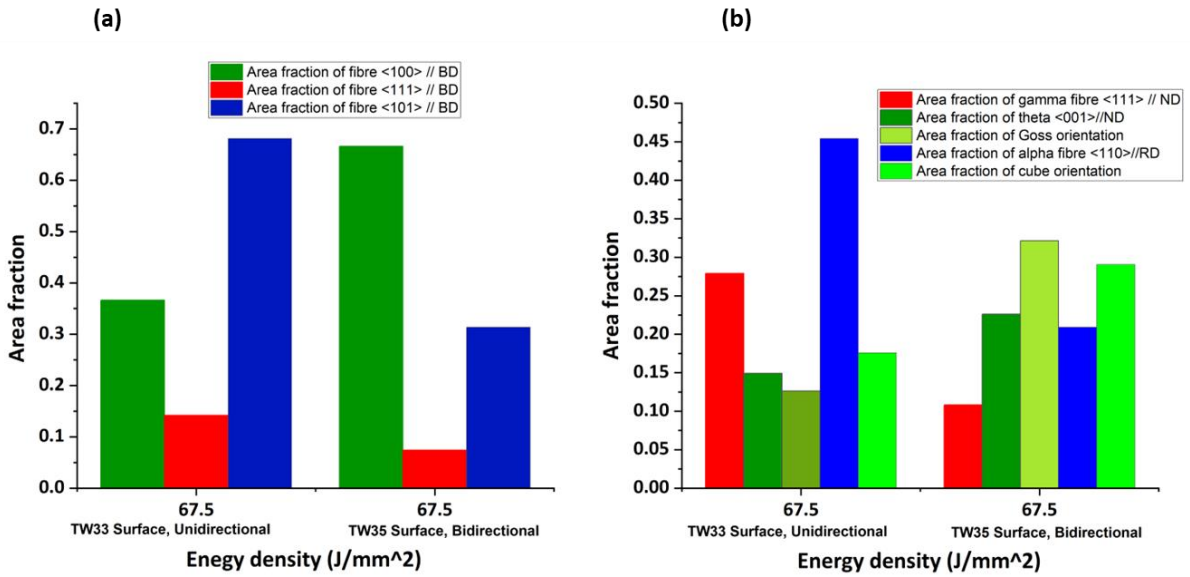

Figure 77. Effect of scanning strategy on fibre orientation in additive-manufactured thin walls in the BD direction.

6.12 Multi-material deposition

Most mechanical components are typically made from a single material which is due to manufacturing changes to fabric multi-material components. However, with LMD, it is possible to vary the composition of the deposited material simply by changing the metal powder. A recent study [387] has shown that different materials, such as 316L stainless steel and low carbon steel, can be manufactured for high-performance tools using direct laser deposition. In addition, it was shown that depositing 316L stainless steel for the initial layers can mitigate crack formation [388]. Therefore, in the current research work, to mitigate cracking in electrical steels during the printing process, using 316L austenitic steel as a foundation layer while depositing FeSi with 6.5 wt% silicon has proven effective. Previous

attempts to directly deposit FeSi on substrates of mild steel encountered significant issues, including delamination and cracking, which made the process unfeasible for larger-scale applications. By introducing a three-layer foundation of 316L, deposited with optimised parameters (600 W laser power, 380 mm/min scan speed), and then applying a single pass of FeSi with adjusted parameters (430 W and 380 mm/min), the bonding at the interface between the mild steel substrate and deposited materials was significantly improved. This not only reduced crack propagation but also enabled continued deposition, particularly in the foundation layers where cracking was previously prevalent.

The IPF map in Figure 78 (single layer of FeSi deposition = 3 passes per layer) shows a strong <001> crystal orientation along the BD, which is highly desirable for improving the magnetic properties of FeSi-based components. The fibre orientation analysis reveals that the area fraction of <001>//BD is 0.57, confirming the dominance of the <001> texture in the BD. Additionally, the area fractions for <101>//BD and <111>//BD are 0.12 and 0.04, respectively, indicating that the material exhibits a strong <001> development with minimal contributions from other orientations. This strong <001> texture, combined with a relatively low γ value, suggests the presence of easy magnetisation in the BD with weak hard magnetisation. Such crystallographic texture is ideal for magnetic applications, as it enhances the magnetic performance of the material, particularly in applications where directional magnetic properties are critical. Moreover, the weighted average equivalent circle diameter of the grains, measured at 685 µm, demonstrates a favourable grain structure for minimising hysteresis losses, further improving the material's magnetic efficiency. The absence of significant delamination at the interface, despite the differing chemical compositions of 316L stainless steel and FeSi alloy, can be attributed to a combination of metallurgical compatibility and thermal behavior. Firstly, both alloys have relatively similar coefficients of thermal expansion, which minimises thermal mismatch during solidification and cooling, thereby reducing interfacial stresses that could lead to delamination [389, 390]. Secondly, the presence of silicon in both materials may enhance atomic diffusion across the interface during the laser deposition process, promoting strong metallurgical bonding. Prior research [391] in additive manufacturing of dissimilar materials has shown that when materials share thermal and chemical compatibility, the risk of interfacial defects such as delamination, porosity, or cracking is significantly reduce. This study demonstrates that multi-material deposition using LMD is not only feasible but can also enhance the performance of the deposited FeSi 6.5 wt%. The success of this method opens new avenues for the manufacturing of advanced magnetic components with tailored properties. Future work should focus on further refining the deposition parameters to reduce cracking during the cooling process, especially in the FeSi layer, and on exploring the scalability of this approach for more complex geometries.

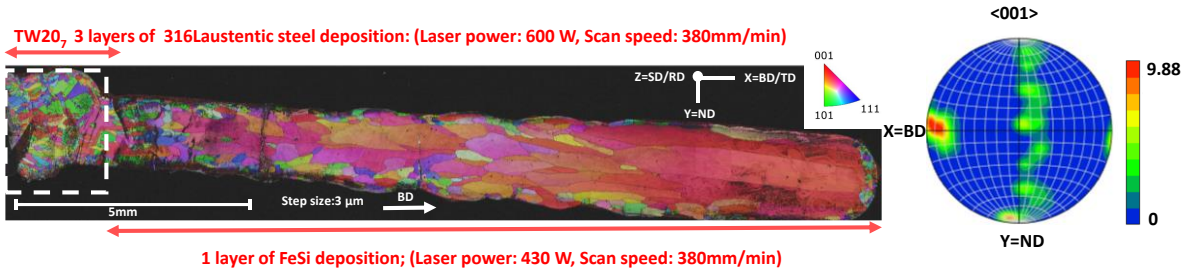

Figure 78. EBSD IPF map of the multi-material deposition in sample $TW20_7$.

6.13 Effect of geometric dimensions on texture development

The geometric dimensions of the samples significantly influence texture and microstructure development, magnetic properties, even when processing parameters remain constant [392]. This study presents novel and promising results demonstrating how variations in geometry can alter crystallographic orientations, particularly the formation of the <001> crystallographic direction. When modifying the sample dimensions—specifically reducing the height from 30 mm to 10 mm and increasing the length from 20 mm to 40 mm while maintaining a thickness of 1.5 mm—significant changes in the crystallographic orientation occur, as depicted in Figure 79 (b). The sample TW34 exhibits a remarkably strong <001> orientation in the build direction, resembling epitaxial growth in well-defined orientation. Notably, despite not incorporating a foundation layer for sample TW34, maintaining a substrate temperature of 200 °C minimised residual stresses and cracking, with an energy density of 61 J/mm², identical to TW27. Unlike TW27, no cracks were observed in TW34, showcasing the impact of geometric design on structural integrity. This finding suggests that by adjusting preheating temperatures based on the sample geometry, the need for foundation layers can be minimised, thereby reducing material waste. Preliminary experiments indicate that maintaining a substrate temperature above 200 °C could facilitate printing without foundation layers, warranting further investigation to confirm these effects on texture formation and <001> orientation. The strong <001> orientation is particularly advantageous for enhancing the magnetic properties of FeSi, which is essential for applications in electrical and magnetic devices. The epitaxial grain growth achieved in sample TW34 not only improves the magnetic performance but also indicates a refined microstructure, ultimately contributing to the material's overall effectiveness in applications requiring high magnetic permeability and low core losses. Sample TW34 was sectioned into three equal parts along the build direction to analyse microstructural variations throughout the additively manufactured component. In each section, both the print start points, and print end point were examined. This approach enables a comparative analysis of microstructure and potential defects or property changes from the bottom to the top of the build. Furthermore, as illustrated in Figure 79 (a) and (b) for samples TW27 and TW34 (showing the start and end points of each sample), the area fractions of crystallographic orientations are presented in Table 8. The data reveals that the fibre formation of the <001> orientation increased significantly in sample TW34 compared to TW27, with the area fraction of <100>

rising from 0.54 in TW27 to 0.83 at the start point of TW34 and slightly decreasing to 0.75 at the end point. The area fraction of <110> for TW34 remained relatively stable, while the <111> orientation saw a slight increase in area fraction from TW27 to TW34, particularly at the end point. This analysis highlights the significance of geometric design in enhancing microstructure and texture, providing valuable insights for optimising additive manufacturing processes.

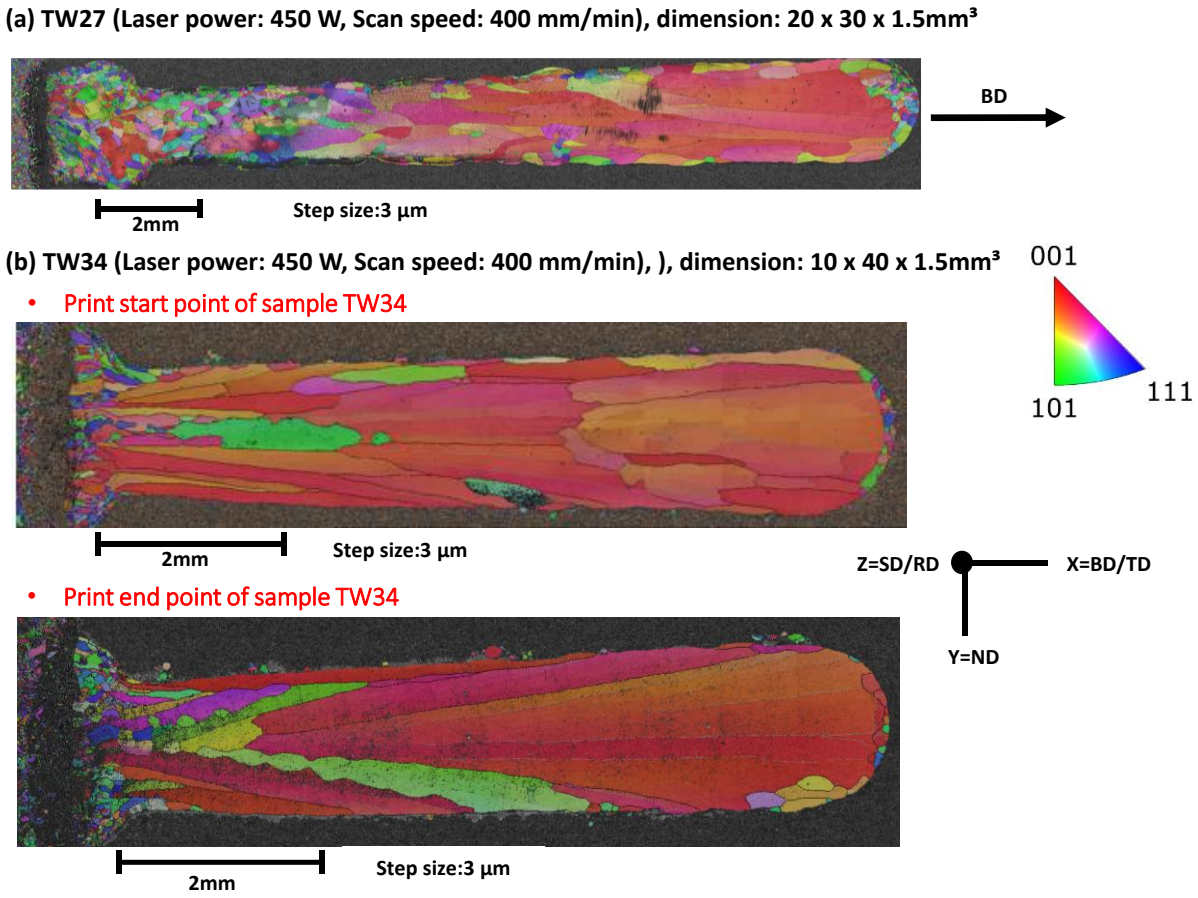

Figure 79.Changes in crystallographic orientation for sample TW27, TW34 after geometric modifications.

Table 8. Area fractions of crystallographic orientations of different samples.

Sample	Aera fraction of fibre <100> //BD	Aera fraction of fibre <110> //BD	Aera fraction of fibre <111> //BD
TW27	0.5428	0.1519	0.0676
TW34 Start point	0.8261	0.0898	0.0167
TW34 End point	0.7524	0.1456	0.0228

6.14 EBSD case studies of cubes FeSi 6.5 wt%

The EBSD data was undertaken for all samples to observe the as-built microstructure. As can be seen in Figure 80, the EBSD map of two different samples C16 (a) and C21 (b) with energy densities of 60 and 90 J/mm^2, respectively. This illustration indicates that the samples contain a <001> texture along the BD direction, as well as grain morphology. In this case, as the laser

power increases from 400 W to 600 W while maintaining a constant scan speed of 400 mm/min, the front view of sample C21 showed that majority of the grains preferentially orient along the BD. This result illustrates the hypothesis of grain growth along the BD direction as the laser energy density increased from 60 to 90 J/mm^2, (C16) and (C21) respectively. As shown in Figure 80 (b), epitaxial growth can occur across the molten pool boundaries in certain areas. This happens because the crystal barriers are smaller compared to the nucleation barriers. This phenomenon is observed when the direction of heat flow in the neighbouring molten pool is nearly aligned with the crystallographic orientation of the previous pool. This observation is also noted by [393, 394]. As the energy density increases by 50%, the total heat input to the deposited FeSi material rises, leading to a larger melt pool, longer cooling times, and a reduced thermal gradient within the melt pool. This environment allows grains to grow larger before solidification occurs. Furthermore, increased energy density can cause remelting and over-melting of previously deposited layers, altering the microstructure and promoting the growth of larger grains [395]. Furthermore, several researchers have reported [396-398] that both primary and secondary dendrite arm spacing decrease with higher cooling rates and thermal gradients, leading to finer grains. This observation supports the hypothesis that in this scenario, such changes occur when the energy density is low. Conversely, higher energy density may increase primary and secondary dendrite arm spacing due to lower cooling rates, resulting in larger grains.

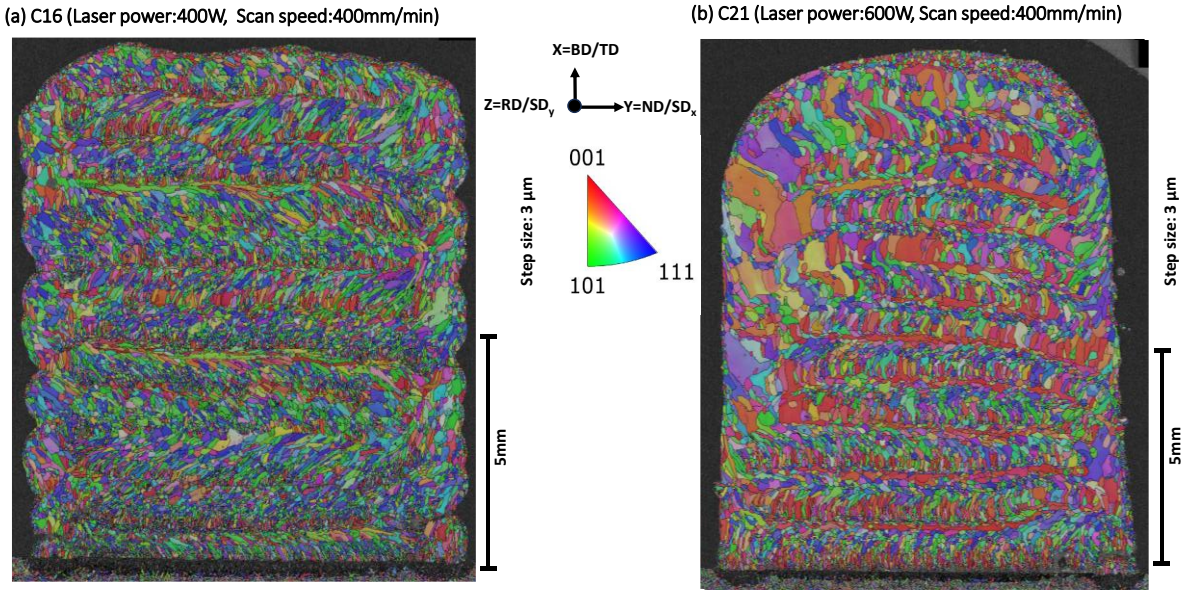

Figure 80. EBSD maps (a and b) and IPFs for C16 and C21 in build directions.

It has been previously mentioned and supported by other researchers [383] that the preferred grain growth directions, such as <001>, are influenced by heat flow directions and the competition between grains during the solidification process. The different heat flow directions and resulting solidification textures observed in samples C16 and C21 can be attributed to varying processing parameters (Figure 81). As shown, the melt pool boundaries differ at various energy densities. For sample C16, based on the laser power and scanning

pattern, the primary heat flow direction during solidification is at an angle of approximately 60^0, perpendicular to the edge of melt pool boundary. A similar effect has been observed in the additive manufacturing of Inconel 718 [383]. During the deposition of the first layers of FeSi materials, grains were randomly oriented. However, after depositing several layers, the laser path and scan patterns in EBSD map became evident, revealing that the preferred growth direction <001> in sample C16 is less aligned with the maximum heat flow direction, which is about 60^0. In contrast, for sample C21, where the energy density was increased to 90 J/mm², the preferred growth direction <001> is more closely aligned with the maximum heat flow direction, which is approximately 90^0. This alignment could explain the higher area fraction of fibres aligned in the building direction for sample C21 (0.27) compared to C16 (0.14). Additionally, the lowest gamma fibre alignment in the BD is observed in sample C21 (0.20), whereas for sample C16, the gamma fibre <111>//BD area fraction is 0.26. These differences highlight the impact of energy density on grain orientation, solidification, and texture development behaviour of FeSi in the LMD process.

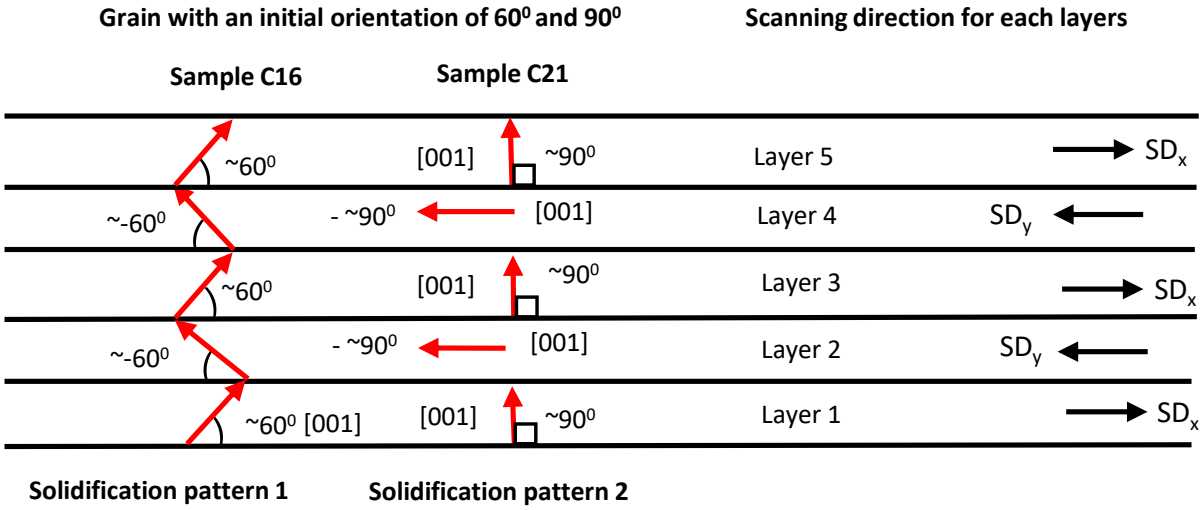

Figure 81. Schematic diagram of dendrite growth patterns in grains with different orientations during laser scanning.

The textures of samples C16 and C21 are shown in Figure 82. In sample C21, a dominant texture emerges, influenced by the elongated grain morphology caused by increasing the laser power from 400 W to 600 W, while keeping the scan speed constant at 400 mm/min. This results in a higher texture intensity in C21 compared to C16. Furthermore, the competitive grain growth phenomenon during layer-by-layer deposition and directional solidification, induced by the thermal gradient and heat flow in the LMD process, fosters a preferred growth direction of <001> for new crystals in BCC metallic materials [399]. In this scenario, certain regions exhibit almost epitaxial grain growth during solidification towards the deposition direction, which can be compared with the crystallographic orientation of grains in sample C16. The pronounced dominance of <001> directional solidification texture becomes apparent in sample C21 as the laser power is increased to 600 W. As previously noted, the rotation angle of the laser for each printing layer of cubes was set at 90°. The

results collected from EBSD mapping show that this 90° rotation appears to mitigate elongation and preferential orientation of grains. Nevertheless, with the increase in laser power to 600 W, grains in the 90° scan strategy exhibited a more pronounced crystallographic texture, favouring growth along the <001> direction. It can be logical that increasing laser power at a lower scanning speed would be advantageous in enhancing texture, particularly along the <001> direction, and in mitigating anisotropy by generating a larger melt pool. Similar effects were reported by [400], where rotation angles such as 90° were favoured for the growth of the <001> direction compared to a 45° rotation angle. Additionally, based on the results obtained in this experiment, changing the scanning strategy and angle between layers can change the melt-pool orientation, which in turn affects the heat flux and flow of materials [401, 402]. Moreover, a similar observation was reported by [223]. Reducing the scanning angle rotation from 90°, 75°, 60°, 45°, 30°, 15°, to 0° illustrated an increase in the magnitude of the <001> fibre texture of FeSi in the BD and a decrease in the <111> texture aligned in the BD. Furthermore, a unidirectional strategy (no rotation, 0°) would be ideal to increase the magnitude of <001> fibre texture [400]. The main reason is that there is no shifting between deposited layers, allowing multiple layers to melt over each other from bottom to top, thereby creating a larger thermal gradient in the BD. This is an ideal condition for epitaxial grain growth in the BD. Therefore, it can be said that when the samples are not built perpendicular to the BD, the resulting texture would be weaker. Therefore, it can be concluded that the scanning strategy has a significant impact on epitaxial grain growth, as has been previously reported by [401, 402].

Different energy densities (and consequently different cooling rates) reveal different texture of FeSi 6.5 wt% manufactured by the LMD process as shown in Figure 82. In the ODF $\varphi_2=0^0$ section for samples C16 and C21, it is illustrated that by increasing the energy density from 60 to 90 J/mm^2, the rotated cube, cube, and near rotated Goss texture (011)[$0\bar{1}1$] are not present in sample C21. However, a near Brass (011)[211] is still visible but less pronounced, and a strong Goss texture appears in sample C21. In the ODF $\varphi_2=45°$ section, the γ-fibre (111)[$\bar{1}\bar{1}2$] showed some development, and the (113) [$\bar{1}\bar{2}2$] and rotated Brass component orientations are also visible but with moderate intensity. The overall texture indicates some directional solidification influence, but it is not strong at a power of 400 W. At a higher laser power of 600 W, the area fraction of fibre <100>//BD increased by approximately 86% (0.14 to 0.27), the area fraction of γ-fibre <111> // BD decreased by 22% (0.26 to 0.20), and <101> fraction area decreases by around 29% (0.41 to 0.3). This suggests that the higher energy input from the 600 W laser caused a bigger melt-pool, homogeneous nucleation, growth, and solidification, promoting the development of strong texture components such as the Goss texture. Similar results were reported by [350] regarding the dependency of morphological and crystallographic texture intensities on laser energy input in AM processes, such as SLM. It was observed that by increasing the laser power from 400 W to 1000 W, the morphological and crystallographic texture of austenitic stainless steel underwent significant changes. Overall, a weak texture was observed in the ODF plots for sample C16, likely because the laser energy input (60 J/mm²) was insufficient to induce significant microstructural changes,

leading to a predominantly random grain orientation with only slight development of preferred textures. Increasing the laser power to 600 W resulted in a higher energy input (90 J/mm²), which significantly influenced the crystallographic texture, promoting more noticeable orientation alignment. This effect can be attributed to the larger melt pool size and steeper thermal gradient associated with higher energy densities, which encourage more directional solidification. The enhanced thermal effects lead to faster solidification rates, promoting the formation of columnar grains and more defined crystallographic orientations, thereby strengthening texture development. These observations suggest that higher energy inputs improve the driving forces for controlled grain growth and texture formation [177].

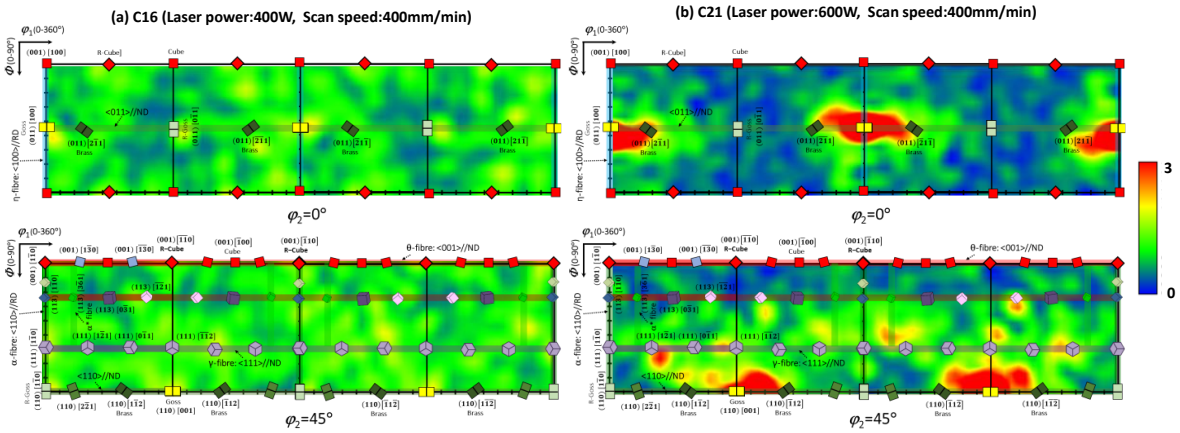

Figure 82. Texture of cross-sections and 3D-plots of ODF for FeSi 6.5wt%.

6.15 Effect of energy density on fibre formations of cubes

The formation of fibre texture in electrical steel during manufacturing processing is crucial because it enhances magnetic performance, creates directional properties, stabilises the microstructure, and improves mechanical strength. This texture significantly impacts the material's efficiency in applications like transformers and electric motors, ensuring optimal performance and durability [214, 403]. The line graphs in Figure 83 illustrate the area fractions of different fibre orientations in electrical steel samples manufactured using LMD, plotted against energy density which determined through MTEX measurements along the BD direction (sdv: ±0.10%). These fibres, oriented along the BD, have varying impacts on magnetic properties due to the magneto crystalline anisotropy of electrical steel. In Figure 83 (a), the area fraction of fibre <100>//BD increases with energy density, ranging from about 0.10 to 0.25. This significant increase (approximately 150%) indicates that higher energy densities during the LMD process favour the nucleation and growth of the <100> orientation, which is known for its easy axis for magnetic properties. The high energy input promotes rapid solidification and cooling rates, enhancing the alignment of grains in this favourable orientation, with a strong linear correlation ($R^2 = 0.95$). Figure 83 (b) shows a decrease in the area fraction of fibre <101>//BD as energy density increases, dropping from around 0.45 to 0.30. This decrease of about 33% suggests that the conditions created by higher energy densities are less favourable to the formation of the <101> orientation. This fibre has a medium axis for magnetic properties, and the shift in energy input likely alters the thermal

gradients and cooling rates, reducing its prevalence, with a strong linear correlation (R^2 = 0.98). In Figure 83 (c), the area fraction of fibre <111>//BD decreases with energy density, falling from approximately 0.26 to 0.21 . This reduction of about 19% indicates that higher energy densities during LMD disfavour the formation of the <111> orientation, which is associated with a hard magnetic axis. The LMD process's rapid solidification and cooling rates likely impede the alignment of grains in this less favourable orientation for magnetic properties, with a very strong linear correlation (R^2 = 0.92). The observed trends in fibre formation can be attributed to the unique thermal cycles and rapid solidification rates inherent to the LMD process. Under specific conditions, moderate energy densities can lead to faster cooling rates, which promote the formation of fibres with easy magnetic axes, such as <100>, while reducing the dominance of fibres with hard magnetic axes, like <111> (hard magnetic axis), thereby enhancing magnetic performance. This optimisation of grain orientations through LMD enhances the magnetic performance of electrical steel by increasing the fraction of fibres that align with easy magnetic axes and reducing those that align with hard magnetic axes [214].

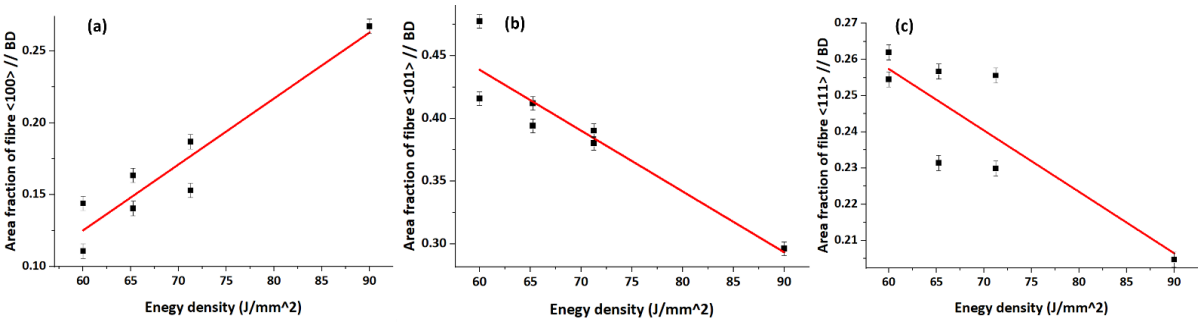

Figure 83. Effect of energy density on fibre orientation in LMD cubes samples in <100>//BD direction, <101>//BD, <111>//BD.

Figure 84 shows the area fractions of various fibre orientations in electrical steel samples manufactured using LMD, plotted against energy density (sdv: ±0.10%). These fibres, oriented along the normal direction (ND) and rolling direction (RD), have different impacts on magnetic properties due to the magneto crystalline anisotropy of electrical steel. In Figure 84 (a), the area fraction of theta fibre <001>//ND decreases with increasing energy density, dropping from about 0.16 to below 0.05. This significant reduction (approximately 69%) indicates that higher energy densities during the LMD process reduce the formation of the theta fibre, which is beneficial for magnetic properties. The decrease suggests that the specific thermal cycles and rapid cooling rates at higher energy densities may not favour the nucleation of this favourable orientation as effectively, with a strong linear correlation (R^2 = 0.90). Figure 84 (b) shows a decrease in the area fraction of alpha fibre <110>//RD, falling from around 0.50 to about 0.25 as energy density increases. This decrease of approximately 50% implies that higher energy densities during LMD reduce the dominance of alpha fibre, which is detrimental to magnetic properties. The reduction suggests that higher energy inputs and associated thermal gradients may impede the formation of this unfavourable fibre orientation, with a strong linear correlation (R^2 = 0.96)

. Figure 84 (c), the area fraction of gamma fibre <111>//ND, slightly increases with energy density, fluctuating around 0.25 to 0.30. This modest increase (about 20%) indicates that higher energy densities may slightly favour the formation of gamma fibre, which is known to be detrimental to magnetic properties. This graph suggests that certain thermal conditions during the LMD process might promote the alignment of grains in this less favourable orientation. Figure 84 (d) showed a reduction in the cube orientation fraction with increasing energy density, from approximately 0.045 to 0.025, a decrease of about 44%. This suggests that higher energy density during LMD randomizes texture, enhancing magnetic isotropy beneficial for magnetic properties in FeSi electrical steel. The observed decrease indicates that higher energy inputs and associated faster cooling rates limit the nucleation and growth of cube texture, consistent with findings that DED process parameters influence texture evolution and magnetic performance [100]. Figure 84 (e), the area fraction of Goss orientation exhibits a clear upward trend with increasing energy density, starting at approximately 0.03 at 60 J/mm² and reaching about 0.15 at 90 J/mm². This significant increase of around 400% suggests that higher energy densities during the process strongly favour the formation of the Goss orientation, which is crucial for optimising magnetic properties. The pronounced rise in Goss orientation with energy density indicates that the associated thermal cycles and cooling rates at higher energy inputs are conducive to the alignment of grains in this preferred orientation. This trend could be due to enhanced grain growth and reduced solidification rates at elevated energy densities, leading to more pronounced textural development, with a very strong linear correlation ($R^2 = 0.97$). Consequently, controlling energy density is critical in tailoring the microstructure for desired magnetic characteristics, with potential implications for material performance in applications where magnetic properties are paramount. Overall, these observations highlight the significant impact of the LMD process parameters on the formation of different fibre orientations in electrical steel. Higher energy densities tend to reduce the formation of detrimental fibre textures, such as alpha and gamma, while promoting beneficial textures like the cube fibre, enhancing magnetic properties. However, they significantly increase the formation of the Goss orientation, which is highly advantageous for improving magnetic properties. Optimising energy inputs during the LMD process is crucial for enhancing the magnetic performance of electrical steel by promoting favourable fibre orientations and minimising the formation of unfavourable ones.

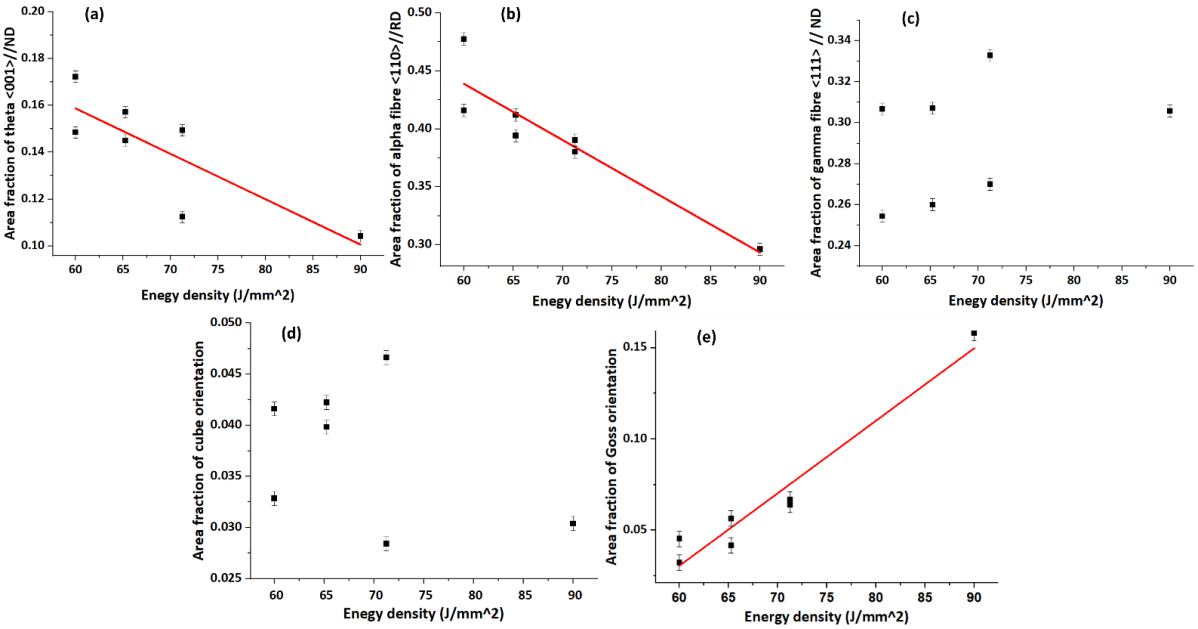

Figure 84. The impact of energy density on fibre formation in cubes sample in the <110>//BD direction, <001>//ND, <111>//ND, cubes and Goss orientation.

6.16 Effect of laser energy density on grain size evolution of cubes

The influence of laser energy density on microstructural evolution of FeSi 6.5wt% cubes parts was examined in this study. Advanced materials analysis techniques, including EBSD, were employed to characterise the LMD FeSi 6.5wt% parts. The EBSD maps were collected and analysed using the AZtech Crystal software. The weighted average equivalent circle diameter was utilised as a reliable metric to determine the average grain size, ensuring a representative value for the overall grains. As it can be seen in Figure 85 (a) sample C16, with a laser power of 400 W and a scan speed of 400 mm/min, predominantly produces smaller grain size, with approximately 82% grain size falling within the 0-200 µm range. In contrast, sample C21 in Figure 85 (b), which uses a higher laser power of 600 W with the same scan speed, shows a broader distribution of grain sizes. Specifically, C21 has around 55% of its grain sizes in the 0-200 µm range. This represents a 33% decrease in the proportion of small grain size compared to C16. For medium grain sized (200-400 µm), C16 has about 16% while C21 has 25%, indicating a 56% increase in the proportion of medium grain sized. The most significant change is observed in the larger grain sizes (400-600 µm), where C16 has only about 1% of grain sizes, compared to C21, which has about 20%. This represents a 1900% increase in the proportion of larger grain sizes when the laser power is increased from 400 W to 600 W. Increasing the laser energy density during LMD leads to an evolution in grain size for several reasons. Higher energy density delivers more heat to the material, resulting in a larger molten pool that promotes greater melting and encourages larger grain formation as the material remains liquid for longer periods. Elevated temperatures also increase atomic mobility, allowing atoms to rearrange more freely, which facilitates the growth of larger grains during solidification. Additionally, a larger melt pool means longer solidification times, allowing smaller grains to dissolve and coalesce into larger structures. Finally, higher energy input can

slow down cooling rates, providing more time for grain growth before the material completely solidifies. Collectively, these factors contribute to the evolution of larger grain sizes as energy density increases [316, 404]. In summary, the observations indicate that by carefully adjusting the laser power, the LMD process can be tailored to produce specific grain size distributions, thus optimising the mechanical and physical properties (like magnetic performance) and efficiency of the deposited material for various applications.

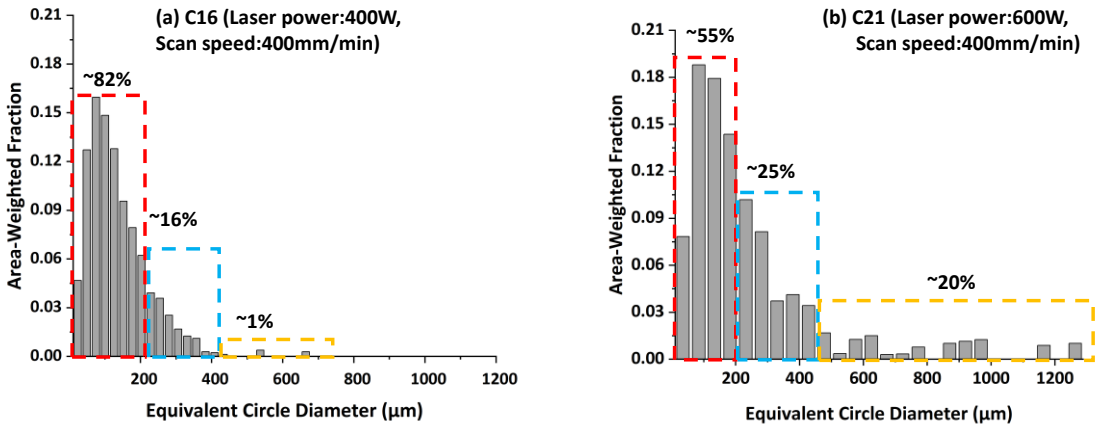

Figure 85. Grain development based on area weighted fraction of different samples (a) C16, (b) C21.

In Figure 86, the average weighted average equivalent circle diameter versus energy density for identical samples are illustrated. This illustration enables a clear understanding of how the weighted average equivalent circle diameter changes with varying energy density, showcasing the impact of energy density on grain size. The results show that there is little variation in the grain size of the cube samples, even with the use of different scanning strategies such as bidirectional and unidirectional. This observation remains consistent even when samples share identical power and scanning speed parameters. For example, samples C15 and C20, both with 475 W power and 400 mm/min scanning speed yet employing different scanning strategies, demonstrate similar grain sizes. The uniformity maintained in process parameters, such as power and scanning speed, likely contributes to the similarity in grain size between these samples. By calculating the weighted average equivalent circle diameter of identical samples, any distinctions introduced by varying scanning strategies are effectively accounted for grain development. This highlights the importance of process parameters in controlling grain growth, regardless of the scanning strategy used, which contrasts with the findings for thin-wall samples, where the printing strategy had a stronger effect on the microstructure. Moreover, the error bars (sdv: 0.20%) in the graph indicate the variability in the measured grain sizes of identical samples, with a near-perfect linear correlation (R^2 = 0.99). The provided line graph demonstrates a clear positive correlation between energy density and grain size, with a near-linear relationship. As energy density increases from 60 J/mm² to 90 J/mm², the weighted average equivalent circle diameter consistently increases, indicating that higher energy densities promote larger grain sizes. At 60 J/mm², the average grain diameter is approximately 160 µm. When the energy density

increases to 70 J/mm², the grain size grows to around 180 µm, representing a 12.5% increase. As the energy density rises to 90 J/mm², the grain size further increases to about 240 µm, which is a 50% increase from the 60 J/mm² energy density. In comparison to Galdbadi's [5] work on SLM with the same alloy, where grain sizes were smaller and thinner due to lower energy input, the larger grains observed here are likely a result of the higher energy densities associated with LMD. This contrast highlights the stronger impact of energy input on grain growth in LMD compared to the LPBF, where lower energy densities typically limit grain size. This trend highlights the significant influence of energy density on grain size during laser processing. Higher energy densities lead to increased heat input, which enhances grain growth by supplying more energy for grains to expand. The direction of this grain growth is determined by the temperature gradient, while the size of the grains can be controlled by the solidification rate. Together, these factors play a crucial role in optimising the microstructure of materials processed with laser techniques [404].

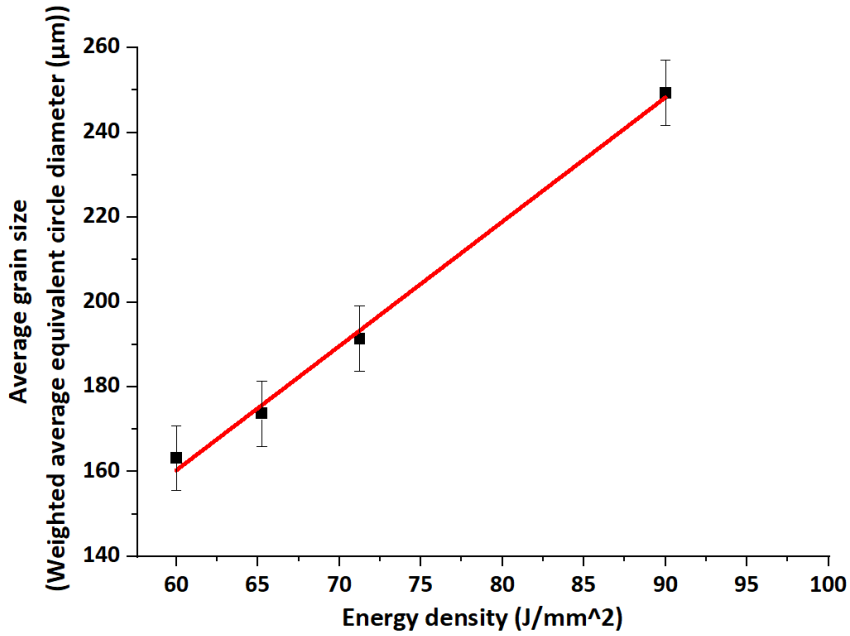

Figure 86. Effect of the laser energy density on grain growth in cube samples.

6.17 Kernel average misorientation analysis of cube samples

The calculation of KAM in this study followed the same principles as those applied to the thin-wall samples. Misorientations less than 2° and grain boundaries greater than 10° were excluded, focusing the analysis on sub-grain boundaries and local dislocations. Additionally, sub-grain boundaries larger than 2.5° were not considered to concentrate on the region's most relevant for magnetic performance. The average KAM values for the low and high laser power samples (C16 and C21, respectively), at a constant scan speed of 400 mm/min, are shown in Figure 87. It was observed that the average KAM values for samples C16 and C21 are approximately 0.9^0 and 0.55^0, respectively. This indicates that by increasing the laser power from 400 W to 600 W, not only the grain size increase, but the KAM values decreased as well. This suggests that in the smaller grains, especially in sample C16, higher

misorientation occurred. However, the increase in energy density did not significantly affect the percentage of sub-grains and grain boundaries in either sample, both of which showed similar values—about 15% of the grains (2°–10°) were identified as sub-grains, with the remaining 85% as grain boundaries (>10°). Across all cube samples, the KAM values range from 0.38° to 9°. Sample C19 exhibited the lowest average KAM value, while sample C16 showed the highest. Based on the KAM values, since the average KAM is less than 1°, it can be suggested that the samples are unlikely to contain HAGBs. However, these samples do contain LAGBs, as the misorientation falls between 2.5° and 10°. LAGBs are beneficial for magnetic properties, as previously mentioned [405]. Furthermore, increasing the laser power or energy density results in less misorientation and more grains oriented in the BD.

In relation to dislocation density, the KAM values also provide valuable insights. Higher KAM values typically indicate increased local misorientations, which are associated with higher densities of geometrically necessary dislocations (GNDs) [406]. Sample C16, which exhibited the highest KAM value (~0.90°), likely contains a high density of dislocations and localised strain, including pile-up formation at grain boundary intersections [407]. In contrast, sample C20, with the lowest KAM value (~0.38°), indicates a much lower dislocation density. These differences correspond to variations in laser power and energy density during the additive manufacturing process. While direct magnetic property measurements were not performed in this study, prior research shows a strong correlation between dislocation density and magnetic behavior in Fe-Si alloys. Dislocation structures and grain boundary characteristics—particularly the presence of LAGBs—play a key role in preserving magnetic moment and minimising domain wall pinning [405]. Their study confirmed that low-angle boundaries maintain magnetic moments comparable to the grain interior, while high-angle boundaries and regions of high dislocation density can locally suppress magnetism. Therefore, in the context of this study, lower KAM values (and thus lower dislocation densities) suggest improved conditions for soft magnetic behavior in Fe-Si. In conclusion, KAM values provide a useful indirect metric for evaluating microstructural features that influence magnetic properties. By adjusting laser power and energy input, it is possible to control dislocation density and misorientation, ultimately contributing to enhanced mechanical and magnetic performance in Fe-Si components produced by additive manufacturing.

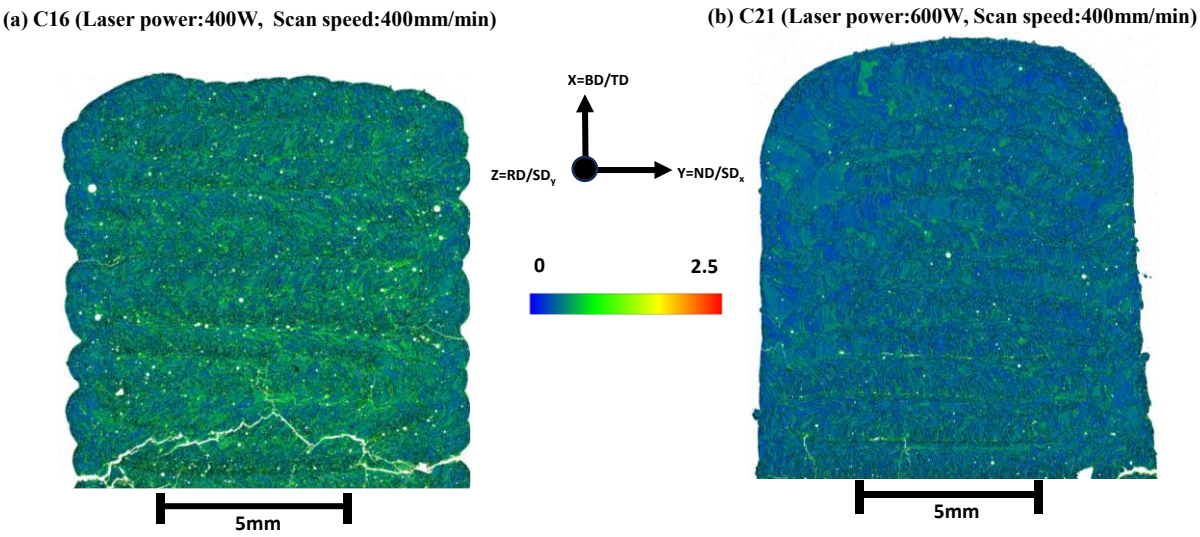

Figure 87. Overview of KAM map (a), and (b), of sample C16 and C21.

Chapter 7

7 Challenges and insights in 3D-printing of stators for electrical motor

7.1 Introduction

Electrical machines, such as axial flux machines, require high torque density, which is essential for applications like electric vehicles, wind turbines, robotics, and other industrial uses. A key material used in axial flux machines is soft magnetic materials, including composites and electrical steel. Most electrical machines use electrical steel for laminated stator cores to reduce energy losses in service. These laminated stators are oriented perpendicular to the main flux path to minimise eddy current paths without negatively affecting the magnetising flux Figure 88 (a). In radial flux machines, the stator laminations are stacked axially, whereas axial flux machines benefit from laminations Figure 88 (b). Soft magnetic materials such as Fe-6.5 wt% Si can be manufactured for rotating electric machines using novel processes such as SLM, which improves electrical resistivity and reduces eddy current losses by 50%, further enhancing machine performance [79]. Compared to the conventional electrical steel laminations. In this section, the stator is designed and subsequently manufactured to investigate the microstructure, texture, porosity, and crack development during the LMD process. The goal was to fabricate a part as close as possible to the electrical steel laminates available in the market, particularly by incorporating features such as gears, aiming to replicate the properties and performance of commercial laminates.

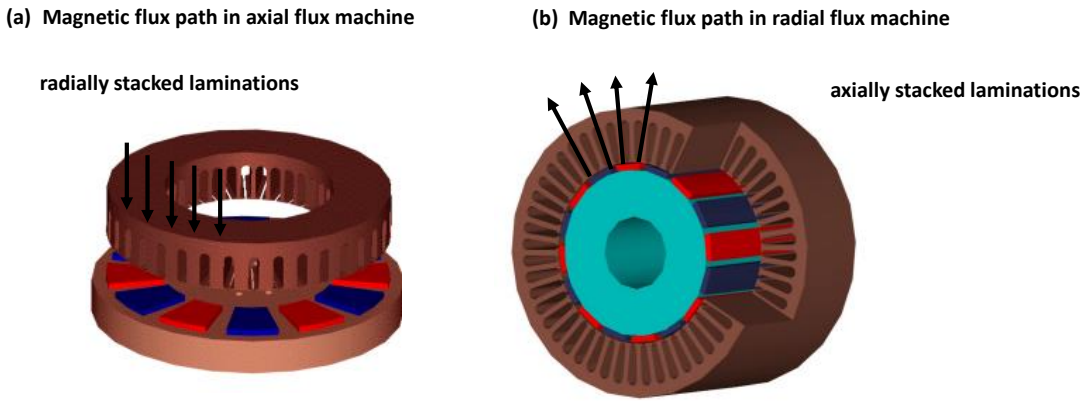

Figure 88. Configurations of axial-flux machine (a) and radial flux machine (b) [408].

A motor typically consists of a rotor and a stator, with the stator acting as the stationary component that generates the magnetic field required for the rotor's motion. In this case, the stator is positioned around the cylindrical substrate and is designed to facilitate electromagnetic flux for motor operation. The goal of this work is to manufacture stator discs using the LMD process while optimising parameters to achieve optimised microstructure for this application and minimise defects such as cracks. Based on previous experiments and data obtained from manufacturing thin walls, specific process parameters were selected for manufacturing the stator disc. These parameters included a laser power of 425 W, a scan speed of 400 mm/min, an energy density of 63.8 J/mm², a powder feed rate of 2.5 g/min, a z-step of 0.45 mm, and a hatch spacing of 0.60 mm. Before printing, the cylindrical substrate

was preheated to 200 °C, which, as explained in *Section 4.2 (Laser Metal Deposition Results)*, was chosen as a balanced temperature to mitigate cracking and delamination while avoiding the distortion issues observed at higher preheating levels [264-270, 272]. This value was recommended by the industry partner and aligns with reported preheating ranges for brittle alloys in AM, where moderate temperatures (~150–250 °C) are effective in reducing residual stresses without compromising part integrity.

Using these conditions, six stator discs of varying heights (denoted as S1 to S6) were manufactured. Despite challenges typically associated with geometry control in LMD, the process resulted in a relatively uniform thickness across the discs, demonstrating that precise parameter selection can improve dimensional accuracy. The final thickness achieved was within an acceptable range, confirming that LMD can effectively produce controlled geometries for stator applications. Figure 89 shows that sample S1 exhibited no macro cracks between the FeSi deposited material and the substrate. To increase the height of the discs, three layers of foundation were added around the cylindrical substrate during manufacturing, followed by continuous printing of FeSi. However, samples S4 and S6, which used identical processing parameters but had extended disc lengths, exhibited catastrophic cracks across their thickness. Notably, sample S4 shattered after the printing process during the cooling phase due to thermal stress from the increased length.

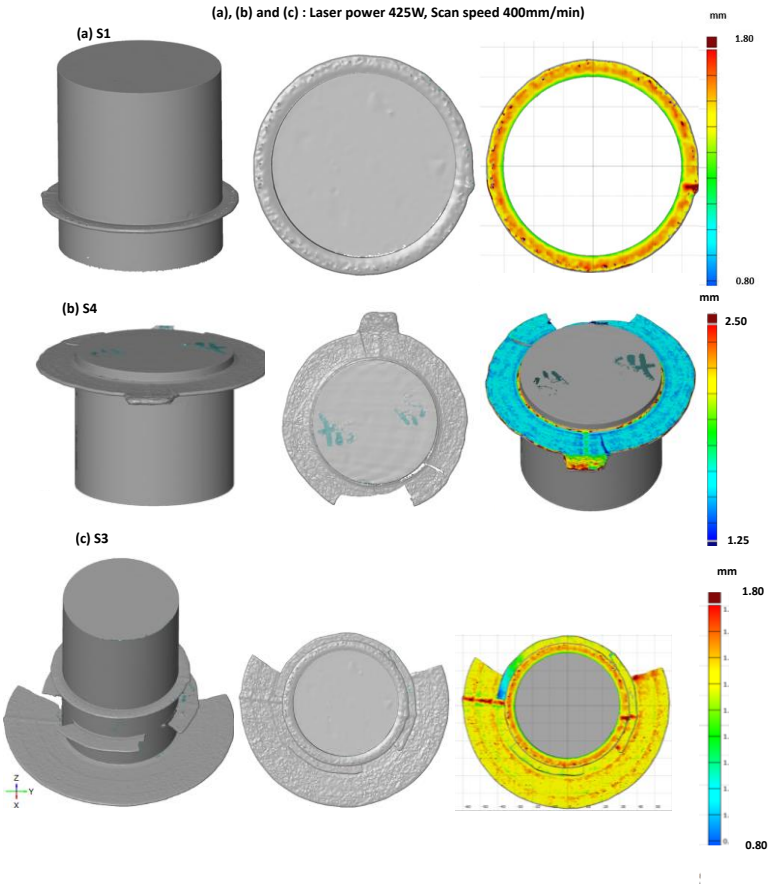

Figure 89. Inspection of manufactured stator discs deposited on a cylindrical substrate using the Hexagon Absolute Arm with 3D laser scanning.

7.2 Crack and porosity analysis of stator disc using optical microscope, MIPAR, and XCT

The occurrence of cracks in electrical steel disks during the LMD printing process, where the substrate rotates and the laser remains fixed, can be attributed to several interconnected factors. Firstly, the rotating substrate introduces uneven heating and cooling cycles, leading to significant residual stresses within the deposited layers and the substrate itself. These thermal gradients create stress concentrations that exceed the material's tolerance, resulting in crack initiation [176]. Moreover, electrical steel's specific thermal properties and coefficients of thermal expansion can intensify these issues if not carefully managed during printing. Variations in temperature across the substrate surface due to the fixed laser can further provoke thermal mismatch between layers and the substrate, compromising material integrity and increasing susceptibility to cracking. This mismatch can cause differential expansion and contraction rates, which contribute to the buildup of internal stresses. Additionally, inadequate metallurgical bonding between deposited layers and the substrate, often influenced by insufficient preheating temperatures or inconsistent material feed rates, can weaken the structural integrity of the printed part. This weak bonding can lead to delamination and subsequent crack propagation during the cooling phase. When the layers do not bond properly, it creates interfaces that are more prone to crack initiation under thermal or mechanical loads [214].

Another critical factor is porosity within the deposited material. Porosity refers to the presence of voids within the material, which significantly impacts crack growth. These voids act as stress concentrators, where cracks can easily initiate and propagate. Porosity can arise from various sources, such as improper melting or solidification during the printing process, contamination, or gas entrapment. In sample S6, the porosity level in the cross-section area fraction is 1.52%, and this sample also exhibits higher surface area porosity of 3.48% due to its larger area size Figure 90 (a) and (b) respectively. The increased porosity in the surface area further compromises the material's mechanical properties, facilitating crack initiation and growth. The higher porosity at the surface can lead to early failure as surface cracks tend to propagate more rapidly [283]. The presence of porosity not only reduces the load-behaviour capacity of the material but also serves as initiation points for cracks, which can grow under cyclic loading or thermal stresses. Over time, these cracks can join together, as it can be seen in leading to catastrophic failure of the component.

(a) Cross-section of sample S6 **(b)** Surface area of sample S6

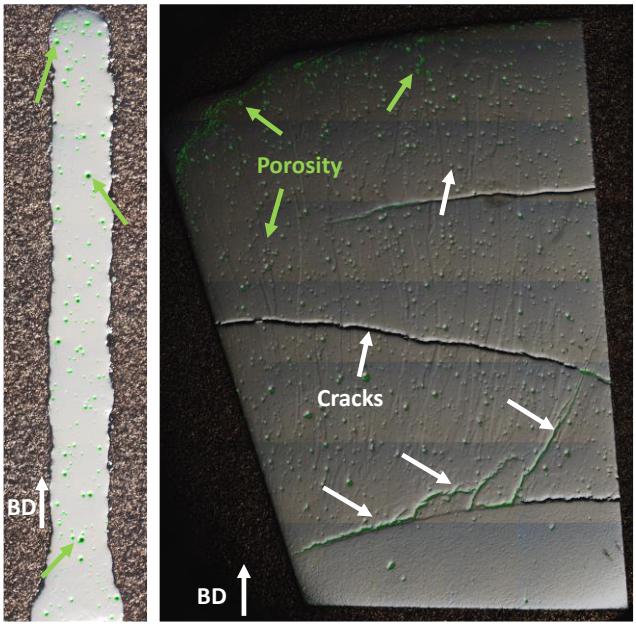

Figure 90. Illustrated optical images from different area of sample S6 (a) cross section of S6 (b) surface area of S6.

The XCT (Nikon XTH 320 using a 225 kV head) images can also provide a detailed visualisation of the internal and surface porosities and the corresponding crack networks within the material, highlighting the correlation between these defects and the observed failures. As seen in Figure 91, there are fewer porosities in the cross-section of sample S3 due to the larger area, whereas the surface area exhibits higher porosity levels. The 3D visualisation explains the correlation between these defects and the observed failures, offering essential insights into the material's structural integrity and potential points of weakness. This analysis is vital for understanding the defect formation under different conditions and for improving its performance in practical applications.

The XCT images of sample S3 reveal insightful details about its porosity. The cross-sectional view indicates minimal porosity due to a larger material area, suggesting a solid internal structure with fewer voids. This uniformity implies enhanced magnetic properties, strength and durability, minimising potential weaknesses. However, the surface area image illustrates higher porosity with uneven distribution of pores. These surface imperfections will be addressed in further processing, as they negatively affect magnetic performance. Additionally, the factor of thickness on magnetic properties will also be considered during this process. In 3D visualisation, pore distribution and volume are highlighted, with larger pores evident in specific regions. Colour-coded volume representation correlates defects with structural weaknesses, offering a comprehensive view. Notably, despite identical processing parameters, sample S3 shows no cracks unlike S4 and S6. This absence of cracks may be attributed to lower cross-sectional porosity, indicating robustness against stress without compromising structural integrity. Figure 91 (a), (b) and (c) illustrates these findings: minimal porosity in the cross-section and higher levels on the surface. The 3D view links defects to

observed failures, crucial for assessing structural integrity and enhancing performance in practical applications for such parts like stator discs. To overcome these challenges, it is crucial to maintain precise control over processing parameters such as preheating temperatures, laser settings, and material feed rates. Additionally, modifying the substrate material or changing the substrate from a solid cylindrical form to a hollow tube could enhance heat absorption and distribution. A hollow tube allows for more efficient heat dissipation during the printing process, preventing excessive heat buildup that can cause residual stress and distortion. Additionally, this design change reduces the thermal gradient across the material, which improves the bonding between the deposited material and the substrate, leading to stronger, more reliable results. Furthermore, implementing post-processing techniques such as inter-pass stress relief heat treatment and stress relief annealing may be necessary to reduce residual stresses and improve the overall durability of the printed components. By optimising these factors and minimising porosity, manufacturers can mitigate the risk of cracking and ensure the successful application of LMD technology in electrical steel printing processes.

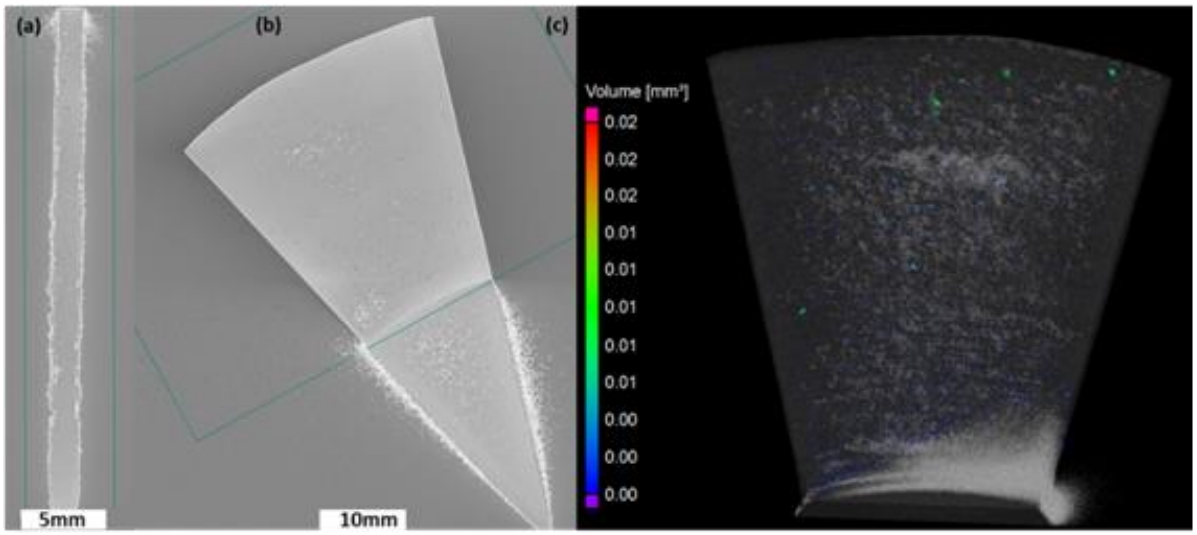

Figure 91. Porosity analysis showing the cropped image from XCT data for sample S3 in different areas.

7.3 Microstructural characteristics of stator discs FeSi 6.5 wt%

The provided IPF maps in Figure 92 offer detailed insights into grain size and <001> crystal orientation for different samples, specifically the ST4 tooth gear and sample S6, examined both in cross-section and on the surface. The ST4 tooth gear exhibits the largest grain size at 1588 µm, with a prominent <001> crystal orientation along the longitudinal direction (BD), indicated by the predominant red coloration in the IPF map resembling a single crystal due to the large grain size. This strong <001> orientation suggests grains are aligned in a manner that enhances magnetic properties. The larger grain size indicates slower cooling rates due to higher laser heat input in the small section area and a high thermal gradient, allowing grains to grow into columnar shapes and develop a well-defined orientation along the BD direction [409]. In relation to electrical steel, the ST4 tooth gear's large, elongated grains with a strong

<001> orientation would positively impact its magnetic properties. Such grain orientation can reduce hysteresis losses and improve magnetic permeability, particularly in the direction of grain elongation (which is in parallel to the BD), enhancing the efficiency of magnetic flux alignment suitable for applications in transformers and electric motors where magnetic properties are critical. Sample S6 was analysed through its cross-section and surface to understand variations in grain structure and crystal orientation across its thickness. The cross-section reveals a grain size of 1031 µm, smaller and thinner than the ST4 tooth gear but still relatively large. The IPF map shows a mix of orientations with a noticeable presence of <001> oriented grains, though less dominant compared to the ST4 tooth gear, indicating moderately controlled grain growth influenced by intermediate cooling rates during the printing process, promoting some preferred orientations, but also resulting in diverse grain structures. These variations can influence the magnetic properties of the material, particularly in terms of orientation-dependent magnetisation behavior [410].

The surface of sample S6 also displays a larger grain size same as the cross-section sample S6, reflecting larger and thicker grains compared to the cross-section. Initially deposited layers show a more randomised crystal orientation with fewer <001> oriented grains same to the cross-section, suggesting rapid cooling and solidification at the interface between the first deposited layer and the substrate led to higher nucleation rates and smaller, more randomly oriented grains. Observations indicate that the magnetic properties of silicon steel in sample S6 exhibit variation across its thickness, influenced by the differences in grain structure and cooling rates. The relatively large grains and moderate <001> orientation in the cross-section still provide beneficial magnetic properties, though less pronounced than in the ST4 tooth gear. Conversely, the interface areas between the substrate and first deposited layers, with finer and more randomised grain structure, show characteristics that may negatively affect the overall performance, such as higher hysteresis losses and lower magnetic permeability due to the absence of dominant grain orientation. There is a clear gradient in grain size from the largest in the ST4 tooth gear (1588 µm), through the cross-section of sample S6 (1031 µm), and the surface of sample S6, attributed to differences in cooling rates and thermal gradients during solidification. The ST4 tooth gear's larger grains indicate slower cooling, while the finer grains on the interface areas of sample S6 suggest rapid cooling. The ST4 tooth gear exhibits a strong <001> orientation, which is beneficial for specific material properties. In contrast, the cross-section and surface of sample S6 show moderately <001> oriented grains, reflecting partial control over grain growth direction. Additionally, S6 displays a more elongated grain structure with <001> orientation, attributed to slower cooling, making it ideal for achieving a preferred crystal orientation. Consistent laser power (425 W) and scan speed (400 mm/min) across all samples highlight that observed differences in grain size and orientation primarily result from variations in cooling rates and thermal gradients experienced during processing.

In summary, the ST4 tooth gear's larger grain size and strong <001> orientation along the BD make it well-suited for magnetic applications. These properties enhance magnetic

performance in electrical steel, reducing hysteresis losses and improving magnetic permeability in the direction of grain elongation. Sample S6, with its varying grain sizes and orientations through thickness, provides a broader perspective on how different cooling rates and solidification conditions affect microstructural development. The cross-section of sample S6 shows moderate control over grain orientation, while the surface displays larger, thicker, and less randomised grain structure, highlighting the complex interplay between processing parameters and resulting microstructures. Understanding these variations is crucial for optimising material properties, including magnetic characteristics, through precise control of processing conditions to achieve desired grain size and orientation.

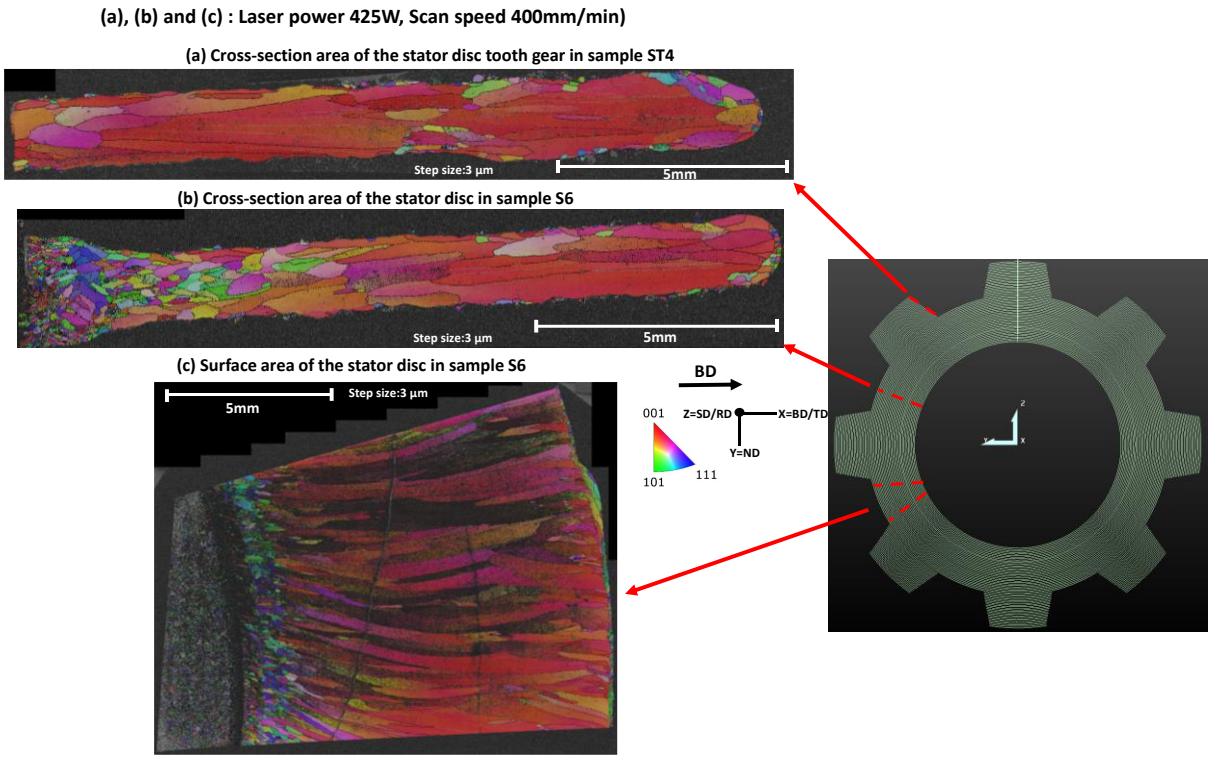

Figure 92. (a), (b), and (c) displays inverse pole figures for cross-sectional and surface area analysis of stator disc samples ST4 and S6.

The EBSD top view (Figure 93) image of sample ST4 tooth gear highlights the variation in grain size and <001> crystal orientation. The average equivalent circle diameter for the grains in the top view of ST4 is 428.85 µm, which is considerably smaller when compared to the cross-sectional grain size of 1588 µm previously illustrated for the ST4 tooth gear. The grain size difference between the top view and cross-section can be quantified by calculating the percentage change, showing a decrease of approximately 73% in grain size from the cross-section to the top view. This notable difference is likely a result of the thermal gradients experienced during the laser metal deposition process. In the cross-section, the grains align and grow larger in the longitudinal direction (which is in parallel to the BD) due to slower cooling rates and the heat dissipation primarily occurring in the direction perpendicular to the building layers. The laser beam's heat source influences the grain nucleation/growth, and in the cross-section, this results in elongated and larger grains. However, in the top view, the

grains exhibit more variation in size, particularly because the cooling rates are faster on the surface and across different regions, limiting the grain growth compared to the bulk of the material.

In the top view, a prominent alignment of <001> oriented grains were observed, which are generally aligned in the BD. This alignment is perpendicular to the thermal gradient, induced by laser beam. The preferential growth of <001> oriented grains is encouraged by the directional solidification that occurs as the material cools during deposition. This alignment is particularly advantageous for electrical steel, as the <001> orientation enhances magnetic properties by reducing magnetic losses in the material. The alignment of <001> grains in the building direction is critical because it depresses the hard magnetisation axis, specifically <111>, which is less prominent here. This is favourable for magnetic performance, as the <111> orientation is typically associated with higher magnetisation resistance. The variation in grain size across different regions of the top view sample can also be attributed to local differences in heat distribution and solidification conditions during the LMD process. Areas closer to the centre of the sample might experience slower cooling, allowing for more significant grain growth, while the edges cool more quickly, resulting in smaller grains. This variation in grain size and distribution is a common feature in additive manufacturing processes, where localised thermal conditions can significantly impact the microstructure [344]. In fact, the grain morphology during solidification is governed by the solidification front instability, which is closely related to undercooling conditions. Increasing the extent of undercooling promotes equiaxed dendritic growth, and this is mainly determined by the thermal gradient (G) and the solid/liquid interface movement speed (R) . A lower G/R ratio increases undercooling, favouring equiaxed solidification morphology. This aligns with the observation in the top view and cross-sectional grain sizes of sample ST4, which highlights the influence of laser power and thermal gradients on grain growth. The grains in the top view are significantly smaller, with a 73% reduction in size compared to the cross-section. The alignment of <001> grains in the BD enhances the material's magnetic properties, while the reduced prominence of the <111> orientation contributes to improved performance for electrical steel applications. The variation in grain size across the top view reflects the local thermal conditions experienced during the LMD process, leading to differing solidification rates across the sample. This is consistent with the results observed for different building orientations, as the geometry configuration and cooling conditions during solidification vary, altering the solid/liquid interface velocity and ultimately affecting the grain morphology [345].

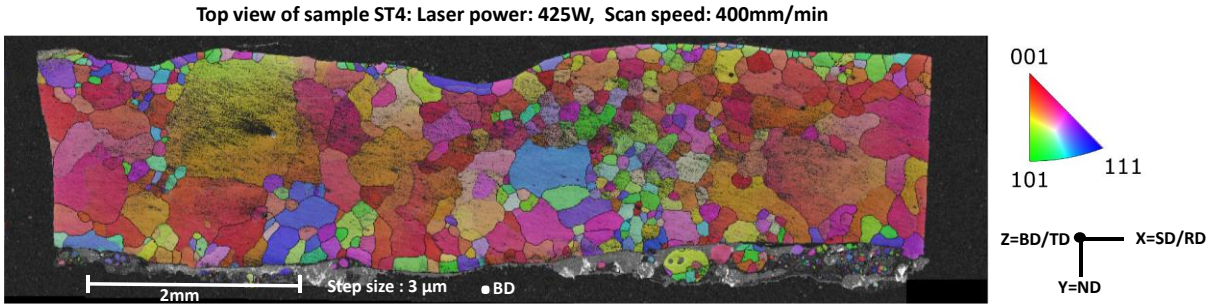

Figure 93. EBSD top view showing variation of <001> oriented grains in ST4 tooth gear.

7.4 Effect of energy density on texture development

Investigating the effect of laser energy density on texture development in electrical steel is crucial for understanding. These have a significant impact on the material's magnetic properties. The bar charts in Figure 94 (a) and (b) illustrate the area fractions of different fibre orientations in electrical steel samples manufactured using LMD which determined through MTEX measurements along the BD direction. These samples are analysed at an energy density of 63.8 J/mm² across different sections: S6 cross section, S6 surface section, and ST4 (Tooth) cross section. In Figure 94 (a), the focus is on fibres oriented along the BD manufactured by AM. The area fraction of fibre <100>//BD is significantly high in all sections, reaching nearly 0.8 in the ST4 (Tooth) cross section and slightly below 0.7 in both the S6 cross section and S6 surface section. This indicates that the LMD process at this energy density strongly promotes the formation of the <100> orientation, which is beneficial for magnetic properties due to its easy axis for magnetisation. The area fractions of fibre <101>//BD and fibre <111>//BD are considerably lower, with <101> peaking around 0.15 and <111> remaining under 0.1 across all sections. This distribution suggests that while the LMD process favours the <100> fibre, it does not significantly promote the formation of <101> and <111> fibres, which are less favourable for magnetic properties due to their medium and hard magnetic axes, respectively. Figure 94 (b) illustrates the area fractions of various fibres oriented along the BD for different sections of LMD discs processed at an energy density of 63.8 J/mm², highlighting the impact of this energy density on fibre orientation as measured by METX in the BD direction. The Goss orientation shows the highest area fraction across all samples, peaking at approximately 0.4 in the S6 cross section. This represents an 11% increase compared to the S6 surface section (0.36) and a 150% increase compared to the ST4 cross section (0.16). This indicates that the LMD process at this energy density strongly favours the formation of Goss orientation, which is beneficial for magnetic properties. The cube orientation is also prominent, with an area fraction of about 0.52 in the ST4 (Tooth) cross section, representing a 247% increase compared to the S6 surface section (0.15) and a 373% increase compared to the S6 cross section (0.11). This suggests that the LMD process effectively promotes grains with cube orientation, which enhances magnetic performance. Theta fibre <001>//ND shows substantial presence, particularly in the ST4 cross section, where it reaches an area fraction of 0.61. This represents a 97% increase compared to the S6 cross section (0.31) and a 281% increase over the S6 surface section (0.16), further supporting the LMD process's role in

promoting fibres with favourable magnetic properties. In contrast, the gamma fibre <111>//ND and alpha fibre <110>//RD, which are generally less favourable for magnetic applications, exhibit much lower area fractions. The gamma fibre peaks at about 0.11 in the S6 surface section, while the alpha fibre reaches a maximum of 0.10 in the S6 cross section. These lower values suggest that the LMD process at this energy density suppresses the formation of these less desirable fibres. Overall, the chart analysis indicates that the LMD process at 63.8 J/mm². Overall, the chart analysis indicates that the LMD process at 63.8 J/mm² results in variation in the formation of fibre orientations, including those favourable for magnetic properties, such as Goss, cube, and theta orientations, alongside the presence of less advantageous fibres like gamma and alpha. This variation in fibre formation across the disc's sections likely come from location-specific factors, such as heat distribution or other conditions during printing, which influence the microstructure. These findings demonstrate the potential of LMD to optimise the microstructure for improved magnetic performance in electrical steel, as evidenced by the area fractions measured in the BD direction.

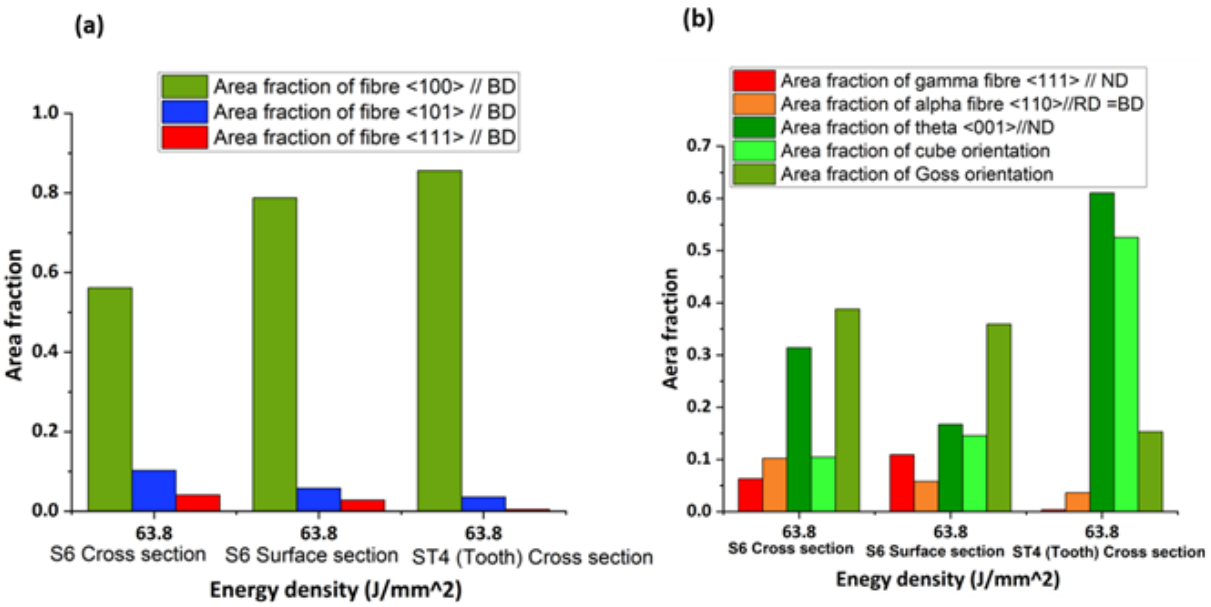

Figure 94. Variation in fibre orientation across different regions of an additive-manufactured discs processed at 63.8 J/mm².

7.5 Orientation distribution functions of discs

The following analysis compares the ODF sections for two different samples, S6 and ST4 (Figure 95). Both samples were produced using the same laser power and scan speed, but the cross-sectional area of the tooth gear in ST4 is smaller compared to the cross-section of S6. For sample S6, the cross-section at in the ODF φ_2=0° section reveals a strong Goss texture (011)[100]. This texture is highly beneficial for magnetic properties due to its high magnetic permeability and low core loss, making it ideal for electrical steels. In contrast, sample ST4 at in the ODF φ_2=0° section shows a strong cube texture (001)[100], which is also favourable for magnetic properties, providing excellent magnetic flux density and reducing magnetic hysteresis losses. In the ODF φ_2=45° cross-section of sample S6, there is a continued presence

of the strong Goss texture (011)[100], accompanied by a weaker (113)[0$\bar{3}$1] texture. The strong Goss texture remains beneficial, while the (113)[0$\bar{3}$1] texture, although weaker, does not significantly weaken from the magnetic properties. For sample ST4 in the same section, a strong cube texture (001)[100] is again observed, along with a strong (113)[0$\bar{3}$1] texture. The cube texture continues to contribute positively to the magnetic properties, and the pronounced (113)[0$\bar{3}$1] texture, while more significant than in S6, does not substantially alter the favourable characteristics provided by the cube texture. A common and positive observation for both samples is the absence of detrimental fibres such as <111> gamma or alpha fibres <111>[110]. These fibres negatively affect magnetic properties by increasing magnetic losses and reducing magnetic permeability. Their absence in both samples indicates favourable microstructures for magnetic applications.

In summary, both S6 and ST4 exhibit strong, desirable textures—Goss and cube—that are advantageous for the magnetic properties of electrical steel. S6 shows a consistent presence of Goss texture across different sections, while ST4 demonstrates a strong cube texture with an additional strong (113)[0$\bar{3}$1] texture at φ_2=45^0. The absence of detrimental γ (gamma) and α (alpha) fibres in both samples further confirms their suitability for magnetic applications in electrical steels. Overall, while both samples are favourable, S6 may have a slight edge due to the consistent presence of Goss texture, which is particularly known for its excellent magnetic properties.

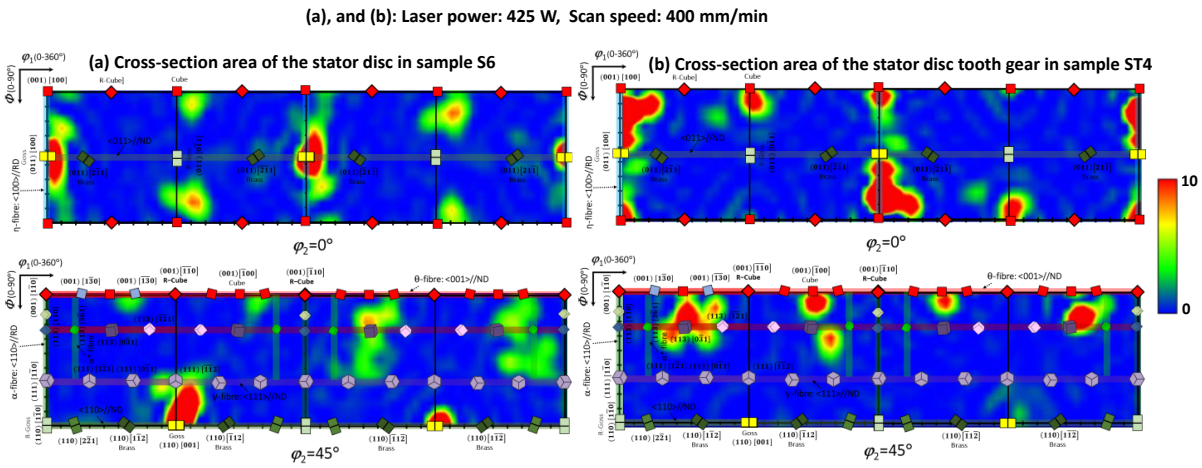

Figure 95. Comparison of texture in the ODF sections of samples S6 and ST4 at φ_2=0° and φ_2=45°.

7.6 Grain size evolution of discs in different areas of sample

Grain size evolution plays a pivotal role in balancing magnetic and mechanical properties in electrical steel. Recent studies [370] highlight its importance in optimising this balance, influencing both mechanical strength and magnetic performance. From crystallographic texture intensity and measured properties, quantitative analyses have concluded that grain size is another critical factor in optimising both mechanical strength and magnetic performance. Understanding and controlling grain size evolution is therefore essential for enhancing the overall effectiveness of electrical steel in different perspectives.

In this study, the LMD process, applied at a consistent energy density of 63.8 J/mm² (laser power of 425 W and scan speed of 400 mm/min), was used to fabricate additive-manufactured disc-shaped sample. Grain size distribution varies across different regions of these sample, labelled S6 and S4, despite uniform processing conditions, due to the influence of each region's location during printing. The bar charts (Figure 96) show grain size distributions in these regions. In the region labelled S6, the distribution includes fractions of 37% for grains around 500 µm, 23% for grains between 500 and 1000 µm, 17% for grains between 1000 and 1500 µm, and 23% for grains around 2500 µm, with 77% of grains falling within the 0-1500 µm range. This indicates a tendency towards smaller grain sizes in S6. In contrast, the region labelled S4 exhibits fractions of 14% at 500 µm, 25% at 1000 µm, 18% at 1500 µm, 17% at 2500 µm, and 26% at 3000 µm, with 57% of grains within the 0-1500 µm range, reflecting a broader spread that includes a notable portion of larger grains (e.g., 26% at 3000 µm). These differences in grain size distribution within the same sample arise because the location of each region within the printed disc affects how it experiences temperature gradients and cooling rates during the LMD process. For example, S6's smaller grains suggest it cooled faster, likely due to its position (e.g., near the surface or an edge), where heat dissipates more quickly, restricting grain growth. Conversely, S4's larger grains indicate slower cooling, possibly in a central or thicker area where heat is retained longer, allowing grains to grow larger due to prolonged exposure to elevated temperatures. This variation highlights how microstructural development depends on positional factors like cooling rate and temperature distribution across the disc, even under identical processing parameters.

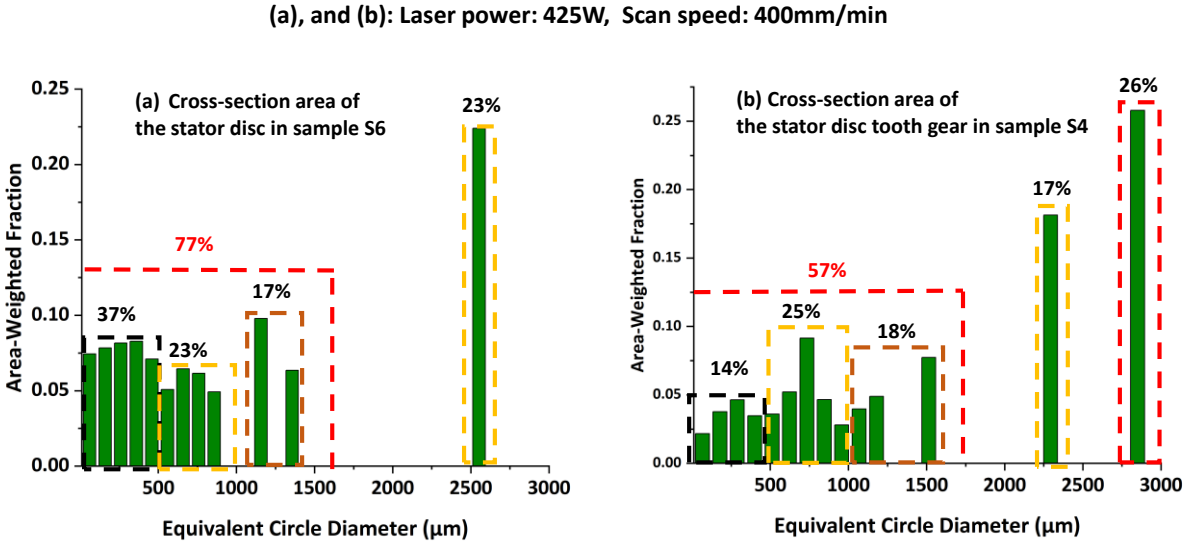

Figure 96. Grain size distribution in regions (a) S6 and (b) S4 of an additive-manufactured disc processed at 63.8 J/mm.

7.7 Kernel average misorientation analysis of disc samples

The KAM analysis of the FeSi 6.5 wt% alloy discs samples, produced using the LMD process, reveals important microstructural details, particularly focusing on sub-grain boundaries and dislocation structures. It is important to note that, for this KAM analysis, grain boundaries

with misorientations of 2° or less than that, as well as sub-grain boundaries with misorientations above 10°, were excluded. This approach helps to concentrate on local dislocation structures and misorientations, which are more relevant for analysing the magnetic performance of the material. The cross-section of sample S4 shows an average KAM value of 0.58°, indicating low local misorientations. The KAM map shows that 45% of the boundaries in this sample are sub-grain boundaries, and 54.8% are grain boundaries. However, given the focus of the KAM analysis, these boundaries are not typical high-angle boundaries. Instead, they reflect regions where geometrically necessary dislocations (GNDs) cause minor lattice misorientations, indicating a relatively low level of internal plastic deformation.

In LMD, the regions of minor lattice misorientations typically observed are not indicative of large-scale misorientations but are instead due to the presence of GNDs. These dislocations form to accommodate local plastic deformation gradients within the grains, which arise from the rapid thermal gradients and cooling rates inherent in the LMD process. As a result, these minor misorientations reflect a relatively low level of internal plastic deformation, which is characteristic of the localised nature of the deformation during deposition. The formation of GNDs is crucial in LMD, as they help the material adjust to the strain induced by the laser's thermal effects, influencing both the microstructure and mechanical properties of the final deposit [411]. These small misorientations, captured by the KAM analysis, are associated with the development of sub-grain structures. Since grain boundaries with misorientations below 2° and sub-grain boundaries above 10° were excluded, the analysis is specifically focused on detecting slight lattice distortions within grains due to dislocations, rather than large-angle grain boundary misorientations [359].

The comparison between the cross-section (S4) and surface area (S6) of the same sample, despite using the same processing parameters (laser power of 425 W and a scan speed of 400 mm/min), shows different KAM distributions Figure 97. This variation is likely due to several factors inherent to the LMD process, including localised thermal gradients and non-uniform cooling rates, which affect the microstructure and dislocation density in different regions of the sample. For instance, certain areas of the sample might cool faster or slower, resulting in local differences in dislocation density and sub-grain formation. This, in turn, leads to different KAM values when comparing the cross-section and surface area. Additionally, during the preparation of sample S6, issues like solvent residue, surface cracks, and non-indexed regions caused by uneven surfaces can introduce noise into the KAM maps. These issues result in artificially elevated KAM values, making it difficult to draw precise conclusions about the actual microstructure in those regions. Such preparation-induced noise is particularly evident in areas where KAM analysis may not accurately reflect the underlying dislocation structure or sub-grain boundaries. The observed differences in KAM values between sections of the same sample can therefore be attributed to a combination of processing factors—such as localised cooling behaviour and solidification patterns, as well as sample preparation issues that create artifacts and distort the KAM measurements. These variations, despite identical

processing parameters, highlight the sensitivity of KAM to local conditions within the additive manufacturing process and reinforce the importance of careful sample preparation. The low KAM values are closely linked to low local misorientations within the microstructure, indicating a lower density of dislocations and less internal strain vice versa is true [412]. This is highly beneficial for the magnetic properties of FeSi 6.5 wt% electrical steel for several reasons such as lower core losses, reduced magnetocrystalline anisotropy, minimised pinning of magnetic domain walls, improved magnetic saturation, lower coercivity.

In summary, the KAM analysis of your FeSi 6.5 wt% samples focus on small misorientations within grains caused by dislocations, excluding larger grain boundary misorientations to better understand the influence of GNDs and sub-grain formation. Regions with low KAM values, which indicate low dislocation density and minimal internal strain, are particularly beneficial for the magnetic properties of the material. These low KAM regions help reduce magnetocrystalline anisotropy, lower core losses, and minimise domain wall pinning, all of which contribute to higher magnetic permeability, lower coercivity, and improved magnetic saturation [413]. The observed differences in KAM values between the cross-section (S4) and surface area (S6) can largely be explained by local variations in thermal gradients, cooling rates, and preparation artifacts, despite the consistent use of LMD processing parameters. This highlights the importance of controlling the LMD process and sample preparation to achieve optimal microstructure and magnetic performance in electrical steel.

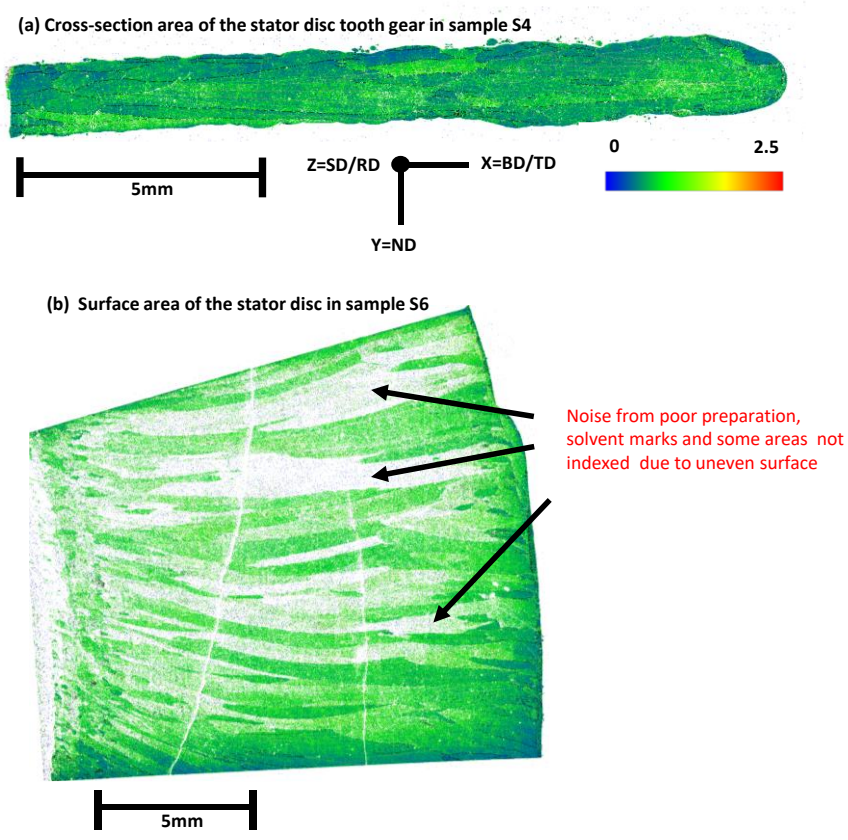

Figure 97. Overview of KAM map (a), cross section of sample S4 and (b), surface area of sample S6.

Chapter 8

8 Key achievements, contributions to knowledge, and final reflections

This project represents a significant advancement in the additive manufacturing (AM) of soft magnetic materials, particularly high-silicon electrical steel (FeSi 6.5 wt%), for applications in electrical machines. By tackling long-standing challenges such as cracking susceptibility and the optimisation of crystallographic texture, this research delivers groundbreaking innovations in material science, AM processes, and electrical machine design. Critically, the project is distinguished by its ability to achieve controlled grain alignment along the orientation—a vital factor for minimising magnetic losses—while suppressing undesirable textures that impair performance. The project is distinguished by its ability to achieve controlled grain alignment along the <001> orientation, a critical factor for magnetic performance, while minimising undesirable <111> textures. It successfully defined the optimum process parameters for fabricating high-silicon steel components using the laser metal deposition (LMD) process. These achievements collectively represent a leap forward in the development of advanced manufacturing techniques for magnetic materials and their application in high-performance electrical machines.

The research overcame key technical barriers, demonstrating innovative solutions to challenges associated with the brittleness of high-silicon content electrical steels, porosity, cracking, and suboptimal texture in AM components. It also provided a comprehensive understanding of how processing parameters influence the microstructural and textural evolution of FeSi 6.5 wt%, ultimately establishing a strong foundation for integrating LMD technology into the manufacturing of electrical machines. Furthermore, this study not only addressed existing challenges in the field but also highlighted the untapped potential of AM technologies in revolutionising the electromechanical industry. The criticality of this work lies in its potential to enable more energy-efficient electrical machines, reducing global energy consumption and supporting sustainable practices in an industry facing increasing demands for low-loss materials. The research findings contribute broadly to material science and AM, creating new opportunities for the design and manufacture of advanced electrical machines.

The key achievements of this research have been presented at multiple international conferences and published in various peer-reviewed journals, ensuring broad dissemination within both academic and industrial communities. These publications serve to solidify the impact of this study, ensuring its findings are accessible and influential within the fields of additive manufacturing and electrical machine design.

8.1 Chapter 1: Importance of non-grain oriented electrical steels (NGOES)

This chapter provided a comprehensive overview of the importance of non-grain-oriented electrical steels (NGOES) in electrical applications, emphasising their superior magnetic properties, such as high permeability, low energy losses, and high saturation magnetisation. These properties make NGOES an essential material for energy-efficient and high-performance electrical machines. However, the incorporation of high silicon content,

especially above 3.2 wt%, introduces brittleness, which complicates production using conventional manufacturing methods. Our research demonstrated that AM techniques, particularly LMD, offer transformative potential to overcome these limitations. By enabling the fabrication of components with large columnar grains and optimised textures, LMD enhances the magnetic performance of high-silicon steels, addressing critical barriers to their widespread application.

The chapter also explored the metallurgical factors influencing the performance of NGOES, including silicon content, grain size, and crystallographic texture, emphasising the necessity of precise control over these parameters. This research positioned LMD as a promising solution for the sustainable and efficient production of NGOES, highlighting the need for further advancements in hybrid manufacturing approaches that combine AM with thermomechanical processing. Such approaches are vital for achieving improved material quality and meeting the growing demand for environmentally sustainable manufacturing practices in the electrical machine industry. The findings discussed in this chapter are comprehensively reinforced and expanded in the publication “Manufacturing of Non-Grain-Oriented Electrical Steels: Critical Review”. This paper investigates deeper into the challenges of NGOES manufacturing and highlights innovative solutions, providing a critical analysis that complements and validates the insights presented in this chapter.

NGOES are one of the most widely and extensively used for electrical steel applications due to their superior properties such as high permeability, high magnetisation saturations, and low losses. Therefore, NGOES are expected to be the driving force in the global market for electric power consumption in the future due to energy efficiency, CO_2 regulation, environment impact and its cost effectiveness compared to GOES. A number of metallurgical factors have a considerable impact on the magnetic properties of NGOES, such as Si content, grain size, sheet thickness, crystallographic texture, and contamination levels. These variables are capable of some degree of manipulation during the manufacturing process. This review chapter provides a concise overview of the current manufacturing technology of NGOES, highlighting its significance as a key material for electrical machines and generators' stators and rotors, and also the rising demand in the modern needs. Improving the efficiency of electric motors is crucial for consumers and the environment. To take advantage of the benefits of electrical steels, it is essential to develop new manufacturing techniques that optimise the microstructure and achieve high Si production. The current manufacturing routes for electrical steel sheet fabrication have been thoroughly studied from a metallurgical standpoint. It has been demonstrated that increasing the Si content in NGOES up to 6.5 wt.% can improve their magnetic properties. Due to the formation of brittle phases at higher Si levels, mass production of materials with a high Si content (above 3.2%) using conventional manufacturing methods presents challenges. In the presence of such brittle phases, it is very challenging to fabricate these materials. As a result, alternative manufacturing techniques have been reviewed in terms of their capabilities and limitations, as described in different sections. These alternative methods provide promising avenues for overcoming the obstacles

posed by the high Si content of NGOES, paving the way for enhanced manufacturing processes and improved performance of electrical machines and generators.

Skew rolling and cross rolling techniques were found to be effective in developing the desired microstructure by altering the plain strain conditions at different rolling stages. Whereas processes such as ASR and R-BUT introduce shear plastic deformation across the sheet thickness, which is essential for achieving desirable crystallographic orientations, particularly the <001> texture, while preventing the formation of undesirable <111> fibre during the final stage of annealing heat treatment. It should be noted that implementing any of these processes would necessitate infrastructure modifications. In addition, the efficiency of these operations is highly dependent on process parameters, which can be difficult to control in cases such as ASR and may incur substantial infrastructure costs in the cases of skew rolling and R-BUT. Alternatively, PVD and CVD methods have demonstrated the ability to produce NGOES with a high Si content at low production volumes. This is accomplished through the diffusion of Si into the material's core. However, due to the significant cost involved and environmental concerns, these operations are not considered sustainable. Recent studies have demonstrated that AM technologies have great potential for the fabrication of NGOES with high Si contents (e.g., 6.9 wt.% Si). The flexibility of AM processes permits the use of powder materials with customised chemical compositions. In addition, AM can facilitate the development of large columnar <001> grains along the building direction, which is advantageous for magnetic applications in electrical steel through process optimisation. It is noted that careful process optimisation is essential to avoid both microscopic and macroscopic defects that could impair the magnetic performance of the final products. Additionally, utilising AM to produce thin sheets presents a technical challenge. This difficulty may be overcome through a hybrid approach by combining AM with thermomechanical operations. For instance, the hybrid method may involve AM fabrication of NGOES components with customised chemical compositions, followed by high temperature rolling (below the recrystallisation temperature) to achieve the desired thickness.

To enhance the magnetic properties of NGOES, achieving a columnar grain structure with fewer grain boundaries would be ideal, this can be achieved through the appropriate processing parameters in the AM process. Consequently, the industry is ready to transition from old paradigms (conventional fabrication) to innovative technologies such as AM. This shift is not limited to manufacturing soft magnetic materials but extends to other critical aerospace materials as well. The appeal lies in AM's flexibility, reduced waste, faster prototyping, and ability to manufacture complex structures. However, improvements are still necessary to enable mass production efficiently. Having discussed how thermomechanical processes and AM could potentially improve the texture, microstructure, magnetic, and mechanical properties of NGOES, resulting in electrical motors with higher efficiency, future research on NGOES necessitates exploring new ideas, develop new materials, and concepts. For example, recent studies [386] have highlighted the use of polymeric matrices for coating soft electronics, offering excellent insulation and corrosion protection. This approach can be

applied to coat the stator of electrical machines (NGOES) manufactured by thermomechanical, or AM, addressing cracks that may occur during the manufacturing process. A similar approach was taken by another study [387], where microscopic cracks obtained from LPBF of 6.5% FeSi were filled with epoxy resin, resulting in improved mechanical performance by 40%.

In terms of developing alternative soft magnetic materials, exploring new options may offer solutions to enhance the performance of electrical machines. Numerous reports suggest that, among all substances, only three elements exhibit ferromagnetic properties at room temperature: Fe, Ni, and Co. These materials are essential minerals used for electrical machines. However, the extraction and processing of cobalt, in particular, present significant challenges. Nonetheless, in 2018, scientists at the University of Minnesota reported that ruthenium (Ru) possesses unique magnetic properties at room temperature. It is believed that Ru, specifically in its metastable tetragonal phase, represents the fourth ferromagnetic material, potentially revolutionising the electrical industry. These findings suggest that, based on the Jahn-Teller magnetisation effect [414], ferromagnetic materials can be produced from a substance beyond the commonly known three elements. This breakthrough could be a game-changer in numerous everyday applications, including electric motors, transformers, generators, and sensors. However, its limitations in terms of cost, availability, supply security, recyclability, and technical challenges need to be carefully considered before widespread use [415, 416]. For future research in manufacturing NGOES, several pathways are recommended. Primarily, optimising process parameters remains paramount. This includes developing new alloy compositions tailored specifically for NGOES applications, further exploring AM for NGOES mass production, advancing coating techniques, investigation of crack formations, and enhancing characterisation methods. Additionally, emphasis on research efforts focused on recycling NGOES and reducing energy consumption in the manufacturing process to minimise the environmental footprint of production is required.

8.2 Chapters 2, 3 and 4: LMD technology and applications, characterisation and results

This study provided an in-depth examination of LMD technology, emphasising its transformative capabilities for the additive manufacturing of magnetic materials. Through a particular analysis of the process parameters, including laser power, scanning speed, and energy density, the research highlighted their critical influence on the physical and metallurgical properties of the deposited components. It demonstrated how the optimisation of these parameters can significantly enhance the properties of soft magnetic materials while extending their service life and reliability. By systematically correlating parameter adjustments to material outcomes, this work established a robust framework for tailoring the performance of high-silicon steel components manufactured via LMD.

The detailed characterisation of feedstock powders, substrate preparation, and LMD platform conditions highlighted the importance of precise material and process control. Experimental trials validated the suitability of FeSi powder for AM applications and revealed key insights into optimising process parameters to enhance the magnetic properties of printed

components. By expanding the understanding of parameter-property relationships, this research provided a valuable contribution to the growing field of AM for magnetic materials, offering pathways for future industrial applications.

In summary, the laser metal deposition method is a crucial additive manufacturing technique that may be used to create functioning components and repair expensive items that were previously unrepairable. The changing physical, metallurgical, mechanical, and tribological characteristics of the deposited components are significantly influenced by the processing conditions. This chapter examined the crucial processing variables in the LMD process. The laser power, scanning speed, powder flow rate, gas flow rate, laser beam diameter, and overlap percent are the process parameters that were examined. Each of these processing factors how it affected the characteristics and economics of the LMD process was thoroughly investigated. The chapter demonstrated that these processing variables must be optimised depending on the desired qualities from the deposited component. The chapter has also discussed the application of this technology to surface modification, and other factors. This technique is crucial to the future of manufacturing since it gives the potential to produce new components, repair materials, allowing for more efficient use of materials over a longer period of time. This procedure allows for the manufacturing a new component and or even repair of several parts that were previously unrepairable. Furthermore, it is possible to manufacture and remanufacture outdated components by altering the design and utilising the LMD method to create a new part on an old part, avoiding the need to discard the outdated machinery. By employing the technique to deposit more resilient materials on the surface of base materials, the LMD method is also helpful for increasing the service life of components as well as manufacturing a new components from scratch [201].

These chapters outline the materials and methods used in the study, detailing the feedstock powder characterisation, substrate preparation, and the LMD platform employed. It covers the methodologies for evaluating deposition components, including material preparation and microstructure assessment. The study investigates the properties of FeSi powder used in additive manufacturing, with specific focus on its chemical composition and particle sizes. High-silicon electrical steel powder was characterised using different techniques such as Hall flowmeter, SEM confirming its consistency of it. SEM analysis revealed spherical particles with some satellite particles, and EDS analysis confirmed the presence of key elements such as Fe, Si, and Al. MIPAR software quantified the particle size and shape from SEM images, indicating a range of particle sizes and shapes, with most particles being relatively circular. Substrates were prepared from mild steel blocks by cutting and shaping them into cylindrical forms using a bandsaw and EDM machine. A hybrid LMD system, incorporating a CNC Milling machine and Ytterbium fibre laser, was used for various depositions, including single tracks, thin walls, cubes, to investigate process parameters. The optimisation of laser power, scan speed, and energy density was crucial for producing high-quality FeSi components. Key findings included an optimal laser power of 450 W for minimal defects and improved magnetic properties, and an ideal scan speed of 400 mm/min for stable tracks and reduced porosity. The study

identified optimal energy densities and parameters for producing geometrically accurate and high-quality components, guiding adjustments such as reducing z-step to prevent overbuilding and optimising scanning strategies.

Experimental trials for FeSi thin wall manufacturing involved varying power, scan speed, and energy density. Energy levels were color-coded in Table 5: low (yellow), medium (green), and high (red). Initial trials (TW201 to TW203) revealed issues with cracks, delamination, and debonding, leading to adjustments in power and scan speed. Subsequent trials (TW204 to TW207) included varied passes and powers, with improved results in bonding and reduced defects. A notable trial (TW208) used a combination of 316L austenitic steel and FeSi, yielding promising results with minimal delamination but one crack. Preheating experiments aimed to mitigate cracking and delamination. Preheating to 200°C generally led to successful results, although some delamination occurred at 90°C. 3D scanning using the Hexagon absolute arm laser accurately measured the height and thickness of thin walls and cubes, showing that correct processing parameters achieved desirable dimensions and reduced defects. The next phase of the project involved producing 7 cubes using various scanning strategies and energy densities to analyse their effects on geometry, cracks, and microstructure. Temperature measurements during additive manufacturing showed peaks with each new layer followed by declines over time. This highlights the importance of maintaining adequate temperature control to reduce residual stress, which in turn minimises defects and ensures strong bonding between layers. In summary, the experiments highlight the importance of optimising processing parameters and preheating to improve the quality of FeSi thin walls and cubes. Adjustments led to improvements in bonding and reduction in defects, providing a foundation for further exploration with varied scanning strategies and energy densities. This detailed analysis of trials and process parameters is essential for advancing additive manufacturing techniques and applications.

Hardness testing further validated the material's performance, with higher energy densities yielding increased hardness due to improved layer fusion and reduced porosity. The formation of ordered phases, such as DO_3 and B_2, was identified as a likely contributor to enhanced hardness, emphasising the importance of further phase characterisation studies to confirm their presence and impact. The study examines micro-hardness through Vickers testing on thin walls, cubes, and discs of electrical steel with 6.5 wt% silicon content. Results showed a clear correlation between energy density and hardness, with both thin walls and cubes demonstrating increased hardness with higher energy densities. For thin walls, hardness increased by approximately 3.6% with higher energy density and by 7.2% with larger grain size. Cubes showed a similar trend, with hardness rising by about 4.4% as energy density increased and by 3.9% as grain size grew. These increases in hardness can be attributed to better fusion between layers at higher energy densities, which reduces porosity and enhances the material's microstructure. It can be suggested that rapid cooling rates associated with higher energy densities lead to finer grains that inhibit dislocation movement, thus increasing hardness. The chapter also notes that larger grain sizes contribute to hardness due to the

formation of ordered phases or intermetallic compounds (Do_3 and B_2) in high-silicon steel alloys. These phases act as barriers to dislocation movement, further enhancing hardness. Observations reveal that thin walls and cubes processed under optimal parameters show substantial increases in hardness, with thin walls achieving a maximum hardness of 385.8 HV_1 and cubes reaching up to 376 HV_1. The study highlights that the hardness data varies significantly between the first deposited layer and subsequent layers. Thin walls show a marked increase in hardness from around 150 HV_1 at the first layer to approximately 400 HV_1 at 1 to 2 mm height, stabilising between 350 and 400 HV_1 up to 20 mm. Cubes exhibit stable hardness with minor fluctuations, ranging from 350 to 400 HV_1. Discs processed with consistent parameters also show a rise in hardness, peaking around 400 HV_1 at 1 to 2 mm and stabilising between 350 to 400 HV_1 up to 15 mm. The initial lower hardness in discs is attributed to the interaction with the substrate and processing conditions, with increased hardness observed in later layers due to optimised processing. Overall, the chapter highlights the importance of processing parameters in determining the hardness and properties of Fe-Si alloys. Higher energy densities improve hardness by ensuring better layer fusion and reducing defects, while larger grain sizes contribute to increased hardness through ordered phase formation. The findings confirm that optimised LMD processing conditions are crucial for enhancing material properties, which is vital for applications in electromagnetic devices like transformers and electric motors.

8.3 Chapter 5: porosity and crack mitigation

Chapter 5 addressed the persistent challenges of porosity and cracking in FeSi 6.5 wt% components produced via LMD, providing critical insights into defect formation and mitigation. The study revealed that laser processing parameters, such as power and scan speed, play a pivotal role in determining the prevalence of defects like metallurgical pores, keyhole pores, and incomplete fusion. It demonstrated that higher laser power improves melting efficiency, reducing porosity, while increased scan speed promotes rapid solidification, minimising pore formation. Based on systematic experimentation, the process windows for manufacturing FeSi 6.5 wt% were successfully established, achieving a porosity percentage of less than 0.3% with no visible cracks.

Advanced techniques, including preheating the substrate and modification of laser parameters, were shown to be effective strategies for minimising defects. X-ray computed tomography provided detailed insights into internal flaw structures, offering a comprehensive understanding of defect characteristics and their origins. The research also emphasised the significant impact of LMD's complex thermal history on microstructural evolution, particularly grain size, texture, and crystallographic orientation. These findings are instrumental in guiding future efforts to optimise the LMD process, ensuring high-quality components with minimal defects. The insights presented in this chapter are further explored and substantiated in the publication “Process window for manufacturing soft magnetic FeSi 6.5% by laser metal deposition”. This paper elaborates on the process parameters, experimental methodologies,

and critical findings of chapter 5, contributing to the advancement of additive manufacturing techniques for soft magnetic materials.

This chapter presents an analysis of porosity and cracks in FeSi thin walls and cubes produced using LMD. The focus was on understanding how various laser parameters and scanning strategies impact these defects and subsequently affect the material's mechanical and magnetic properties. Samples were sectioned using an EDM machine and underwent a precise grinding and polishing process, which included grinding with SiC water-cooled papers of varying grits, polishing with Mg oil-based Metadi, and concluding with microcloth polishing. This preparation aimed to ensure accurate evaluation of porosity and cracks.

The types of porosity identified were metallurgical pores, keyhole pores, and incomplete fusion. Optical and SEM revealed that large, irregularly shaped metallurgical pores were attributed to gas entrapment and insufficient scan speeds. Keyhole pores, which were small and spherical, were linked to instability in the melt pool. Incomplete fusion resulted from inadequate energy input leading to poor interlayer bonding and discontinuities. The impact of processing parameters on these defects was significant. Higher laser power improved penetration and melting, reducing pores size but not eliminating it. With increasing power, pores became smaller but remained uniformly distributed. Increased scan sped led to a decrease in both the amount and size of porosity, attributed to reduced cooling time and improved solidification. Cracks, observed primarily due to high thermal gradients and stresses intensified by FeSi's high silicon content, were affected by laser power and scan speed. Higher laser powers and slower speeds generally increased crack size. Effective preheating and optimised parameters were crucial to mitigating these issues. The X-ray computed tomography (XCT) provided non-destructive insights into internal porosity and cracks, showcasing the effectiveness of process adjustments. Higher laser power generally improved quality by reducing internal voids and enhancing material fusion.

In conclusion, the study highlights the importance of managing porosity and cracks during the LMD of FeSi thin walls and cubes. Effective control of laser power and scan speed is essential for minimising porosity. Higher laser power typically enhances melting and reduces porosity, while faster scan speeds improve solidification and decrease pore formation. Cracks are significantly influenced by thermal gradients and residual stresses, with higher laser power and slower scan speeds increasing the risk of cracking. Preheating and careful control of process parameters can help mitigate some cracking issues, although the inherent properties of FeSi pose challenges. XCT analysis proves invaluable in identifying and addressing internal defects, emphasising the need for optimised processing parameters to enhance material quality and reduce defects.

8.4 Chapter 6: Microstructure and texture evolution in LMD FeSi 6.5%

Chapter 6 investigated into the microstructural and textural evolution of FeSi 6.5 wt% components fabricated via LMD, revealing critical insights into the interplay between processing conditions and material properties. The research demonstrated that controlled laser energy input and scanning strategies are essential for achieving uniform grain alignment,

particularly along the <001> orientation, which is crucial for enhancing magnetic performance. Higher energy densities were found to promote larger melt pools, directional solidification, and the development of <001> textures, resulting in improved magnetic properties.
The analysis revealed distinct grain structures influenced by variations in scanning speed, with faster speeds producing finer equiaxed grains that reduce the risk of cracks. Conversely, slower speeds led to larger grains that, while beneficial for texture alignment, are more susceptible to residual stress-induced cracking. The study also highlighted the influence of scanning strategies, such as rotational scanning, on texture development, with 90° rotations enhancing <001> alignment. However, unidirectional scanning was identified as the optimal strategy for promoting epitaxial grain growth in cube samples and minimising disturbances to the thermal gradient.

Detailed Kernel Average Misorientation (KAM) analysis demonstrated that higher energy densities result in reduced local misorientation and dislocation densities, improving both mechanical and magnetic performance. These findings highlight the importance of laser energy density, scan speed, and scanning strategy in optimising grain size, texture, and fibre orientation, offering valuable guidelines for tailoring the properties of FeSi 6.5 wt% components.

This chapter also extended its findings to compare results with 316L austenitic steel as a foundation layer for FeSi 6.5 wt%, showing that optimised parameters significantly improved bonding, reduced cracking, and enhanced the <001> texture. Geometric modifications played a critical role in texture refinement, further enhancing structural integrity. Together, these results emphasise the importance of energy density, scan speed, and strategy in optimising microstructure and texture, offering a path forward for producing high-performance magnetic components via the LMD. The insights and findings presented in this chapter are further explored in the publication “Additive Manufacturing Innovations: Microstructure Optimisation for Ultra-High Silicon Electrical Steel Components”. This paper expands on the textural evolution, processing conditions, and magnetic performance of FeSi 6.5 wt% components, complementing the chapter's findings and offering deeper insights into the optimisation of LMD processes for soft magnetic materials.

Laser metal deposition involves a complex interplay between the laser source, powder feed, and substrate material, which results in a distinctive thermal history within the component. This section evaluates the microstructure of FeSi 6.5 wt% deposited via LMD and explores the changes that occur throughout the process. The microstructure of the as-deposited FeSi 6.5wt% generally features columnar grains extending up to several millimetres in length, aligned along the BD. Notable variations, such as fine equiaxed grains, are observed at the first and last layers and along the edges of the deposited samples. These variations are attributed to significant temperature gradients within the molten pool, which promote rapid columnar grain growth and reduce the likelihood of new nucleation sites during solidification. The fine grains in specific regions result from increased cooling rates caused by the substrate

acting as a thermal sink and exposure to the atmosphere on multiple sides, leading to a faster solidification process.

Optimising processing parameters, such as laser power, is crucial to preventing defects like cracks, keyhole and porosity at the bottom of the melt pool. Thermal phenomena, including conduction, convection, and radiation, play a critical role in the stability of the melt pool during additive manufacturing. A conduction-mode melt pool is ideal, free from defects like gas porosity and keyhole; however, high laser power can introduce turbulence in the melt pool, leading to such defects. The size of the melt pool is notably large due to high laser power, which has a more significant impact than other factors such as feed rate and powder mass flow. In thin structures like thin walls, substrate preheating deepens the melt pool in conduction mode. The formation of layer bands, similar to those observed in previous studies which is attributed to the superheating effect, which initiates melting in the previous layer's melt pool and forms a narrow band with temperatures exceeding the solidus temperature. The melt pool's curved surface and solidification substructure, growing primarily parallel to the BD, are influenced by high thermal gradients and the tilt of the melt pool toward the laser movement.

Defects such as pores can significantly impact microstructural development. Pores act as thermal sinks, absorbing heat and disrupting normal heat conduction, leading to abnormal temperature increases in the melt pool. This results in two distinct grain regions: equiaxed grains at the pore tip due to blocked heat conduction and higher cooling rates, and elongated grains due to increased heat input and directional solidification. During the solidification of BCC materials like FeSi, atoms preferentially align with less closely packed planes, such as {001}, due to their lower energy configurations. The development of the <001> crystal orientation along the build direction is observed, consistent with findings from other studies where <001>-oriented grains dominate due to their alignment with the thermal gradient and heat flow.

Crystallographic texture analysis was performed using EBSD data. The IPF maps reveal variations in grain size and orientation due to thermal conditions during LMD. The surface view shows elongated grains with a uniform size, aligning with the laser movement. The IPF maps reveal a preference for <001> directions in the BD, which is crucial for enhance magnetic properties such as permeability and reducing core losses. Differences between the cross-section and surface section of the samples are evident. The ODFs for TW21 (with low energy density 63.8 J/mm^2) show strong near-cube fibres in the cross-section and a strong Goss texture in the surface section, arising from varying thermal gradients, mechanical stresses, and surface energy conditions during deposition.

The texture obtained from the pole figures for different samples (TW15, TW18, and TW30) processed with low to high energy densities show that increasing energy input develop the <001> texture and promotes a uniform crystallographic orientation. TW15, with an energy input of 60 J/mm^2, exhibits a moderate <001> texture along the BD as compared to other

samples. As energy input increases to 70 J/mm² for TW18, the texture becomes more balanced among <001>, <101>, and <111> orientations. TW30, with the highest energy input of 75 J/mm², displays a pronounced <001> texture and uniform crystallographic orientation. The EBSD maps and IPFs given in this chapter highlight the correlation between grain morphology, energy density, and <001> texture, showing that increasing laser energy density promotes epitaxial grain growth and enhances the <001> texture along the BD.

The texture obtained from the ODFs for FeSi 6.5 wt% samples TW15 (400 W), TW18 (465 W), and TW30 (500 W) are analysed. TW15 exhibits a more diffuse texture with fewer pronounced components, while TW18 and TW30 display stronger and more defined cube textures compared to the other samples. For example, in the φ2= 0° section, TW18 and TW30 transition to a strong cube texture with increasing laser energy, which is beneficial for magnetic properties. In the φ2= 45° section, TW18 and TW30 show a transition to a strong cube texture close to (113)[121] and Goss orientations, with the absence of <111>//BD (γ-fibre) or <110>//RD (α-fibre) orientations, indicating a favourable texture for magnetic applications. EBSD images of the top side of samples TW15 (400 W) and TW30 (500 W) reveal that TW15 has smaller, more uniform grains with an average diameter of 220 µm, while TW30 has larger grains with an average diameter of 800 µm, about 3.6 times larger than TW15. Higher laser power promotes directional solidification, resulting in a greater proportion of <001> oriented grains in TW30 compared to TW15, enhancing the magnetic performance of the electrical steel. The relationship between energy density and the area fraction of different fibre orientations shows that increasing energy density promotes the formation of <100> fibres while reducing <111> fibres, which positively affects magnetic properties. Increasing energy density from 55 to 81 J/mm² results in a 260 % increase in the weighted average equivalent circle diameter, from 500 µm to over 1800 µm. Factors influencing grain size include thermal gradient, solidification rate, and residual stress. Higher laser power leads to a broader and coarser grain size distribution, with larger grains observed in samples prepared at higher laser power, indicating that higher energy density promotes more significant grain growth during solidification.

This study explores how scanning speed influences grain development in FeSi 6.5% components produced through LMD. As scanning speed increases from 360 to 400 mm/min, grain size reduces by as much as 57%, indicating a notable refinement in the microstructure. However, beyond 400 mm/min, the grain size shows irregular changes due to the complex interplay of heat flow and cooling rates. EBSD analysis highlights those higher speeds, such as scan speed of 440 mm/min (as seen in sample TW27), foster finer, equiaxed grains and reduce the likelihood of cracks. Conversely, slower speeds (e.g., scan speed of 365 mm/min in sample TW19) encourage larger, columnar grains, which are more susceptible to cracking because of increased residual stresses during solidification. Additionally, scanning strategies play a crucial role in shaping the microstructure. Unidirectional scanning produces smaller, elongated grains with a more uniform texture, though slightly misaligned from the BD. In contrast, bidirectional scanning leads to larger, more irregular grain structures due to

alternating thermal gradients, resulting in greater microstructural variability. These variations can influence the material's mechanical and magnetic properties. Ultimately, selecting the optimal scanning speed and strategy is key to improving both the mechanical integrity and magnetic performance of the material by refining grain size and orientation.

The use of 316L austenitic steel as a foundation layer during LMD of FeSi 6.5 wt% effectively addresses challenges such as cracking and poor bonding that occur with direct FeSi deposition on mild steel substrate. A three-layer 316L foundation, optimised with specific laser power and scan speed, significantly improves interface bonding and reduces crack propagation. This method not only prevents delamination—due to similar thermal expansion coefficients between 316L and FeSi—but also enhances the material's magnetic properties, as shown by a strong <001> crystallographic orientation. Additionally, the grain structure, with an average diameter of 685 µm, minimises hysteresis losses, further improving magnetic efficiency. These findings demonstrate the feasibility of multi-material deposition using LMD to enhance FeSi magnetic performance. The study also highlights the impact of geometric dimensions on texture development. Adjusting sample dimensions—specifically reducing height and increasing length—strengthens the <001> orientation, as seen in sample TW34, which showed epitaxial growth in well-defined orientation and no cracking, even without a foundation layer. This suggests that careful control of geometry and substrate temperature can minimise residual stresses and improve structural integrity. A substrate temperature above 200°C may further eliminate the need for foundation layers, offering a new way to reduce material distortion.

The EBSD analysis of FeSi 6.5 wt% samples, specifically cubes, provides valuable insights into the influence of laser energy density on the microstructure. Two representative samples, C16 and C21, were examined, with energy densities of 60 and 90 J/mm², respectively. The EBSD maps reveal distinct textures and grain morphologies for these samples. In C16 (E=60 J/mm²), the grain orientation almost predominantly aligns with the <001> direction along the build direction (BD). In contrast, C21 (E=90 J/mm²) exhibits a more pronounced alignment <001> of grains along the BD. As the laser power increased from 400 W to 600 W while maintaining a constant scan speed of 400 mm/min, the grain orientation in C21 became more aligned along the BD compared to C16, indicating a hypothesis of enhanced grain growth along this direction with increased energy density. Roughly epitaxial growth was observed in areas where the direction of heat flow in neighbouring molten pools aligned with the crystallographic orientation of the previous pool. This effect occurs due to the reduced nucleation barriers compared to crystal barriers. Increased energy density results in a larger melt pool, longer cooling times, and reduced thermal gradients, allowing grains to grow larger during solidification. Higher energy densities can also cause remelting and over-melting of previously deposited layers, altering the microstructure and promoting larger grain growth. Conversely, lower energy densities lead to finer grains due to higher cooling rates and thermal gradients. Crystallographic results provide a clearer picture of the preferred crystallographic orientations. In C21, with increased laser power, a pronounced <001> texture is evident,

attributed to the elongated grain morphology resulting from the higher energy input. The rotational strategy of 90° for each printing layer appears to influence the texture development, with higher laser power favouring <001> orientation and mitigating anisotropy by generating a larger melt pool. Studies suggest that no rotation (0°) is ideal for enhancing the <001> texture due to a larger thermal gradient and better epitaxial growth conditions. The scanning strategy and energy density significantly impact texture, with higher energy densities leading to more pronounced textural development. Also, higher energy densities favour the formation of <100> fibres, which are beneficial for magnetic properties, while reducing the formation of <101> and <111> fibres, which are less favourable. The observed trends are attributed to the thermal cycles and rapid solidification rates inherent in the LMD process, which optimise the alignment of grains in favourable orientations and minimise those in less desirable ones.

This study also examined grain size evolution with varying laser energy densities. Higher laser powers resulted in a broader distribution of particle sizes, with significant increases in larger particles. For instance, sample C21 showed a 33% reduction in small particles, a 56.25% increase in medium-sized particles, and a 1900% increase in large particles compared to C16. This indicates that adjusting laser power can tailor the grain size distribution, optimising mechanical properties and efficiency. In conclusion, EBSD analysis demonstrates that laser energy density plays a crucial role in determining the microstructural characteristics of FeSi 6.5 wt% cubes. Increased energy densities lead to larger grain sizes, more pronounced textures, and favourable fibre orientations, enhancing the material's properties for various applications.

The KAM analysis of the cube samples has provided crucial insights into the microstructural aspects like dislocation densities. It was observed that higher laser power resulted in larger grain sizes and lower KAM values, indicating reduced local misorientation. Samples with smaller grain sizes showed higher KAM values, correlating with greater local dislocation densities and potential stress concentrations. However, the presence of LAGBs, common across all samples, was found to benefit the magnetic properties. By varying laser power and energy density during the AM process, it was possible to influence key microstructural characteristics. Higher KAM values were associated with higher dislocation densities, which in turn affected both mechanical and magnetic properties. Lower KAM values indicated lower dislocation densities and better alignment of grains along the build direction, leading to enhanced material performance. Ultimately, KAM analysis proved to be a valuable tool for optimising AM parameters, helping reduce misorientation and residual stress while improving both mechanical integrity and magnetic properties. These findings highlight the importance of microstructural control in achieving high-performance materials through LMD techniques.

Overall, in this chapter, EBSD case-studies of FeSi 6.5 wt% cubes were explored to understand the impact of laser energy density on texture formation, grain size evolution, and misorientation distributions. The analysis highlighted the relationship between energy density and the development of specific fibre textures, grain growth mechanisms, and defect

distributions within the samples. These findings provide critical insights into optimising process parameters for additive manufacturing of FeSi components. Building on these results, the next chapter will investigate into the challenges and advancements in 3D-printing stators for electrical motors, translating these microstructural insights into practical applications.

8.5 Chapter 7: 3D printing of stators for electrical motors

Chapter 7 extended the research into practical applications, demonstrating the fabrication of stator discs for electrical motors using LMD. This investigation showcased how optimised processing parameters, such as laser power, scan speed, and substrate preheating, directly influence the microstructure, texture, and mechanical properties of the final components. The study revealed that shorter dimensions stator discs exhibited significant cracking due to residual stresses arising from uneven heating and cooling cycles. Porosity was identified as a major contributor to crack formation, particularly in samples with higher porosity levels, which compromised their mechanical integrity.

Grain structure analysis revealed distinct microstructures with a strong <001> orientation, beneficial for magnetic properties. These samples also lacked detrimental fibre textures, confirming their suitability for electrical motor applications. Variations in grain size and texture between samples highlighted the need for precise control over processing conditions to achieve optimal performance. This chapter conclusively demonstrated the viability of LMD for manufacturing high-performance components for electrical machines. By successfully translating laboratory findings into practical applications, this work bridges the gap between experimental research and industrial implementation, marking a significant milestone in the advancement of AM for magnetic materials.

The chapter provides an in-depth examination of AM fabricated stator discs for electrical motors, focusing on the impacts of the LMD process on their microstructure characteristics and mechanical properties. It starts with an overview of the importance of electrical machines, such as axial flux machines, and their reliance on soft magnetic materials to enhance performance and reduce energy losses. As was highlighted, the potential of additive manufacturing techniques, specifically laser metal deposition to produce advanced soft magnetic materials like FeSi 6.5 wt%, which can significantly improve electrical resistivity and reduce eddy current losses compared to traditional laminated stators. The chapter details the manufacturing process of stator discs, employing an optimised process parameters based on our observation in the previous chapter (5 and 6) which is a laser power of 425 W, scan speed of 400 mm/min, and preheating the substrate to 200°C to enhance bonding and mitigate crack formation. Analysis revealed that while discs like sample S1 did not show macro cracks, discs such as samples S4 and S6 experienced significant cracking, with S4 even shattering during cooling. These findings indicate challenges in increasing the length of discs, related to uneven heating and cooling cycles that introduce residual stresses and thermal gradients, intensifying crack formation. Additionally, porosity was found to contribute to crack growth by acting as stress concentration, with sample S6 exhibiting considerable porosity levels that compromised its mechanical properties.

The examination of grain structure and crystallographic orientation through EBSD analysis highlighted significant differences between samples S4 and S6. Sample S4 featured larger grain sizes and a strong <001> crystal orientation, enhancing its magnetic performance by reducing hysteresis losses and improving permeability. Conversely, sample S6 showed smaller grain sizes and a mix of orientations, with moderate <001> orientation. This variation in grain size and orientation is attributed to differences in cooling rates and thermal gradients during processing, highlighting the importance of optimising processing conditions to enhance material performance. Further analysis of grain size distribution and texture revealed that sample S6 had a higher proportion of smaller grains and a consistent Goss texture, beneficial for magnetic performance. Sample S4 exhibited a broader grain size distribution and a strong cube texture, with additional (113)[$0\bar{3}1$] texture, also favourable for magnetic properties. Both samples lacked detrimental texture, confirming their suitability for magnetic applications. Overall, while both samples exhibit desirable characteristics, S6's consistent Goss texture offers a slight advantage in magnetic performance, making it particularly suitable for electrical steel applications. In conclusion, this chapter demonstrates that the LMD process and its processing conditions significantly shape the microstructure and magnetic properties of 3D-printed stator discs. Optimising these parameters is key to enhancing component performance and durability. Notably, sample S6, with its consistent Goss texture and smaller grain sizes, outperforms sample S4 in magnetic properties, highlighting the advantages of tailored processing conditions for electrical motor applications. Furthermore, LMD's capability, especially when paired with a rotating table, surpasses SLM in fabricating radial samples, offering a distinct strength in this work and addressing why LMD was chosen over SLM for such geometries.

8.6 General comments on optimum AM parameters for FeSi 6.5 wt% components

The best-performing magnetic FeSi 6.5 wt% parts, as determined in this project and supported by detailed investigations in the referenced studies, are achieved with optimal additive manufacturing (LMD) parameters of a scan speed of 400 mm/min, laser power of 400–500 W, and substrate preheating to 200°C, within an energy density range of 61–68 J/mm². These conditions minimise defects porosity <0.3% and crack-free structures) while promoting columnar grains with a strong <001> //BD fibre texture and enhanced cube texture, which could improve magnetic permeability, reduce core losses, and support superior magnetic performance. Higher energy density within this range (up to 68 J/mm²) further strengthens the cube texture and increases grain size, favouring the <001> orientation for better magnetisation response. Samples produced under these parameters exhibit stable hardness between 350–400 HV_1, with average variations of ±30 HV_1 (±10%) for thin walls, ±19 HV1 (±5%) for cubes, and ±26 HV1 (±7%) for discs, indicating consistent material properties. Substrate preheating at 200°C is essential for mitigating thermal stresses and defects, as evidenced by microstructural analyses. However, further optimisation of grain sizes and porosity is recommended for future research to ensure reliable performance in electrical motor applications.

8.7 Future work and recommendations

To build upon the insights of this study and further enhance the understanding of LMD for manufacturing FeSi 6.5% components, future research should focus on optimising both material and process parameters to improve both microstructural characteristics and magnetic properties. This can be achieved by exploring a variety of research avenues as outlined below. Each of these areas presents significant opportunities to refine current practices and push the boundaries of additive manufacturing techniques applied to electrical steels.

8.7.1 Material modifications

One critical aspect for future exploration is the modification of the material composition to enhance mechanical and magnetic properties while addressing the challenge of embrittlement. A promising direction is to investigate the potential of reducing the silicon content or introducing other elements such as aluminium to improve the ductility of FeSi 6.5 wt%. This could reduce the material's susceptibility to cracking during processing, which is particularly important in applications where mechanical strength and flexibility are crucial. However, any modification to the material must be carefully balanced with maintaining the optimal magnetic properties, as silicon plays a significant role in the magnetic characteristics of electrical steels. Research efforts should aim to identify other alloying elements that could provide a favourable balance between ductility and magnetism, and testing these modified alloys under the laser deposition process will be key. Further studies may also explore the possibility of introducing surface treatments or coatings to enhance the material's mechanical properties while preserving its magnetism. These modifications could be guided by computational thermodynamics, density functional theory (DFT) models, or using CALPHAD for phase diagram techniques to predict phase stability, alloy behavior, and magnetic performance, providing a scientific basis for experimental design.

8.7.2 Process optimisation

The laser deposition process is highly sensitive to parameter selection, and future work should investigate into further optimising laser power, scan speed, and substrate temperature to reduce defects such as cracking and porosity. By refining these parameters, it will be possible to produce components with more uniform microstructures that meet the required mechanical and magnetic properties. In particular, the preheating of substrates and controlling cooling rates are crucial for reducing thermal stresses that lead to cracking. Research should focus on refining these parameters further and establishing a more comprehensive process window. Additionally, energy density, an essential factor in LMD, plays a role in layer fusion and defect minimisation. Identifying the optimal energy density to maximise layer bonding while reducing defects such as porosity and cracking will be critical. Further printing trials using cube samples, which offer a different geometry than the stator discs, should be conducted. These trials will help uncover new insights regarding the effects of scan speed, laser power, and energy density on porosity, cracking, and grain growth. More trials should also focus on aligning the <001> crystal direction in the build direction (BD) to enhance the material's magnetic properties and performance.

8.7.3 Geometric design

Geometric design plays a vital role in the mechanical properties of parts manufactured via additive manufacturing, and this warrants further investigation. Modifying component geometries, such as adjusting length, height, or thickness, can significantly influence the susceptibility to residual stresses and cracking. It is also essential to explore the use of foundation layers to better support the manufacturing process and improve part stability. Moreover, adjusting the substrate's preheating temperature above 200°C could help to reduce the risk of thermal stresses and cracking. The inclusion of foundation layers in the BD can provide better support and help improve these issues. Additionally, simulating melt pool dynamics and solidification behaviour will offer predictive insights into the influence of design changes on material performance. These simulations could help understand the formation and propagation of cracks in AM parts and guide the selection of optimal geometries that minimise these risks.

8.7.4 Crack orientation in magnetic flux

A novel area for exploration is investigating how cracks interact with the magnetic flux in FeSi 6.5 wt% materials. While cracks can often reduce mechanical strength, they may have a potential to align in ways that improve magnetic performance. In particular, cracks oriented parallel to the magnetic flux might alter the flux path in beneficial ways, increasing the efficiency of the magnetic performance of the material. Further studies should examine the relationship between crack orientation and magnetic flux direction, offering new insights into how material defects could be leveraged to enhance the performance of electrical steels in magnetic applications.

8.7.5 Microstructural characterisation

Microstructural analysis is essential for understanding the impact of processing conditions on material properties. Advanced techniques such as transmission electron microscopy (TEM) should be employed to examine dislocation densities and their relationship with both mechanical and magnetic properties. Dislocation densities provide valuable insight into the strength and magnetic behaviour of the material. Moreover, X-ray diffraction (XRD) could be used to identify brittle phases, such as DO_3 and B_2, which can adversely affect the material's performance. Investigating the impact of these phases and their stability under various processing conditions will provide further insight into the relationship between microstructure and material performance. Additionally, different scanning strategies could be explored to achieve an ideal texture, which may improve both the mechanical and magnetic properties of the component. Optimising scanning strategies will allow for better control over grain size and orientation, particularly the alignment of the <001> crystal direction in the build direction.

Furthermore, the effect of oxidation on the overall magnetic properties of Fe–Si was not explicitly considered in this thesis, as oxidation was actively minimised through controlled directed energy deposition (DED) processing conditions and was therefore not treated as a dominant factor influencing manufacturability. The scope of this work focused on manufacturability, metallurgy, microstructure, texture, and mechanical properties. All

deposits were produced under continuous, localised argon shielding directly over the melt pool, with argon also used as the carrier gas during powder delivery to minimise oxygen exposure. The powder mass flow rate was calibrated over a defined period using a digital balance with ±0.01 g repeatability and maintained at 2.5 g/min, ensuring consistent powder delivery conditions and limiting oxidation-related variability. In the first trial, the substrates were not preheated; however, in subsequent trials they were cleaned with acetone, surface-machined prior to deposition, and preheated to 200 °C to minimise thermal gradients and reduce cracking. Preheating reduced cooling rates and residual stresses and, under the assumed uniform heating and inert shielding conditions, oxidation during deposition was considered negligible. As a result, oxidation effects were regarded as secondary relative to microstructural evolution, cracking behaviour, and texture development, which formed the primary focus of this study. It is recommended for future work to evaluate oxidation effects through controlled exposure tests and magnetic property measurements, particularly to assess long-term surface stability and performance under service conditions.

Residual stresses are indeed relevant to the DED manufacturability of brittle Fe–Si alloys, as steep thermal gradients during layer deposition can drive crack initiation and propagation. However, direct quantification of residual stresses was not pursued in this study. Instead, insights into their effects on crack formation and microstructural integrity were inferred from literature on comparable Fe–Si materials processed via LPBF and conventional rolling. In AM processes such as DED, residual stresses are highly localised, anisotropic, and transient, shaped by dynamic thermal cycles that make robust correlations with alloy composition or process parameters difficult without dedicated in-situ measurements, such as real-time X-ray diffraction or neutron scattering. Such detailed mapping fell beyond the scope of this project, which focused on direct, actionable indicators of build quality, including crack morphology, grain-scale damage, and texture evolution. Future work could extend these findings by explicitly measuring residual stresses and integrating them with the present microstructural observations to refine process optimisation further.

8.7.6 Heat treatment

The application of heat treatments, such as hot isostatic pressing (HIP), presents an important opportunity for improving the mechanical properties of LMD-manufactured FeSi 6.5 wt%. HIP can reduce porosity and residual stresses, which are known to compromise the material's performance. Comprehensive trials involving heat treatments should investigate the relationship between grain growth, heat treatment duration, and geometry to identify the optimal parameters for reducing defects. Understanding how heat treatments can be integrated into the post-processing of LMD components will be crucial in improving material performance in real-world applications. Heat treatment parameters, including pressure, temperature, and time, should be thoroughly explored to achieve the best results.

8.7.7 Mechanical and electrical performance

Further mechanical testing is needed to better understand the behaviour of FeSi 6.5% components, particularly in terms of fatigue resistance and crack growth. Even if cracks are present, there may be potential to improve the material's durability by using methods such

as filling gaps, bonding, or improving the thermal conductivity of the cracks using conductive epoxy resin. Fatigue testing would provide valuable insights into the long-term performance of these materials under cyclic loading, while the use of crack repair techniques could enhance the lifespan of components without sacrificing magnetic performance. Furthermore, electrical performance, such as the impact of cracks on eddy current losses, should be investigated in future work. By refining both mechanical and electrical testing techniques, the overall durability and efficiency of LMD-manufactured FeSi 6.5% components can be improved.

8.7.8 Surface quality and eddy currents

One key area for future research should be focused on improving the surface finish of LMD components to reduce eddy current losses, which are a significant source of energy loss in electrical steels. This can be achieved through better control of the laser deposition parameters to minimise surface roughness and improve the homogeneity of the material. Additionally, aligning the grain texture with the magnetic flux direction could further enhance the material's magnetic properties, improving efficiency. Magnetic testing, including the measurement of eddy current losses, should be prioritised to evaluate the effectiveness of various surface finishing techniques and microstructural optimisations. This will ensure that the material performs optimally in practical applications, particularly in motors and transformers.

8.7.9 Application development

Finally, the exploration of practical applications for FeSi 6.5 wt% components in industries such as electronics, energy, and electrical engineering is essential. As magnetic properties are crucial for these industries, developing components with optimised mechanical and magnetic characteristics will be of great interest to industry stakeholders. Collaborations with industry partners will facilitate the real-world testing and validation of these components in demanding applications. Future research should also explore how to scale up the manufacturing process to meet industrial demands, focusing on cost-effectiveness, speed, and scalability. Further application development can help bridge the gap between theoretical research and practical, real-world implementation, paving the way for innovations in energy-efficient technologies and high-performance electrical devices.

8.7.10 Conclusion and broader implications

This research demonstrates the promising potential of LMD in manufacturing FeSi 6.5 wt% components with improved microstructure and texture, which can lead to significant advancements in magnetic properties. Future work should focus on refining material composition, optimising process parameters, and exploring sustainable manufacturing practices to meet the growing demand for energy-efficient technologies. By addressing these areas, additive manufacturing can play a pivotal role in advancing the development of next-generation materials and devices, pushing the boundaries of magnetic performance in a wide range of industrial applications. The insights from this research will contribute to innovations in energy-efficient motors, transformers, and other components crucial to modern electrical and energy systems.

References:

[1] Vallack H, Haq G, Whitelegg J, Cambridge H. Policy pathways towards achieving a zero-carbon transport sector in the UK in 2050. World Transp Policy Pract. 2014;20:28-42.
[2] Gumbleton-Wood D, Atkinson GJ, Sjöberg L. Electromagnetic properties of soft magnetic composites and electrical steels at high frequencies considering material manufacturing techniques. 2019 IEEE International Electric Machines & Drives Conference (IEMDC): IEEE; 2019. p. 2027-34.
[3] Dorner D, Zaefferer S, Lahn L, Raabe D. Overview of Microstructure and Microtexture Development in Grain-oriented Silicon Steel. Journal of Magnetism and Magnetic Materials. 2006;304:183-6.
[4] Kestens L, Jacobs S. Texture control during the manufacturing of nonoriented electrical steels. Texture, Stress, and Microstructure. 2008;2008.
[5] Garibaldi M, Ashcroft I, Simonelli M, Hague R. Metallurgy of high-silicon steel parts produced using Selective Laser Melting. Acta Materialia. 2016;110:207-16.
[6] Xu Y, Jiao H, Qiu W, Misra RDK, Li J. Effect of cold rolling process on microstructure, texture and properties of strip cast Fe-2.6% Si steel. Materials. 2018;11:1161.
[7] Garibaldi M, Ashcroft I, Lemke J, Simonelli M, Hague R. Effect of annealing on the microstructure and magnetic properties of soft magnetic Fe-Si produced via laser additive manufacturing. Scr Mater. 2018;142:121-5.
[8] Jang P, Lee B, Choi G. Effects of annealing on the magnetic properties of Fe–6.5% Si alloy powder cores. Journal of Applied Physics. 2008;103:07E743.
[9] Goodall A. Enabling 3D magnetic circuits by the additive manufacturing of soft magnetic material: University of Sheffield; 2022.
[10] Lukaszczyk M. Improving efficiency in electric motors. World Pumps. 2014;2014:34-41.

[11] Worrell E, Bernstein L, Roy J, Price L, Harnisch J. Industrial energy efficiency and climate change mitigation. Energy efficiency. 2009;2:109.
[12] Saidur R, Rahim N, Ping H, Jahirul M, Mekhilef S, Masjuki HH. Energy and emission analysis for industrial motors in Malaysia. Energy Policy. 2009;37:3650-8.
[13] Gundabattini E, Kuppan R, Solomon DG, Kalam A, Kothari DP, Abu Bakar R. A review on methods of finding losses and cooling methods to increase efficiency of electric machines. Ain Shams Engineering Journal. 2021;12:497-505.
[14] Jimoh A, Findlay R, Poloujadoff M. Stray losses in induction machines: part I, definition, origin and measurement. IEEE transactions on Power Apparatus and Systems. 1985:1500-5.
[15] Magdaleno–Adame S, Fakhravar A, Kefalas T. Comparative Study of Grain Oriented and Non–Grain Oriented Electrical Steels in Magnetic Shunts of Power Transformers.
[16] Petrun M, Steentjes S. Iron-loss and magnetization dynamics in non-oriented electrical steel: 1-D excitations up to high frequencies. IEEE Access. 2020;8:4568-93.
[17] Tiismus H, Kallaste A, Belahcen A, Vaimann T, Rassõlkin A, Lukichev D. Hysteresis measurements and numerical losses segregation of additively manufactured silicon steel for 3D printing electrical machines. Applied Sciences. 2020;10:6515.
[18] Zhu Z, Chu W, Guan Y. Quantitative comparison of electromagnetic performance of electrical machines for HEVs/EVs. CES Transactions on Electrical Machines and Systems. 2017;1:37-47.
[19] Douglass GAMaJG. Premium Efficiency Motor Selection and Application Guide – A Handbook for Industry. USA: Washington State University Energy Program for the U.S; 01 February 2014.
[20] Komatsubara M. Recent Activities in Research of Electrical Steels. KAWASAKI STEEL TECHNICAL REPORT-ENGLISH EDITION-. 1999:42-7.
[21] Jain V, Patra S, Halder C, Hasan SM, Ghosh A. Study on the formation of alligator crack and edge crack in high silicon grain oriented electrical steel during cold rolling. Journal of Applied Physics. 2022;132.

[22] Sanjari M, Mehdi M, He Y, Hilinski EJ, Yue S, Kestens LA, Edrisy A. Tracking the evolution of annealing textures from individual deformed grains in a cross-rolled non-oriented electrical steel. Metallurgical and Materials Transactions A. 2017;48:6013-26.
[23] Hayakawa Y, Szpunar JA. The role of grain boundary character distribution in secondary recrystallization of electrical steels. Acta Materialia. 1997;45:1285-95.
[24] Füzer J, Birčáková Z, Zeleňáková A, Hrubovčák P, Kollár P, Predmerský M, Huňady J. Investigation of total losses of non-oriented electrical steels. Acta Physica Polonica A. 2010;118:1018-9.
[25] Ouyang G, Chen X, Liang Y, Macziewski C, Cui J. Review of Fe-6.5 wt%Si high silicon steel—A promising soft magnetic material for sub-kHz application. Journal of Magnetism and Magnetic Materials. 2019;481:234-50.
[26] Cullity BD. Introduction to magnetic materials / [internet resource]. 2nd ed.. ed: Hoboken, New Jersey : IEEE/Wiley; 2015.
[27] Xu Z, Sha Y, He Z, Zhang F, Liu W, Zhang H, Zuo L. Complete Goss secondary recrystallization by control of the grain size and texture of primary recrystallization in grain-oriented silicon steel. Materials. 2021;14:5383.
[28] Hayakawa Y. Mechanism of secondary recrystallization of Goss grains in grain-oriented electrical steel. Science and Technology of advanced MaTerialS. 2017;18:480-97.
[29] Hayakawa Y. Electrical Steels. In: Caballero FG, editor. Encyclopedia of Materials: Metals and Alloys. Oxford: Elsevier; 2022. p. 208-13.
[30] Liu J, Zhang H, Shan N, Sha Y, Zhang F, Zuo L. Improvement of Texture and Magnetic Properties in 4.5 wt.% Si Grain-Oriented Electrical Steels. Materials Research. 2019;22.
[31] Matsumura K, Fukuda B. Recent developments of non-oriented electrical steel sheets. IEEE transactions on magnetics. 1984;20:1533-8.
[32] Mirzadeh M, Narjes G, Ponick B. Evaluation of High-Tech Electrical Steel in a High-Speed Permanent Magnet Synchronous Machine for an

Aircraft Application. Cham: Springer International Publishing; 2021. p. 119-29.
[33] Elgamli E, Anayi F. Advancements in electrical steels: A comprehensive review of microstructure, loss analysis, magnetic properties, alloying elements, and the influence of coatings. Applied Sciences. 2023;13:10283.
[34] Oda Y, Okubo T, Takata M. Recent development of non-oriented electrical steel in JFE steel. JFE Tech Rep. 2016;21:7-13.
[35] Hayakawa Y. Electrical Steels. Reference Module in Materials Science and Materials Engineering: Elsevier; 2020.
[36] Wrobel R, Mecrow B. Additive Manufacturing in Construction of Electrical Machines – A Review. 2019 IEEE Workshop on Electrical Machines Design, Control and Diagnosis (WEMDCD)2019. p. 15-22.
[37] Electrical Steel Market Size, Share & Trends Analysis Report By Product (Grain Oriented, Non-Grain Oriented), By Application (Transformers), By Region, And Segment Forecasts, 2019 - 2025. 2019:80.
[38] Fortunati S, Cicalè S, Schneider J, Franke A, Kawalla R. Developments in the field of electrical steels over the last years. Proc 7th International Conf Magnetism and Metallurgy WMM18, June Rome, Italy2016. p. 29.
[39] Petryshynets I, Kováč F, Petrov B, Falat L, Puchý V. Improving the magnetic properties of non-oriented electrical steels by secondary recrystallization using dynamic heating conditions. Materials. 2019;12:1914.
[40] Cong J-Q, Guo F-H, Qiao J-L, Qiu S-T, Wang H-J. Texture Evolution during Recrystallization and Grain Growth in Non-Oriented Electrical Steel Produced by Compact Strip Production Process. Materials. 2021;15:197.
[41] Inambao M. Transportation, pollution and the environment. International Journal of Applied Engineering Research. 2018;13:3187-99.
[42] Liu R, Li MH, Zhang HN. Opportunities and Challenges of Electric Vehicles Development in Mitigating Climate Change in China. IOP Conference Series: Earth and Environmental Science. 2017;86:012010.

[43] Manda VK, Yadav A, Yalamarti RP. Tata Motors: Driving into the Future with Sustainability and Innovation. Handbook of Digital Innovation, Transformation, and Sustainable Development in a Post-Pandemic Era: CRC Press. p. 343-68.
[44] Tietz M, Biele P, Jansen A, Herget F, Telger K, Hameyer K. Application-specific development of non-oriented electrical steel for EV traction drives. 2012 2nd International Electric Drives Production Conference (EDPC): IEEE; 2012. p. 1-5.
[45] Kawano M, Fujiyama T, Aoki T. Electrical steels for high-functional automotive electrical components corresponding to energy saving. Fuel. 2003;10:1.
[46] Wasay A. Non-grain orinted electrical steel market definition and segments. Januray 2024

[47] Garside M. Major countries in silicon production from 2010 to 2020. Mining, Metals & Minerals. Apr 27, 2021.
[48] ENERGY I, AGENCY. Global EV Outlook 2024 Moving towards increased affordability. International Energy Agency (IEA); April 2024.
[49] Wang A, Tian B, Li Y, Xu S, Zeng L, Pei R. Transient Magnetic Properties of Non-Grain Oriented Silicon Steel under Multi-Physics Field. Materials. 2022;15:8305.
[50] Scholz AE, Trifonov D, Hornung M. Environmental life cycle assessment and operating cost analysis of a conceptual battery hybrid-electric transport aircraft. CEAS Aeronautical Journal. 2021.
[51] Ovdiienko O, Hryhorak M, Marchuk V, Bugayko D. An assessment of the aviation industry's impact on air pollution from its emissions: worldwide and the Ukraine. Environmental & Socio-economic Studies. 2021;9:1-10.
[52] Tom L, Khowja M, Vakil G, Gerada C. Commercial aircraft electrification—Current state and future scope. Energies. 2021;14:8381.
[53] Domone J. The challenges and benefits of the electrification of aircraft. SNC-Lavalin's Atkins. 2018.

[54] Delogu G, Porru M, Serpi A. A Brief Overview on Commercial Aircraft Electrification: Limits and Future Trends. 2021 IEEE Vehicle Power and Propulsion Conference (VPPC): IEEE; 2021. p. 1-5.
[55] Nevot MC. Analysis of a hybrid propulsion system for a ultra light aircraft: University of Liege; 2024.
[56] Li Z, Ma Y, Hu A, Zeng L, Xu S, Pei R. Investigation and Application of Magnetic Properties of Ultra-Thin Grain-Oriented Silicon Steel Sheets under Multi-Physical Field Coupling. Materials. 2022;15:8522.
[57] Erickson C. Cobalt miners seeking to expand in Congo face human rights accusations. S&P Global Market Intelligence; February 2, 2022.
[58] Maloney D. The material at the heart of the grid. February 15, 2024.
[59] Jones B, Elliott RJR, Nguyen-Tien V. The EV revolution: The road ahead for critical raw materials demand. Applied Energy. 2020;280:115072.
[60] Pitron G. The Geopolitics of the rare-metals race. The Washington Quarterly. 2022;45:135-50.
[61] Lu S-M. A review of high-efficiency motors: Specification, policy, and technology. Renewable and Sustainable Energy Reviews. 2016;59:1-12.
[62] Ward M, Allwood JM, Azevedo J, Cleaver C, Cullen J, Dunant C, Fellin T, Hawkins W, Horrocks I, Horton P. Absolute zero: delivering the UK's climate change commitment with incremental changes to today's technologies. 2019.
[63] Kauth F, Seume JR, Radespiel R, Semaan R, François DG, El Sayed M Y, Behr C, Schwerter M, Leester-Schädel M, Vasista S. Progress in efficient active high-lift. 35th AIAA Applied Aerodynamics Conference2017. p. 3559.
[64] Analytics C. Publications selected from Web of Science Core Collection, in webofscience. In: Analytics C, editor. London, UK12.01.2024.
[65] Saidur R. A review on electrical motors energy use and energy savings. Renewable and Sustainable Energy Reviews. 2010;14:877-98.

[66] Selema A, Ibrahim MN, Sergeant P. Metal additive manufacturing for electrical machines: Technology review and latest advancements. Energies. 2022;15:1076.
[67] Kowal D, Sergeant P, Dupré L, Vandenbossche L. The effect of the electrical steel properties on the temperature distribution in direct-drive PM synchronous generators for 5 MW wind turbines. IEEE transactions on magnetics. 2013;49:5371-7.
[68] Talebian S, Rodrigues T, Das Neves J, Sarmento B, Langer R, Conde J. Facts and figures on materials science and nanotechnology progress and investment. ACS nano. 2021;15:15940-52.
[69] Silveyra JM, Ferrara E, Huber DL, Monson TC. Soft magnetic materials for a sustainable and electrified world. Science. 2018;362:eaao0195.
[70] Hultman L, Jack A. Soft magnetic composites-materials and applications. IEEE International Electric Machines and Drives Conference, 2003 IEMDC'03: IEEE; 2003. p. 516-22.
[71] Couderchon G, Tiers J. Some aspects of magnetic properties of Ni-Fe and Co-Fe alloys. Journal of Magnetism and Magnetic Materials. 1982;26:196-214.
[72] Senda M, Nagai Y. Magnetic properties of Fe/Co, Fe/CoFe, and (Fe/Co)/SiO2 multilayer films. Journal of Applied Physics. 1989;65:3151-6.
[73] Fiorillo F, Bertotti G, Appino C, Pasquale M. Soft magnetic materials. Wiley Encyclopedia of Electrical and Electronics Engineering: John Wiley & Sons, Inc.; 2016. p. 1-42.
[74] Collocott SJ. Magnetic Materials: Domestic Applications. In: Buschow KHJ, Cahn RW, Flemings MC, Ilschner B, Kramer EJ, Mahajan S, et al., editors. Encyclopedia of Materials: Science and Technology. Oxford: Elsevier; 2001. p. 4804-12.
[75] Lumsden G, Singamneni S, Ludbrook B, Weijers H, Badcock RA. Additively manufactured polymer composites for superconducting motor coil structures. IEEE Transactions on Applied Superconductivity. 2023;33:1-5.
[76] Yoshida R, Kitajima J, Sakae T, Sato M, Mizuno T, Shimoda Y, Kubota A, Wada S, Kichiji T, Kumagai H. Effect of Magnetic Properties

of Magnetic Composite Tapes on Motor Losses. Energies. 2022;15:7991.
[77] Cros J, Viarouge P, Chalifour Y, Figueroa J. A new structure of universal motor using soft magnetic composites. IEEE Transactions on Industry Applications. 2004;40:550-7.
[78] Kim C-W, Jang G-H, Kim J-M, Ahn J-H, Baek C-H, Choi J-Y. Comparison of axial flux permanent magnet synchronous machines with electrical steel core and soft magnetic composite core. IEEE transactions on magnetics. 2017;53:1-4.
[79] Nishanth F, Goodall AD, Todd I, Severson EL. Characterization of an axial flux machine with an additively manufactured stator. IEEE Transactions on Energy Conversion. 2023.
[80] Henaux C, Nogarede B, Harribey D. A new concept of modular permanent magnet and soft magnetic compound motor dedicated to widespread application. IEEE transactions on magnetics. 2011;48:2035-43.
[81] Moses AJ. Energy efficient electrical steels: Magnetic performance prediction and optimization. Scripta materialia. 2012;67:560-5.
[82] Ma D, Sun C, Li Y, Tian B, Wang L, Pei R. Study of magnetic properties of electrical steels with different Si content considering the effect of temperature. AIP Advances. 2023;13.
[83] Tumanski S. Handbook of magnetic measurements: CRC press; 2016.
[84] Petrovic DS. Non-oriented electrical steel sheets. Mater Tehnol. 2010;44:317-25.
[85] Ros-Yañez T, Houbaert Y, Fischer O, Schneider J. Production of high silicon steel for electrical applications by thermomechanical processing. Journal of Materials Processing Technology. 2003;141:132-7.
[86] Yan Y, Sun Q, Chen J, Pan H. The initiation and propagation of edge cracks of silicon steel during tandem cold rolling process based on the Gurson–Tvergaard–Needleman damage model. Journal of Materials Processing Technology. 2013;213:598-605.
[87] Yu JH, Shin JS, Bae JS, Lee ZH, Lee TD, Lee HM, Lavernia EJ. The effect of heat treatments and Si contents on B2 ordering reaction in

high-silicon steels. Materials Science and Engineering: A. 2001;307:29-34.
[88] Lemke JN, Simonelli M, Garibaldi M, Ashcroft I, Hague R, Vedani M, Wildman R, Tuck C. Calorimetric study and microstructure analysis of the order-disorder phase transformation in silicon steel built by SLM. Journal of Alloys and Compounds. 2017;722:293-301.
[89] Roy RK, Ghosh M, Panda A, Ghosh R, Mitra A. Development of rapidly solidified 6.5 wt% silicon steel for magnetic applications. Transactions of the Indian Institute of Metals. 2010;63:745-50.
[90] Jong Hee Park TSS. Introduction to chemical vapor deposition. ASM international. June 2001;407.
[91] Haiji H, Okada K, Hiratani T, Abe M, Ninomiya M. Magnetic properties and workability of 6.5% Si steel sheet. Journal of Magnetism and Magnetic Materials. 1996;160:109-14.
[92] Liang Y, Lin J, Ye F, Li Y, Wang Y, Chen G. Microstructure and mechanical properties of rapidly quenched Fe–6.5 wt.% Si alloy. Journal of Alloys and Compounds. 2010;504:S476-S9.
[93] Li R, Shen Q, Zhang L, Zhang T. Magnetic properties of high silicon iron sheet fabricated by direct powder rolling. Journal of Magnetism and Magnetic Materials. 2004;281:135-9.
[94] Kasai S, Namikawa M, Hiratani T. Recent progress of high silicon electrical steel in JFE steel. JFE Technical Report. 2016:14-9.
[95] Ouyang G, Chen X, Liang Y, Macziewski C, Cui J. Review of Fe-6.5 wt% Si high silicon steel—A promising soft magnetic material for sub-kHz application. Journal of Magnetism and Magnetic Materials. 2019;481:234-50.
[96] Xie J, Pan H, Fu H, Zhang Z. High Efficiency Warm-cold Rolling Technology of Fe-6.5wt%Si Alloy Sheets. Procedia Engineering. 2014;81:149-54.
[97] Elgamli E, Anayi F, Shouran M. Impact of manganese diffusion into non-oriented electrical steel on power loss and permeability at different temperatures. Frontiers in Materials. 2023;9:1108308.
[98] He Q, Liu Y, Zhu C, Xie X, Zhu R, Li G. Effect of Phosphorus Content on Magnetic and Mechanical Properties of Non-Oriented Electrical Steel. Materials. 2022;15:6332.

[99] Bian X, Zeng Y, Nan D, Wu M. The effect of copper precipitates on the recrystallization textures and magnetic properties of non-oriented electrical steels. Journal of Alloys and Compounds. 2014;588:108-13.
[100] Varahabhatla SM, Chaudhary V, Sharma A, Mantri SA, Dasari S, Sarkar SK, Joshi S, Ramanujan RV, Dahotre NB, Banerjee R. A low coercivity, high Si content, directed energy deposited Fe-6%Si electrical steel. Journal of Alloys and Compounds. 2025;1036:181863.
[101] Adamczyk JM, Birchall SE, Rothermel ET, Whetten SR, Barrick EJ, Pearce CJ, Delaney RE, Pegues JW, Johnson KL, Susan DF. Characterization of Fe-6Si soft magnetic alloy produced by laser-directed energy deposition additive manufacturing. Jom. 2024;76:863-74.
[102] Wang Y, Gao Z, Luo L, Chen C, Zhao Z, Song R, Zhang Y. Magnetic Domains and Their Power Spectral Densities in Non-Oriented Electrical Steel after Thermal Compression at Different Rates. Materials. 2023;16:5311.
[103] Boehm L, Hartmann C, Gilch I, Stoecker A, Kawalla R, Wei X, Hirt G, Heller M, Korte-Kerzel S, Leuning N. Grain size influence on the magnetic property deterioration of blanked non-oriented electrical steels. Materials. 2021;14:7055.
[104] Kustas AB, Chandrasekar S, Trumble KP. Magnetic properties characterization of shear-textured 4 wt% Si electrical steel sheet. Journal of Materials Research. 2016;31:3930-8.
[105] Hawezy D. The influence of silicon content on physical properties of non-oriented silicon steel. Materials Science and Technology. 2017;33:1560-9.
[106] Wang Z, Li S, Cui R, Wang X, Wang B. Influence of grain size and blanking clearance on magnetic properties deterioration of non-oriented electrical steel. IEEE transactions on magnetics. 2018;54:1-7.
[107] Stöcker A, Weiner M, Korpała G, Prahl U, Wei X, Lohmar J, Hirt G, Heller M, Korte-Kerzel S, Böhm L. Integrated Process Simulation of Non-Oriented Electrical Steel. Materials. 2021;14:6659.
[108] RELATIVNO KMAII, NEORIENTIRANIH PVG. Correlation between the excess losses and the relative permeability in fully finished non-oriented electrical steels. Materiali in tehnologije. 2014;48:997-1001.

[109] Verbeken K, Gomes E, Schneider J, Houbaert Y. Correlation between the magnetic properties and the crystallographic texture during the processing of non oriented electrical steel. Solid State Phenomena: Trans Tech Publ; 2010. p. 189-94.
[110] Jiao H, Xu Y, Xiong W, Zhang Y, Cao G, Li C, Niu J, Misra RDK. High-permeability and thin-gauge non-oriented electrical steel through twin-roll strip casting. Materials & Design. 2017;136:23-33.
[111] Liu H-T, Liu Z-Y, Sun Y, Qiu Y-Q, Li C-G, Cao G-M, Hong B-D, Kim S-H, Wang G-D. Formation of {001}< 510> recrystallization texture and magnetic property in strip casting non-oriented electrical steel. Materials Letters. 2012;81:65-8.
[112] Tamimi S, He Y, Sanjari M, Pirgazi H, Kockelmann W, Robinson F, Mohammadi M, Kestens L. Mechanical properties and crystallographic texture of non-oriented electrical steel processed by repetitive bending under tension. Materials Science and Engineering: A. 2022;835:142665.
[113] Honda K. On magnetization of single crystals of iron. Sci Rep Tohoku Imp Univ. 1926;15:721.
[114] Chikazumi S, Graham CD. Physics of ferromagnetism. Oxford Oxford university press; 27 Feb. 1997.
[115] Maciusowicz M, Psuj G. Use of time-frequency representation of magnetic Barkhausen noise for evaluation of easy magnetization axis of grain-oriented steel. Materials. 2020;13:3390.
[116] Maciusowicz M, Psuj G. Time-frequency analysis of barkhausen noise for the needs of anisotropy evaluation of grain-oriented steels. Sensors. 2020;20:768.
[117] Petrovic DS. Non-oriented electrical steel sheets. Materiali in tehnologije. 2010;44:317-25.
[118] Hayakawa Y, Kurosawa M. Orientation relationship between primary and secondary recrystallized texture in electrical steel. Acta Materialia. 2002;50:4527-34.
[119] Hayakawa Y, Szpunar JA. A new model of Goss texture development during secondary recrystallization of electrical steel. Acta Materialia. 1997;45:4713-20.

[120] Cardoso AVdM, Paolinelli SdC, Silveira CC, Cota AB. Secondary recrystallization characteristics of 3%Si grain-oriented electrical steel. Journal of Materials Research and Technology. 2019;8:217-21.
[121] Kestens L, Jonas J, Van Houtte P, Aernoudt E. Orientation selective recrystallization of nonoriented electrical steels. Metallurgical and Materials Transactions A. 1996;27:2347-58.
[122] Park J-T, Szpunar JA, Cha S-Y. Effect of heating rate on the development of annealing texture in nonoriented electrical steels. ISIJ international. 2003;43:1611-4.
[123] Hunady J, Cernik M, Hilinski E, Predmersky M, Magurova A. Influence of chemistry and hot rolling conditions on high permeability non-grain oriented silicon steel. Journal of Metals, Materials and Minerals. 2005;15:17-23.
[124] Kubota T, Fujikura M, Ushigami Y. Recent progress and future trend on grain-oriented silicon steel. Journal of Magnetism and Magnetic Materials. 2000;215:69-73.
[125] You D, Park H. Developmental trajectories in electrical steel technology using patent information. Sustainability. 2018;10:2728.
[126] da Costa Paolinelli S, Da Cunha MA, Cota AB. The influence of hot rolling finishing temperature on the structure and magnetic properties of 2.0% Si non-oriented silicon steel. Materials Science Forum: Trans Tech Publ; 2007. p. 787-92.
[127] Tong C. Introduction to materials for advanced energy systems: Springer International Publishing; January 2, 2019.
[128] Xiong X, Hu S, Dang N, Hu K. Effect of stress-relief annealing on microstructure, texture and hysteresis curve of mechanically cut non-oriented Fe-Si steel. Materials Characterization. 2017;132:239-47.
[129] Mehdi M, He Y, Hilinski EJ, Edrisy A. Effect of skin pass rolling reduction rate on the texture evolution of a non-oriented electrical steel after inclined cold rolling. Journal of Magnetism and Magnetic Materials. 2017;429:148-60.
[130] Chu S, Zhou B, Mao B. State of the art and prospects on the metallurgical design and manufacturing process of grain-oriented electric steels Journal of Magnetism and Magnetic Materials February, 2025;614:172739.

[131] Li Y, Song S, Dou Y, Chen T. Influence of tensile stress on the magnetic properties of ultra-thin grain-oriented electrical steel. AIP Advances. 2023;13.
[132] Zhang B, Liang Y, Wen S, Wang S, Shi X, Ye F, Lin J. High-strength low-iron-loss silicon steels fabricated by cold rolling. Journal of Magnetism and Magnetic Materials. 2019;474:51-5.
[133] Gutiérrez-Castañeda EJ, Salinas-Rodríguez A. Effect of annealing prior to cold rolling on magnetic and mechanical properties of low carbon non-oriented electrical steels. Journal of Magnetism and Magnetic Materials. 2011;323:2524-30.
[134] Rodrigues DL, Nishikawa TSP, Almeida AA, Landgraf FJ, Martin RV. The effect of recovery annealing on the magnetic and mechanical properties of nonoriented electrical steels. IEEE transactions on magnetics. 2014;50:1-4.
[135] Garibaldi M, Gerada C, Hague R. Laser additive manufacturing of soft magnetic cores for rotating electrical machinery: materials development and part design: University of Nottingham; 2018.
[136] Cramer CL, Nandwana P, Yan J, Evans SF, Elliott AM, Chinnasamy C, Paranthaman MP. Binder jet additive manufacturing method to fabricate near net shape crack-free highly dense Fe-6.5 wt.% Si soft magnets. Heliyon. 2019;5.
[137] Momin A. Review of Electrical Steels with their Properties and Recent Trends for Improvement. Technology. 2024;17:4270-86.
[138] Waeckerlé T, Mekhiche M, Brun C. Improvement of magnetic permeability in pure iron sheets. Journal of Magnetism and Magnetic Materials. 1994;133:195-7.
[139] Yashiki H, Okamoto A. Effect of hot-band grain size on magnetic properties of non-oriented electrical steels. IEEE transactions on magnetics. 1987;23:3086-8.
[140] Verbeken K, Schneider J, Verstraete J, Hermann H, Houbaert Y. Effect of Hot and Cold Rolling on Grain Size and Texture in Fe-2.4wt%Si Strips. Magnetics, IEEE Transactions on. 2008;44:3820-3.
[141] Sidor JJ, Verbeken K, Gomes E, Schneider J, Calvillo PR, Kestens LAI. Through process texture evolution and magnetic properties of high

Si non-oriented electrical steels. Materials Characterization. 2012;71:49-57.
[142] Verbeken K, Kestens L, Jonas JJ. Microtextural study of orientation change during nucleation and growth in a cold rolled ULC steel. Scripta materialia. 2003;48:1457-62.
[143] Huňady J, Černík M, Hilinski EJ, Predmerský M, Magurová A. Influence of chemistry and hot rolling conditions on high permeability non-grain oriented silicon steel. Journal of Magnetism and Magnetic Materials. 2006;304:e620-e3.
[144] Ray R, Jonas J. Transformation textures in steels. International Materials Reviews. 1990;35:1-36.
[145] de Dafé SSF, Paolinelli SdC, Cota AB. Influence of thermomechanical processing on shear bands formation and magnetic properties of a 3% Si non-oriented electrical steel. Journal of Magnetism and Magnetic Materials. 2011;323:3234-8.
[146] Castro SF, Gallego J, Landgraf FJG, Kestenbach HJ. Orientation dependence of stored energy of cold work in semi-processed electrical steels after temper rolling. Materials Science and Engineering: A. 2006;427:301-5.
[147] Lucke R. Texture and microstructure of hot rolled steel. Scr Metallurg Mater(texture). 1992;26:1221-6.
[148] Pan H, Zhang Z, Mo Y, Xie J. Strong 〈001〉 recrystallization texture component in 6.5wt% Si electrical steel thin sheets by secondary cold rolling and annealing. Journal of Magnetism and Magnetic Materials. 2016;419:500-11.
[149] Jahangiri M, Bajgholi A, Zhaam A. Development of a new three-stage cold rolling manufacturing technology for grain-oriented silicon steel sheets. The International Journal of Advanced Manufacturing Technology. 2014;75:1291-8.
[150] Kasai S, Namikawa M, Hiratani T. Recent progress of high silicon electrical steel in JFE steel. JFE Steel Corporation, Tokyo, Japan, JFE Tech Rep. 2016;21.
[151] Li X, He XD, Li Y, Sun Y. Preparation of high silicon steel by EB-PVD. Materials Science Forum: Trans Tech Publ; 2007. p. 1813-6.

[152] Fajfar P, Lah AŠ, Kraner J, Kugler G. Asymmetric rolling process. Materials and Geoenvironment. 2017;64:151-60.
[153] Sanjari M, He Y, Hilinski EJ, Yue S, Kestens LA. Texture evolution during skew cold rolling and annealing of a non-oriented electrical steel containing 0.9 wt% silicon. Journal of Materials Science. 2017;52:3281-300.
[154] Rout M, Pal S, Singh S. A Metal Forming Process SpringerLink; June, 2015. p. 41-64.
[155] de Araujo Cardoso RF, Cunha MAd, Brandão LPM. Optimization of the magnetic losses of electrical steels through addition of Al and Si using a hot dipping process. Journal of Materials Research and Technology. 2013;2:276-81.
[156] Sha Y, Zhang F, Zhou S, Pei W, Zuo L. Improvement of recrystallization texture and magnetic property in non-oriented silicon steel by asymmetric rolling. Journal of Magnetism and Magnetic Materials. 2008;320:393-6.
[157] M. Shirazi H, Georges R, Hernandez R, Blais C. Effect of the cross-rolling and austempering heat treatment on the microstructure, texture, and mechanical properties of a low alloyed steel used in rotary cutting tools. The International Journal of Advanced Manufacturing Technology. 2022;120:3787-804.
[158] Sanjari M, He Y, Hilinski EJ, Yue S, Kestens LAI. Development of the {113}〈uvw〉 texture during the annealing of a skew cold rolled non-oriented electrical steel. Scripta materialia. 2016;124:179-83.
[159] Humphreys FJ, Hatherly M. Recrystallization and related annealing phenomena: elsevier; 2012.
[160] Mix T, Gröninger M, Jin Z, Reuter K, Studnitzky T, Lindemann-Geipel I, Weißgärber T. Additive manufacturing of low loss electrical steel sheets for high efficiency electrical devices. IEEE Transactions on Transportation Electrification. 2023.
[161] Mercelis P, Kruth JP. Residual stresses in selective laser sintering and selective laser melting. Rapid Prototyping Journal. 2006;12:254-65.
[162] Kempen K, Vrancken B, Thijs L, Buls S, Van Humbeeck J, Kruth J-P. Lowering thermal gradients in selective laser melting by pre-heating

the baseplate. Solid Freeform Fabrication Symposium Proceedings2013.
[163] Chen S, Butler J, Melzer S. Effect of asymmetric hot rolling on texture, microstructure and magnetic properties in a non-grain oriented electrical steel. Journal of Magnetism and Magnetic Materials. 2014;368:342-52.
[164] Liravi F, Vlasea M. Powder bed binder jetting additive manufacturing of silicone structures. Additive Manufacturing. 2018;21:112-24.
[165] Tofail SAM, Koumoulos EP, Bandyopadhyay A, Bose S, O'Donoghue L, Charitidis C. Additive manufacturing: scientific and technological challenges, market uptake and opportunities. Materials Today. 2018;21:22-37.
[166] Bhargav A, Sanjairaj V, Rosa V, Feng LW, Fuh Yh J. Applications of additive manufacturing in dentistry: A review. Journal of Biomedical Materials Research Part B: Applied Biomaterials. 2018;106:2058-64.
[167] Ye F, Liang Y, Wang Y, Lin JP, Chen G. Fe-6.5 wt.% Si high silicon steel sheets produced by cold rolling. Materials Science Forum: Trans Tech Publ; 2010. p. 1428-33.
[168] Ngo TD, Kashani A, Imbalzano G, Nguyen KTQ, Hui D. Additive manufacturing (3D printing): A review of materials, methods, applications and challenges. Composites Part B: Engineering. 2018;143:172-96.
[169] Rodriguez-Vargas BR, Stornelli G, Folgarait P, Ridolfi MR, Miranda Pérez AF, Di Schino A. Recent advances in additive manufacturing of soft magnetic materials: A review. Materials. 2023;16:5610.
[170] Romero A, Morales AL, Herranz G. Enhancing properties of soft magnetic materials: A study into hot isostatic pressing and sintering atmosphere influences. Metals. 2021;11:643.
[171] Tseng M-L, Aslam MI, Ismail EA, Awwad FA, Gorji NE. CT scan, EBSD and nanoindentation analysis of 3D-printed parts with post-process heat-treatment. Metallurgical Research & Technology. 2024;121:101.

[172] Stornelli G, Faba A, Di Schino A, Folgarait P, Ridolfi MR, Cardelli E, Montanari R. Properties of additively manufactured electric steel powder cores with increased Si content. Materials. 2021;14:1489.
[173] Shen X, Meng F, Lau KB, Wang P, Lee CHT. Texture and microstructure characterizations of Fe-3.5wt%Si soft magnetic alloy fabricated via laser powder bed fusion. Materials Characterization. 2022;189:112012.
[174] Meng F, Huang S, Lau KB, Zhou Y, Deng Y, Wang P, Shen X, Lee CHT. Texture components and magnetic properties of laser powder bed fusion fabricated near grain-oriented and near non-oriented silicon steel. Materials & Design. 2023;231:112037.
[175] Selema A, Beretta M, Van Coppenolle M, Tiismus H, Kallaste A, Ibrahim MN, Rombouts M, Vleugels J, Kestens LAI, Sergeant P. Evaluation of 3D-Printed Magnetic Materials For Additively-Manufactured Electrical Machines. Journal of Magnetism and Magnetic Materials. 2023:170426.
[176] Goodall AD, Chechik L, Mitchell RL, Jewell GW, Todd I. Cracking of soft magnetic FeSi to reduce eddy current losses in stator cores. Additive Manufacturing. 2023;70:103555.
[177] Stornelli G, Vargas BRR, Folgarait P, Ridolfi MR, Sgambetterra M, Di Schino A. Development of FeSi steel with increased Si content by laser powder bed fusion technology for ferromagnetic cores application: Microstructure and properties. MRS Advances. 2023;8:1195-9.
[178] Goll D, Schurr J, Trauter F, Schanz J, Bernthaler T, Riegel H, Schneider G. Additive manufacturing of soft and hard magnetic materials. Procedia CIRP. 2020;94:248-53.
[179] Goodall AD, Nishanth FNU, Severson EL, Todd I. Loss performance of an additively manufactured axial flux machine stator with an eddy-current limiting structure. Materials Today Communications. 2023;35:105978.
[180] Zaied M, Ospina-Vargas A, Buiron N, Favergeon J, Fenineche N-E. Additive Manufacturing of Soft Ferromagnetic Fe 6.5% Si Annular Cores: Process Parameters, Microstructure, and Magnetic Properties. IEEE transactions on magnetics. 2022;58:1-9.

[181] Shin J, Bae J, Kim H, Lee H, Lee TD, Lavernia E, Lee Z. Ordering–disordering phenomena and micro-hardness characteristics of B2 phase in Fe–(5–6.5%) Si alloys. Materials Science and Engineering: A. 2005;407:282-90.
[182] David S, Vitek J. Correlation between solidification parameters and weld microstructures. International Materials Reviews. 1989;34:213-45.
[183] Pohl H, Simchi A, Issa M, Dias HC. Thermal Stresses in Direct Metal Laser Sintering 366. 2001 International Solid Freeform Fabrication Symposium2001.
[184] Garibaldi M, Ashcroft I, Hillier N, Harmon SAC, Hague R. Relationship between laser energy input, microstructures and magnetic properties of selective laser melted Fe-6.9%wt Si soft magnets. Materials Characterization. 2018;143:144-51.
[185] Garibaldi M, Ashcroft I, Lemke JN, Simonelli M, Hague R. Effect of annealing on the microstructure and magnetic properties of soft magnetic Fe-Si produced via laser additive manufacturing. Scripta materialia. 2018;142:121-5.
[186] Arregui L, Garmendia I, Pujana J, Soriano C. Study of the geometrical limitations associated to the metallic part manufacturing by the LMD process. Procedia CIRP. 2018;68:363-8.
[187] DebRoy T, Wei HL, Zuback JS, Mukherjee T, Elmer JW, Milewski JO, Beese AM, Wilson-Heid Ad, De A, Zhang W. Additive manufacturing of metallic components–process, structure and properties. Progress in Materials Science. 2018;92:112-224.
[188] Frazier WE. Metal additive manufacturing: a review. Journal of materials engineering and performance. 2014;23:1917-28.
[189] Jinoop AN, Paul C, Bindra K. Laser-assisted directed energy deposition of nickel super alloys: a review. Proceedings of the Institution of Mechanical Engineers, Part L: Journal of Materials: Design and Applications. 2019;233:2376-400.
[190] Azarniya A, Colera XG, Mirzaali MJ, Sovizi S, Bartolomeu F, St Weglowski Mk, Wits WW, Yap CY, Ahn J, Miranda G, Silva FS, Madaah Hosseini HR, Ramakrishna S, Zadpoor AA. Additive manufacturing of Ti–6Al–4V parts through laser metal deposition (LMD): Process,

microstructure, and mechanical properties. Journal of Alloys and Compounds. 2019;804:163-91.
[191] Saboori A, Aversa A, Marchese G, Biamino S, Lombardi M, Fino P. Microstructure and mechanical properties of AISI 316L produced by directed energy deposition-based additive manufacturing: A review. Applied Sciences. 2020;10:3310.
[192] Thompson SM, Bian L, Shamsaei N, Yadollahi A. An overview of Direct Laser Deposition for additive manufacturing; Part I: Transport phenomena, modeling and diagnostics. Additive Manufacturing. 2015;8:36-62.
[193] Cramer CL, Nandwana P, Yan J, Evans SF, Elliott AM, Chinnasamy C, Paranthaman MP. Binder jet additive manufacturing method to fabricate near net shape crack-free highly dense Fe-6.5 wt.% Si soft magnets. Heliyon. 2019;5:e02804.
[194] Ramalho F, Alves M, Correia M, Vilhena L, Ramalho A. Study of laser metal deposition (LMD) as a manufacturing technique in automotive industry. International Conference of Progress in Digital and Physical Manufacturing: Springer; 2019. p. 225-39.
[195] Ahsan MN, Paul CP, Kukreja LM, Pinkerton AJ. Porous structures fabrication by continuous and pulsed laser metal deposition for biomedical applications; modelling and experimental investigation. Journal of Materials Processing Technology. 2011;211:602-9.
[196] Kittel J, Gasser A, Wissenbach K, Zhong C, Schleifenbaum JH, Palm F. Case study on AM of an IN718 aircraft component using the LMD process. Procedia CIRP. 2020;94:324-9.
[197] Kratky A. Production of hard metal alloys. Patent# US. 1937;2076952.
[198] Isaac H. Method of forming structures wholly of fusion deposited weld metal. Google Patents; 1942.
[199] Teh WH, Tan LP, Chen S, Wei F, Lee JJ, Padhy SP, Chaudhary V, Tan CC, Ramanujan RV. Breaking conventional limits of silicon content in Fe-xSi magnetic alloys through additive manufacturing. Journal of Alloys and Compounds. 2024;983:173829.

[200] Gandhi D, Mukherjee M, Rajak B, Arora KS. Directed energy deposition (DED) of Fe-6.5 wt% Si electrical steel. Progress in Additive Manufacturing. 2025:1-11.
[201] Mahamood RM. Laser metal deposition process of metals, alloys, and composite materials: Springer International Publishing; 2018.
[202] Selcuk C. 13 - Joining processes for powder metallurgy parts. In: Chang I, Zhao Y, editors. Advances in Powder Metallurgy: Woodhead Publishing; 2013. p. 380-98.
[203] Steen WM. Laser cutting. Laser material processing: Springer; 1998. p. 103-46.
[204] Mahamood RM. Laser metal deposition process of metals, alloys, and composite materials: Springer; 2018.
[205] Mahamood RM, Akinlabi ET. Scanning speed influence on the microstructure and micro hardness properties of titanium alloy produced by laser metal deposition process. Materials Today: Proceedings. 2017;4:5206-14.
[206] Gharbi M, Peyre P, Gorny C, Carin M, Morville S, Le Masson P, Carron D, Fabbro R. Influence of a pulsed laser regime on surface finish induced by the direct metal deposition process on a Ti64 alloy. Journal of Materials Processing Technology. 2014;214:485-95.
[207] Gharbi M, Peyre P, Gorny C, Carin M, Morville S, Le Masson P, Carron D, Fabbro R. Influence of various process conditions on surface finishes induced by the direct metal deposition laser technique on a Ti–6Al–4V alloy. Journal of Materials Processing Technology. 2013;213:791-800.
[208] Mahamood RM, Akinlabi ET, Shukla M, Pityana S. Characterizing the effect of laser power density on microstructure, microhardness, and surface finish of laser deposited titanium alloy. Journal of Manufacturing Science and Engineering. 2013;135.
[209] Kang X, Dong S, Wang H, Yan S, Liu X, Xu B. Effect of laser power on gradient microstructure of low-alloy steel built by laser melting deposition. Materials Letters. 2020;262:127073.
[210] Ravi G, Qiu C, Attallah MM. Microstructural control in a Ti-based alloy by changing laser processing mode and power during direct laser deposition. Materials Letters. 2016;179:104-8.

[211] Erinosho MF, Akinlabi ET, Pityana S. Influence of processing parameters on laser metal deposited copper and titanium alloy composites. Transactions of Nonferrous Metals Society of China. 2015;25:2608-16.
[212] Yu J, Rombouts M, Maes G, Motmans F. Material properties of Ti6Al4 v parts produced by laser metal deposition. Physics Procedia. 2012;39:416-24.
[213] Mahamood RM, Akinlabi ET, Shukla M, Pityana SL. Laser metal deposition of Ti6Al4V: a study on the effect of laser power on microstructure and microhardness. Proceedings of the International MultiConference of Engineers and Computer Scientists. March, 2013;2.
[214] Karami R, Butler D, Tamimi S. Manufacturing of non-grain-oriented electrical steels: review. The International Journal of Advanced Manufacturing Technology. 2024.
[215] Lee H, Choi Y, Ahn J, Lee K, Kim Y, Choi J, Lee H, Kim J. Effect of process parameters on the texture evolution of Fe-6.5 wt% Si soft magnetic alloys manufactured via laser powder bed fusion. Journal of Materials Processing Technology. 2024;331:118521.
[216] A.Bayode ETAM, IAENG, and S. Pityana Characterization of laser metal deposited 316L stainless steel. Proceedings of the World Congress on Engineering. June, 2016;2.
[217] Mahamood RM, Akinlabi ET. Effect of scanning speed and gas flow rate on surface roughness of LMD titanium-alloy. Proceedings of the World Congress on Engineering and Computer Science: sn; 2016.
[218] Mahamood RM, Akinlabi ET, Shukla M, Pityana S. Scanning velocity influence on microstructure, microhardness and wear resistance performance of laser deposited Ti6Al4V/TiC composite. Materials & Design. 2013;50:656-66.
[219] Yang J, Fu Z, Ye J, Kübrich D, Körner C. Electron beam-based additive manufacturing of Fe93.5Si6.5 (wt.%) soft magnetic material with controllable magnetic performance. Scripta materialia. 2022;210:114460.
[220] Mahamood RM, Akinlabi ET, Shukla M, Pityana S. The role of transverse speed on deposition height and material efficiency in laser

deposited titanium alloy. Proceedings of the International MultiConference of Engineers and Computer Scientists2013.
[221] Chen J, Li J, Song R, Bai L, Shao J, Qu C. Effect of the scanning speed on microstructural evolution and wear behaviors of laser cladding NiCrBSi composite coatings. Optics & Laser Technology. 2015;72:86-99.
[222] Senthilkumaran K, Pandey PM, Rao P. Influence of building strategies on the accuracy of parts in selective laser sintering. Materials & Design. 2009;30:2946-54.
[223] Goodall AD, Chechik L, Livera F, Todd I. Importance of surface roughness on the magnetic properties of additively manufactured FeSi thin walls. Acta Materialia. 2024;263:119501.
[224] Song BU, Choi JP, Lee P-H, Jung M-K, Shin D, Ha T, Lee I. Efficient Optimization of Magnetic Properties of Fe–4.5 Si Alloy in Laser Powder Bed Fusion (LPBF). International Journal of Precision Engineering and Manufacturing-Green Technology. 2025;12:1133-46.
[225] Kustas AB, Susan DF, Johnson KL, Whetten SR, Rodriguez MA, Dagel DJ, Michael JR, Keicher DM, Argibay N. Characterization of the Fe-Co-1.5 V soft ferromagnetic alloy processed by Laser Engineered Net Shaping (LENS). Additive Manufacturing. 2018;21:41-52.
[226] Brandl E, Michailov V, Viehweger B, Leyens C. Deposition of Ti–6Al–4V using laser and wire, part I: Microstructural properties of single beads. Surface and Coatings Technology. 2011;206:1120-9.
[227] Wu X, Liang J, Mei J, Mitchell C, Goodwin P, Voice W. Microstructures of laser-deposited Ti–6Al–4V. Materials & Design. 2004;25:137-44.
[228] Tang L, Ruan J, Landers RG, Liou F. Variable Powder Flow Rate Control in Laser Metal Deposition Processes. Journal of Manufacturing Science and Engineering. 2008;130.
[229] Mahamood RM, Akinlabi ET. Processing parameters optimization for material deposition efficiency in laser metal deposited titanium alloy. Lasers in Manufacturing and Materials Processing. 2016;3:9-21.
[230] Shukla M, Mahamood RM, Akinlabi ET, Pityana S. Effect of laser power and powder flow rate on properties of laser metal deposited

Ti6Al4V. International Journal of Mechanical and Mechatronics Engineering. 2012;6:2475-9.
[231] Koley S, Bramley K, Ganguly S. Study on development of wire-arc additive manufacturing of Fe-49Co-2V alloy for soft-magnetic applications. Journal of Alloys and Compounds. 2025;1025:180337.
[232] Shen X, Liogas KA, Qun Liang VS, Lek YZ, Meng F, Shen Y, Huber JE, Reed RC, Wang P, Korsunsky AM, Lee CHT. Mitigating core energy losses in Fe-Si alloys fabricated by direct energy deposition through oxide inclusions and abnormal Goss grain growth. Materials & Design. 2025;252:113730.
[233] Son JY, Lee KY, Lee SH, Choi CH. Effects of Oxidized Metal Powders on Pore Defects in Powder-Fed Direct Energy Deposition. Micromachines (Basel). 2024;15.
[234] Iantaffi C, Leung CLA, Chen Y, Guan S, Atwood RC, Lertthanasarn J, Pham M-S, Meisnar M, Rohr T, Lee PD. Oxidation induced mechanisms during directed energy deposition additive manufactured titanium alloy builds. Additive Manufacturing Letters. 2021;1:100022.
[235] Luo Z, Fan Xa, Zhang Y, Yang Z, Wang J, Wu Z, Liu X, Li G, Li Y. Influence of oxidation temperature on microstructure and electromagnetic performance of Fe-Si/Fe2SiO4 soft magnetic composites. Journal of Alloys and Compounds. 2021;862:158595.
[236] Wolf M. Improving the efficiency of the DMLD process: how particle size and laser spot size influence process quality and efficiency. Laser Technik Journal. 2016;13:32-4.
[237] Verhaeghe G, Hilton P. The effect of spot size and laser beam quality on welding performance when using high-power continuous wave solid-state lasers. International Congress on Applications of Lasers & Electro-Optics: Laser Institute of America; 2005. p. 507.
[238] Francis Z, Beuth J. The effect of beam spot size on melt pool geometry in direct metal additive manufacturing processes. Materials Science & Technology (MS&T). 2016.
[239] Schneider MF. Laser cladding with powder and effect of some machining parameters on clad properties: University of Twente; March, 1998.

[240] Mahamood RM, Akinlabi E, Shukla M, Pityana SL. Characterization of laser deposited Ti6Al4V/TiC composite powders on a Ti6Al4V substrate. 2014.
[241] Standard test methods for flow rate of metal powders using the hall flowmeter funnel. USA: American Society for Testing and Materials 2017.
[242] Powders M, Flowmeter H. Standard guide for characterizing properties of metal powders used for additive manufacturing processes. ASTM Int: F3049–14 ASTM International. 2014:1.
[243] German RM. Powder metallurgy and particulate materials processing: the processes, materials, products, properties, and applications: Metal Powder Industries Federation; May, 2005.
[244] Dunkley J, Telford B. Control of" Satellite" Particles in Gas Atomisation. Advances in Powder Metallurgy and Particulate Materials. 2002:3-103.
[245] Goldstein JI, Newbury DE, Michael JR, Ritchie NW, Scott JHJ, Joy DC. Scanning electron microscopy and X-ray microanalysis: springer; 2017.
[246] Sosa JM, Huber DE, Welk B, Fraser HL. Development and application of MIPAR™: a novel software package for two-and three-dimensional microstructural characterization. Integrating Materials and Manufacturing Innovation. 2014;3:123-40.
[247] Neikov OD, Lotsko DV, Gopienko VG. Handbook of Non-Ferrous Metal Powders: Technologies and Applications: Elsevier; 2019.
[248] He S, Park S, Shim D-s, Yao C, Li M, Wang S. Effect of substrate preheating on the microstructure and bending behavior of WC-Inconel 718 composite coating synthesized via laser directed energy deposition. International Journal of Refractory Metals and Hard Materials. 2023;115:106299.
[249] Heppler W. Crystal Preparation at LBL 1976 to 1986. 1989.
[250] Devito F, Mazzarisi M, Dassisti M, Lavecchia F. Causal technological model for predicting void fraction and energy consumption in material extrusion process of polylactic acid. Journal of Manufacturing Processes. 2024;129:187-201.

[251] Ebnesajjad S. Chapter 4 - Surface and Material Characterization Techniques. In: Ebnesajjad S, editor. Surface Treatment of Materials for Adhesive Bonding (Second Edition). Oxford: William Andrew Publishing; 2014. p. 39-75.
[252] Guyett PC, Chew D, Azevedo V, Blennerhassett LC, Rosca C, Tomlinson E. Optimizing SEM-EDX for fast, high-quality and non-destructive elemental analysis of glass. Journal of Analytical Atomic Spectrometry. 2024;39:2565-79.
[253] Schwartz AJ, Kumar M, Adams BL, Field DP. Electron backscatter diffraction in materials science: Springer; January, 2009.
[254] Engler O, Zaefferer S, Randle V. Introduction to texture analysis: macrotexture, microtexture, and orientation mapping: CRC press; 2024.
[255] Brinell A. Standard test method for microindentation hardness of materials. ASTM Committee: West Conshohocken, PA, USA. 1999;384:399.
[256] Thompson A, Maskery I, Leach RK. X-ray computed tomography for additive manufacturing: a review. Measurement Science and Technology. 2016;27:072001.
[257] Iskander M, Li L. Particle Size and Shape Descriptors. In: Iskander M, Li L, editors. Dynamic Image Analysis of Granular Materials: Particle Granulometry for Geotechnical, Material, and Geological Applications. Cham: Springer Nature Switzerland; 2024. p. 25-61.
[258] Collins TJ. ImageJ for microscopy. Biotechniques. 2007;43:S25-S30.
[259] Standard Practice for Determining Average Grain Size Using Electron Backscatter Diffraction (EBSD) in Fully Recrystallized Polycrystalline Materials. American Society for Testing

Materials; November, 2019.
[260] Nadoum A, Robinson F, Birosca S. On the correlation between magnetic domain and crystallographic grain orientation in grain oriented electrical steels. Journal of Magnetism and Magnetic Materials. 2020;494:165772.

[261] Zhao C, Yu Z, Du W, Zhang Z, Ma L, Zhang T, Bai Y, Chen S. Laser Cladding of High-Temperature Alloy: Research Status and Development. Advanced Engineering Materials. 2025;27:2402956.
[262] Karami R, Butler D, Javadi Y, Tamimi S. Process window for manufacturing soft magnetic FeSi 6.5% by laser metal deposition. MATEC Web of Conferences: EDP Sciences; 2024. p. 02011.
[263] Tang SB, Zhang H, Tang CA, Liu HY. Numerical model for the cracking behavior of heterogeneous brittle solids subjected to thermal shock. International Journal of Solids and Structures. 2016;80:520-31.
[264] Li C, Liu ZY, Fang XY, Guo YB. Residual Stress in Metal Additive Manufacturing. Procedia CIRP. 2018;71:348-53.
[265] Rangaswamy P, Griffith ML, Prime MB, Holden TM, Rogge RB, Edwards JM, Sebring RJ. Residual stresses in LENS® components using neutron diffraction and contour method. Materials Science and Engineering: A. 2005;399:72-83.
[266] Moat RJ, Pinkerton AJ, Li L, Withers PJ, Preuss M. Residual stresses in laser direct metal deposited Waspaloy. Materials Science and Engineering: A. 2011;528:2288-98.
[267] Moheimani SK, Iuliano L, Saboori A. The role of substrate preheating on the microstructure, roughness, and mechanical performance of AISI 316L produced by directed energy deposition additive manufacturing. The International Journal of Advanced Manufacturing Technology. 2022;119:7159-74.
[268] Zhang K, Wang S, Liu W, Long R. Effects of substrate preheating on the thin-wall part built by laser metal deposition shaping. Applied Surface Science. 2014;317:839-55.
[269] Kováč F, Petryshynets I, Kočiško R, Petroušek P, Falat L. Effect of Preheating on the Mechanical Workability Improvement of High-Strength Electrical Steels during Tandem Cold Rolling. Metals. 2023;13:1415.
[270] Kempen K, Vrancken B, Buls S, Thijs L, Van Humbeeck J, Kruth J-P. Selective laser melting of crack-free high density M2 high speed steel parts by baseplate preheating. Journal of Manufacturing Science and Engineering. 2014;136:061026.

[271] Gargalis L. Optimisation of silicon content in Fe-Si alloys processed via Laser Powder Bed Fusion for an additively manufactured soft magnetic core: University of Nottingham; 2021.
[272] Buchbinder D, Meiners W, Pirch N, Wissenbach K, Schrage J. Investigation on reducing distortion by preheating during manufacture of aluminum components using selective laser melting. Journal of laser applications. 2014;26.
[273] Li R, Wang G, Zhao X, Dai F, Huang C, Zhang M, Chen X, Song H, Zhang H. Effect of path strategy on residual stress and distortion in laser and cold metal transfer hybrid additive manufacturing. Additive Manufacturing. 2021;46:102203.
[274] Shi RR, Chen SY, Peng YG, Zhang Z. Effect of preheating temperature on microstructure of Fe based alloy coating by laser direct metal deposition. Key Engineering Materials. 2016;703:94-9.
[275] Cianniello V, De Caprio V, Eredia C, Cascone E, D'Auria D. Additive manufacturing, reverse engineering, and metrology to support mechanical design: future developments among the INAF facilities. Ground-based and Airborne Instrumentation for Astronomy X: SPIE; 2024. p. 2974-82.
[276] Lu X, Chiumenti M, Cervera M, Li J, Lin X, Ma L, Zhang G, Liang E. Substrate design to minimize residual stresses in Directed Energy Deposition AM processes. Materials & Design. 2021;202:109525.
[277] Pinkerton AJ, Li L. An analytical model of energy distribution in laser direct metal deposition. Proceedings of the Institution of Mechanical Engineers, Part B: Journal of Engineering Manufacture. 2004;218:363-74.
[278] Lakso GE, Marcinkowski M. Plastic deformation in Fe-Si alloys. Metallurgical and materials transactions B. 1974;5:839-45.
[279] Chen X, Vuorinen E, Grahn J. In-situ SEM observation on fracture behavior of austempered silicon alloyed steel. China Foundry. 2009;6:185-90.
[280] Hong Y, Zhou C, Zheng Y, Zhang L, Zheng J. The cellular boundary with high density of dislocations governed the strengthening mechanism in selective laser melted 316L stainless steel. Materials Science and Engineering: A. 2021;799:140279.

[281] Komatsubara M, Sadahiro K, Kondo O, Takamiya T, Honda A. Newly developed electrical steel for high-frequency use. Journal of Magnetism and Magnetic Materials. 2002;242:212-5.
[282] Omura T, Zaizen Y, Fukumura M, Senda K, Toda H. Effect of hardness and thickness of nonoriented electrical steel sheets on iron loss deterioration by shearing process. IEEE transactions on magnetics. 2015;51:1-4.
[283] Sanaei N, Fatemi A. Defects in additive manufactured metals and their effect on fatigue performance: A state-of-the-art review. Progress in Materials Science. 2021;117:100724.
[284] Zhang K, Chen Y, Marussi S, Fan X, Fitzpatrick M, Bhagavath S, Majkut M, Lukic B, Jakata K, Rack A. Pore evolution mechanisms during directed energy deposition additive manufacturing. Nature communications. 2024;15:1715.
[285] Ustinovshikov Y, Sapegina I. Morphology of ordering Fe-Si alloys. Journal of Materials Science. 2004;39:1007-16.
[286] Ng GK, Bi G, Teh KM, Zheng H. An investigation on porosity in laser metal deposition. International Congress on Applications of Lasers & Electro-Optics: Laser Institute of America; 2008. p. 105.
[287] Sinha S, Mukherjee T. Mitigation of gas porosity in additive manufacturing using experimental data analysis and mechanistic modeling. Materials. 2024;17:1569.
[288] dos Santos Paes LE, Pereira M, Xavier FA, Weingaertner WL, Vilarinho LO. Lack of fusion mitigation in directed energy deposition with laser (DED-L) additive manufacturing through laser remelting. Journal of Manufacturing Processes. 2022;73:67-77.
[289] Li S, Zhang S, Habetler TG, Harley RG. Modeling, Design Optimization, and Applications of Switched Reluctance Machines—A Review. IEEE Transactions on Industry Applications. 2019;55:2660-81.
[290] Zhang B, Li Y, Bai Q. Defect formation mechanisms in selective laser melting: a review. Chinese Journal of Mechanical Engineering. 2017;30:515-27.
[291] Qiu J, Lu T, Yao N, Chen X, Li K, Sun B, Chen Y, Zhang X-C, Tu S-T. New insights into fatigue anisotropy of an additively manufactured medium-entropy alloy: From the perspectives of crack initiation and

crack propagation. Virtual and Physical Prototyping. 2024;19:e2411025.
[292] Brennan M, Keist J, Palmer T. Defects in metal additive manufacturing processes. Springer; July, 2021. p. 4808–18.
[293] Bidare P, Mehmeti A, Jiménez A, Li S, Garman C, Dimov S, Essa K. High-density direct laser deposition (DLD) of CM247LC alloy: microstructure, porosity and cracks. The International Journal of Advanced Manufacturing Technology. 2022;120:8063-74.
[294] Choo H, Sham K-L, Bohling J, Ngo A, Xiao X, Ren Y, Depond PJ, Matthews MJ, Garlea E. Effect of laser power on defect, texture, and microstructure of a laser powder bed fusion processed 316L stainless steel. Materials & Design. 2019;164:107534.
[295] König H-H, Pettersson NH, Durga A, Van Petegem S, Grolimund D, Chuang AC, Guo Q, Chen L, Oikonomou C, Zhang F, Lindwall G. Solidification modes during additive manufacturing of steel revealed by high-speed X-ray diffraction. Acta Materialia. 2023;246:118713.
[296] Guo W, Feng B, Yang Y, Ren Y, Liu Y, Yang H, Yang Q, Cui L, Tong X, Hao S. Effect of laser scanning speed on the microstructure, phase transformation and mechanical property of NiTi alloys fabricated by LPBF. Materials & Design. 2022;215:110460.
[297] Kim Y, Lee H, Ha T, Kim J, Choi JP. Effects of laser beam profiles on the microstructure and magnetic properties of L-PBF soft magnetic alloys. Scientific reports. 2025;15:22336.
[298] Babuska TF, Wilson MA, Johnson KL, Whetten SR, Curry JF, Rodelas JM, Atkinson C, Lu P, Chandross M, Krick BA. Achieving high strength and ductility in traditionally brittle soft magnetic intermetallics via additive manufacturing. Acta Materialia. 2019;180:149-57.
[299] Zhang R, Dou R, Wen Z, Liu X. Effects of pressure and temperature on the effective thermal conductivity of oriented silicon steel iron core under atmospheric condition. International Journal of Heat and Mass Transfer. 2018;125:780-7.
[300] Carter LN, Essa K, Attallah MM. Optimisation of selective laser melting for a high temperature Ni-superalloy. Rapid Prototyping Journal. 2015;21:423-32.

[301] Chen J, Lin X, Wang T, Yang H, Huang W. The hot cracking mechanism of 316 L stainless steel cladding in rapid laser forming process. Xiyou Jinshu Cailiao yu Gongcheng(Rare Metal Materials and Engineering). 2003;32:183-6.
[302] Wittig J, Frommeyer G. Deformation and fracture behavior of rapidly solidified and annealed iron-silicon alloys. Metallurgical and Materials Transactions A. 2008;39:252-65.
[303] INOKUTI Y, IKEDA S, ITO Y. Inhibition of Hot Cracking in Grain Oriented Silicon Steel Containing a Small Amount of Molybdenum. Transactions of the Iron and Steel Institute of Japan. 1985;25:228-32.
[304] Zhao Z, Song R, Wang Y, Zhang Y, Hu C, Wang Y. Early interlaminar cracks and tensile fractures in Non-oriented electrical sheets caused by uncoordinated deformations during cold rolling. Engineering Failure Analysis. 2021;127:105573.
[305] Andreiev A, Hoyer K-P, Hengsbach F, Haase M, Tasche L, Duschik K, Schaper M. Powder bed fusion of soft-magnetic iron-based alloys with high silicon content. Journal of Materials Processing Technology. 2023;317:117991.
[306] Pilehrood AE, Mashhuriazar A, Baghdadi AH, Sajuri Z, Omidvar H. Effect of laser metal deposition parameters on the characteristics of stellite 6 deposited layers on precipitation-hardened stainless steel. Materials. 2021;14:5662.
[307] Ball S, Ghayoor M, Pasebani S, Tabei A. Statistical Analysis of Porosity and Process Parameter Relationships in Metal Additive Manufacturing. Procedia Manufacturing. 2021;53:343-7.
[308] Chen S-g, Gao H-j, Zhang Y-d, Wu Q, Gao Z-h, Zhou X. Review on residual stresses in metal additive manufacturing: formation mechanisms, parameter dependencies, prediction and control approaches. Journal of Materials Research and Technology. 2022;17:2950-74.
[309] Zhong C, Biermann T, Gasser A, Poprawe R. Experimental study of effects of main process parameters on porosity, track geometry, deposition rate, and powder efficiency for high deposition rate laser metal deposition. Journal of laser applications. 2015;27.

[310] Qu M, Guo Q, Escano LI, Nabaa A, Hojjatzadeh SMH, Young ZA, Chen L. Controlling process instability for defect lean metal additive manufacturing. Nature communications. 2022;13:1079.
[311] Segerstark A, Andersson J, Svensson L-E, Ojo O. Effect of Process Parameters on the Crack Formation in Laser Metal Powder Deposition of Alloy 718. Metallurgical and Materials Transactions A. 2018;49:5042-50.
[312] Zhao C, Ma C, Du W, Yu Z, Zhang Z. Study on the reduction of residual stress in laser cladding layers through groove texture. Scientific reports. 2024;14:15911.
[313] Shi X, Gu D, Li Y, Dai D, Ge Q, Sun Y, Chen H. Thermal behavior and fluid dynamics within molten pool during laser inside additive manufacturing of 316L stainless steel coating on inner surface of steel tube. Optics & Laser Technology. 2021;138:106917.
[314] Cheng J, Xing Y, Dong E, Zhao L, Liu H, Chang T, Chen M, Wang J, Lu J, Wan J. An overview of laser metal deposition for cladding: Defect formation mechanisms, defect suppression methods and performance improvements of laser-cladded layers. Materials. 2022;15:5522.
[315] Ji W, Liu C, Dai S, Deng R. Microstructure, properties and crack suppression mechanism of high-speed steel fabricated by selective laser melting at different process parameters. Chinese Journal of Mechanical Engineering. 2023;36:46.
[316] Wang J, Zhu R, Liu Y, Zhang L. Understanding melt pool characteristics in laser powder bed fusion: An overview of single- and multi-track melt pools for process optimization. Advanced Powder Materials. 2023;2:100137.
[317] Yadroitsev I, Bertrand P, Smurov I. Parametric analysis of the selective laser melting process. Applied Surface Science. 2007;253:8064-9.
[318] Dahotre NB, Harimkar S. Laser fabrication and machining of materials: Springer Science & Business Media; 2008.
[319] Khairallah SA, Anderson AT, Rubenchik A, King WE. Laser powder-bed fusion additive manufacturing: Physics of complex melt flow and formation mechanisms of pores, spatter, and denudation zones. Acta Materialia. 2016;108:36-45.

[320] Li C-S, Yang C-L, Cai G-J, Wang Q-W. Ordered phases and microhardness of Fe–6.5% Si steel sheet after hot rolling and annealing. Materials Science and Engineering: A. 2016;650:84-92.
[321] Wawszczak R, Baczmański A, Marciszko M, Wróbel M, Czeppe T, Sztwiertnia K, Braham C, Berent K. Evolution of microstructure and residual stress during annealing of austenitic and ferritic steels. Materials Characterization. 2016;112:238-51.
[322] Wronski S, Wrobel M, Baczmanski A, Wierzbanowski K. Effects of cross-rolling on residual stress, texture and plastic anisotropy in f.c.c. and b.c.c. metals. Materials Characterization. 2013;77:116-26.
[323] Chen Z, Sun W, Huang Y, Zhou H, Yang K, Lu J. The effect of laser energy density on microstructural evolution and mechanical properties of laser clad 316L stainless steel for repair. Surface and Coatings Technology. 2022;448:128899.
[324] Caiazzo F, Caggiano A. Laser direct metal deposition of 2024 Al alloy: trace geometry prediction via machine learning. Materials. 2018;11:444.
[325] Tammas-Williams S, Zhao H, Léonard F, Derguti F, Todd I, Prangnell PB. XCT analysis of the influence of melt strategies on defect population in Ti–6Al–4V components manufactured by Selective Electron Beam Melting. Materials Characterization. 2015;102:47-61.
[326] Ahmed N, Barsoum I, Haidemenopoulos G, Al-Rub RKA. Process parameter selection and optimization of laser powder bed fusion for 316L stainless steel: A review. Journal of Manufacturing Processes. 2022;75:415-34.
[327] Park J-T, Szpunar JA. Effect of initial grain size on texture evolution and magnetic properties in nonoriented electrical steels. Journal of Magnetism and Magnetic Materials. 2009;321:1928-32.
[328] Garibaldi M, Ashcroft I, Lemke J, Simonelli M, Hague R. Effect of annealing on the microstructure and magnetic properties of soft magnetic Fe-Si produced via laser additive manufacturing. Scripta materialia. 2018;142:121-5.
[329] Li J, Cao L, Xu J, Wang S, Zhou Q. In situ porosity intelligent classification of selective laser melting based on coaxial monitoring and image processing. Measurement. 2022;187:110232.

[330] Akbari P, Ogoke F, Kao N-Y, Meidani K, Yeh C-Y, Lee W, Barati Farimani A. MeltpoolNet: Melt pool characteristic prediction in Metal Additive Manufacturing using machine learning. Additive Manufacturing. 2022;55:102817.
[331] Lu N, Lei Z, Hu K, Yu X, Li P, Bi J, Wu S, Chen Y. Hot cracking behavior and mechanism of a third-generation Ni-based single-crystal superalloy during directed energy deposition. Additive Manufacturing. 2020;34:101228.
[332] Ocylok S, Alexeev E, Mann S, Weisheit A, Wissenbach K, Kelbassa I. Correlations of Melt Pool Geometry and Process Parameters During Laser Metal Deposition by Coaxial Process Monitoring. Physics Procedia. 2014;56:228-38.
[333] Chen Q, Zhao Y, Strayer S, Zhao Y, Aoyagi K, Koizumi Y, Chiba A, Xiong W, To AC. Elucidating the effect of preheating temperature on melt pool morphology variation in Inconel 718 laser powder bed fusion via simulation and experiment. Additive Manufacturing. 2021;37:101642.
[334] Zhu Y, Tian X, Li J, Wang H. Microstructure evolution and layer bands of laser melting deposition Ti–6.5 Al–3.5 Mo–1.5 Zr–0.3 Si titanium alloy. Journal of Alloys and Compounds. 2014;616:468-74.
[335] Ho A, Zhao H, Fellowes JW, Martina F, Davis AE, Prangnell PB. On the origin of microstructural banding in Ti-6Al4V wire-arc based high deposition rate additive manufacturing. Acta Materialia. 2019;166:306-23.
[336] DebRoy T, Wei H, Zuback J, Mukherjee T, Elmer J, Milewski J, Beese AM, Wilson-Heid Ad, De A, Zhang W. Additive manufacturing of metallic components–process, structure and properties. Progress in Materials Science. 2018;92:112-224.
[337] Vishnu AR, Marvi-Mashhadi M, Nieto-Fuentes JC, Rodríguez-Martínez JA. New insights into the role of porous microstructure on dynamic shear localization. International journal of plasticity. 2022;148:103150.
[338] Sundarram SS, Li W. The effect of pore size and porosity on thermal management performance of phase change material

infiltrated microcellular metal foams. Applied Thermal Engineering. 2014;64:147-54.
[339] Suwas S, Ray RK. Crystallographic texture of materials: Springer; 2014.
[340] Fonda RW, Rowenhorst DJ. Crystallographic Variability in Additive Manufacturing. IOP Conference Series: Materials Science and Engineering: IOP Publishing; 2022. p. 012007.
[341] Kou S. Welding metallurgy. New Jersey, USA. 2003;431:223-5.
[342] Navrátilová E, Neděla V. Characterization of Burnt Clays by X-ray Diffraction Analysis, Chemical Analysis and Environmental Scanning Electron Microscopy. Microscopy and Microanalysis. 2016;22:1862-3.
[343] Hou C-K. The effects of grain size on the magnetic properties of fully processed, continuous-annealed low-carbon electrical steels. IEEE transactions on magnetics. 1996;32:471-7.
[344] Shao J, Yu G, He X, Li S, Chen R, Zhao Y. Grain size evolution under different cooling rate in laser additive manufacturing of superalloy. Optics & Laser Technology. 2019;119:105662.
[345] Sanjari M, Mahmoudiniya M, Pirgazi H, Tamimi S, Ghoncheh MH, Shahriairi A, Hadadzadeh A, Amirkhiz BS, Purdy M, de Araujo EG, Kestens L, Mohammadi M. Microstructure, texture, and anisotropic mechanical behavior of selective laser melted maraging stainless steels. Materials Characterization. 2022;192:112185.
[346] Dezfoli ARA, Hwang W-S, Huang W-C, Tsai T-W. Determination and controlling of grain structure of metals after laser incidence: Theoretical approach. Scientific reports. 2017;7:41527.
[347] Hojati M, Baktash A. Design and fabrication of a new hybrid stepper motor with significant improvements in torque density. Engineering Science and Technology, an International Journal. 2021;24:1116-22.
[348] Liang R-Y, Yang P, Mao W-M. Effect of initial Goss texture sharpness on texture evolution and magnetic properties of ultra-thin grain-oriented electrical steel. Acta Metallurgica Sinica (English Letters). 2017;30:895-906.

[349] Li J, Ren H, Liu C, Shang S. The effect of specific energy density on microstructure and corrosion resistance of CoCrMo alloy fabricated by laser metal deposition. Materials. 2019;12:1321.
[350] Niendorf T, Leuders S, Riemer A, Richard HA, Tröster T, Schwarze D. Highly anisotropic steel processed by selective laser melting. Metallurgical and materials transactions B. 2013;44:794-6.
[351] Sidor Y, Kovac F, Kvackaj T. Grain growth phenomena and heat transport in non-oriented electrical steels. Acta Materialia. 2007;55:1711-22.
[352] Hijam J, Balhara R, Vadali M. Investigating double-scan strategies for reducing heat-affected zone in laser surface melting. Optics & Laser Technology. 2024;170:110289.
[353] AZtecCrystal. UK: Aztech Corporation; May, 2019.
[354] Liu Y, Shi J. Epitaxial Growth and Stray Grain Control toward Single-Crystal Metallic Materials by Additive Manufacturing: A Review. Advanced Engineering Materials. 2023;25:2201917.
[355] Ledwig P, Pasiowiec H, Cichocki K, Lisiecka-Graca P, Gola K, Wróbel R, Dubiel B. Tailoring Microstructure and Mechanical Properties of Additively Manufactured Inconel 625 by Remelting Strategy in Laser Powder Bed Fusion. Metallurgical and Materials Transactions A. 2024;55:2485-508.
[356] He Y, Hilinski E, Li J. Texture evolution of a non-oriented electrical steel cold rolled at directions different from the hot rolling direction. Metallurgical and Materials Transactions A. 2015;46:5350-65.
[357] Zhang L, Yang P, Mao W. Opposite Relationship between Orientation Selection and Texture Memory in the Deformed Electrical Steel Sheets during α→γ→α Transformation. Journal of Materials Science & Technology. 2017;33:1522-30.
[358] Hsu W, Sun P, Kao P, Chang L. Correlation between the deformation microstructure after rolling and the recrystallization nucleation of a non-oriented electrical steel. IOP Conference Series: Materials Science and Engineering: IOP Publishing; 2015. p. 012027.
[359] Rui S-S, Han Q-N, Wang X, Li S, Ma X, Su Y, Cai Z, Du D, Shi H-J. Correlations between two EBSD-based metrics Kernel Average Misorientation and Image Quality on indicating dislocations of near-

failure low alloy steels induced by tensile and cyclic deformations. Materials Today Communications. 2021;27:102445.
[360] Wu F, Zhou L, Soulard J, Silvester B, Davis C. Quantitative characterisation and modelling of the effect of cut edge damage on the magnetic properties in NGO electrical steel. Journal of Magnetism and Magnetic Materials. 2022;551:169185.
[361] Kaappa S, Santa-aho S, Honkanen M, Vippola M, Laurson L. Magnetic domain walls interacting with dislocations in micromagnetic simulations. Communications Materials. 2024;5:256.
[362] Yilmaz C, Poul M, Lahn L, Raabe D, Zaefferer S. Dislocation-assisted particle dissolution: A new hypothesis for abnormal growth of Goss grains in grain-oriented electrical steels. Acta Materialia. 2023;258:119170.
[363] Birosca S, Nadoum A, Hawezy D, Robinson F, Kockelmann W. Mechanistic approach of Goss abnormal grain growth in electrical steel: Theory and argument. Acta Materialia. 2020;185:370-81.
[364] Sakakibara Y, Kubushiro K. Stress evaluation at the maximum strained state by EBSD and several residual stress measurements for plastic deformed austenitic stainless steel. World Journal of Mechanics. 2017;7:195-210.
[365] Pham M-S, Dovgyy B, Hooper PA, Gourlay CM, Piglione A. The role of side-branching in microstructure development in laser powder-bed fusion. Nature communications. 2020;11:749.
[366] Zhao C, Bai Y, Zhang Y, Wang X, Xue JM, Wang H. Influence of scanning strategy and building direction on microstructure and corrosion behaviour of selective laser melted 316L stainless steel. Materials & Design. 2021;209:109999.
[367] Bachmann F, Hielscher R, Schaeben H. Texture analysis with MTEX–free and open source software toolbox. Solid state phenomena. 2010;160:63-8.
[368] He Y, Hilinski EJ. Textures of non-oriented electrical steel sheets produced by skew cold rolling and annealing. Metals. 2021;12:17.
[369] Müller M, Bailly D, Hirt G. Microstructure evolution and magnetic properties of a 4.5 wt% silicon steel produced by twin-roll casting. steel research international. 2022;93:2200554.

[370] Cheng Z, Liu J, Yu C, Zhong B, Chen S, Fu B, Birosca S. Balancing Magnetic and Mechanical Properties of Non-oriented Electrical Steel: Correlation Between Microstructure and Properties. Acta Metallurgica Sinica (English Letters). 2024.
[371] Lin Z, Zhou Y, Zuo S, Cai X, Feng K, Wang K, Wei H, Xiao F, Jin X. Crystallographic Texture Control of Niti Alloy by Adjusting the Thermal Gradient of Laser Powder Bed Melting. Available at SSRN 4745122.
[372] Bernauer C, Sigl ME, Grabmann S, Merk T, Zapata A, Zaeh MF. Effects of the thermal history on the microstructural and the mechanical properties of stainless steel 316L parts produced by wire-based laser metal deposition. Materials Science and Engineering: A. 2024;889:145862.
[373] Borhani MR, Rajabi M, Razavi RS, Jamaati R. Investigating the relationship between mechanical properties and residual stress in the laser cladding process of Inconel 625 superalloy. Heliyon. 2023;9.
[374] Zou X, Yan Z, Zou K, Gang Zhang S, Liu W, Song L. Residual stress control of 316 L stainless steel using pulsed-wave laser additive manufacturing. Optics & Laser Technology. 2022;150:107910.
[375] Gockel J, Sheridan L, Narra SP, Klingbeil NW, Beuth J. Trends in solidification grain size and morphology for additive manufacturing of Ti-6Al-4V. The Journal of The Minerals, Metals & Materials Society September, 2017;69:2706-10.
[376] Dong K, Guo T, Zhang Y, Zhang R, Lin W, Nan X, Qiu Q, Yi X. Effect of Scanning Speed on Microstructure and Properties of Laser Cladding Fe-0.3 C-15Cr-1Ni High Hardness Corrosion-Resistant Alloy Coating on 3Cr13 Surface. steel research international. 2024;95:2300637.
[377] Vukkum VB, Gupta RK. Review on corrosion performance of laser powder-bed fusion printed 316L stainless steel: Effect of processing parameters, manufacturing defects, post-processing, feedstock, and microstructure. Materials & Design. 2022;221:110874.
[378] Liu W, Li G, Lu J. Modeling solidification cracking: A new perspective on solid bridge fracture. Journal of the Mechanics and Physics of Solids. 2024;188:105651.
[379] Xuan D, Zhou C, Zhou Y, Jiang T, Fan W, Mao Y. Effect of cooling rate on the order degree, residual stress, and room temperature

mechanical properties of Fe-6.5wt.%Si alloy. Journal of Magnetism and Magnetic Materials. 2023;571:170550.
[380] Liu W, Al-Hammadi G, Saleheen KM, Abdelrahman A, Liu H, Zhang Z. Impact of pulsed laser parameters and scanning pattern on the properties of thin-walled parts manufactured using laser metal deposition. Nanomanufacturing and Metrology. 2022;5:381-93.
[381] Kudzal A, McWilliams B, Hofmeister C, Kellogg F, Yu J, Taggart-Scarff J, Liang J. Effect of scan pattern on the microstructure and mechanical properties of Powder Bed Fusion additive manufactured 17-4 stainless steel. Materials & Design. 2017;133:205-15.
[382] Shah K, Pinkerton AJ, Salman A, Li L. Effects of melt pool variables and process parameters in laser direct metal deposition of aerospace alloys. Materials and Manufacturing Processes. 2010;25:1372-80.
[383] Wei H, Mazumder J, DebRoy T. Evolution of solidification texture during additive manufacturing. Scientific reports. 2015;5:16446.
[384] Monu MC, Afkham Y, Chekotu JC, Ekoi EJ, Gu H, Teng C, Ginn J, Gaughran J, Brabazon D. Bi-Directional scan pattern effects on residual stresses and distortion in as-built nitinol parts: a trend analysis simulation study. Integrating Materials and Manufacturing Innovation. 2023;12:52-69.
[385] Cobbinah PV, Matsunaga S, Yamabe-Mitarai Y. Controlled crystallographic texture orientation in structural materials using the laser powder bed fusion process—a review. Advanced Engineering Materials. 2023;25:2300819.
[386] Sanjari M, He Y, Hilinski EJ, Yue S, Kestens LAI. Texture evolution during skew cold rolling and annealing of a non-oriented electrical steel containing 0.9 wt% silicon. Journal of Materials Science. 2017;52:3281-300.
[387] Perini M, Amirabdollahian S, Bosetti P. Building Multi-Material components by Direct Laser Deposition. MATEC Web of Conferences: EDP Sciences; 2019. p. 01006.
[388] Li Y, Koukolíková M, Džugan J, Brázda M. High temperature fracture behavior of 316L stainless steel-Inconel 718 functionally graded materials manufactured by directed energy deposition: Role of

interface orientation and heat treatment. Materials Science and Engineering: A. 2024;898:146389.
[389] Kannan R, Lee Y, Pierce D, Unocic K, Fillingim B, Feldhausen T, Rossy AM, Wang H, Nandwana P. Additive manufacturing as a processing route for steel-aluminum bimetallic structures. Materials & Design. 2023;231:112003.
[390] Gandy D, Sridharan N, Babu SS, Peter WH, Leonard DN, Cakmak E, Dehoff RR, Jordan BH. Design, fabrication, and characterization of graded transition joints. Welding Journal. 2017;96.
[391] Razzaq S, Pan ZX, Li HJ, Ringer SP, Liao XZ. Joining dissimilar metals by additive manufacturing: A review. Journal of Materials Research and Technology. 2024;31:2820-45.
[392] Goodall AD, Yiannakou G, Chechik L, Mitchell RL, Jewell GW, Todd I. Geometrical control of eddy currents in additively manufactured Fe-Si. Materials & Design. 2023;230:112002.
[393] Cao Y, Bai P, Liu F, Hou X. Grain growth in IN718 superalloy fabricated by laser additive manufacturing. Materials Science and Technology. 2020;36:765-9.
[394] Zhang X, Xu H, Li Z, Dong A, Du D, Lei L, Zhang G, Wang D, Zhu G, Sun B. Effect of the scanning strategy on microstructure and mechanical anisotropy of Hastelloy X superalloy produced by Laser Powder Bed Fusion. Materials Characterization. 2021;173:110951.
[395] Amine T, Newkirk JW, Liou F. An investigation of the effect of direct metal deposition parameters on the characteristics of the deposited layers. Case Studies in Thermal Engineering. 2014;3:21-34.
[396] Chopra M, Tewari S. Growth-speed dependence of primary arm spacings in directionally solidified Pb-10 Wt Pct Sn. Metallurgical Transactions A. 1991;22:2467-74.
[397] Tewari SN, Shah R. Macrosegregation during dendritic arrayed growth of hypoeutectic Pb-Sn alloys: influence of primary arm spacing and mushy zone length. Metallurgical and Materials Transactions A. 1996;27:1353-62.
[398] Steinbach S, Ratke L. Effects of controlled convections on dendritic microstructure and segregation during microgravity-solidification. Proc of the 18th ESA Symposium on European Rocket

and Balloon Programmes and Related Research, Visby, Sweden, ESA SP-6472007. p. 373-8.
[399] Wang T, Zhu YY, Zhang SQ, Tang HB, Wang HM. Grain morphology evolution behavior of titanium alloy components during laser melting deposition additive manufacturing. Journal of Alloys and Compounds. 2015;632:505-13.
[400] Evangelou A, Stylianou R, Loizou A, Kim D, Liang A, Reed P, Constantinides G, Kyratsi T. Effects of process parameters and scan strategy on the microstructure and density of stainless steel 316 L produced via laser powder bed fusion. Journal of Alloys and Metallurgical Systems. 2023;3:100027.
[401] Jia H, Sun H, Wang H, Wu Y, Wang H. Scanning strategy in selective laser melting (SLM): a review. The International Journal of Advanced Manufacturing Technology. 2021;113:2413-35.
[402] Dovgyy B, Piglione A, Hooper PA, Pham M-S. Comprehensive assessment of the printability of CoNiCrFeMn in Laser Powder Bed Fusion. Materials & Design. 2020;194:108845.
[403] Zou X, Liu Q, Qiu S. A Study on the Formation of Fiber Texture in the Subsurface Layer of Hot-Rolled Plate of 3.2% Si Grain-Oriented Steel. Metals. 2023;13:1597.
[404] Gu D, Shi Q, Lin K, Xi L. Microstructure and performance evolution and underlying thermal mechanisms of Ni-based parts fabricated by selective laser melting. Additive Manufacturing. 2018;22:265-78.
[405] Ii S, Hirayama K, Tsurekawa S. Experimental confirmation of grain boundary magnetism in Fe–Si and Fe–Sn Alloys by TEM-EELS. Materials Transactions. 2019;60:636-41.
[406] Kamaya M, Kubushiro K, Sakakibara Y, Suzuki S, Morita H, Yoda R, Kobayashi D, Yamagiwa K, Nishioka T, Yamazaki Y. Round robin crystal orientation measurement using EBSD for damage assessment. Mechanical Engineering Journal. 2016;3:16-00077-16-.
[407] Gussev MN, Leonard KJ. In situ SEM-EBSD analysis of plastic deformation mechanisms in neutron-irradiated austenitic steel. Journal of Nuclear Materials. 2019;517:45-56.

[408] Parviainen A. Design of axial-flux permanent-magnet low-speed machines and performance comparison between radial-flux and axial-flux machines. 2005.
[409] Kurz W, Giovanola B, Trivedi R. Theory of microstructural development during rapid solidification. Acta metallurgica. 1986;34:823-30.
[410] Ivo RF, Rodrigues DdA, Santos JCd, Freitas FNC, Herculano LFG, Abreu HFGd, Rebouças Filho PP. Study and classification of the Crystallographic Orientation Distribution Function of a non-grain oriented electrical steel using computer vision system. Journal of Materials Research and Technology. 2019;8:1070-83.
[411] Shen X, Sheng H, He Y, Liogas KA, Boon Lau K, Wang P, Meng F, Chen K, Jia N, Ramamurty U, Lee CHT. Evaluation of microstructure, mechanical and magnetic properties of laser powder bed fused Fe-Si alloy for 3D magnetic flux motor application. Materials & Design. 2023;234:112343.
[412] Köhnen P, Létang M, Voshage M, Schleifenbaum JH, Haase C. Understanding the process-microstructure correlations for tailoring the mechanical properties of L-PBF produced austenitic advanced high strength steel. Additive Manufacturing. 2019;30:100914.
[413] Lee H, Park J-T. Effect of Cold Rolling Reduction on Recrystallization Texture and Magnetic Anisotropy of Non-Oriented Electrical Steel. In: Holm EA, Farjami S, Manohar P, Rohrer GS, Rollett AD, Srolovitz D, et al., editors. Proceedings of the 6th International Conference on Recrystallization and Grain Growth (ReX&GG 2016). Cham: Springer International Publishing; 2016. p. 185-9.
[414] Odkhuu D, Rhim S, Park N, Nakamura K, Hong SC. Jahn-Teller driven perpendicular magnetocrystalline anisotropy in metastable ruthenium. Physical Review B. 2015;91:014437.
[415] Quarterman P, Sun C, Garcia-Barriocanal J, Dc M, Lv Y, Manipatruni S, Nikonov DE, Young IA, Voyles PM, Wang J-P. Demonstration of Ru as the 4th ferromagnetic element at room temperature. Nature communications. 2018;9:2058.
[416] Hunt AJ, Farmer TJ, Clark JH. Elemental sustainability and the importance of scarce element recovery. 2013.

Appendices:

Circular economy of electrical steels

It is essential to establish a comprehensive design principle for the recycling of electrical machine parts in order to address the growing demand for sustainable practises in the electrical steel industry. Not only does this facilitate the remanufacturing of electrical steel, but it also plays a crucial role in mitigating environmental concerns. Critical materials are distributed unevenly across the globe, primarily concentrated in a few regions marked by volatile political environments and insecure supply chains. Recycling them is highly energy-intensive due to their low concentration in alloys, resulting in unavoidable costs. However, with the increasing demand for electrification, these critical materials have become essential for enhancing the performance of electrical motors . For instance, it is difficult-to-obtain rare earth elements and critical materials such as Nb, Dy, Co, Ge, Sm, Ni, and Ru are essential for manufacturing electrical steels with enhanced magnetic properties. However, these elements can be recycled effectively by concentrating on the end-of-life processing of electric motor components. This method might enable the extraction of heavy and rare substances, thereby contributing to the conservation of natural resources. Furthermore, from an economic standpoint, the conventional production of electrical motors gains higher costs and maintenance expenses than the remanufacturing of electrical machines. Therefore, it is crucial to consider the economic benefits of recycling the Fe-Si cores of large transformers, especially when these components have outlived their intended lifespan . This method represents a straightforward and economical solution. In addition, the conversion of electrical steel scrap containing these elements into powder by the gas atomisation process could open the door to alternative manufacturing processes, such as direct powder rolling (DPR) or even AM, for the production of electrical steel parts. The approach has been reported in the work of Duz and Moxson where a blended powder of Ti was successfully used in the DPR process to produce titanium sheets, foil, and plates. This technique has the potential to compete with emerging AM processes, providing ample opportunities for further development in this field. Establishing recycling design principles for electrical machine parts has great potential for remanufacturing electrical steel, reducing environmental impact, addressing resource scarcity, and investigating cost-effective manufacturing alternatives.

Recycling electrical machines is of utmost importance due to its significant impact on resource efficiency, waste reduction, and material reuse within the scope of electric motors . The implementation of circular economy practices necessitates the adoption of various strategies, namely remanufacturing, refurbishment, repairing, reusing, and recycling, as effective means to achieve the objectives of circular economy principles. The primary goal of the circular economy for electrical steel is to create opportunities for sustainable resource utilisation in the supply chain of critical materials. This can be achieved by following the steps outlined in Figure 1, which aim to reduce environmental impact and minimise waste from both new manufacturing and the reuse of old products. Remanufacturing involves the disassembly,

repairing, and reassembly of electrical machine parts to restore the machine. Meanwhile, refurbishment focuses on restoring the functionality of electrical machines through cleaning and repair processes. Repairing targets specific failures, extending the lifespan of electrical machines without full disassembly. The reusing stage focuses on finding new purposes for electrical parts and reducing the demand for new parts. Finally, the recycling stage involves the disassembly of electrical machines to recover raw materials for manufacturing new parts. The idea for recycling electrical machine parts involves several key stages. Initially, in the recycling process, electrical machinery parts can undergo disassembly using robotics (automated), manual methods, or a combination of both. Subsequently, a shredding process is employed for smaller electrical machines, breaking them down into smaller components. During the shredding process, materials are sorted either mechanically or manually, separating ferrous and non-ferrous materials using magnets. These materials are then directed through isolated tubes to a conveyor belt for additional processing. Alternative materials like soft magnetic composites can be assembled, crushed, and separated more easily, leading to less copper contamination compared to other soft magnetic materials such as electrical steels, as noted in a recent report. Following this, the shredded materials are transferred to an atomization process for melting, thereby producing powders at the end of the process. These powders are subsequently screened and meshed to various sizes, with the chemical composition of the powder analysed using energy dispersive spectroscopy (EDS spectra). If the powder contains acceptable impurities, it can be utilised for appropriate processes, such as AM. It is important to acknowledge that this approach is based on hypothesis, and the outcome is uncertain yet. However, it is considered worthy of exploration. By implementing these strategies, not only can the lifespan of electrical machines be extended, but also the environmental impact can be minimised, contributing to the development of a sustainable circular economy model. Moreover, the integration of digitalisation, automation, and data exchange plays a crucial role in enabling and optimising the recycling processes associated with electric motors, as highlighted by recent research . Such advancements are essential in driving sustainable development and enhancing resource management within the electric motor industry. Thus, recycling electrical steel is essential for implementing circular economy strategies and leveraging digitalisation and automation drive sustainable development and enhance resource management in the industry.

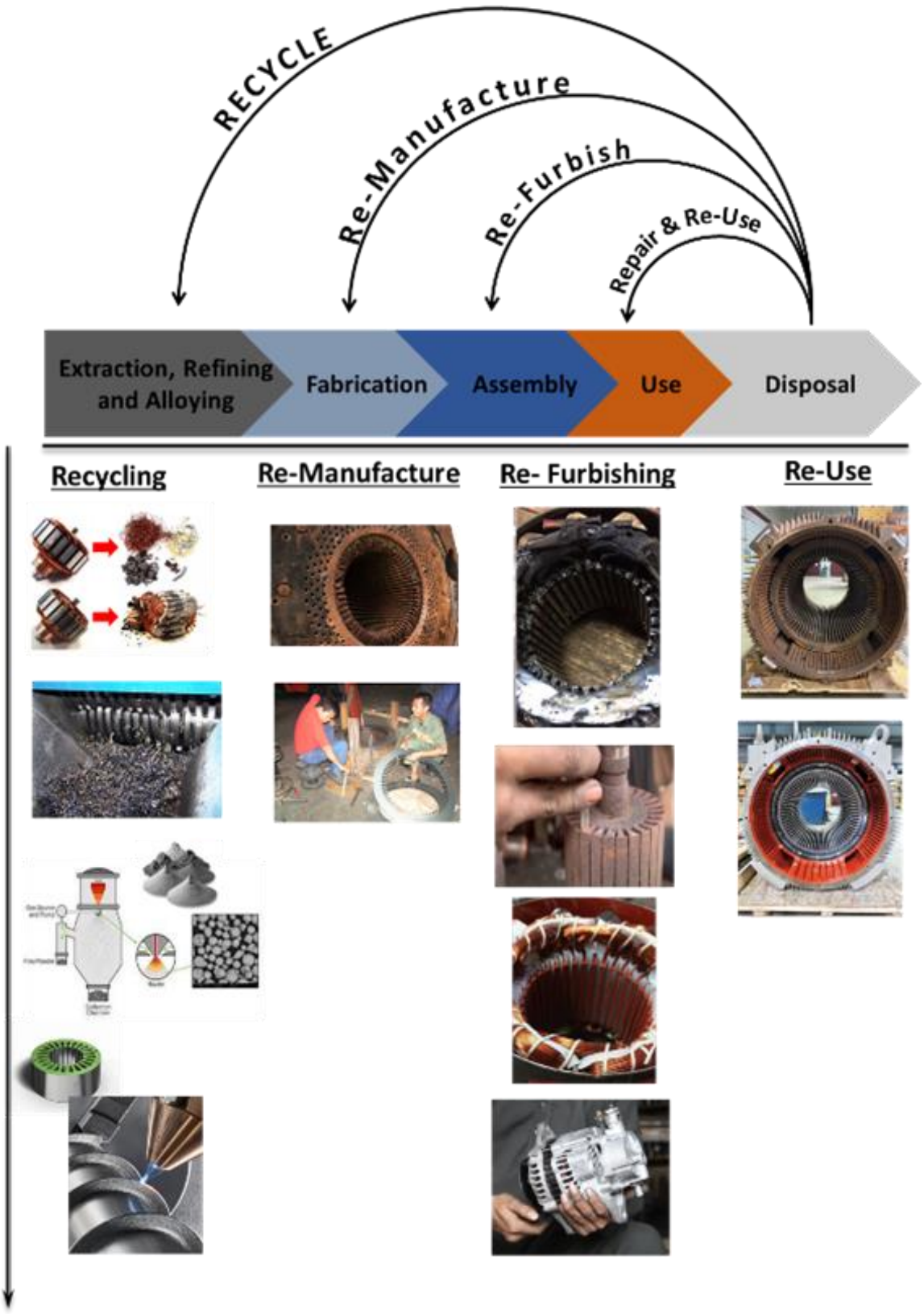

Figure 1. Circular economy of electrical steel Fe-Si.

Application of the LMD process in component repair and remanufacturing

High-value items that were previously impossible to repair or prohibitively expensive can now be repaired using the LMD technology . Repairing some small component by conventional methods parts can cause damage to the parts, due to significant HAZ area impact. Since the laser in the LMD process is employed as the energy source and has unique characteristics that enable it to be provided entirely to the targeted region due to its high directionality and coherency, that is why the LMD technique produces a very low heat affected zone. In the LMD process, rapid cooling prevents the melt pool from remaining too long and causes a low HAZ area which is another factor that contributes to LMD's effectiveness in successful repairing metallic parts. Furthermore, by employing the LMD technique, small components may be created and repaired with good accuracy due to the high resolution. The LMD process's capacity to create a new component on an existing part, while maintaining excellent metallurgical integrity, is another distinguishing feature. These key features make the LMD method well-suited for use in product repair applications . Capabilities of the LMD process such as repairing parts can also help to reduce the amount of scrap generated and carbon footprint. This technique is already being used by several industries, notably the aerospace, agriculture, and automobile sectors, to repair their critical components. For instance, this technology has been used in the oil exploration industry to coat hard materials such as tungsten carbide to increase the wear-resistance of cylindrical components. Additionally, the construction sector uses the LMD technology to coat wear-resistant blades for digging activities . Another application of the LMD technique is the repair of aerospace compressor turbine blades, as illustrated in Figure 2. These high-value, critical components posed a significant challenge for repair when manufactured as single, solid units. However, the LMD technique provides a viable solution, allowing for effective restoration without the need for scrapping, even when there are minor scratches that could compromise their functionality . Another sector that greatly benefits from the repair services provided by the LMD technology is the maritime industry . For instance, the repair of piston ring groves with high accuracy without causing any damage to the base materials. Research carried out by Nowotney et al. investigated the use of the LMD technology to restore corroded rifle barrels. The goal of this research was to develop a reliable procedure for fixing a broken gun barrel and to create the ideal substance to coat the barrel's surface to increase its useful life. The outcome of this investigation demonstrated that, with the right process settings, a damaged component can be successfully repaired using the LMD procedure. In this research , the composite, made up of a CoCrMo filler alloy and a strong TiC coating, was revealed to have greater wear-resistance qualities than any other material examined in this study. In addition to that, Bi and Gasser evaluated at the viability of employing the LMD technology with appropriate melt pool control to restore a damaged turbine blade (nickel super alloys) knife edge. In this project the metallurgical characteristics of the deposited layers were investigated, and a path-dependent process control method was employed in this work to avoid hot-cracking and increase the dimensional stability of the deposition. The analysis found that none of the samples taken from the deposit's top had any microcracks.

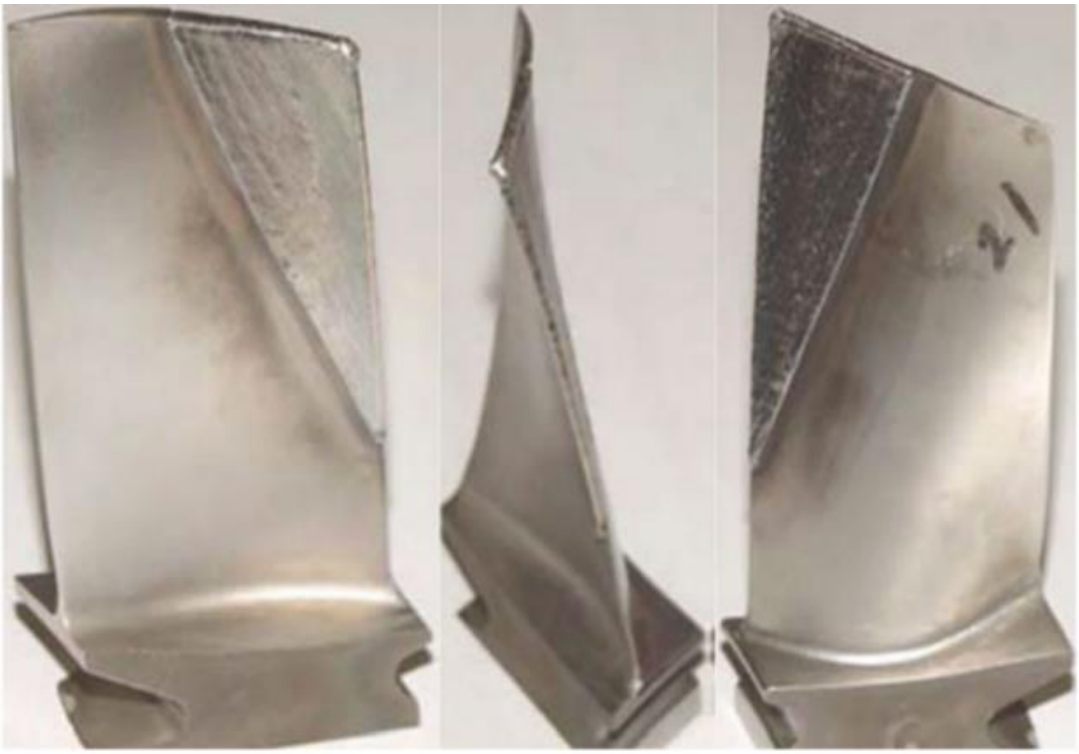

Figure 2. Repaired of a blisk air foil via LMD process .

One of the main benefits of additive manufacturing technique is the special ability of the LMD method to manufacture a new component on top of the original part with high metallurgical integrity. An outdated piece of equipment can be rebuilt with enhanced functioning and design using the LMD technology. This can be done without having to discard the old machinery, extending the useful life of the material, and lowering the requirement for material recycling, both of which assist to minimise global warming. Research is constantly being done to better position this additive manufacturing technology for effective remanufacturing. Wilson et al. used a semi-automated geometric reconstruction method and the LMD technique to research the remanufacturing of broken turbine airfoils. Lei et al. carried out a comparable examination into remanufacturing of defective impeller blades by using the LMD process Figure 3. The investigation concluded that the LMD could be used successfully in product remanufacturing. The microstructure analysed showed that no fractures or porosities, furthermore, the microhardness and tensile characteristics of the parts were demonstrated to have improved. Thus, the LMD is a promising method for cost-effective, environmentally friendly product remanufacturing. The LMD technology will assist to prolong the life of materials by contributing to resources as well as reducing discard. Moreover, the LMD technology can be used to modify and manufacture outdated equipment .

Figure 3. Illustration of defective impeller blades before and after.